Radiation and Background Levels in a CLIC Detector due to Beam-Beam Effects

Optimisation of Detector Geometries and Technologies

DISSERTATION

zur Erlangung des akademischen Grades

doctor rerum naturalium
(Dr. rer. nat.)
im Fach Physik

eingereicht an der
Mathematisch-Naturwissenschaftlichen Fakultät I
der Humboldt-Universität zu Berlin

von
Dipl.-Phys. André Sailer

Präsident der der Humboldt-Universität zu Berlin:
Prof. Dr. Jan-Hendrik Olbertz

Dekan der Mathematisch-Naturwissenschaftlichen Fakultät I:
Prof. Stefan Hecht, Ph.D.

Gutachter:
1. Prof. Dr. Thomas Lohse
2. Dr. Klaus Mönig
3. Prof. Mark Thomson

Tag der mündlichen Prüfung: 22. November 2012

In memory of my Grandfather

Abstract

The high charge density—due to small beam sizes—and the high energy of the proposed CLIC concept for a linear electron–positron collider with a centre-of-mass energy of up to 3 TeV lead to the production of a large number of particles through beam-beam interactions at the interaction point during every bunch crossing (BX). A large fraction of these particles safely leaves the detector. A still significant amount of energy will be deposited in the forward region nonetheless, which will produce secondary particles able to cause background in the detector. Furthermore, some particles will be created with large polar angles and directly cause background in the tracking detectors and calorimeters. The main sources of background in the detector, either directly or indirectly, are the incoherent e^+e^- pairs and the particles from $\gamma\gamma \to$ hadron events. The background and radiation levels in the detector have to be estimated, to study if a detector is feasible, that can handle the Compact Linear Collider (CLIC) background conditions.

Based on full detector simulations of incoherent e^+e^- pairs with the GEANT4 based MOKKA program, the detector geometry of a CLIC detector is optimised to minimise the background in the vertex detector. Following the optimisation of the geometry, the background and radiation levels for incoherent pairs and $\gamma\gamma \to$ hadron events are estimated. The possibility of identifying high energy electron showers with the most forward calorimeter, the BeamCal, is investigated.

During the optimisation of the detector layout, the hit density from backscattering particles in the innermost vertex layer is reduced from $14 \cdot 10^{-3}$ hits per square millimetre and bunch crossing to $0.5 \cdot 10^{-3}$ Hits/mm^2/BX. The total hit density from incoherent pairs is found to be $6 \cdot 10^{-3}$ Hits/mm^2/BX, with an additional $0.7 \cdot 10^{-3}$ Hits/mm^2/BX from $\gamma\gamma \to$ hadron events. Including safety and cluster factors, an occupancy of 2% for 20×20 µm^2 pixel sensors in the innermost vertex layer is estimated, which will require fast time-stamping of hits, but no multi-hit capable readout system. A total ionising dose of 50 Gy/yr and an equivalent neutron flux of $1.5 \cdot 10^{10}$ n_{eq}/cm^2/yr are found for the innermost vertex layer, which will require moderately radiation tolerant sensors. The occupancy at the inner radii of the hadronic calorimeter endcap, due to neutrons produced by showers in the BeamCal, is found to be too large, and either smaller pad sizes, or an improved shielding are necessary to reduce the occupancy to acceptable levels. It is possible to identify electron showers on top of the incoherent pair background in the BeamCal, and the identification efficiency is found to be beneficial to reject background events for the search of particles from beyond the Standard Model.

Zusammenfassung

Der Kompakte Linearbeschleuniger CLIC, ist ein Konzept für einen zukünftigen Elektron–Positron Beschleuniger mit einer Schwerpunktsenergie von 3 TeV. Die hohen Ladungsdichten, verursacht durch kleine Strahlgrößen, und die hohe Strahlenergie am CLIC, führen zur Produktion einer großen Menge von Teilchen durch Strahl-Strahl-Wechselwirkungen. Ein großer Teil dieser Teilchen wird den Detektor ohne Wechselwirkung verlassen, aber eine signifikante Menge Energie wird dennoch im Vorwärtsbereich des Detektors deponiert. Dadurch werden Sekundärteilchen erzeugt, von denen Einige Untergrund im Detektor verursachen werden. Es werden auch einige Teilchen mit inhärent großem Polarwinkel erzeugt, die direkt Untergrund in den Spurdetektoren und Kalorimetern verursachen können. Die Hauptursache von Untergrund im Detektor, entweder direkt oder durch Sekundärteilchen, sind inkohärente e^+e^- Paare und Teilchen aus hadronischen $\gamma\gamma$ Ereignissen. Die Untergrund- und Strahlungspegel im Detektor müssen bestimmt werden, um zu untersuchen, ob ein Detektor mit den Untergrundbedingungen bei CLIC zurechtkommen kann.

Mit Hilfe von Simulation der inkohärenten Paare in dem auf GEANT4 basierendem Programm MOKKA, wird die Geometrie eines auf Detektors für CLIC optimiert um den Untergrund im Vertexdetektor zu minimieren. In diesem optimiertem Detektor werden die Untergrund- und Strahlungspegel durch inkohärente e^+e^- Paare und hadronischen $\gamma\gamma$ Ereignissen bestimmt. Des Weiteren wird die Möglichkeit untersucht, ob Schauer von hochenergetischen Elektron bei kleinen Polarwinkeln im BeamCal zu identifizieren sind.

Durch die Optimierung der Detektorgeometrie wurde die Trefferdichte in der innersten Lage des Vertexdetektors von $14 \cdot 10^{-3}$ Treffer pro Quadratmillimeter und Strahlkreuzung (BX) auf $0.5 \cdot 10^{-3}$ Treffer/mm^2/BX reduziert. Die gesamte Trefferdichte beträgt $6 \cdot 10^{-3}$ Treffer/mm^2/BX durch inkohärente Paare und $0.7 \cdot 10^{-3}$ Treffer/mm^2/BX durch hadronische $\gamma\gamma$ Ereignisse. Inklusive Sicherheits- und Clusterfaktoren ergibt sich ein Belegungsgrad von 2% für Sensoren mit einer Pixelgröße von $20 \times 20\ \mu\mathrm{m}^2$. Für die innerste Lage des Vertexdetektors ergibt sich eine Dosis von 50 Gy/yr und ein äquivalenter Neutronenfluss von $1.5 \cdot 10^{10}\ \mathrm{n_{eq}/cm^2/yr}$. Neutronen, die bei Schauern im BeamCal entstehen, führen zu einem zu hohen Belegungsgrad in den inneren Radien der hadronischen Kalorimeterendkappe. Kleinere Sensorzellen oder eine bessere Abschirmung des Kalorimeters sind notwendig. Es ist möglich mit dem BeamCal hochenergetische Elektronen im Untergrund der inkohärenten Paare zu identifizieren. Die Identifikationseffizienz ist hoch genug um die Anzahl der Ereignisse von zwei Photonen Tau-Paarproduktion signifikant zu reduzieren, und die Suche nach Teilchen außerhalb des Standardmodells zu unterstüzen

Contents

1 Introduction

During the past several decades the Standard Model (SM) of particle physics was established. Its last building block, the Higgs Boson, will be found or ruled out in the coming months by the Large Hadron Collider (LHC), a proton–proton collider with a nominal centre-of-mass energy of $\sqrt{s} = 14$ TeV [1]. The ATLAS and CMS experiments are reducing the possible range of the Higgs masses, and only a small region remains for a SM Higgs boson around a mass of 125 GeV[*], or above 600 GeV [2, 3]. It is also expected that the LHC will find evidence of physics beyond the Standard Model. Regardless of the new physics discovered, a lepton collider will be useful to study the new phenomena with greater precision than it might be possible at a proton–proton collider [4].

In a lepton collider the centre-of-mass energy can be chosen with high precision giving better control over the initial state. One proposal for a future lepton collider is the Compact Linear Collider (CLIC), a linear electron–positron collider with a nominal centre-of-mass energy of 3 TeV. CLIC is based on room-temperature copper cavities, with a small bunch spacing of 0.5 ns and large gaps between bunch trains.

A circular electron–positron collider, like LEP, is not possible at higher energies, because of the synchrotron radiation emitted by the particles in the bending fields. On the other hand, at a linear collider, the large luminosities required to study new physics, can only be reached with small beam sizes. Unfortunately, the high energies and small beam sizes lead to a different type of synchrotron radiation, called *beamstrahlung*, as well as to the production of a large number of background particles covering the low polar angle region and causing background in the detector.

In 2012 a Conceptual Design Report (CDR) for the CLIC accelerator, detailing the technological feasibility issues will be published [5]. The report concentrates on a machine optimised for 3 TeV. The preferred energy, from a physics point-of-view, will be determined largely based on the results from the LHC.

The accelerator and detector design studies are closely linked: It has to be studied if a detector is feasible, which can handle the CLIC beam and background conditions, and which will deliver the full physics potential of the collider. The R&D still needed for various detector systems has to be identified. These topics are addressed in the recently published CLIC physics and detectors conceptual design report [4].

The detectors studied for CLIC are based on the detector concepts for the International Linear Collider (ILC), a linear electron–positron collider based on superconducting cavities, and a centre-of-mass energy between 500 GeV and 1 TeV [6]. Detailed background studies were done for the International Large Detector (ILD) detector concept of the ILC [7, 8], but the higher energy and shorter bunch spacing require CLIC specific background studies and optimisations.

The focus of this thesis is on the estimate of the occupancy and radiation levels in the various

---

[*] The natural units with $\hbar = c = 1$ are used.

subdetectors from the beam-induced backgrounds at CLIC. The rate of hits from the backgrounds needs to be known to design sensors with small enough granularities, as the occupancy in the detectors must not be too large to avoid spoiling the single point resolution of the individual sensors, or reducing the efficient pattern recognition of the whole tracking system. A too large occupancy might also reduce the shower separation and energy resolution in the calorimeters.

The ionising and non-ionising radiation induced by the backgrounds must be estimated, as they reduce the efficiency of the sensors over time and thus limit their lifetime. It is also studied how the detector layout affects the background rate, and what the optimal layout—given constraints from the accelerator—is.

For the subdetector most affected by the beam-induced backgrounds, the most forward electromagnetic calorimeter called *BeamCal*, the identification efficiency for high energy electrons is studied. In the BeamCal the energy deposit from the background during a single bunch crossing is at least a factor 20 above possible energy deposits from high energy electrons. The signal to background ratio is further reduced by the small bunch spacing, complicating the identification of high energy electrons even more.

The thesis is structured as follows. It starts with a short description of the CLIC accelerator in Chapter 2, detailing the main beam parameters, the two-beam acceleration scheme, and the features constraining the detector layout. In Chapter 3 the effects of the beam-beam interaction is discussed: how the small beam sizes necessary for the required luminosity lead to a significant amount of background that the detector has to be able to handle. The detector model used in the detailed simulation studies is described in Chapter 4; the main subdetectors of the detector are described, as well as the relevant impacts of the accelerator and engineering constraints. Chapter 5 describes the optimisation of the detector with respect to the background in the vertex detector. In Chapter 6 the estimated of the background, and radiation levels in the tracking detectors are presented. The background levels in the calorimeters are discussed in Chapter 7. The BeamCal is discussed in Chapter 8. The radiation doses and the possibility of electron tagging are studied. In Chapter 9 the electron tagging with the BeamCal is applied in a Monte Carlo study on the two-photon background for the measurement of the mass of the supersymmetric stau particle. Chapter 10 contains a summary and the conclusions.

2 Compact Linear Collider (CLIC)

The maximum centre-of-mass energy of the Large Electron–Positron Collider (LEP) was limited by the energy loss through synchrotron radiation, which is inversely proportional to the bending radius and the fourth power of the particle mass. To achieve a significantly higher centre-of-mass energy the radius of the ring would need to be increased.

With a linear electron–positron collider synchrotron radiation losses can be almost completely avoided. However, as the particles only pass the accelerator cavities once, a large accelerating gradient is needed to keep the length of the accelerator at a reasonable level. There are currently two proposals for a linear electron–positron collider: the International Linear Collider (ILC) [6] and the Compact Linear Collider (CLIC) [5].

The International Linear Collider (ILC) is based on superconducting niobium cavities with a centre-of-mass energy of up to $\sqrt{s} = 1.0$ TeV. The gradient of superconducting cavities is limited by the breakdown of the superconductive state. Such a breakdown occurs if the surface magnetic field, induced by the accelerating Radio Frequency (RF), exceeds a critical value [9]. The average gradient of the superconducting niobium cavities for the ILC is foreseen to be 31.5 MV/m [6].

The Compact Linear Collider (CLIC) derives its name from the high gradient of 100 MV/m, which would allow to build a shorter accelerator with the same beam energy as a superconducting equivalent. The CLIC baseline design is a centre-of-mass energy of $\sqrt{s} = 3$ TeV. In order to reach this gradient room temperature copper cavities have to be used. However, the RF pulses used for the acceleration of the beam have to be very short to reduce the heating of the cavity walls [5]. The pulse length and gradient are further limited by the maximal allowed breakdown rate of $3 \cdot 10^{-7}$ per pulse and per metre of structure [5].

2.1 Luminosity

Next to the centre-of-mass energy, the rate of collisions, or luminosity, is another important parameter of a collider. The production cross-section for lepton pairs (with a mass $m \ll \sqrt{s}$) is about 87 nb$/s$[GeV^2] [10], and at $\sqrt{s} = 3$ TeV amounts to around 10 fb. An instantaneous luminosity of a few 10^{34} cm^{-2}s^{-1} is necessary to collect large enough statistical samples in a reasonable time. The 3 TeV CLIC has an instantaneous luminosity of $\mathscr{L} = 5.9 \cdot 10^{34}$ cm^{-2}s^{-1}, and is expected to collect an integrated luminosity of 500 fb^{-1} per year with a fully commissioned machine running 200 days per year and an effective up-time of 50% [4].

The instantaneous luminosity depends on the (effective) transverse beam sizes $\sigma_{X,Y}$, the bunch population N, the repetition frequency f_{rep} of the trains, the number of bunches per train n_{b}, and

Table 2.1: Nominal machine parameters for the 3 TeV CLIC [11] and 14 TeV LHC [1].

	CLIC 3 TeV	LHC 14 TeV
Colliding particles	Electron–Positron	Proton–Proton
Instantaneous luminosity	$5.9 \cdot 10^{34}$ cm^{-2}s^{-1}	$1.0 \cdot 10^{34}$ cm^{-2}s^{-1}
IP size in X / Y / Z direction	45 nm / 1 nm / 44 µm	16.7 µm / 16.7 µm / 7.55 cm
Bunch charge	$3.72 \cdot 10^{9}$	$1.15 \cdot 10^{11}$
Bunch-crossing separation	0.5 ns	25 ns
Bunches per train	312	2808
Repetition rate	50 Hz	11.2 kHz
Crossing angle	20 mrad	0.28 mrad

the geometrical enhancement factor H_D [10],

$$\mathscr{L} = \frac{N^2 f_\mathrm{rep} n_\mathrm{b}}{4\pi \sigma_X \sigma_Y} H_\mathrm{D}. \tag{2.1}$$

The parameters (Table 2.1) were optimised to deliver the desired instantaneous luminosity with the most efficient machine. Large bunch charge and short bunch spacing are favoured for a high RF-to-beam efficiency, but they are limited by wake fields. The number of bunches, in combination with the bunch spacing, is limited by the pulse length [5].

Since the other parameters are constrained, the only way to achieve the desired luminosity is using very small bunch sizes, of the order of a few nanometres. For comparison, Table 2.1 also lists the nominal bunch parameters for the 14 TeV LHC. The luminosity of both machines is similar, but the bunches at the LHC are orders of magnitudes larger than at CLIC. To achieve a similar luminosity the larger bunch sizes are offset by a faster repetition rate and larger bunch charge possible at a circular collider.

2.2 Two-Beam Acceleration Scheme

The RF power used in acceleration cavities is normally provided by klystrons connected to the cavities. The number of klystrons that would be needed to accelerate the main beam at CLIC directly is too large, and their efficiency is too low [5]. Therefore a two-beam acceleration scheme is used to accelerate the beam to its nominal collision energy. A low energy (2.4 GeV) high current (100 A) *drive beam* is used to transfer the energy from conventional klystrons to the lower current *main beam*.

The drive beam is accelerated in a 140 µs long pulse consisting of bunches at a frequency of about 500 MHz (2 ns bunch spacing), and subtrains of 244 ns length. After the acceleration to 2.4 GeV, every second subtrain is delayed by 244 ns in the *delay loop*, which produces subtrains of 244 ns length with a bunch spacing of 1 ns followed by a gap of 244 ns. The following two *combiner rings* (see top half of Figure 2.1) decrease the bunch spacing by a factor 12, which results in a drive beam consisting of 24 subtrains of 244 ns length with a bunch spacing of 83 ps (a frequency of 12 GHz) and a gap between the trains of 5.85 µs [5].

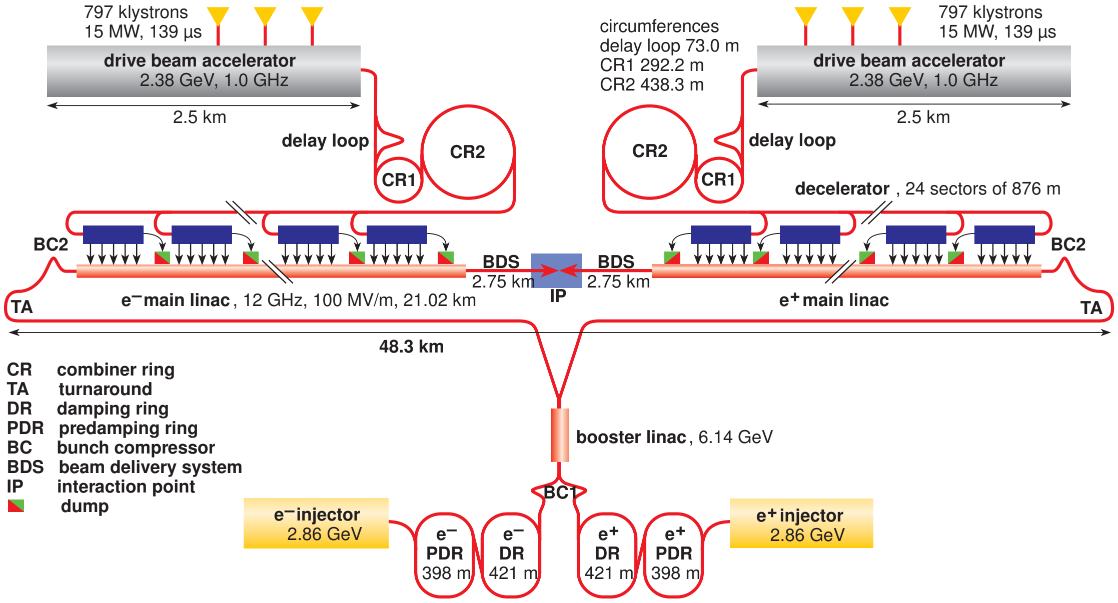

Figure 2.1: CLIC accelerator complex layout for $\sqrt{s} = 3$ TeV [5]

The 24 subtrains of the drive beam are transferred to the acceleration sectors (blue rectangles in Figure 2.1). In the acceleration sectors the drive beam is decelerated to 240 MeV in power extraction structures, and the RF power is transferred to the acceleration cavities for the main beam.

The electron bunches for the main beam are produced by a DC-photo gun, a technique which allows for a polarised electron beam. To produce the positron bunches electrons are accelerated to 5 GeV. These electrons pass through a thin target to produce photons, which are converted to electron–positron pairs in a second target. The positrons are then collected and accelerated towards the pre-damping and damping ring, after which they are also accelerated to 9 GeV and send towards the main beam accelerator [5]. Both the electron and positron bunches are generated with a bunch spacing of 1.0 ns. After the damping rings the bunch spacing is reduced to 0.5 ns with a delay loop similar to the one used for the drive beam.

After a long transfer line and a turnaround, the 9 GeV beams pass through 24 acceleration sectors, which are fed by the 24 subtrains of the drive beam. The main linear accelerators each have a length of 21 km. At the end of the main accelerator the beams are at the nominal beam energy of 1.5 TeV.

2.3 Beam Delivery System

The main accelerator is followed by the 2.8 km long Beam Delivery System (BDS), which transports the main beam to the collision at the Interaction Point (IP). Its main purpose is focusing the bunches to the small sizes. It also serves to protect the detector from machine induced backgrounds and is equipped to measure the energy and polarisation of the beams [5].

The last element of the BDS is the final focus quadrupole (QD0). The distance from the end of the QD0 to the IP is called $L^\star$. Vertical offsets of the QD0, caused by vibration, will directly translate into an offset of the beams at the IP. A QD0 stabilised to 0.15 nm at frequencies above 4 Hz is mandatory to preserve the luminosity [5]. The closer this quadrupole is positioned to the IP the smaller the impact of vibrations on the luminosity. In the accelerator baseline the QD0 is placed at $L^\star = 3.5$ m.

The QD0 is a hybrid between a permanent and an electromagnetic quadrupole. The core of the quadrupole has a radius of 3.5 cm, and the yoke with the coils has a diameter of around 60 cm [12]. In the current detector designs, the QD0 is placed inside the detector and thus has an impact on the layout of the detector forward region.

2.4 Crossing Angle

The distance between two bunches at CLIC is around 15 cm. To avoid parasitic collisions and deflections between bunches outside of the IP an angle between the electron and positron beam is needed [13]. The crossing angle cannot be too small due to the production of coherent pairs (discussed in Section 3.5) and the multi-bunch kink instability; its maximum value is given by the interaction of the beam with the detector solenoid field.

The coherent pairs require an exit cone in the detector with an opening of 10 mrad around the nominal beam line. To allow for enough space for the core of the QD0 close to the IP, a crossing angle of at least 20 mrad is needed [13].

The multi-bunch kink instability is caused by the deflection of the bunches. Because of the beam-beam interaction a vertical offset at the IP will lead to a vertical deflection. If the transverse distance between the incoming and outgoing beams is too small, this will lead to the deflection of the incoming beams, and to an even larger offset at the IP. The instability can be significantly reduced with a 20 mrad crossing angle [13].

Without a crossing angle the detector solenoid would be parallel to the beams. With the crossing angle the beams are affected by the solenoid field. The solenoid deflects the beams and causes the emission of synchrotron radiation, which leads to a blow up of the beam size. With a crossing angle of 20 mrad the luminosity loss is acceptable [13].

The reduced geometrical overlap of the colliding bunches caused by the crossing angle will be corrected by ‘Crab’ cavities. Crab cavities are used to rotate the bunches, so that they move slightly sideways and the optimal overlap between the bunches, and maximum luminosity, is kept [5].

3 Beam-Beam Interactions and Backgrounds at CLIC

In this chapter the interplay between the beam parameters (Table 2.1) and the resulting conditions at the Interaction Point (IP) of a high energy electron–positron linear collider will be described. The small bunches in combination with the charge density and high energy lead to strong forces between the particles of the colliding bunches. The forces deflect the particles, which results in a form of synchrotron radiation, called beamstrahlung, and in the production of a large number of charged background particles.

An in-depth discussion of the beam-beam interactions can be found in the references [14, 15, 16, 17, 18]; of which a summary is given here. To illustrate the beam-beam interaction and the dependence of the beam-beam interaction on the bunch parameters in an analytical model, the example of a static, homogeneous, and cylindrical charge distribution is used. In a real situation the charge distribution is not static, homogeneous, or cylindrical, and the actual beam-beam interactions have to be estimated through a Monte Carlo simulation. The qualitative dependence of the beam-beam effects on the bunch parameters, however, can be established with the simplified analytical model.

3.1 Simplified Description of the Beam-Beam Interaction

The charge density ρ_0 of a homogeneous cylindrical bunch with N particles of charge $-e$, length L, and radius R is

$$\rho_0 = \frac{-eN}{\pi L R^2}. \tag{3.1}$$

From the charge density the electric field $\vec{E}$ and magnetic field $\vec{B}$ can be calculated. They depend on the radial distance $r \leq R$ to the centre of the bunch,

$$\vec{E}(r) = \vec{e}_r \frac{-Ne}{\varepsilon_0 2\pi L R^2} r, \tag{3.2}$$

$$\vec{B}(r) = \vec{e}_\phi \frac{-Ne}{2\pi L R^2} \mu_0 v r, \tag{3.3}$$

where $\vec{e}_r$ is the unit vector in radial direction, $\vec{e}_\phi$ the unit vector in azimuthal direction, and the velocity of the bunch v, which is parallel to the cylinder axis.

The force $\vec{F}_{\text{intern}}$ on the particles in the same bunch,

$$\vec{F}_{\text{intern}} = -e(\vec{E} + \vec{v} \times \vec{B}) = \vec{e}_r \frac{Ne^2}{\varepsilon_0 2\pi L R^2} \left(1 - v^2\right) r = \vec{e}_r \frac{Ne^2}{\gamma^2 \varepsilon_0 2\pi L R^2} r, \tag{3.4}$$

is negligible for large $\gamma = (1 - v^2)^{-1/2} = E_{\mathrm{Beam}}/m_{\mathrm{e}}$, but for the forces $\vec{F}_{\mathrm{extern}}$ on the particles of the other bunch—with opposite charge and moving in the opposite direction—the $\vec{E}$ and $\vec{B}$ field add up,

$$\vec{F}_{\mathrm{extern}} = e(\vec{E} - \vec{v} \times \vec{B}) = -\vec{e}_r \frac{Ne^2}{\varepsilon_0 2\pi L R^2} \left(1 + v^2\right) r \approx -\vec{e}_r \frac{Ne^2}{\varepsilon_0 2\pi L R^2} 2r. \tag{3.5}$$

The force on a particle of mass m_{e}, and the gamma factor γ_{p} of the particle passing through the bunch give the equation of motion for the radial position $r(t)$,

$$\gamma_{\mathrm{p}} m_{\mathrm{e}} \ddot{r}(t) = -\frac{Ne^2}{\varepsilon_0 \pi L R^2} r(t). \tag{3.6}$$

The initial radial position of the particle at a distance $r_0 = r(t = 0)$ from the centre and movement parallel to the direction of the bunch $\dot{r}(t = 0) = 0$ result in

$$r(t) = r_0 \cos\left(\sqrt{\frac{Ne^2}{\pi \varepsilon_0 m_{\mathrm{e}} L R^2 \gamma_{\mathrm{p}}}} t\right), \tag{3.7}$$

or in terms of the longitudinal position $z = ct$ inside the bunch

$$r(z) = r_0 \cos\left(\sqrt{\frac{Ne^2 L}{\pi \varepsilon_0 m_{\mathrm{e}} R^2 \gamma_{\mathrm{p}}}} \frac{z}{L}\right). \tag{3.8}$$

3.1.1 Disruption

From the period of the oscillating motion (3.8) of the particle the disruption parameter D can be defined as

$$D = \frac{Ne^2 L}{\pi \varepsilon_0 m_{\mathrm{e}} R^2 \gamma_{\mathrm{p}}} = \frac{4N r_{\mathrm{e}} L}{R^2 \gamma_{\mathrm{p}}}, \tag{3.9}$$

with the classical electron radius $r_{\mathrm{e}} = e^2/(4\pi\varepsilon_0 m_{\mathrm{e}})$.

For $D < 1$ the particle is moved towards the centre of the bunch; for $D > 1$ the particle will perform an oscillating motion around the centre of the bunch. The deflection of the beam particles leads to the so-called pinch of the bunches, which reduces their size, and therefore to the geometrical enhancement factor H_{D} in Equation 2.1.

3.1.2 Deflection Angle

From the path of the particle in the bunch (3.8) the maximum deflection angle $\mathrm{d}r/\mathrm{d}z$ can be estimated [17]:

$$\frac{\mathrm{d}r}{\mathrm{d}z} = -r_0 \frac{\sqrt{D}}{L} \sin\left(\sqrt{D} \frac{z}{L}\right). \tag{3.10}$$

At the end of the bunch ($z = L$) the deflection angle θ for $D \ll 1$ is

$$\theta \approx -r_0 \frac{D}{L} = -r_0 \frac{4N r_{\mathrm{e}}}{R^2 \gamma_{\mathrm{p}}}. \tag{3.11}$$

The maximum deflection angle therefore is inversely proportional to the energy of the particle ($\gamma_{\mathrm{p}} = E/m$).

For particles with the same charge as the oncoming beam the force is repelling instead of attracting. The equation of motion

$$\gamma_{\mathrm{p}} m_{\mathrm{e}} \ddot{r}(t) = + \frac{Ne^2}{\varepsilon_0 \pi L R^2} r(t), \tag{3.12}$$

with a particle starting parallel to the direction of the oncoming bunch and at a distance r_0 gives for the radial position inside the bunch

$$r(z) = r_0 \cosh\left(\sqrt{\frac{Ne^2 L}{\pi \varepsilon_0 m_{\mathrm{e}} R^2 \gamma_{\mathrm{p}}}} \frac{z}{L}\right) = r_0 \cosh\left(\sqrt{D}\frac{z}{L}\right). \tag{3.13}$$

Similarly to (3.10) the deflection angle is

$$\frac{\mathrm{d}r}{\mathrm{d}z} = r_0 \frac{\sqrt{D}}{L} \sinh\left(\sqrt{D}\frac{z}{L}\right). \tag{3.14}$$

For large values of D, the deflection angle can become quite large while a particle is passing through the oncoming bunch. However, outside of the bunch, the force becomes smaller ($\propto 1/r$), so that the right-hand side of Equation 3.12 is no longer valid. Due to the γ_{p} factor on the left-hand side of (3.12), the deflection angle will always depend inversely on the energy of the deflected particle.

3.2 Beamstrahlung

The pinch effect due to the attraction of the oppositely charged bunches increases the luminosity. However, the deflected particles will also produce a form of synchrotron radiation, called *beamstrahlung*, which is characterised by the beamstrahlung parameter Υ_{av} [14, 16, 17]. It can be expressed as the average field (B or E) in the bunch divided by the Schwinger critical field [19] $B_{\mathrm{c}} = m_{\mathrm{e}}^2/e$,

$$\Upsilon_{\mathrm{av}} = \gamma \frac{< B >}{B_{\mathrm{c}}} \propto \frac{\gamma N r_{\mathrm{e}} \lambda_{\mathrm{e}}}{LR}, \tag{3.15}$$

with the Compton wave-length for electrons $\lambda_{\mathrm{e}} = 1/m_{\mathrm{e}}$. The amount of beamstrahlung increases proportionally with an increase in the beam-beam force.

For Gaussian beams, instead of the length L and the radius R the r.m.s. bunch sizes $\sigma_{X,Y,Z}$ are used, in this case the average and maximum beamstrahlung parameters are [14, 16, 17, 20]

$$\Upsilon_{\mathrm{av}} \approx \frac{5}{6} \frac{\gamma N r_{\mathrm{e}} \lambda_{\mathrm{e}}}{\sigma_Z (\sigma_X + \sigma_Y)}, \tag{3.16}$$

$$\Upsilon_{\mathrm{max}} \approx \frac{12}{5} \Upsilon_{\mathrm{av}}. \tag{3.17}$$

The beamstrahlung can be further characterised by the average number of photons n_γ produced per initial particle during a collision [16]

$$n_\gamma \approx 2.54 \left(\frac{\alpha \sigma_Z}{\gamma \lambda_e} \Upsilon \right) \frac{1}{(1+\Upsilon^{2/3})^{1/2}}, \tag{3.18}$$

where α is the fine-structure constant. The radiation of photons leads to an energy loss. The average relative energy loss δ of the initial beam particles due to beamstrahlung is [16]

$$\delta \approx 1.24 \left(\frac{\alpha \sigma_Z}{\gamma \lambda_e} \Upsilon \right) \frac{\Upsilon}{(1+(1.5\Upsilon)^{2/3})^2}. \tag{3.19}$$

To achieve a large luminosity the product of the transverse bunch sizes should be small (2.1), and their sum should be large (3.16) to limit the energy loss due to beamstrahlung. Therefore flat beams are usually used for linear collider designs, e.g., at CLIC $\sigma_X/\sigma_Y \approx 45$. With $\Upsilon_{\mathrm{av}} \approx 5$ the beamstrahlung at CLIC is a very important phenomenon.

3.3 Simulation of the Beam-Beam Interaction

In order to take the dynamically changing bunch geometries (due to deflection), reduced particle energies (due to beamstrahlung), and their impact on the fields into account a Monte Carlo simulation has to be used.

The Monte Carlo programs CAIN [21] and GUINEAPIG [22], simulate the crossing of the bunches through the use of macro-particles. Each macro particle represents several thousand beam-particles. The macro-particles are distributed according to the distribution of charges in the bunches and used to calculate the fields, forces, and movements of the particles during the crossing of the two bunches. The crossing of the bunches is divided into several steps, and for each step the forces, movements and other possible effects, such as beamstrahlung, are simulated.

Comparisons between CAIN and GUINEAPIG have shown that both programs produce similar results [22, 23]. For the simulation of the beam-beam interaction at CLIC GUINEAPIG is used. The initial particle distributions of the bunches are generated by a simulation of the main linac and the BDS [24][*].

The results from the GUINEAPIG simulation for the parameters classifying the beam-beam interactions are given in Table 3.1. Here, also the results for the analytical formulae shown above are compared to the results from the simulation. For the calculated luminosity the enhancement factor $H_{\mathrm{D}} = 1$ was taken. The largest difference between the formulae and the simulation is the average energy loss of the beam particles, which is overestimated by the analytical expression compared to the simulation.

3.4 Luminosity Spectrum

The energy loss of individual beam particles leads to collision energies below the nominal centre-of-mass energy. This so called luminosity spectrum or differential luminosity is also obtained

---

[*] More details on running GUINEAPIG are given in Appendix A.

Table 3.1: The instantaneous luminosity $\mathscr{L}$, maximal beamstrahlung parameter Υ_{max}, the number of beamstrahlung photons per bunch particle n_γ, and the average relative energy loss of the particles δ calculated by the respective equations in the text and from the simulation with GUINEAPIG for CLIC at $\sqrt{s} = 3$ TeV.

Parameter (Equation)	Analytical	Simulation
$\mathscr{L}$ $[10^{34}\ \mathrm{cm}^{-2}\mathrm{s}^{-1}]$ (2.1)	3.8	5.9
Υ_{max} (3.17)	12	15
n_γ (3.18)	1.8	2.1
δ (3.19)	0.37	0.27

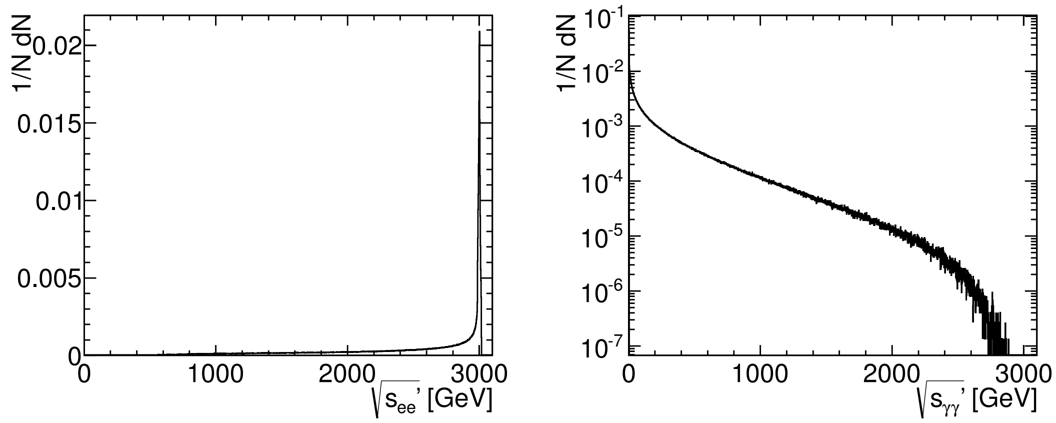

(a) Differential e^+e^- luminosity

(b) Differential $\gamma\gamma$ luminosity

Figure 3.1: Distribution of effective centre-of-mass energies $\sqrt{s'}$ for (a) e^+e^- and (b) $\gamma\gamma$ collisions as predicted by GUINEAPIG.

from GUINEAPIG.

The distribution of e^+e^- centre-of-mass energies $\mathrm{d}N/\mathrm{d}\sqrt{s}$ is shown in Figure 3.1a. Despite the large average energy loss, the majority of events still takes place at the nominal centre-of-mass energy, but the tail extends almost to zero. The total instantaneous e^+e^- luminosity is $5.9 \cdot 10^{34}\ \mathrm{cm}^{-2}\mathrm{s}^{-1}$ with $2.0 \cdot 10^{34}\ \mathrm{cm}^{-2}\mathrm{s}^{-1}$ in the top 1% of the energy [4]. Asymmetric radiation of beamstrahlung from two colliding particles can result in events with a boost parallel to the beam axis.

There is also a significant luminosity for $\gamma\gamma$ interactions, because of the large flux of photons. On average every particle in a bunch radiates 2.1 photons (Table 3.1). The total $\gamma\gamma$ luminosity is $4.7 \cdot 10^{34}\ \mathrm{cm}^{-2}\mathrm{s}^{-1}$, however, as can be seen in Figure 3.1b, the peak of the $\gamma\gamma$ luminosity is at very small centre-of-mass energies.

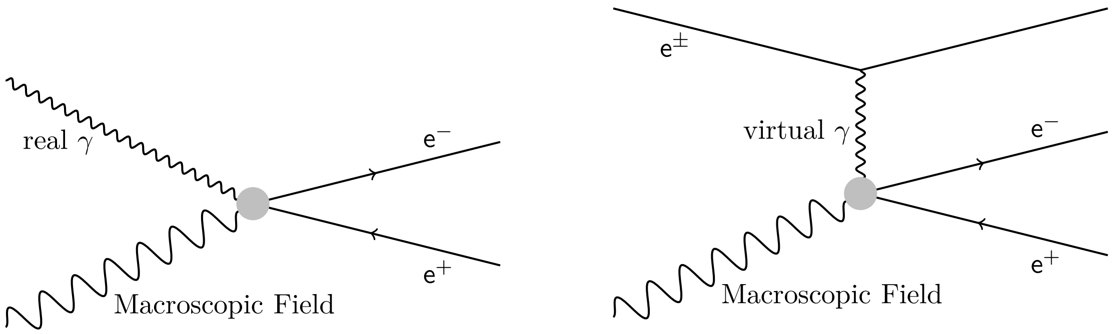

(a) Coherent pair production

(b) Trident cascade

Figure 3.2: Coherent and Trident pair production processes [22, 26]

3.5 Coherent Electron–Positron Pair Production

Due to the strong fields during the collisions (i.e., $B \geq B_c$) individual particles interact with the coherent field of the oncoming bunch and produce e^+e^- pairs. There are two processes: the interaction of a real photon—e.g., from beamstrahlung—with the field, the coherent pair production [25] (Figure 3.2a); and the interaction of an electron—via a virtual photon—with the field, which leads to the trident cascade [26] (Figure 3.2b).

The coherent production processes can be interpreted as follows: a virtual electron–positron pair around a photon gains enough energy from the external field to be kicked on-shell; the energy and momentum are conserved by the field [16].

3.5.1 Coherent Pairs

The number of coherent pairs n_{coh} produced per primary beam particle is given by [25]

$$n_{\mathrm{coh}} \approx \frac{4\sqrt{3}}{25\pi}\left(\frac{\alpha\sigma_Z}{\gamma\lambda_e}\Upsilon\right)^2 \times \begin{cases} 0.5\exp\left(-\frac{16}{3\Upsilon}\right) & ,\Upsilon \lesssim 1 \\ 2.6\Upsilon^{-2/3}\ln\Upsilon & ,\Upsilon \gg 1. \end{cases} \tag{3.20}$$

For small values of Υ the coherent pair process is exponentially suppressed, but the process becomes important for larger values of Υ, e.g., at a 3 TeV CLIC machine.

3.5.2 Trident Pairs

Similarly to the coherent pair production probability, the number of particles from the trident cascade n_{tri} can be expressed as [25]

$$n_{\mathrm{tri}} = \frac{4\sqrt{3}}{25\pi}\left(\frac{\alpha\sigma_Z}{\gamma\lambda_e}\Upsilon\right) \times 2.6\alpha\ln\Upsilon \qquad ,\Upsilon \gg 1. \tag{3.21}$$

The factor $\left(\frac{\alpha\sigma_z}{\gamma\lambda_e}\Upsilon\right)$ is present for both the coherent pairs (3.20) and the trident pairs (3.21) and also in the average energy loss of the initial particles (3.19). This energy loss has to be limited, for a reasonable luminosity spectrum with a large fraction of events at the nominal centre-of-mass energy, which will also limit the number of coherent and trident pairs [25, 26].

3.5.3 Minimum Energy of Coherently Produced Particles

The minimum energy E_{min} of a particle produced via a coherent process is [25]

$$E_{\mathrm{min}} = \frac{E_{\mathrm{Beam}}}{k\Upsilon}. \tag{3.22}$$

The factor k is given between 5 [25] and 20 [16]. At CLIC, with $\Upsilon_{\mathrm{max}} \approx 15$ the minimum energy is found to be between 20 GeV and 5 GeV. As a result, the large number of coherently produced particles has only a limited impact on the detector: they are travelling in the direction of the outgoing beam, because their deflection angle is small due to their high energy.

3.5.4 Coherent and Trident Pairs at CLIC

The total number of coherently produced particles at CLIC, estimated by the GUINEAPIG simulation, is around 10% of the number of particles in the two bunches or about $7 \cdot 10^8$ per Bunch Crossing (BX). The number of particles produced from the trident cascade is a factor hundred below that, around $7 \cdot 10^6$ particles [27].

Although there is a large number of coherent particles, their production angle is small, and because of the large energy, so is their deflection angle. Figure 3.3a shows the energy spectrum of the coherent and trident pairs: their maximum energy is 1.5 TeV, and the cut-off is at 10 GeV for the coherent pairs, within the range predicted by Equation 3.22. The energy spectrum for the trident pairs is broader and extends to lower energies, but the minimal energy is above 1 GeV.

Figure 3.3b shows the total energy of the coherent and trident pairs in a given polar angle θ[†]. Most energy is concentrated at small polar angles. At 10 mrad there is less than 0.5 TeV/mrad per bunch crossing. To avoid large energy deposits from the coherent pairs, there must not be any material present in a cone with a half-opening angle of about 10 mrad around the outgoing beam axis [13]. This fact has an impact on the crossing angle at CLIC (see Section 2.4).

3.6 Incoherent Electron–Positron Pair Production

The direct interaction of individual particles will also lead to the production of electron–positron pairs. Similarly to the coherent production of pairs, the photon flux for real photons via beamstrahlung, and the flux of virtual photons play a role. The two sources of photons lead to three different processes. The Breit–Wheeler (BW) interaction of two real photons, the Bethe–Heitler (BH) process of one real and one virtual photon, and the Landau–Lifschitz (LL) process, in which two virtual photons interact. Figure 3.4 shows the Feynman graphs for these processes.

[†] The polar angle is generally given with respect to the outgoing beam axis.

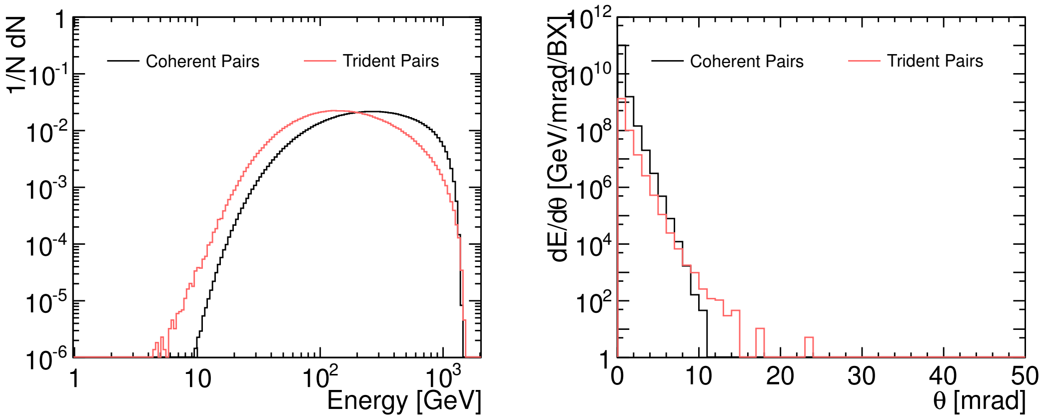

(a) Energy spectrum

(b) Angular dependence of the energy

Figure 3.3: (a) Energy spectrum and (b) angular distribution of the energy for coherent electron–positron pairs.

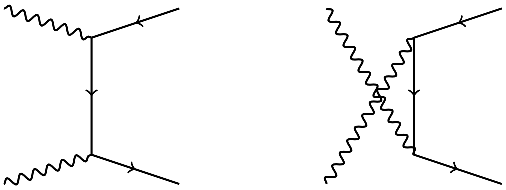

(a) Breit–Wheeler

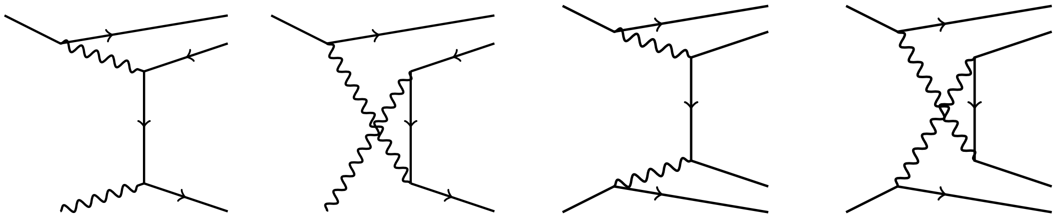

(b) Bethe–Heitler

(c) Landau–Lifschitz

Figure 3.4: Incoherent pair production processes [22].

The kernel of all processes is the pair production by two photons [28]. The real photon spectrum is described by the beamstrahlung photons. The virtual photon spectrum can be described by the Weizsäcker–Williams equivalent photon approximation [14, 16, 28]. The effective total cross-sections for a single final state particle are [16]:

$$\sigma_{\mathrm{BW}} = 4.9\frac{\alpha^2 r_{\mathrm{e}}^2}{\gamma^2}\, K^2 \left(\frac{\gamma m_{\mathrm{e}}}{p^\star}\right)^{4/3} \log\frac{1}{\tau_0}, \tag{3.23}$$

$$\sigma_{\mathrm{BH}} = 15.4\frac{\alpha^2 r_{\mathrm{e}}^2}{\gamma^2}\, K \left(\frac{\gamma m_{\mathrm{e}}}{p^\star}\right)^{5/3} [\tau_0^{1/3} - \tau_0^{-1/3}] \left[\log\frac{p^\star \tau_0}{2\gamma m_{\mathrm{e}}} + 0.21\right], \tag{3.24}$$

$$\sigma_{\mathrm{LL}} = 5.09\frac{\alpha^2 r_{\mathrm{e}}^2}{\gamma^2} \left(\frac{\gamma m_{\mathrm{e}}}{p^\star}\right)^{2} \log\frac{1}{\tau_0} \left[\log\frac{p^\star \tau_0}{2\gamma m_{\mathrm{e}}} \log\frac{p^\star}{2\gamma m_{\mathrm{e}} \tau_0} + 3\log\frac{p^\star}{2\gamma m_{\mathrm{e}}} + 4.44\right], \tag{3.25}$$

with the minimal required transverse momentum $p^\star$, and $\tau_0 = \tan\theta_0/2$ the tangent of half the minimal angle θ_0 of the produced particle. The factor

$$K = \left(\frac{\sigma_Z}{\gamma \lambda_{\mathrm{e}}}\right) (\Upsilon)^{2/3} \tag{3.26}$$

describes the dependence on the beam parameters. The effective Landau–Lifschitz cross-section does not depend directly on the beam parameters, but only on the instantaneous differential luminosity.

The production threshold for the incoherent $\mathrm{e}^+\mathrm{e}^-$ pairs is twice the electron mass, therefore the majority of the particles produced through these processes will be deflected strongly by the fields of the oncoming bunch and their initial production angle is not important for the final angular distribution.

For higher energy particles and larger production angles, for which deflection is less important, the rate can be estimated using the effective cross-sections. With the CLIC parameters (Table 2.1), and with the momentum $p^\star = 20$ MeV and angle $\theta_0 = 7.3°$—corresponding to the values necessary to reach the vertex detector (see Section 4.3)—the effective cross-sections for electrons and positrons (i.e., a factor 2) are $2\sigma_{\mathrm{BW}} = 0.6$ µb, $2\sigma_{\mathrm{BH}} = 7.6$ µb, and $2\sigma_{\mathrm{LL}} = 8.4$ µb. With a luminosity of $3.8\mu\mathrm{b}^{-1}/\mathrm{BX}$ about 63 particles can be expected in every bunch crossing at large initial angles. The total number of incoherent $\mathrm{e}^+\mathrm{e}^-$ particles per bunch crossing, regardless of their momentum or production angle, is $3.3 \cdot 10^5$ according to the GUINEAPIG simulation [27].

3.6.1 Incoherent Muon Pairs

The same incoherent processes which produce electron–positron pairs can also produce muon pairs. The rate of muons and electron pairs is the same for events with a transverse momentum above the muon mass. The total number of incoherent muon pairs produced at CLIC results in 12 muons per bunch crossing in the full solid angle [26].

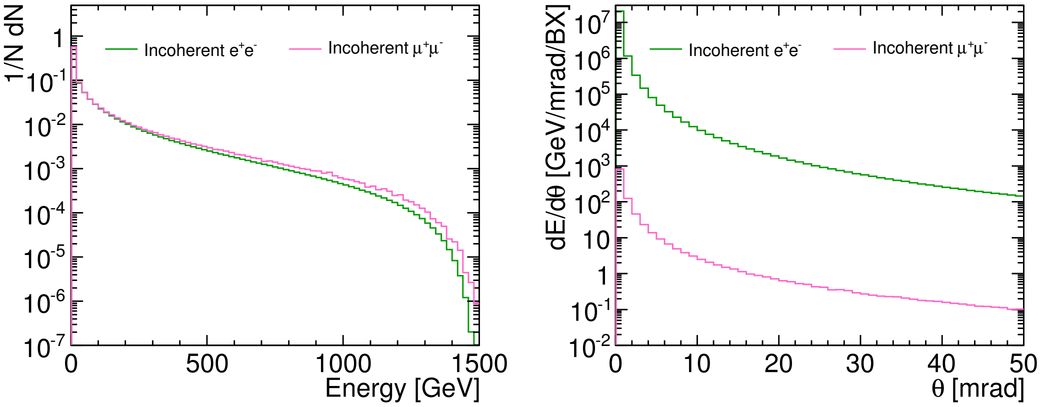

(a) Energy spectrum

(b) Angular distribution of the energy

Figure 3.5: (a) Energy spectrum and (b) angular distribution of the energy for incoherent electron–positron and muon pairs.

3.6.2 Energy and Angular Spectrum of Incoherent Pairs

Figure 3.5a shows the energy distribution of the incoherent e^+e^- and muon pairs. For both processes the energy distribution peaks at the lowest possible energy, the respective rest mass of the electrons or muons.

The energy distribution vs. the polar angle, after deflection through beam-beam interaction, is shown in Figure 3.5b. Because of their larger number, the energy from incoherent e^+e^- pairs is much larger than for the muon pairs. The energy from incoherent electron–positron pairs is larger than from the coherent or trident pairs at polar angles larger than 10 mrad. The large number of particles and their large deflection angle make the incoherent e^+e^- pairs one of the most important backgrounds.

For a better estimate of the expected rate in the detector the transverse momentum of the particles has to be taken into account, as shown in Figure 3.6, where the transverse momentum is plotted against the polar angle. The transverse momentum of the particle determines its bending radius in a magnetic field and the polar angle influences where the maximal distance to the detector axis is first reached. The position of the detector components of radius R_{Det} and length Z_{Det} can be translated into this p_{T}–θ coordinate system [29]

$$p_{\mathrm{T}}[\mathrm{GeV}] \approx 0.3 B[\mathrm{T}] \cdot \frac{R_{\mathrm{Det}}[\mathrm{m}]}{2}, \tag{3.27}$$

$$\theta = \arctan\left(\frac{\pi}{2}\frac{R_{\mathrm{Det}}}{Z_{\mathrm{Det}}}\right). \tag{3.28}$$

In Figure 3.6 the black lines represent the vertex detector, and the outline of the beam pipe is marked by red lines (see Chapter 4 for a description of the detector). The two vertical red lines, at 100 mrad and 10 mrad, mark the two cones of the beam pipe pointing to the IP (the beam

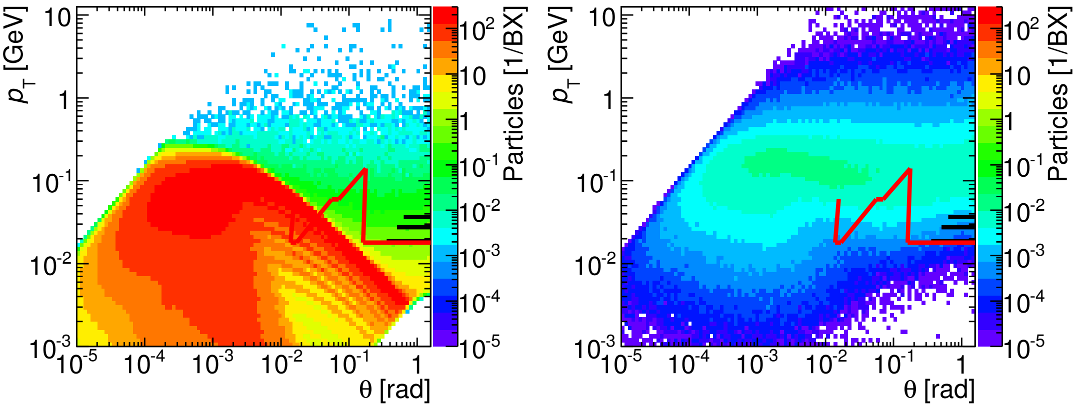

(a) Incoherent e^+e^-

(b) Incoherent muons

Figure 3.6: Transverse momentum p_T against polar angle θ for incoherently produced electron and muon pairs.

pipe is shown in Figure 4.2 and 4.3 of Chapter 4). Particles can only hit a part of the detector, if they are located at larger polar angles and transverse momenta—i.e., above or to the right of the respective lines. The cut-off at the top left of the figure is due to the maximum particle energy of 1.5 TeV, and the cut-off at the lower right of the figure is due to the minimal particle energy of 5 MeV, which is the cut-off chosen in GUINEAPIG. In these figures, all polar angles are with respect to the outgoing beam axis, even though the inner detector elements are aligned with the detector axis. The 10 mrad correction is negligible for the larger polar angles.

The highly populated area in Figure 3.6a comes from particles which have been deflected by the beam-beam force. This area is due to the dependence of the deflection angle on the energy of the particles (Equation 3.11). The central part of the beam-pipe has to stay outside of this region, because the particles interacting with the material of the beam pipe would otherwise cause too much background in the detector.

There are also some particles, which are already produced with large angles, and therefore located above the edge from the deflection of particles [22]. There are about 60 particles per bunch crossing with $p_T > 20$ MeV and $\theta > 7.3°$, estimated with either Equations 3.23, 3.24, and 3.25, or using GUINEAPIG. These particles are one of the biggest source of direct background in the central detector. The magnetic field reduces the reach of the low energy particles, and a previous background study for CLIC estimated that the minimal allowed radius for the vertex detector in a 4 T field is about 30 mm [30]. This corresponds to a transverse momentum of 18 MeV (Equation 3.27). There is still a significant number of particles with a large enough angle and transverse momentum to reach the vertex detector and beyond.

The number of incoherent muons, shown in Figure 3.6b, produced with momentum and angle dangerous to the vertex detector is significant, but smaller than the number of incoherent e^+e^- pairs.

In the simulation the muon cross-section was artificially increased by a factor 10^3, so that the sample corresponds to $9 \cdot 10^4$ bunch crossings, for the e^+e^- pairs the sample only corresponds to 936 bunch crossings.

3.7 Hadronic Background

In the interaction of photons also quark pairs, and therefore hadrons can be produced [14, 31, 32]. The $\gamma\gamma$ cross-sections were only measured at—compared to CLIC—relatively low centre-of-mass energies of up to 200 GeV at the LEP [33, 34], and there is some disagreement on the appropriate extrapolation to higher centre-of-mass energies [35]. However, the beamstrahlung photons (Figure 3.1b) and the Weizsäcker–Williams equivalent photon spectrum [36] both peak at small energies. And at lower centre-of-mass energies the cross-sections have been measured.

The cross-section of the $\gamma\gamma \to$ hadron process $\sigma_{\gamma\gamma}$ for the CLIC studies is taken from Schuler and Sjöstrand [37]

$$\sigma_{\gamma\gamma}(s[\mathrm{GeV}^2]) = 211\ \mathrm{nb} \cdot s^{0.0808} + 215\ \mathrm{nb} \cdot s^{-0.4525}, \tag{3.29}$$

where s is the centre-of-mass energy squared.

Folding the $\gamma\gamma$ luminosity with the cross-section gives the effective cross-section and expected event rate. On average 3.2 $\gamma\gamma \to$ hadron events with a centre-of-mass energy above 2 GeV are expected in each bunch crossing at CLIC [38]. The energies of the two colliding photons are passed from GUINEAPIG to PYTHIA [39] for the generation of the hard interaction and following hadronisation [40].

Figure 3.7 shows the energy spectrum of the final state particles from the $\gamma\gamma \to$ hadron events and the total energy per bunch crossing in a given polar angle. The maximum energy of the particles (1.3 TeV) is smaller than for the other processes. The particles are produced with large angles, but the energy is smaller than that of the incoherent e^+e^- pairs.

Figure 3.8 shows the transverse momentum and polar angle of the final state particles from the $\gamma\gamma \to$ hadron events. The vertex detector and the beam pipe are marked as in Figure 3.6. The minimal c.m.s. energy of 2 GeV can be seen in the cut-off in the centre right of the distribution. The production angle of the particles is more central than for the incoherent pair processes, and the transverse momentum is larger. Even though the number of events per bunch crossing is smaller, the number of particles reaching the detector is similar to the incoherent electron–positron pairs.

3.8 Radiative Bhabha Events

The Bhabha process, the scattering of an electron and positron

$$e^+e^- \to e^+e^- \tag{3.30}$$

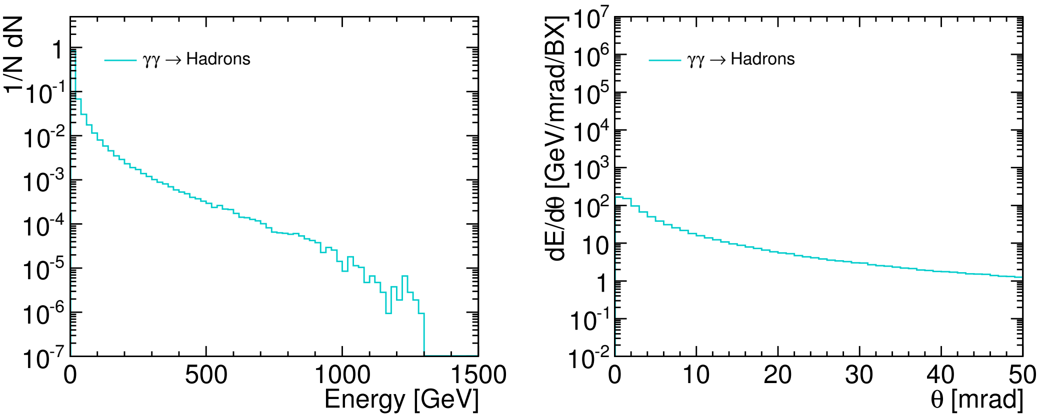

(a) Energy spectrum

(b) Angular distribution of the energy

Figure 3.7: (a) Energy spectrum and (b) angular distribution of the energy for $\gamma\gamma \rightarrow$ hadron events.

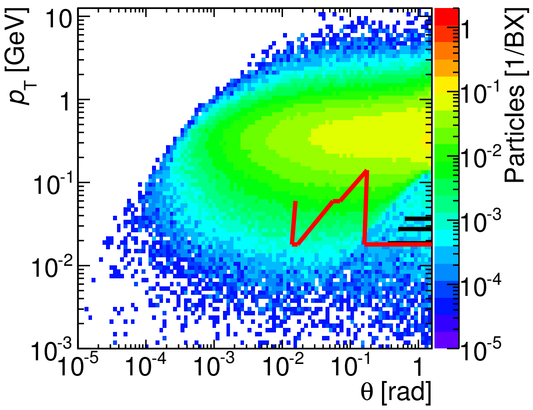

Figure 3.8: Transverse momentum p_{T} against polar angle θ for the final state particles of the $\gamma\gamma \rightarrow$ hadron events.

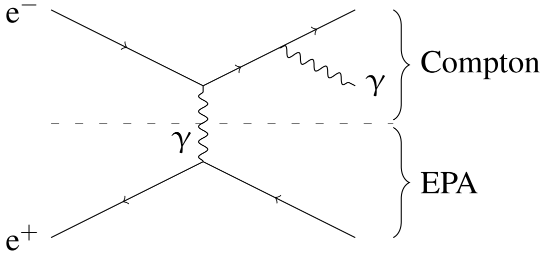

Figure 3.9: Feynman diagram for a radiative Bhabha event. For the cross-section assumed in GUINEAPIG the bottom part is replaced by the equivalent photon approximation (EPA) and the top part is the Compton process.

has a large cross-section, especially at small angles and low c.m.s. energies. The differential cross-section for small scattering angles θ in the centre-of-mass system is given by [41]

$$\frac{\mathrm{d}\sigma_{\mathrm{Bhabha}}}{\mathrm{d}\theta} = \frac{2\pi\alpha^2}{s}\frac{\sin\theta}{\sin^4\theta/2}. \tag{3.31}$$

If one of the particles radiates a photon

$$\mathrm{e}^+\mathrm{e}^- \rightarrow \mathrm{e}^+\mathrm{e}^-\gamma(\gamma\ldots) \tag{3.32}$$

the electron–positron system does not correspond to the centre-of-mass system; and the scattering angle of the radiating particle in the laboratory system is increased. The system is also boosted if one of the scattering particles has lost its energy through beamstrahlung.

In GUINEAPIG only Bhabha events with a small momentum transfer $Q^2 \leq m_\mathrm{e}^2$ are generated. The momentum transfer can be approximated as $Q^2 = s \cdot \sin^2(\theta/2) \approx p_\mathrm{T}^2$ in the centre-of-mass system [41]. Therefore the cut corresponds to a small scattering angle in the centre-of-mass frame. It is assumed that one of the particles, e.g. the electron, radiates a hard photon, which is giving the electron–positron system a boost. Figure 3.9 shows a Feynman diagram for the process. The other particle, here the positron, is replaced by its equivalent photon-spectrum and remains at the small scattering angle. The photon interacts with the electron as in the Compton-scattering process [15, 42]. Only the particle with the large scattering angle is stored.

The Bhabha scattering was also estimated with the 'Wide Angle Bhabha generator' BHWIDE [43], and with the multi purpose Monte Carlo generator WHIZARD [44, 45]. BHWIDE is a Monte Carlo generator specifically developed for Bhabha events and is also working for small angles [46]. Both generators were used with the luminosity spectrum obtained from GUINEAPIG (see Section 3.3). These generators are used to complement the Bhabha scattering simulated with GUINEAPIG at larger momentum transfers.

BHWIDE was run at the nominal centre-of-mass energy $\sqrt{s} = 3$ TeV, minimal outgoing energies for the particles of 10 GeV, and a minimal scattering angle of 1 mrad. The luminosity spectrum is fed into BHWIDE on an event by event basis, similarly to the method used in [47]: The events are generated in the nominal centre-of-mass system at 3 TeV. Then the effective centre-of-mass system from the event s_eff is used to calculate a weight, which in turn is used to

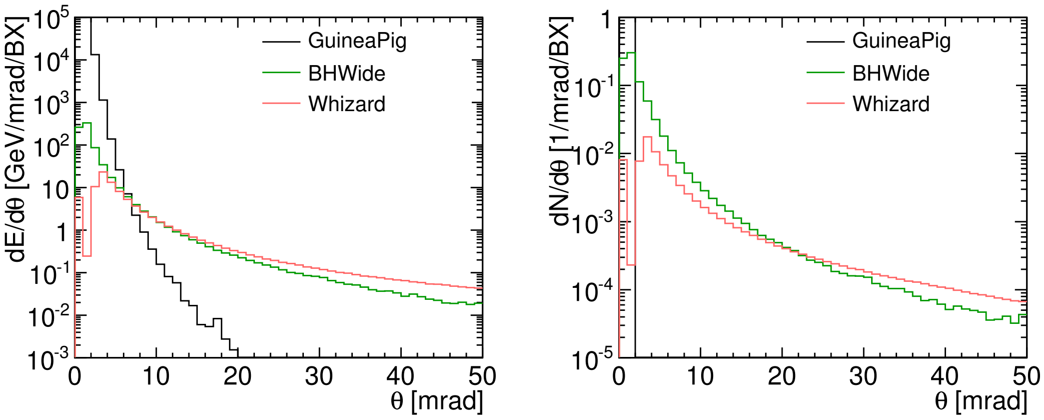

(a) Energy distribution

(b) Particle distribution

Figure 3.10: Distributions for the Bhabha events calculated by GUINEAPIG, BHWIDE, and WHIZARD: (a) Angular distribution of the energy per bunch crossing and (b) number of particles with an energy above 100 GeV per bunch crossing.

determine the total effective cross-section and probability of Bremsstrahlung. After the generation of the final state particles, they are rescaled and boosted to the laboratory frame. Each event has to be weighted according to its effective centre-of-mass energy with the weight $w = s/s_{\mathrm{eff}}$.

WHIZARD was run with a minimum momentum transfer $Q^2 > 16\ \mathrm{GeV}^2$, a minimal energy of the outgoing particles of 4 GeV, and without a minimal scattering angle [48], though the value of $Q^2 \approx p_{\mathrm{T}}^2$ does not allow for events at low energy and low angles—e.g., $\theta = 10$ mrad and $p = 400$ GeV corresponds to $p_{\mathrm{T}} = 4$ GeV. In WHIZARD the cross-section is weighted with the luminosity spectrum, so that no weighting of the events is necessary.

Figure 3.10a shows the energy per bunch crossing from the three generators in a given polar angle. The energy distribution simulated by GUINEAPIG peaks at the lowest angles and extends only up to 20 mrad. The distributions from BHWIDE and WHIZARD differ at the lower polar angle limit, but between 5 mrad and 20 mrad they are in good agreement. For all generators the expected energy above 5 mrad is orders of magnitude below that from incoherent $\mathrm{e}^+\mathrm{e}^-$ pairs.

Figure 3.10b shows the expected rate of particles with an energy above 100 GeV from Bhabha events as a function of the polar angle. Above a polar angle of 10 mrad the rate of particles is below $3 \cdot 10^{-3}/\mathrm{mrad}/\mathrm{BX}$, or about one high energy electron every two bunch trains.

3.9 Summary of Beam-Induced Backgrounds

Figure 3.11a shows the angular distribution of all the different background particles in the angular range of the whole detector. Only the incoherent $\mathrm{e}^+\mathrm{e}^-$ and muons pairs, and the particles from $\gamma\gamma \to$ hadron events extend to a polar angle large enough to cause a large rate of hits in the tracking detectors ($\theta > 100$ mrad).

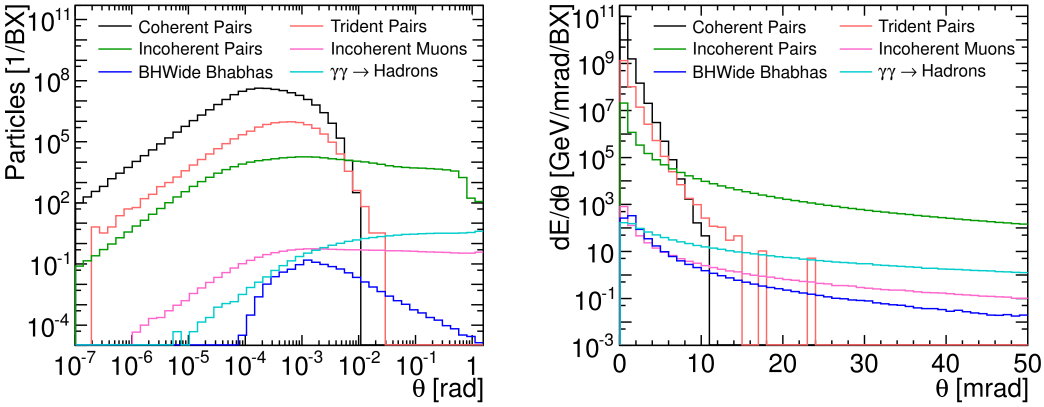

(a) Number of particles (b) Energy

Figure 3.11: (a) Angular distribution for the different background particles. (b) Angular distribution of the energy from the different background particles.

The minimal acceptance of the detector is limited by the coherent processes. In order to keep coherent pairs from hitting the detector in any significant number, the detectors start at a polar angle of 10 mrad with respect to the outgoing beam axis.

The energy from all the different backgrounds with respect to the polar angle is shown in Figure 3.11. The largest energy deposits can be expected from the incoherent e^+e^- pairs and the $\gamma\gamma \to$ hadron events, if the lower limit of the detector is at $\theta = 10$ mrad. Above this angle the energy from the other processes is several orders of magnitude smaller than the energy in the incoherent e^+e^- pairs.

The total number of particles per bunch crossing, the number of particles inside the detector with $\theta > 10$ mrad, and the number of particles inside the central detector with $\theta > 7.3^\circ$ and $p_T > 20$ MeV is given in Table 3.2. The very forward region is dominated by the incoherent e^+e^- pairs. In the central detector, the number of particles from incoherent pairs and $\gamma\gamma \to$ hadron events is similar. In addition there are about three muons per bunch crossing. The other background processes do not cause a significant number of particles per bunch crossing inside the detector.

The majority of the background particles have a fairly low energy. A high energy particle with a large polar angle can be expected only from the Bhabha scattering. The rate of electrons with an energy above 100 GeV from Bhabha scattering is about one particle every second bunch train.

3.10 Beam-Beam Background and Imperfect Collisions

Imperfections of the main linac and the BDS, as well as ground motion, lead to offsets between the beams during collisions [49]. These offsets have an impact on the luminosity and on the

Table 3.2: Production rates per Bunch Crossing (BX) for the different background particles for $\sqrt{s} = 3$ TeV CLIC: Total number of produced particles, number produced inside the detector acceptance, and number of particles in the acceptance of the vertex detector.

	Number of particles per BX		
Background	Total	$\theta > 10$ mrad	$\theta > 7.3°$ and $p_T > 20$ MeV
Coherent pairs	$6.6 \cdot 10^8$	≈ 0	0
Trident pairs	$6.7 \cdot 10^6$	≈ 0	0
Incoherent e^+e^- pairs	$3.3 \cdot 10^5$	$8 \cdot 10^4$	60
Incoherent muons	12.5	5.8	2.8
$\gamma\gamma \rightarrow$ hadrons	102	96 (47 charged)	54 (25 charged)

beam-induced backgrounds.

Because of the small vertical size of the beams ($\sigma_Y = 1$ nm), small vertical offsets already have an impact on the luminosity and backgrounds. To study this effect GUINEAPIG was run with different vertical offsets between the electron and positron beams.

Figure 3.12 shows the total luminosity and the peak luminosity—where the events have an energy within 1% of the nominal centre-of-mass energy—as a function of the vertical offset between the two beams. The luminosity quickly drops with increasing offsets. Backgrounds depending on the luminosity are correlated with this drop. However, since more particles are in a higher field region, beamstrahlung and coherent pair production initially increases with the offset. Figure 3.13 shows the number of coherent and incoherent pairs produced during a bunch crossing for different vertical offsets. The number of incoherent pairs drops, whereas the number of coherent pairs increases by 50% for offsets of up to 10 nm, before the number starts falling.

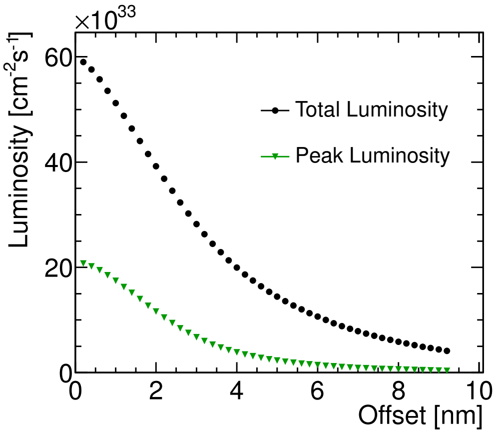

Figure 3.12: Luminosity as a function of the vertical beam offsets. The peak luminosity is the luminosity within 1% of the nominal centre-of-mass energy.

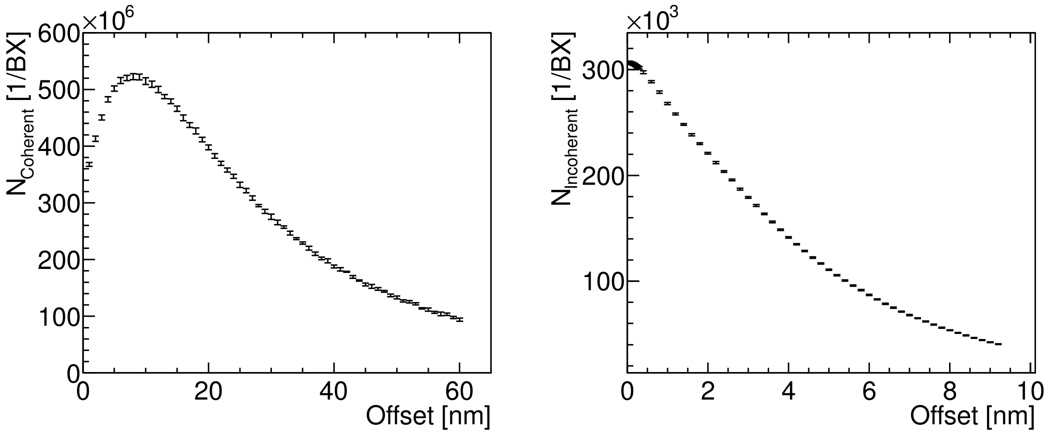

(a) Coherent pairs

(b) Incoherent pairs

Figure 3.13: (a) Number of coherent pairs as a function of the vertical offset of the beams and (b) number of incoherent pairs with $E > 5$ MeV.

3.10.1 Distribution of Coherent Pairs

Although the number of coherent pairs increases with larger offsets, the deflection of the particles will not increase, because the deflective force on the produced particles is decreasing with larger offsets.

For vertical offsets of 0.0 nm, 1.0 nm and 10.0 nm 2000 bunch crossings were simulated with GUINEAPIG. The resulting angular distribution of the energy from the coherent pairs is shown in Figure 3.14a. No significant difference in the energy distribution is visible; the energy from the coherent pairs does not extend to larger polar angles with increased vertical offsets.

3.10.2 Distribution of Incoherent Pairs

For the incoherent pairs the distribution of energy versus polar angle shows the expected drop corresponding to the reduced number of incoherent e^+e^- pairs. However, because of the strong deflection of the particles, the azimuthal distribution is not simply scaled. Particles with the same charge as the oncoming bunch are repelled, and, because of the offset, more strongly either upward or downward (see Figure 3.15). In the GUINEAPIG simulation the electron bunch moving forward (in $+Z$ direction) was shifted downwards, and the positron bunch moving backwards (in $-Z$ direction) was shifted downwards.

Figure 3.16 shows the distribution of particles with a deflection angle $\theta > 10$ mrad and a transverse momentum $p_T > 10$ MeV. In the figure the incoherent pairs are divided between particles moving in positive and negative Z direction. The same signed particles with $p_Z < 0$ are deflected upwards ($0° \leq \phi < 180°$), and the energy distribution compared to the head-on case remains constant. In the other half ($180° \leq \phi < 360°$) less particles reach larger angles, and there is less energy than in the head-on case. For the particles with $p_Z > 0$ the situation is reversed.

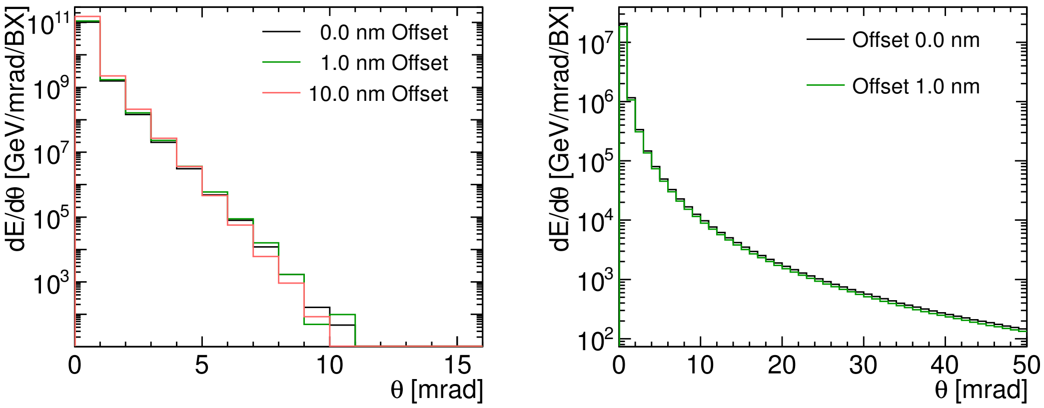

(a) Coherent pairs

(b) Incoherent e^+e^- pairs

Figure 3.14: Total energy carried by the (a) coherent pairs and (b) incoherent e^+e^- pairs as a function of the polar angle θ for different vertical beam offsets.

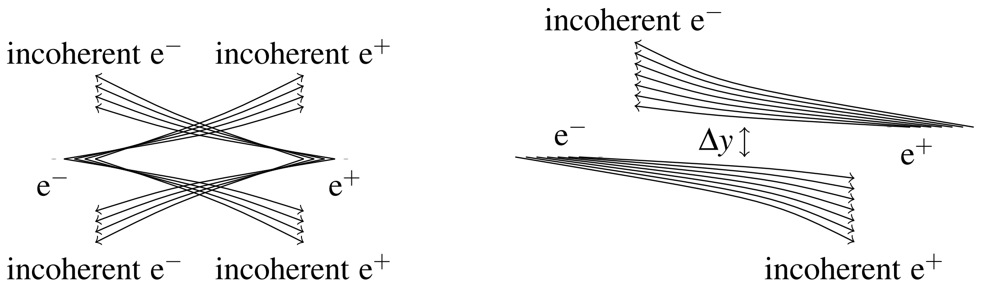

(a) Head-on

(b) Vertical offset

Figure 3.15: Sketches showing the deflection of like signed incoherent pairs for (a) head-on collisions and (b) collisions with a vertical offset Δy.

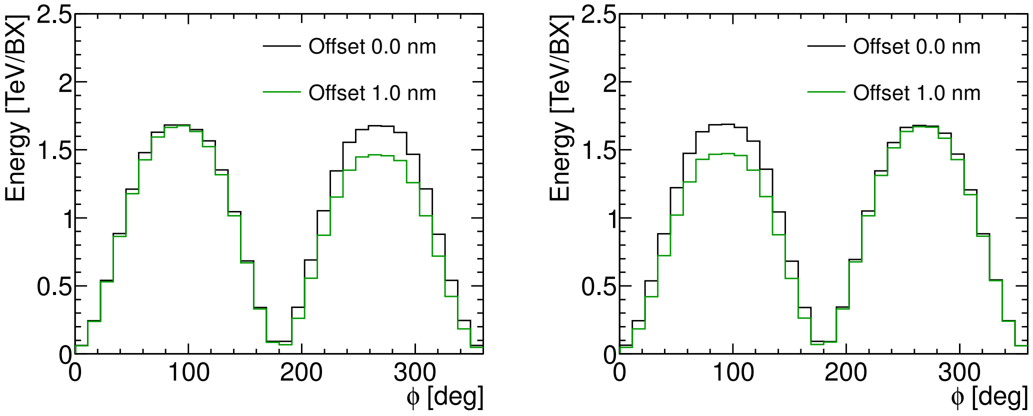

(a) $p_Z < 0$ (b) $p_Z > 0$

Figure 3.16: Energy per bunch crossing as a function of the azimuthal angle ϕ from incoherent e^+e^- pairs with $\theta > 10$ mrad and $p_T > 10$ MeV; (a) forward $p_Z < 0$, (b) backward $p_Z > 0$.

This effect has an impact on the energy distribution in the calorimeters at small polar angles, and increases the fluctuation of the deposited energies of the background particles.

3.11 Machine Induced Backgrounds

So far only backgrounds that are directly produced at the IP were discussed. However, there are also a number of processes that lead to the production of background particles outside of the Interaction Region (IR), which can potentially cause a significant background in the detector.

3.11.1 Synchrotron Radiation

The deflection of the beams in the BDS produces synchrotron radiation. However, the collimation system at CLIC has been designed specifically to reduce this background in the IR [50]. The goal of the optimisation of the BDS was that no synchrotron photon hits the QD0, which has an inner radius of 4.125 mm [51], much smaller than the radius of the vertex detector of 30 mm or the BeamCal inner radius of 32 mm. The background from synchrotron radiation in the detector is therefore expected to be negligible.

3.11.2 Backgrounds from the Post-Collision Line

After leaving the detector the beams and additional particles produced during the collisions are transported to the beam dumps. The beam dumps are located 315 m away from the IP [52].

The estimated flux of photons, at a distance of 3.5 m from IP, coming from the post collision line is about 100 photons/cm^2 per bunch crossing. The average energy of the photons is a few hundred keV [52]. The average neutron flux is about 4 neutrons/cm^2 per bunch crossing with an average kinetic energy of about 1 MeV [52].

The only direct path for these particles to reach the centre of the detector is through the holes in the BeamCal, which has an area of about 32 cm^2. Also, only a small part of the particles produced in the post collision line will reach the detector in time with the primary collisions during a bunch train [52].

3.11.3 Beam-Halo Muons

The background from muons produced in the interaction of particles in the halo of the beam with the collimators in the BDS is expected to lead to 0.05 muons per bunch crossing obtained from both beams and traversing the detector volume [4]. Their impact on the detector is negligible.

4 Detector Model for the Simulations

4.1 Detector Models for CLIC

Two detector concepts were studied for the CLIC detector CDR [4]. These concepts were based on the validated detector proposals for the ILC: the International Large Detector (ILD) [53] and the Silicon Detector (SiD) [54]. The ILC detector concepts had to be adapted to the higher energies, by increasing the Hadronic Calorimeter (HCal) depth, and to the different background environment expected at CLIC.

Both detectors are built with the particle flow paradigm in mind. The goal of particle flow is the reconstruction of all visible particles in an event. The subdetectors best able to reconstruct the particle properties are used to improve the jet energy measurement: charged particle momenta are reconstructed with the tracking detectors, photons with the electromagnetic calorimeter and neutral hadrons with the hadronic calorimeter. To separate the showers initiated by different particles—especially in jets—high granularity calorimeters are needed [55]. Using the particle flow concept the intrinsically poorer energy resolution of the hadronic calorimeter does not harm the jet energy resolution, because only 10% of the jet energy stems from neutral hadrons [55].

The CLIC_ILD_CDR model, as it is described in the following, is the detector model after it was optimised to reduce the background in the vertex detector, and after taking constraints of the forward region and accelerator components into account. In Chapter 5 the optimisation of the detector forward region will be described and justified. More details on the dimensions of the CLIC_ILD_CDR detector model can be found in [56].

4.2 Detector Geometry

A quadrant of the detector model is shown in Figure 4.1. The main parameters of the different subdetectors are summarised in Table 4.1. The detector is 14 m long and has a diameter of 14 m.

Closest to the IP, the detector consists of a silicon based Vertex Detector (VXD) and Forward Tracking Disks (FTDs). In the central barrel region the VXD is followed by the Silicon Inner Tracker (SIT) (see Figure 4.2). This is followed by a Time Projection Chamber (TPC). There are additional silicon sensors beyond the TPC endplates, called the Endcap Tracking Disks (ETDs), and around the TPC barrel, the Silicon External Tracker (SET).

The tracking system is followed by a silicon-tungsten Electromagnetic Calorimeter (ECal) and a scintillator based HCal. Outside the HCal barrel lies the superconducting solenoid coil, which provides a 4 T magnetic field. The magnetic flux is contained by an iron return yoke, which is equipped with active layers for muon identification.

In the forward region the coverage of the ECal is complemented by the Luminosity Calorimeter (LumiCal) and the Beam Calorimeter (BeamCal). Figure 4.2 shows the placement of Lumi-

Table 4.1: General parameters for the CLIC_ILD_CDR detector model. $Z_{\mathrm{Start/End}}$ are the beginning and end in one half of the detector. $R_{\mathrm{In/Out}}$ are the radii of the inscribing circles of each subdetector.

	Z_{Start} [mm]	Z_{End} [mm]	R_{In} [mm]	R_{Out} [mm]
TPC	0	2350	329	1808
ECal Barrel	0	2350	1847	2020
HCal Barrel	0	2350	2058	3296
Coil	0	4256	3395	4145
Yoke Barrel	0	4511	4395	6945
ECal Endcap	2450	2622	242	2089
HCal Ring	2450	2609	2139	3059
HCal Endcap	2650	4240	400	3059
Yoke Plug	4256	4536	690	3059
Yoke Endcap	4536	7086	690	6945
LumiCal[a]	2654	2825	100	290
BeamCal[a]	3181[b]	3441	32	150

[a] LumiCal and BeamCal are centred on the outgoing beam axis.

[b] This includes 100 mm of graphite before BeamCal (see Section 4.5.2).

Cal and BeamCal around the beam pipe. The layout of the forward region is largely governed by the position and size of the final focus quadrupole QD0. In Figure 4.3,which shows the region behind the BeamCal, only the permanent-magnet core of the QD0 is shown: the permanent magnet cylinder is surrounded by copper coils and an iron yoke. The diameter of the QD0 is about 60 cm [12].

4.3 Tracking Detectors

The vertex detector consists of six layers of silicon pixel detectors. Each layer consists of individual ladders spanning the full length of the detector. The layers are arranged in three doublets, with 2 mm between paired layers. Figure 4.4 shows the placement of the individual ladders.

The SIT and SET each consists of two layers of silicon strip detectors. The dimensions, sensor thicknesses, and granularities of the barrel-like tracking detectors are given in Table 4.2.

For the tracking at polar angles below the acceptance of the TPC the silicon based FTDs provide the tracking coverage. The first six disks are placed in three doublets like the layers of the VXD and are assumed to be silicon pixel detectors. The remaining five disks are built from silicon strip detectors. The ETDs between the TPC endplate and the ECal consist of three stereo layers of silicon strip detectors. The coordinates, the silicon thicknesses, and granularity for all disk-like tracking detectors are given in Table 4.3. Details on the performance of the tracking detectors can be found in [57, 58, 59].

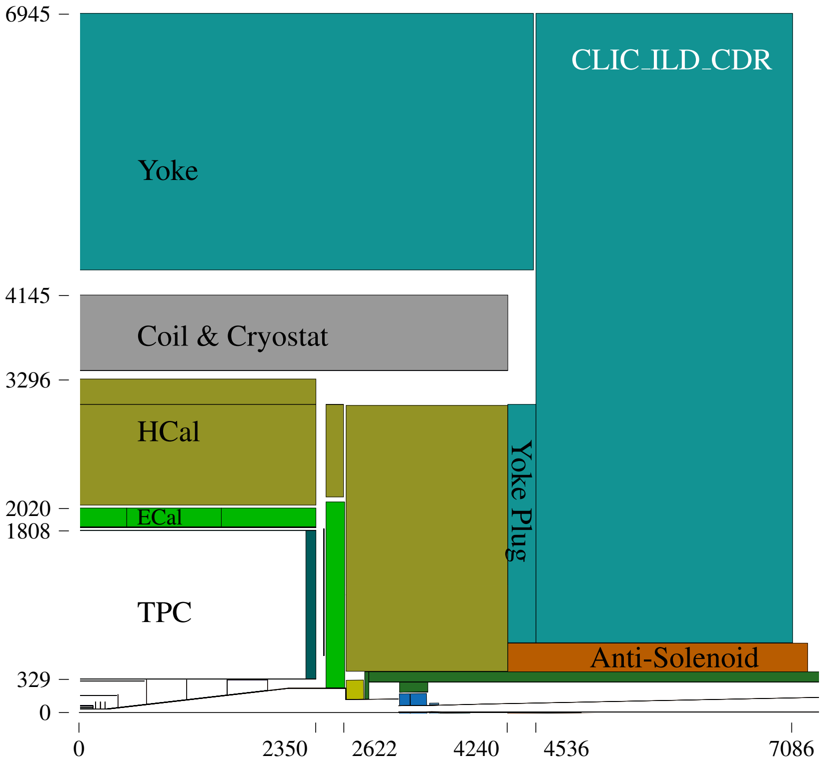

Figure 4.1: Dimensions of the CLIC_ILD_CDR model as implemented for the simulation. All values are given in millimetres.

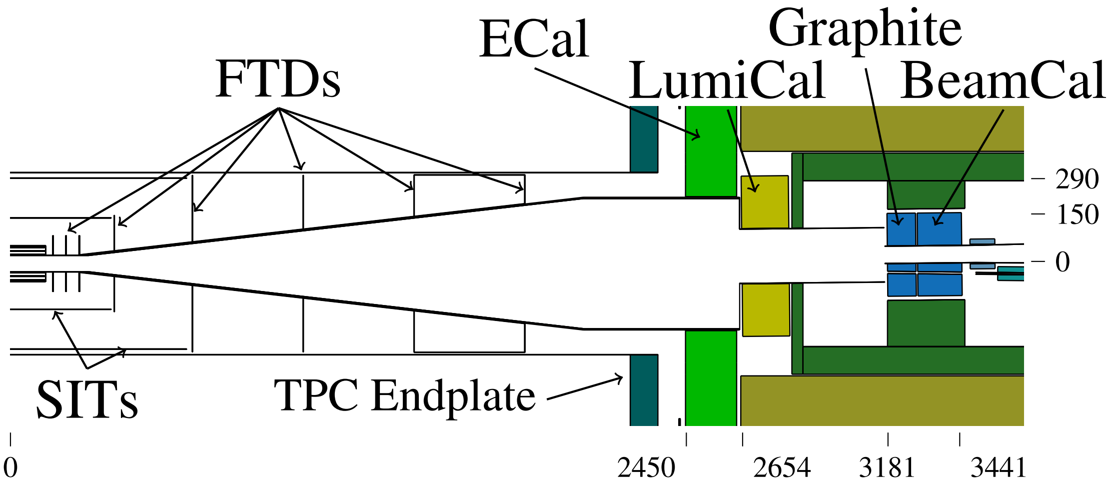

Figure 4.2: Forward Tracking and Calorimeters seen from the top. The overlap in coverage between LumiCal and ECal is visible. LumiCal and BeamCal appear slightly skewed, because they are centred on the outgoing beam axis. All values are given in millimetres.

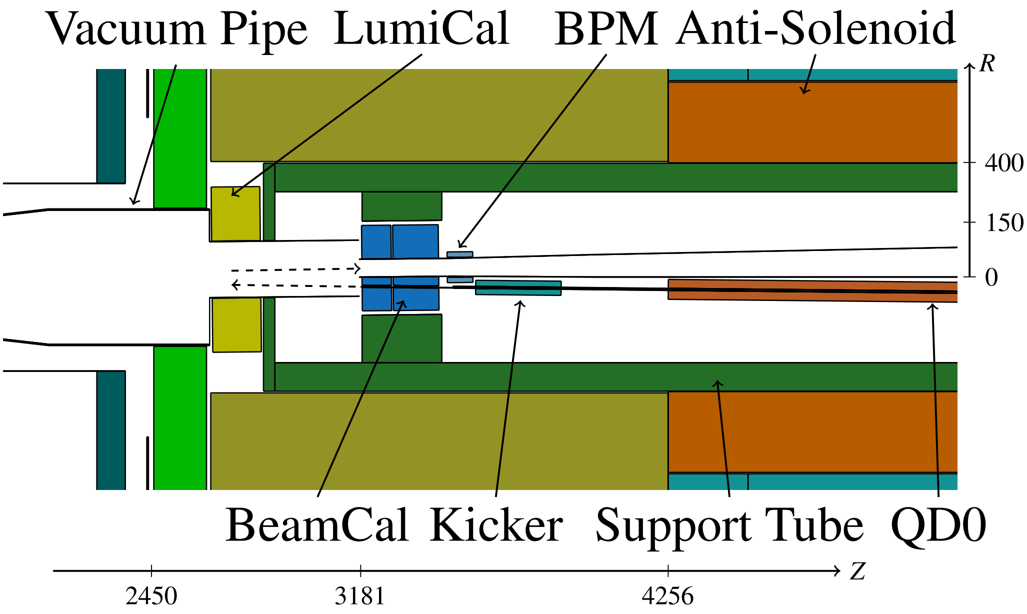

Figure 4.3: Very forward region of the CLIC_ILD_CDR detector model. All values are given in millimetres.

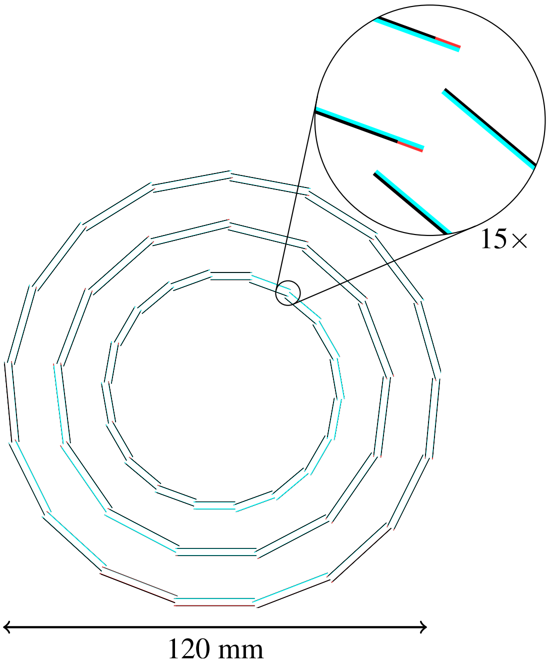

Figure 4.4: Vertex detector ladder arrangement around the beam pipe. The region shows the structure of the ladders: the sensor in black, the carbon support in cyan and the readout electronics on the side of the ladders in red.

Table 4.2: Radius, half-length, silicon thickness, and pixel or strip size for the barrel-like tracking detectors, Vertex Detector (VXD), Silicon Inner Tracker (SIT), and Silicon External Tracker (SET), in CLIC_ILD_CDR.

	Radius [mm]	Half-length [mm]	Si-thickness [μm]	Pixel/Strip size [mm^2]
VXD 1	31	130	50	0.02 × 0.02
VXD 2	33	130	50	0.02 × 0.02
VXD 3	44	130	50	0.02 × 0.02
VXD 4	46	130	50	0.02 × 0.02
VXD 5	58	130	50	0.02 × 0.02
VXD 6	60	130	50	0.02 × 0.02
SIT 1	165	371	275	90 × 0.05
SIT 2	309	645	275	90 × 0.05
SET 1	1833	2350	275	438 × 0.05
SET 2	1835	2350	275	438 × 0.05

Table 4.3: Radii, Z-position, silicon thickness, and pixel or strip size for the planar silicon tracking detectors, Forward Tracking Disks (FTDs) and Endcap Tracking Disks (ETDs), in CLIC_ILD_CDR.

	Inner radius [mm]	Outer radius [mm]	Z-position [mm]	Si-thickness [μm]	Pixel/Strip size [mm^2]
FTD 1	33	102	160	50	0.02 × 0.02
FTD 2	33	102	162	50	0.02 × 0.02
FTD 3	33	102	207	50	0.02 × 0.02
FTD 4	33	102	209	50	0.02 × 0.02
FTD 5	33	102	255	50	0.02 × 0.02
FTD 6	33	102	257	50	0.02 × 0.02
FTD 7	47	175	382	275	100 × 0.05
FTD 8	79	320	665	275	100 × 0.05
FTD 9	126	320	1066	275	100 × 0.05
FTD 10	172	320	1467	275	100 × 0.05
FTD 11	218	320	1868	275	100 × 0.05
ETD 1	419	1823	2426	275	300 × 0.05
ETD 2	419	1823	2428	275	300 × 0.05
ETD 3	419	1823	2430	275	300 × 0.05

Table 4.4: Parameters for the calorimeter layers. The number of layers N_{Layers}, the thickness of one layer d_{Layer}, the absorber material, its thickness d_{Abs}, the active material and its thickness d_{Act} are given.

	N_{Layers}	d_{Layer} [mm]	Absorber	d_{Abs} [mm]	Active	d_{Act} [mm]
ECal 1	20	5.25	Tungsten	2.1	Silicon	0.5
ECal 2	9	7.25	Tungsten	4.1	Silicon	0.5
HCal Barrel	75	16.5	Tungsten	10	Scintillator	5.0
HCal Endcap	60	26.5	Iron	20	Scintillator	5.0
Yoke	18	140	Iron	100	RPC/Gas	2.0

4.4 Calorimeters and Yoke

The ECal is a high granularity sampling calorimeter with tungsten absorber layers and sensitive silicon elements. There are 20 layers of 2.1 mm thick tungsten followed by 9 layers of 4.2 mm thick tungsten. The silicon sensors are 0.5 mm thick, and the size of the individual pads is 5×5 mm^2. The total thickness of the ECal corresponds to 23 radiation lengths (X_0) and one nuclear interaction length (λ_{I}) [56].

The HCal consists of two different absorber types. To reduce the radial dimension inside the solenoid, the HCal barrel uses 10 mm thick tungsten layers as the absorber. In the endcap, where space is less of an issue, 20 mm thick iron plates are used as the absorber. In both parts the gap for the sensitive layers is 6.5 mm. There are 5 mm thick scintillators with a pad size of 30×30 mm^2 between the absorber plates. More details on the structure of the active layers and of the HCal in general can be found in reference [60]. The thickness of the hadronic calorimeter corresponds to 8 λ_{I} [56].

The instrumented return yoke, used for muon identification and as a tail catcher, consists of 10 cm thick iron layers alternating with 4 cm gaps filled with Resistive Plate Chambers (RPCs). The sensitive material in the detectors is a 2 mm thin volume of gas (80% tetra-fluor-ethane, 10% nitrogen and 10% isobutane). For an efficient muon reconstruction not all of the 18 layers implemented in the simulation are needed [61], but with evenly spaced layers the background can be estimated more seamlessly. The readout pad size in the simulation is 30×30 mm^2.

The outer dimensions of the different calorimeters and the yoke are detailed in Table 4.1, the layer structure of the calorimeters and the yoke are given in Table 4.4. Details on the performance of the CLIC_ILD_CDR detector with the particle flow jet energy reconstruction can be found in [62]. The performance of the muon system is described in [63].

4.5 Very Forward Region

The two main elements of the very forward region are the LumiCal and the BeamCal, two electromagnetic detectors. Both detectors are aligned with the outgoing beam axis. Their location and dimensions in the CLIC_ILD_CDR model are given in Table 4.1, and the very forward region is shown in Figure 4.3.

The very forward region also includes the Beam Position Monitor (BPM) and kicker of the intra-train-feedback system, used to correct the vertical offset of the beams during a bunch train [64], and the QD0 [12]. Surrounding the forward region elements is the support tube, which in the simulation is simplified as a 10 cm thick iron cylinder. Outside the support tube and inside the return yoke another 30 cm thick iron cylinder represents the anti-solenoid, which is necessary to protect the QD0 and reduce the main solenoid impact on the incoming beam [4, 65].

For maximal luminosity the QD0 has to be placed as close as possible to the IP. However, the anti-solenoid reduces the HCal endcap acceptance. Therefore, as a trade-off between the luminosity and the reduced acceptance of the HCal endcap, the QD0 is located just after the end of the HCal endcap. As a result the anti-solenoid only reduces the coverage of the muon system.

4.5.1 Luminosity Calorimeter (LumiCal)

The main purpose of the LumiCal is the precise reconstruction of the energy and angle of electrons and positrons from Bhabha events used to measure the luminosity [66]. Details on the performance of the LumiCal at CLIC can be found in [67].

The LumiCal is designed to contain electron showers in very small volumes for a precise reconstruction of the electron angle. It consists of 40 layers of 3.5 mm tungsten absorbers and 0.32 mm silicon sensors. The thickness of each absorber layer corresponds to one radiation length, and 40 layers completely contain showers of 1.5 TeV electrons. The Molière radius—defining the transverse area in which 90% of the shower energy is deposited—of the LumiCal is about 1.5 cm [67]. Each layer also contains 0.2 mm sensor supports (consisting of epoxy, kapton, and copper) and 0.25 mm air gaps. The sensors are divided into pads of azimuthally and radially constant dimensions. There are 64 radial divisions, and each pad covers an azimuthal angle of 7.5°.

Compared to an earlier LumiCal proposal for CLIC [67], the position and outer radius of the LumiCal were changed. The LumiCal has been moved behind the ECal endcap, so that the coverage of the two detectors overlaps. The outer radius of the LumiCal was reduced from the proposed 35 cm to 29 cm. The radius of 29 cm is for the instrumented area only, an additional 3 cm are foreseen for the readout electronics. Figure 4.5a shows a drawing of the forward region with the LumiCal, BeamCal and a more detailed beam pipe with vacuum valves. During the opening of the detector the LumiCal has to move past the vacuum valves dividing the beam pipe into separate sectors (Figure 4.5b). If the LumiCal is too large it cannot open far enough to pass the vacuum valve staying with the inner part of the detector [68].

The effective outer radius of the LumiCal is reduced by the overlap with the ECal endcap. The LumiCal is centred on the outgoing beam axis, whereas the ECal endcap is centred around the detector axis. This causes the overlap region to be dependent on the azimuthal angle. To have an overlap of 2.5 cm or more the inner radius of the ECal was chosen to be 24 cm (Table 4.1). The maximal radius at which the full azimuthal angle of the LumiCal is visible from the IP is therefore about 22 cm.

The required accuracy on the luminosity measurement $\Delta L/L$ for 100 fb^{-1} is 1% [4]. Figure 4.6 shows the statistical error expected for the luminosity measurement. The error was estimated for an integrated luminosity of 100 fb^{-1}, a Bhabha selection efficiency of 50%, a LumiCal with an inner acceptance of 50 mrad, and varying maximal acceptance θ_{max}. The statistical contribution

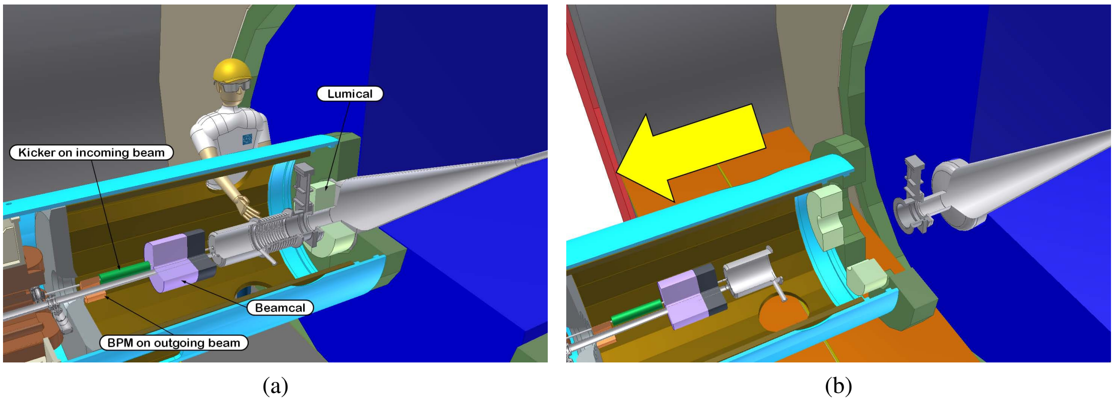

(a) (b)

Figure 4.5: Drawing of the forward region of the detector from [4]. (a) Forward region before the opening of the detector, (b) with an opened LumiCal and a separated beam pipe.

$(\Delta L/L)_{\mathrm{stat}}$ to the total error of the luminosity measurement for either an outer radius of 35 cm ($\theta_{\mathrm{max}} = 134$ mrad) or 22 cm ($\theta_{\mathrm{max}} = 86$ mrad) is below 0.1%. The radius of 22 cm is still large enough to achieve the required precision for the luminosity measurement.

To ensure the energy and angular resolution of the LumiCal, only very little material should be placed before the LumiCal. Therefore a conical shape of the beam pipe from the vertex region to the LumiCal is preferred [69].

4.5.2 Beam Calorimeter (BeamCal)

One of the purposes of the BeamCal is the identification of high energy electrons for electron tagging [70]; the feasibility of electron tagging at CLIC will be further described in Chapter 8. The BeamCal also shields the accelerator equipment positioned downstream from the large flux of incoherent e^+e^- pairs.

The BeamCal completes the coverage of the electromagnetic calorimeter from 43 mrad down to 10 mrad (cf. Table 4.1). Like the LumiCal, the BeamCal consists of 40 layers of 3.5 mm tungsten plates. Because the BeamCal has to absorb a large part of the incoherent electron–positron pairs, the sensor material has to be radiation hard. In the simulation 0.3 mm thick diamond layers are used as the active elements. To reduce the number of particles scattering back into the detector, the IP-facing side of the BeamCal is covered with a 10 cm thick graphite layer.

The implementation of the BeamCal in the ILD detector used an identical cross-section for the absorber and sensor layers, shown in Figure 4.7a. Around the beam pipe for the incoming beam a sector of the absorber plates and sensors is cut out leaving a key-hole shaped open area for the two beam pipes. Figure 4.7b shows the updated layout of the absorber layers. Only the area surrounding the incoming beam pipe is filled with absorber material.

Figure 4.8 shows the cross-section of the active layers in the BeamCal. Figure 4.8a shows the total coverage of the active material, the area between the incoming and outgoing beam pipes are not instrumented. Figure 4.8b shows the individual readout pads. The Molière radius of the

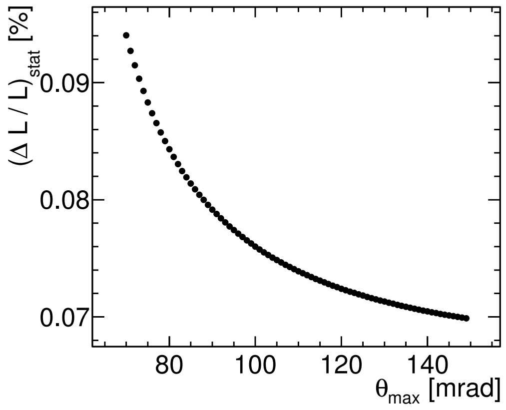

Figure 4.6: Statistical contribution to the luminosity uncertainty for a constant inner acceptance angle of 50 mrad and varying outer acceptance angle θ_{max}.

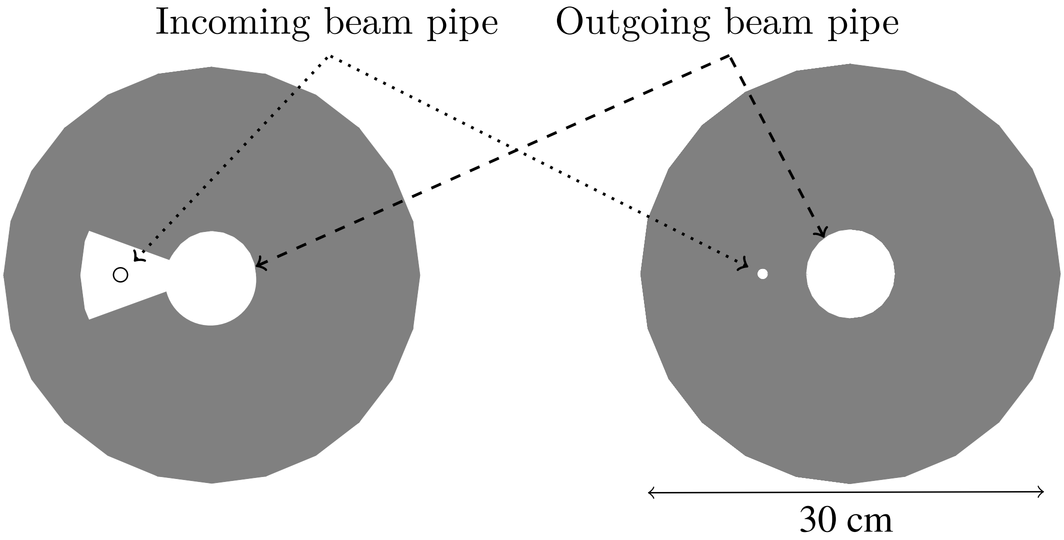

(a) Key-hole cutout

(b) Full coverage

Figure 4.7: Cross section of the two BeamCal designs. In the new design the area between the beam pipes is filled with absorber,

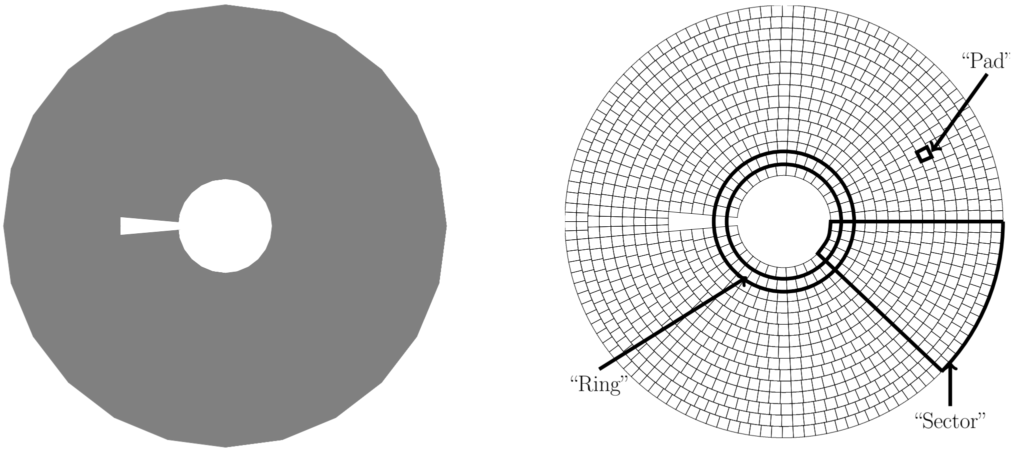

(a) Sensor cross-section (b) Pad layout

Figure 4.8: Sensor coverage for the BeamCal in the CLIC_ILD_CDR detector model

BeamCal is similar to that of the LumiCal, the pad size of each pad is about 8×8 mm^2, or half a Molière radius. The pads with the same radial distance to the centre are called a 'ring', and there are 15 rings. A BeamCal sensor layer consists of eight sectors spanning 42.5° each, the sector near the incoming beam pipe is covering the remaining 20°.

4.6 Beam Pipe

The beam pipe contour can be seen in Figure 4.2 and Figure 4.3. Around the interaction point the beam pipe consists of a beryllium cylinder with an outer diameter of 60 mm and a thickness of 0.6 mm. The cylinder is connected to a conical section, which is pointing to the IP. The material and thickness of the conical section was optimised to reduce the background scattering back from the forward region (see Section 5.7). The conical section of the beam pipe consists of 4 mm thick iron.

The material budget resulting from a beam pipe pointing towards the IP naturally is larger in the angular range covered by the beam pipe. Figure 4.9 shows the number of radiation lengths, that particles with a given polar angle θ with respect to the detector axis have to pass through from two different beam pipes: the beam pipe with a pointing 4 mm thick iron cone, and a non-pointing 0.6 mm thick beryllium cone. The material budgets shown in Figure 4.9 include the material of the VXD and FTDs, which slightly differs between the two models.

The pointing beam pipe causes a large peak in the material budget at $\approx 7^\circ$. On the other hand, the non-pointing beam pipe of 0.6 mm beryllium already shows steep increase in the material budget at $\theta = 10^\circ$ to $0.4\,X_0$.

The maximal radius of the cone is limited by the inner radius of the ECal endcap. Therefore, when the cone reaches a radius of 240 mm, the beam pipe becomes cylindrical. Inside the LumiCal the beam pipe is aligned with the outgoing beam axis, and the radius is limited by the inner radius of the LumiCal. The beam pipe geometry changes again before the BeamCal, when

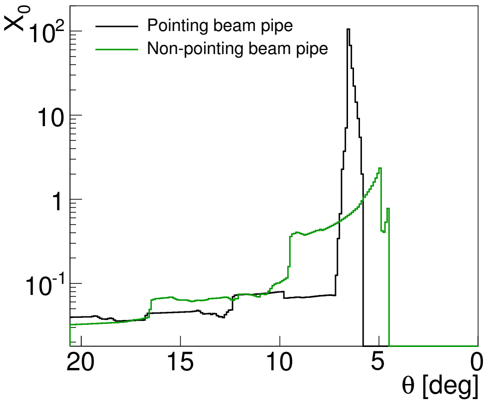

Figure 4.9: Radiation length (X_0) seen by particles with a given polar angle θ for a pointing conical beam pipe of 4 mm iron, and for a non-pointing conical beam pipe of 0.6 mm beryllium and slightly different VXD and FTD placements.

it splits into two separate pipes: a cylindrical beam pipe with a small diameter for the incoming beam, and a conical beam pipe with a half-opening angle of 10 mrad for the outgoing beam. This opening angle is necessary for the coherent pairs to leave the detector ([13] and Section 3.10.1).

4.7 Magnetic Field

The magnetic field used for the simulation is implemented as a detailed field map, which has also been used for ILD background studies at the ILC [8, 53]. The field map is scaled from the $B_Z = 3.5\ T$ used at the ILD to $B_Z = 4\ T$ at CLIC. Figure 4.10 shows the B_Z and B_R components of the magnetic field in the detector. The field extends to $Z = \pm 7$ m and $R = 7$ m. The length of the solenoid coil in the CLIC_ILD_CDR model is longer than in the ILD model, but the magnetic field was not stretched to fit the new coil dimensions. The field map is almost constant $B_Z = 4$ T and $B_R = 0$ up to $Z = 4$ m which extends beyond the BeamCal region. In summary, in the regions relevant for the background studies the magnetic field is described by a realistic field map.

4.8 Detector Simulation Software

The detector is implemented with the MOKKA [71] simulation software. MOKKA is based on the GEANT4 [72, 73] Monte Carlo simulation toolkit. For this thesis, MOKKA version 07-05 was used together with GEANT4 version 9.3p01.

GEANT4 is used to describe the detector geometry and to simulate the interaction of particles with the material of the detector. The *physics list* chosen for the background studies is QGSP_BERT_HP, which includes the High Precision (HP) neutron tracking for neutrons from 20 MeV down to thermal energies.

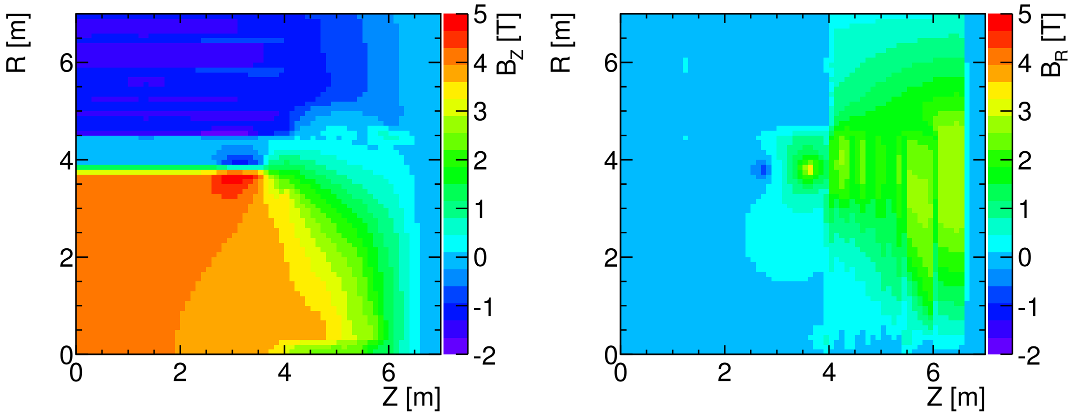

(a) B_Z

(b) B_R

Figure 4.10: Components of the magnetic field map used in the simulation.

The production threshold of secondary particles is controlled by the *range cut* parameter. Only secondaries that can be expected to travel a larger distance than the *range cut* value are tracked by the program. GEANT4 translates the range cut into a minimal energy, that depends on the secondary particle's type and the material; if the expected travelling distance is too short the particle is not created and instead its energy is deposited at the place of the interaction. For the background studies in this thesis a range cut of 5 μm was chosen allowing to track also very low energy particles.

To record the energy deposits in the sensors specific volumes of the geometry are designated as *sensitive detectors*, e.g., the silicon part of the vertex detector. In these volumes the energy deposit, type, and momentum of particles passing through them or being absorbed in them are recorded by MOKKA and written to a file in the Linear Collider I/O (LCIO) data format [74].

MOKKA offers a convenient interface to modify parameters of already defined detectors or subdetectors. Steering parameters can be used to, e.g., replace one BeamCal model by another or change the radius of the layers of the vertex detector. Some subdetectors rely on a database with parameters. Some changes have to be done in the source-code. The threshold of sensitive detectors was removed in the *sensitive detectors* to store all particles, regardless of their energy deposit, to estimate the neutron flux. The new BeamCal model was implemented.

In addition to the actual *sensitive detectors*, such as the silicon layers of the vertex detector, several scoring planes were added in the detector model to identify the origin of secondary particles: The material of the conical beam pipe itself was supplemented with a *sensitive detector* to record the passing of particles, Thin layers of air with the respective cross-sections on the IP facing side of the LumiCal, BeamCal and QD0 were also used to record particles. These additions do not affect the results of the simulation, but they provide additional information on the origin and momentum of particles.

4.9 Silicon Based Tracking Detectors

The principle of a silicon based tracking detector is briefly described, along with the effect of radiation damage on the operation of the detector. More details can be found in, e.g., [75, 76, 77].

Silicon tracking detectors consist of charge-collecting substrates of a few ten to a few hundred micrometre thickness with segmented readout electrodes and subsequent signal amplification and digitisation.

If a charged particle passes through the detector, electron–hole pairs are created. The average energy loss by a Minimum Ionising Particle (MIP) in silicon is about $390\ \mathrm{eV}/\mu\mathrm{m}$ [10], and it takes 3.6 eV to create an electron–hole pair [78]. The electrons or holes are collected on the readout electrodes by an electric field or through thermal diffusion. The position resolution of the passing particle depends on the segmentation of the readout structures. The optimal size of the segmentation depends on the expected rate of particles (the occupancy), and the required spatial resolution.

As the energy deposits in tracking detectors are localised, the occupancy can be reduced if sufficiently small pixels or short strips are used in the sensors; likewise the integration time of the readout can be reduced to separate temporally individual hits. However, both increasing the number of readout channels and reducing the integration time of the readout leads to larger power consumption in the detector. The power has to be transferred into the detector with cables and taken out with a cooling system, increasing the material in the tracking region, and thereby spoiling the track reconstruction through multiple scattering.

4.9.1 Radiation Damage in Silicon Detectors

The integrated rates of background events from incoherent pairs and $\gamma\gamma \to$ hadron events will lead to radiation damage to the detector elements during CLIC operation. To estimate the radiation exposure during one year of operation, an effective run time of 100 days with 50×312 bunch crossings per second is assumed for CLIC (Table 2.1).

Radiation damage can be caused by the Total Ionising Dose (TID): Whereas the electron–hole pair creation through ionising radiation in the silicon bulk is a fully reversible process, it is not the case in the silicon-oxide layer of the sensor surface. Holes can get trapped near the surface of the sensor and cause a change in the internal electric field of the sensor. This changes the electric properties of the silicon–silicon-oxide interface area thus altering the charge collection properties of the sensor and in particular the sharing of charge between neighbouring readout electrodes. Moreover, charge buildup at the silicon–silicon-oxide surfaces of the readout electronics can lead to transistor-level leakage and threshold-voltage shift, affecting the performance of the readout [78, 79, 80].

Radiation damage can also be caused by non-ionising radiation. The so called Non-Ionising Energy Loss (NIEL) causes defects in the silicon bulk of the sensor: increasing the leakage current, reducing the charge collection efficiency, and requiring an increased bias voltage for a full depletion of the device [76, 78].

4.10 Background Analysis

The energy deposits and the passing of particles recorded during the simulation are analysed with programs written in the MARLIN/LCIO [81] and ROOT [82] frameworks.

4.10.1 Estimate of the Hit Density: Cluster Size, Safety Factors, and Occupancy

The number of hits recorded in the subdetectors is estimated taking into account hits with an energy deposit above a threshold. For the pixel layers with 50 μm of sensitive silicon a threshold of 3.4 keV is applied to count hits. In the strip detectors with 275 μm sensitive silicon a threshold of 17 keV is applied. The thresholds correspond to about 20% of the most probable energy deposit by an MIP in silicon. If an interaction in the active medium produces a second particle it will be recorded as an additional hit. Depending on the thickness of the active material and the type of particle, between 5% and 10% additional hits are counted in this approach, therefore the number of hits is slightly overestimated.

The quoted estimates of hit densities in the silicon detectors only describe the number of charged particles traversing the sensors. The occupancy of the sensor is the number of individual pixels or strips with a signal divided by the total number pixels/strips. The deposited energies of these particles will lead to the formation of signal clusters in the pixels or strips due to charge spreading and sharing. A precise estimate for the average cluster size has to take into account the sensor geometry, the momentum and incident angle of the particles, and the design of the respective readout systems. For a rough estimate of the pixel-detector occupancies, the hit densities are multiplied with an assumed average cluster size of five. For the strip detectors, the corresponding assumed average cluster size is three.

The results reported here do not include safety factors for the uncertainties related to the production and simulation of the background processes. For the $\gamma\gamma \rightarrow$ hadrons background, an overall safety factor of two should be applied to the occupancies and energy releases in the detector, taking into account the uncertainties on the accelerator parameters, the two-photon luminosity spectrum, the production cross-section, and the hadronisation model [38].

In detector regions where indirect effects from interactions in the material are important (e.g. in the very forward region and close to the beam pipe), additional safety factors for the uncertainty on the simulation of detector effects have to be applied. For the incoherent pairs, such indirect effects are a major source of background hits (see Chapter 5). This holds in particular for the backscattering and subsequent showering of particles in the forward region. Therefore a larger overall safety factor of five should be applied for the incoherent pairs, to take into account this uncertainty on the simulation of the detector response.

4.10.2 Estimate of the Total Ionising Dose

The TID in the silicon detectors is obtained from the full GEANT4 simulation of the energy loss inside the sensor volumes. Results are obtained for all silicon-based tracking detectors of the CLIC_ILD_CDR detector. The estimated total ionising dose is the sum of all energy deposits in a given volume divided by its mass.

4.10.3 Estimate of the Non-Ionising Energy Loss

The displacement damage from non-ionising energy loss is obtained with the same simulation setup as used for the hit densities. Each hit is scaled with a displacement-damage factor based on the type and kinetic energy of the corresponding particle, resulting in the equivalent flux of 1 MeV neutrons (i.e., the flux of neutrons that leads to the same displacement damage as for the observed spectrum). The NIEL scaling factors for neutrons, protons, pions, and electrons are taken from a tabulated compilation [83].

5 Optimisation of the Detector Geometry

A realistic detector model is necessary to estimate the background, taking into account the constraints from the accelerator. This chapter describes the steps which led to the final design of the forward region of the CLIC_ILD_CDR detector model. For the optimisation of the geometry incoherent $e^{+}e^{-}$ pairs were simulated in the different detector geometries under consideration, and the number of hits in the vertex detector was used to quantify and minimise the background.

5.1 From the ILD Forward Region to the CLIC Forward Region

The first step in adapting the ILD forward region for the ILC into a CLIC detector concept was to take the constraints from the accelerator baseline and background conditions into account: the crossing angle, the QD0 position and the coherent background.

Figure 5.1a shows the forward region of the ILD detector model as it was inherited from the ILC [53]. The forward region contains elements in addition to those described in Section 4.5. It contains the LHCal, which extends the HCal to lower polar angles, as well as a representation for a vacuum pump. The crossing angle at ILC is 14 mrad. It also shows a final focus quadrupole, the beam pipe and support material.

To comply with the baseline of CLIC the quadrupole had to be moved to start at $Z = 3.5$ m, which also meant that the BeamCal had to move closer to the IP. The LHCal and the vacuum pump were removed. Figure 5.1b shows the first iteration of the CLIC forward region layout. The LumiCal and BeamCal were increased to 40 layers. The inner radius of the BeamCal was increased to 25 mm, and correspondingly the beam pipe.

5.1.1 Provenance of Backscattering Particles

Before the background hits in the vertex detector can be minimised, it has to be identified first from where the background originates. The provenance of particles was identified by placing scoring planes in front of potential scattering surfaces in the forward region. Scoring planes were placed in front of the LumiCal, the BeamCal and the QD0. Additionally the beam pipe was defined as a scoring plane.

The provenance of a particle hitting the vertex detector was identified by following the history of the particle back to an entry in one of the scoring planes. Whichever scoring plane was hit first was considered to be the provenance of the backscattering particle. Since all particles have to pass though the beam pipe before they hit the VXD, the beam pipe was only considered to be the provenance if no other scoring plane was hit, and if the particle did not come directly from the IP.

For the geometry of Model 1 (Figure 5.1b) 10 BX of incoherent pairs were simulated in

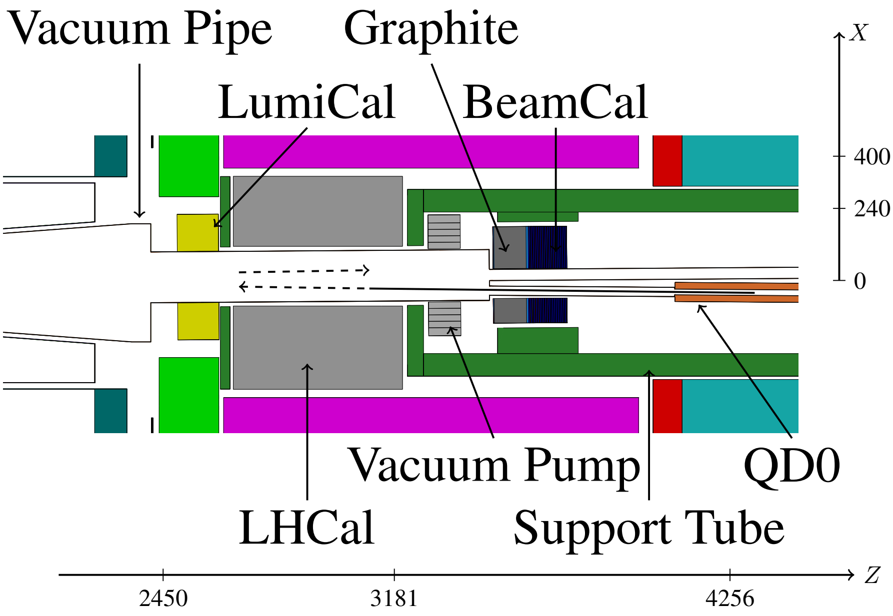

(a) Model 0

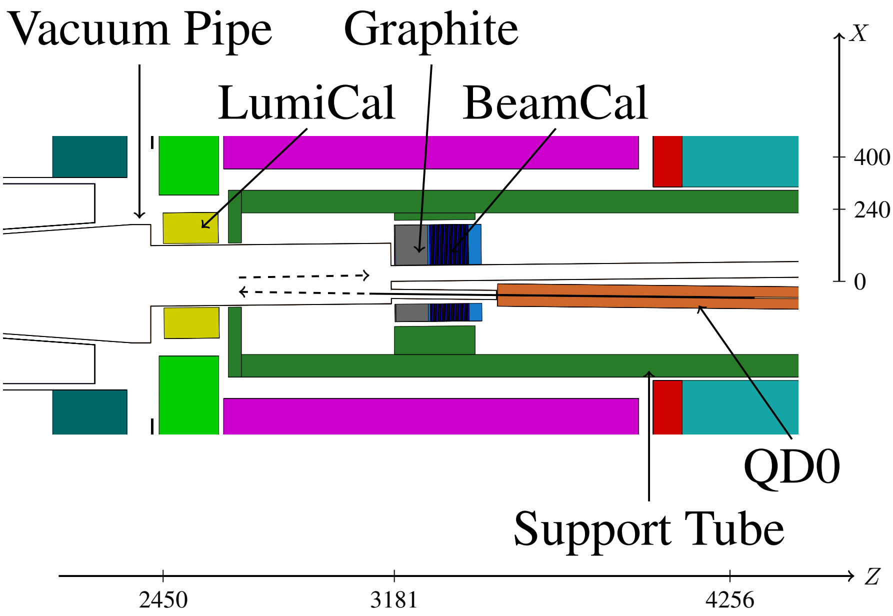

(b) Model 1

Figure 5.1: (a) Forward region inherited from the ILD detector model [53]. (b) Forward region with the QD0 at $Z = 3.5$ m and a cylindrical beam pipe downstream of the BeamCal. All dimensions are in millimetre.

MOKKA. The incoherent pairs were produced using GUINEAPIG with Gaussian particle distributions in the bunches, not with the accurate particle distributions used in later samples.

Figure 5.2a shows the production Z-coordinate of the particles causing a hit in the vertex detector. The particles are differentiated according to their identified provenance. Some hits are caused by particles directly coming from the IP. In the first double layers this corresponds to a hit density of about $5 \cdot 10^{-3}$ Hits/mm^2/BX*. A reduction of this direct component of the background is only possible by increasing the magnetic field or the distance of the vertex detector to the IP.

A second—in this model about ten-times larger—contribution to the background in the VXD are backscattering particles from the forward region. Some of the particles come from the beam pipe covering the front of the BeamCal, or the front face of the BeamCal itself, where the graphite on the IP-facing side of the BeamCal absorbs some, but not all, of the low momentum particles. A large part of the hits is from particles scattering back from the outgoing beam pipe downstream of the BeamCal, because the magnetic field lines, which are parallel to the detector axis, guide low momentum charged particles from the beam pipe to the vertex detector.

The backscattering particles will arrive later than the direct hits in the vertex detector. Figure 5.2b shows the distribution of the time of arrival in the three layers of the vertex detector. The peak around $t = 0$ corresponds to direct hits, with a short tail from curlers or particles hitting the vertex detector further away from the IP. The second wider peak starting at $t = 20$ ns corresponds to the backscattered particles. As the bunch train at CLIC is 156 ns long the backscattering particles from the earlier bunch crossings will arrive during the later bunch crossings and have to be considered for the background as well. The figure also shows that the innermost layer is more strongly affected by the background than the outer ones.

There is a strong azimuthal dependence of hits in the vertex detector from backscattering particles, as can be seen in Figure 5.3, where the distribution of hits in the vertex detector is shown differentiated by provenance. The hits from particles coming from the beam pipe behind the BeamCal cause a large peak near $\phi = 0°$, where the magnetic solenoid field projects the particles from the outgoing beam pipe onto the vertex detector layers.

5.1.2 Conical Beam Pipe Downstream of the BeamCal

The problem with the beam pipe behind the BeamCal and the magnetic field lines pointing directly to the vertex detector is removed by changing the layout to a conical beam pipe with a half-opening angle of 10 mrad. The inner radius of the BeamCal was increased to 35 mm, which corresponds to about 10 mrad at its downstream end. Inside the BeamCal the beam pipe is cylindrical; it takes a conical shape behind it. Figure 5.4 shows this version of the detector forward region (Model 2). The incoming beam pipe inside the BeamCal is still reminiscent of the ILD layout with a radius of 15 mm.

As with Model 1, incoherent e^+e^- pair background corresponding to 10 BX was simulated. The number of hits directly coming from the IP is lower than in the previous model due to an improved identification procedure for the provenance of the particles.

---

*Per bunch crossing means that all hits from one bunch crossing of incoherent e^+e^- pairs are summed up, regardless of their arrival time in the vertex detector.

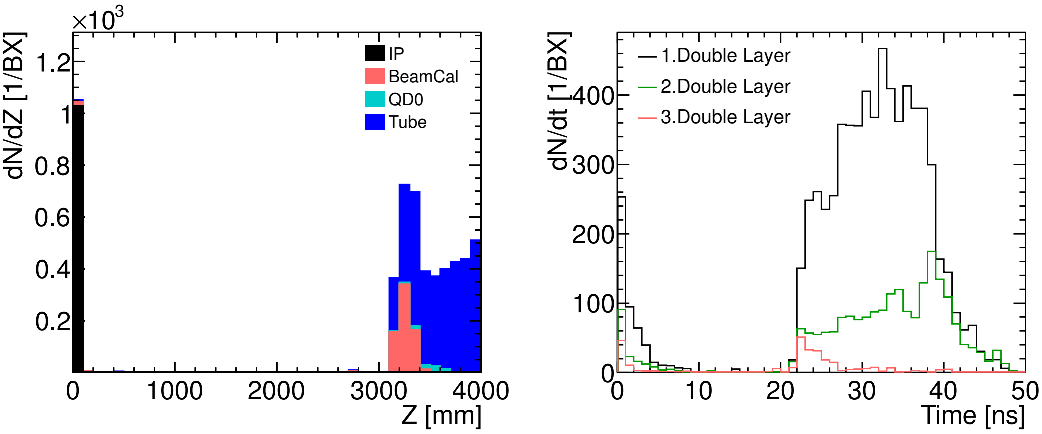

(a)

(b)

Figure 5.2: Hits in the VXD from incoherent e^+e^- pairs simulated with the forward region of Model 1. (a) Stacked histograms of the Z-coordinate of the provenance of particles hitting the vertex detector, different colours mark different identified scattering surfaces. (b) Distribution of the arrival time of the hits in the three double layers of the vertex detector.

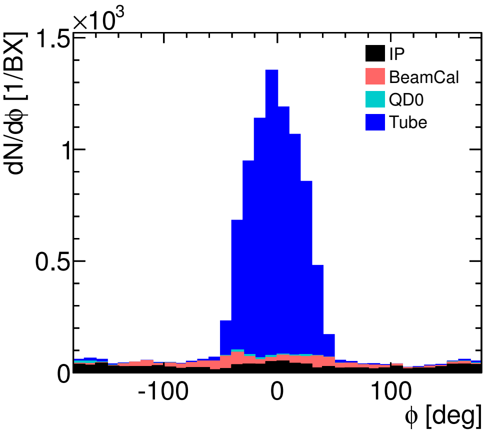

Figure 5.3: Azimuthal distribution of the sum of hits in all layers of the vertex detector by provenance.

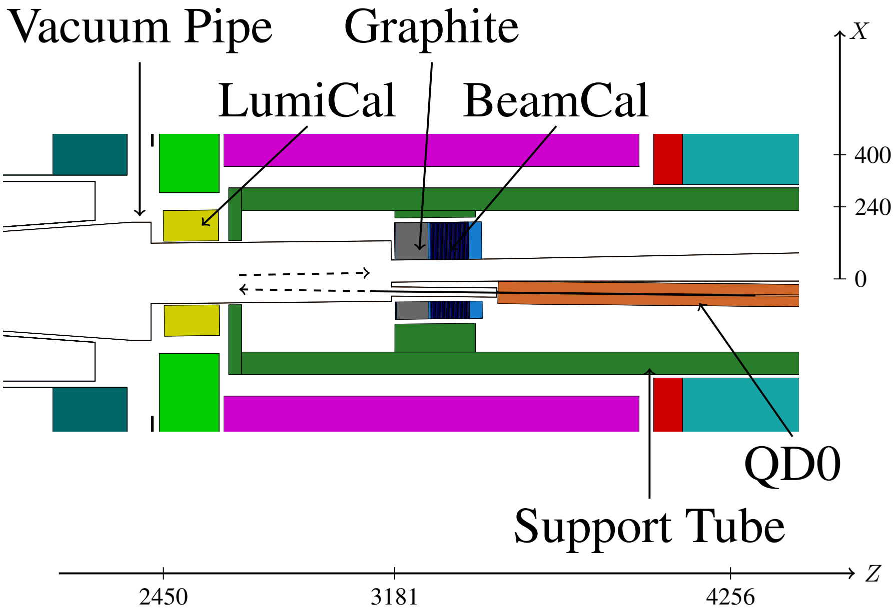

Figure 5.4: Model 2: Forward region with the QD0 at $Z = 3.5$ m and a conical beam pipe. Dimensions are given in millimetre.

Most of the hits from particles originating behind the BeamCal are removed (compare Figure 5.2a with Figure 5.5a), which greatly reduces the number of hits in the vertex detector from backscattering particles (Figure 5.5b). More importantly, the central part of the ‘hot spot’ around $\phi = 0°$ in the vertex detector is removed. However, particles from the inner edge of the BeamCal are still projected onto the vertex detector by the magnetic field.

To avoid this ‘overlap’ between the opening in the BeamCal and the vertex detector several solutions are possible: Using a detector integrated dipole field [84], which would cause the field lines to be parallel to the outgoing beam axis. Then the magnetic field would lead particles back to the IP rather than to the vertex detector. However, a detector integrated dipole in this configuration causes an unacceptable loss of luminosity of about 20% [65]. The second option is moving the BeamCal closer to the IP, until the opening of 10 mrad is smaller than the vertex detector. The BeamCal would have to be placed at $Z = 1.5$ m, giving an inner radius of 15 mm for the 10 mrad half-opening, and 15 mm offset from the detector axis due to the crossing angle for a maximum extent in X of 30 mm. This would place the BeamCal well inside the tracking volume, which is not acceptable either. A third alternative is increasing the vertex detector radius, thus reducing the vertex resolution.

5.2 BeamCal Layout

For the next iteration, the BeamCal was moved 290 mm closer to the IP to accommodate the Kicker and BPM of intra-train-feedback. The start of the conical beam pipe was moved for-

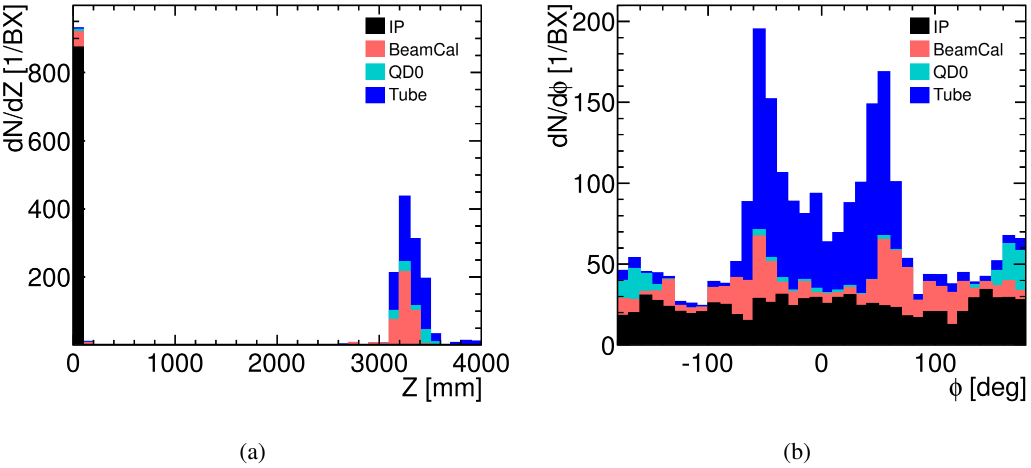

(a)

(b)

Figure 5.5: Hits in the VXD from incoherent e^+e^- pairs simulated with the forward region of model 2 (Figure 5.4). (a) Stacked histograms of the Z-coordinate of the provenance of particles hitting the vertex detector, different colours mark different scattering surfaces. (b) Azimuthal distribution of the sum of hits in all layers of the vertex detector by provenance.

ward correspondingly, but the BeamCal inner radius was not changed. The intra-train-feedback system needs to be placed close to the IP, but must be shielded from the incoherent e^+e^- pair background. In the model the BPM (90 mm length) and Kicker (200 mm length) are represented by iron cylinders with their approximate sizes. Because of the limited lateral space they cannot be placed at the same Z-position. The radius of the incoming beam was reduced between the QD0 and the combined beam pipe on the IP-facing side of the BeamCal. Figure 5.6 shows Model 3 with the updated forward region, including the BPM and kicker.

For this model, 312 BX of incoherent e^+e^- pairs were simulated in MOKKA. The incoherent pairs were generated with GUINEAPIG using the bunch particle distributions coming from the accelerator and BDS simulation [24], which resulted in fewer high p_T and large θ particles causing less direct hits in the vertex detector.

The background from backscattering particles in the vertex detector was only marginally affected by these changes (compare Figure 5.5b and Figure 5.7a). However, the reduced size of the incoming beam pipe makes a large empty sector in the BeamCal apparent. Therefore, as a next step the BeamCal layout was changed (see Section 4.5.2). The space surrounding the incoming beam pipe was filled with absorber material, and the graphite coverage was completed. This improves the shielding of the final focus quadrupole and removes all backscattering particles from its surface. Figure 5.7 shows the azimuthal distribution of hits in the vertex detector with the two different BeamCal layouts; the contribution of hits coming back from the QD0 surface was reduced, as well as the overall number of hits from backscattering particles.

The hit densities per bunch crossing in the different layers of the vertex detector averaged over their length are shown in Figure 5.8. ‘Layout 1’ refers the BeamCal with the key-hole shaped

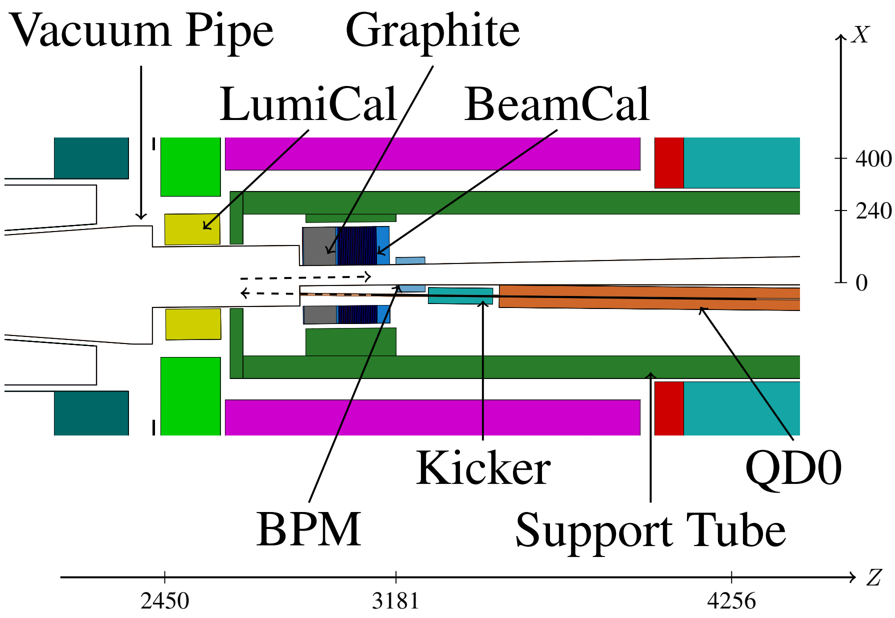

Figure 5.6: Model 3: Forward region with space for the intra-train-feedback components. Dimensions are given in millimetre.

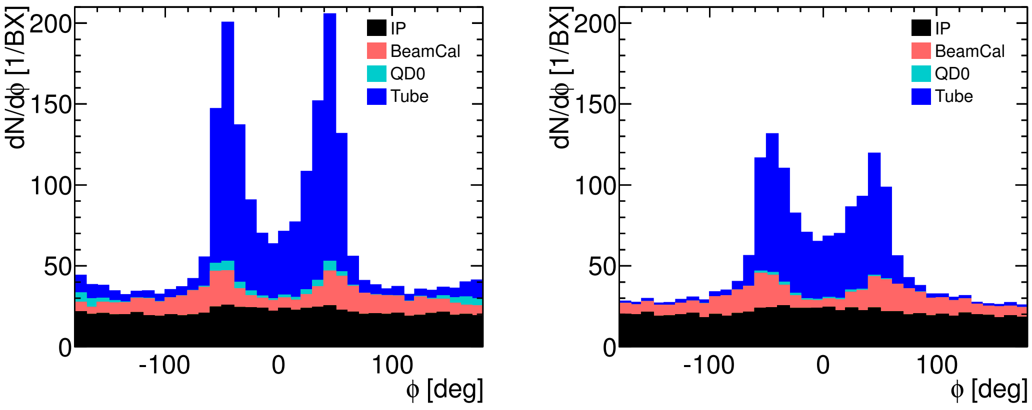

(a)

(b)

Figure 5.7: Azimuthal distribution of the sum of hits in all layers of the vertex detector by provenance: (a) Simulated with the forward region of model 3 (Figure 5.6), and (b) with the same forward region and the improved BeamCal layout.

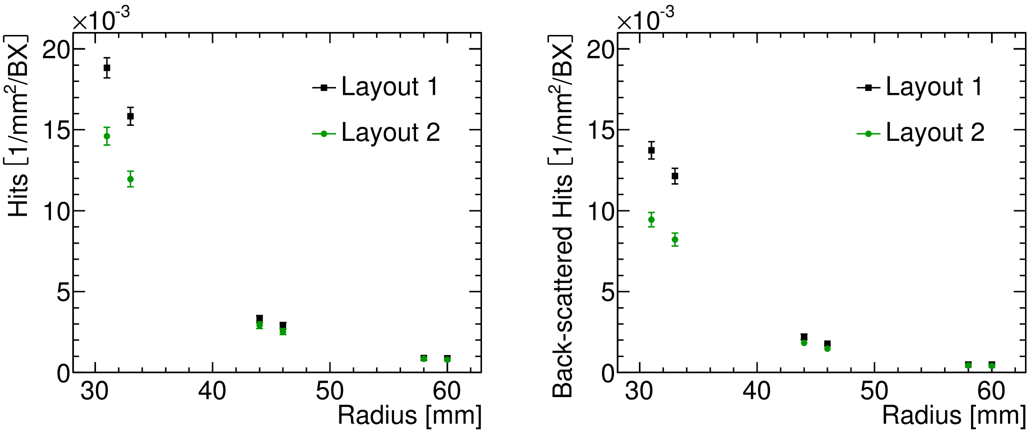

(a) Total hit rate

(b) Hit rate from backscattered particles

Figure 5.8: Hit rate in the different layers of the vertex detector for the two different BeamCal layouts. (a) Total hit rate including the direct component and (b) only the contribution from backscattering particles.

cutout, and 'Layout 2' is the BeamCal with the full coverage. The rate from backscattered particles in the first double layer is reduced by almost 30% with the updated BeamCal layout, from $14 \cdot 10^{-3}$ Hits/mm^2/BX down to $10 \cdot 10^{-3}$ Hits/mm^2/BX. The reduction in the other layers is smaller.

Figure 5.9 shows the rate of hits in the different layers during one bunch train for the different BeamCal layouts. The hits in each layer have been added up for 312 BX with 0.5 ns between each bunch crossing. During the first 20 ns only direct hits contribute to the background. After 20 ns the first backscattering particles arrive and the hit rate rises.

5.3 Changes in the Central Beam Pipe

Given the various constraints further changes in the forward region were not possible. However, a change in the layout of the FTD disks near the vertex detector pointed to possible further improvements for the background from backscattering particles.

In the initial design the conical part of the beam pipe was foreseen to be made of Beryllium, which has a very long radiation length ($X_0 = 35$ cm) and therefore minimises the amount of material in front of the forward tracking disks. However, because of the very shallow angle of particles with respect to the beam pipe, even a thin conical beam pipe still gives a large material budget before the tracking disks.

The last doublet of the pixel forward tracking disks was initially positioned on the conical section of the central beam pipe (Figure 5.10a). The entire beam pipe up to $Z = 2.6$ m was considered to be made out of beryllium with a wall thickness of 1 mm. Realistically, additional support around the beam pipe would be necessary to keep it from buckling under pressure [85].

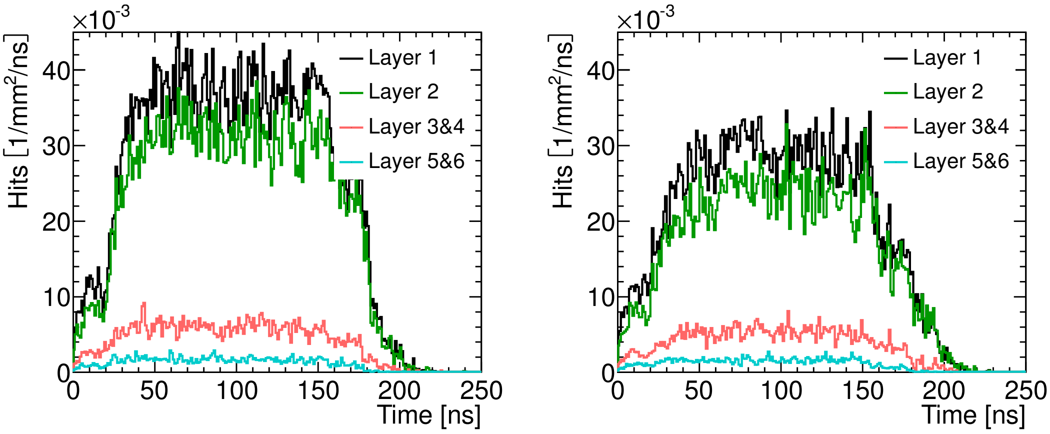

(a) Layout 1

(b) Layout 2

Figure 5.9: Hit densities in the vertex detector layers during one bunch train, for the two different BeamCal models. The entries for layers 3 and 4, and for layers 5 and 6 have been averaged.

Alternatively, the wall thickness would have to be larger, around 1% of the diameter, as for example in the LHCb beam pipe [86].

Later, the inner cylindrical beam pipe length was increased to 260 mm, to position all pixel FTDs before the conical beam pipe begins (Figure 5.10b). The opening angle of the beam pipe was also changed, to point towards the IP. Furthermore, only a small part of the conical beam pipe is still made from beryllium, up to $Z = 377$ mm and $R = 43$ mm. The remaining part of the cone is made of iron. The wall thickness in both parts is 1.2 mm.

This change in the beam pipe geometry, with an increase in the conical beam pipe wall thickness further reduced the background from backscattering particles in the vertex detector. Figure 5.11 shows the background during one bunch train. The maximum hit rate is reduced to $20 \cdot 10^{-3}$ Hits/mm^2/ns compared to $30 \cdot 10^{-3}$ Hits/mm^2/ns with the pure beryllium beam pipe (Figure 5.9b).

5.4 Spectrum of Backscattering Particles

The detector model with the updated BeamCal layout and the hybrid conical beam pipe described in Section 5.3 was used to study the backscattering particles and the background in the vertex detector in more detail.

The graphite layer on the IP-facing side of the BeamCal is 10 cm thick, which corresponds to about 0.5 X_0. This means that about 40% of the electrons will radiate a bremsstrahlung photon. Lower energy electrons will lose some of their energy through ionisation, and photons will be absorbed through the photoelectric effect. Thus the number and energy of the backscattering particles from the front face of the BeamCal will be reduced.

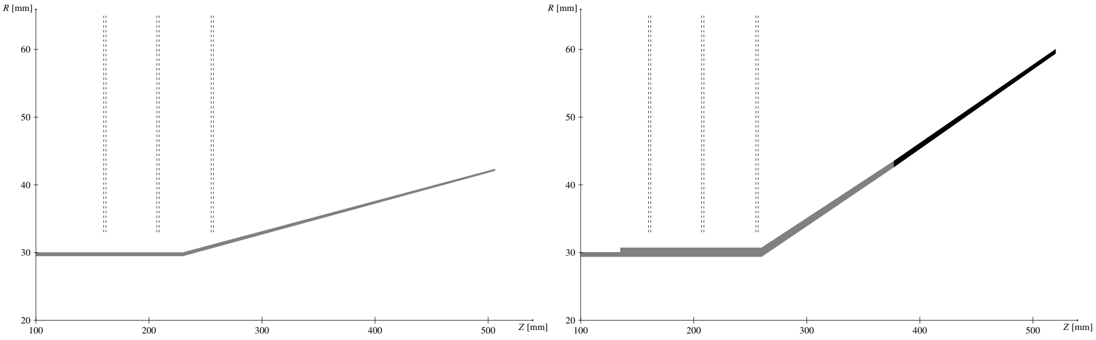

(a) (b)

Figure 5.10: Sketch of the different beam pipe geometries. Gray marks beryllium and black marks iron. The dashed lines give the position of the FTD pixel disks.

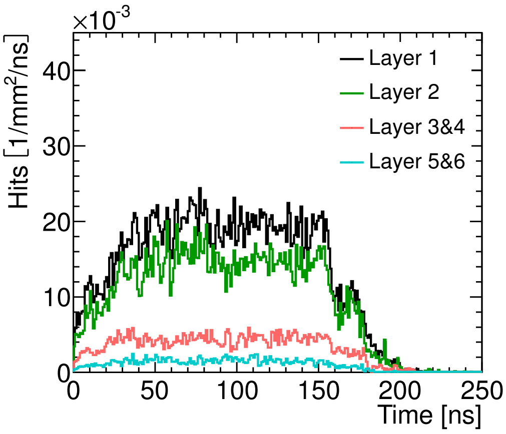

Figure 5.11: Hit densities in the vertex detector layers during one 156 ns long bunch train for the conical beam pipe with a beryllium and iron part. The entries for layer 3 and 4 and for layers 5 and 6 have been averaged.

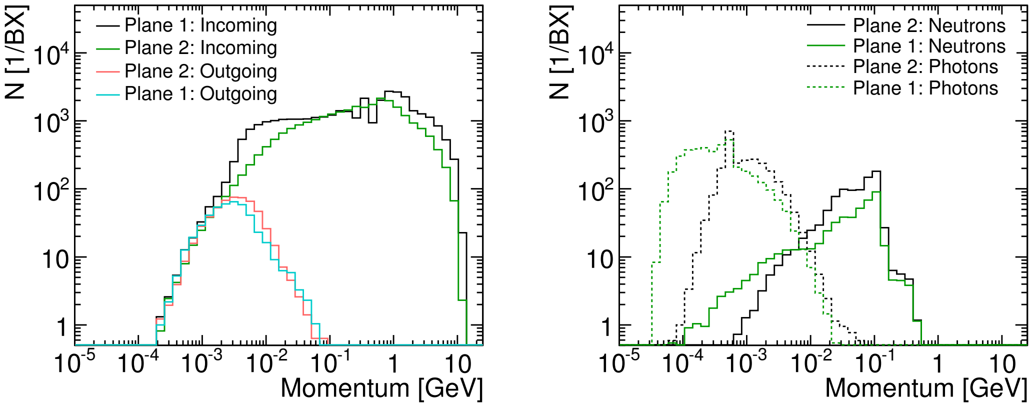

(a) Electrons

(b) Photons and neutrons

Figure 5.12: Momentum spectrum of particles travelling towards and away from the BeamCal. ‘Plane 1’ is located between the graphite layer and the IP and ‘Plane 2’ is located between the graphite and the BeamCal. (a) Electrons travelling towards and away from the BeamCal, (b) photons and neutrons scattering back from the BeamCal. The peak in the photon spectrum at 511 keV comes from electron–positron annihilation.

The momentum spectrum of electrons and positrons hitting the BeamCal is shown in Figure 5.12a. Shown are particles passing a scoring plane with the same radial extent as the BeamCal, either in front of the graphite layer (Plane 1) or between the graphite and the BeamCal (Plane 2). Because of the momentum distribution of the particles, the effect of the deflection during the bunch-crossing from beam-beam interaction, and the magnetic field the distribution of the particle momentum is cut off at 10 GeV, with a most probable particle momentum of around 1 GeV. The figure shows that a number of lower momentum electrons ($p < 100$ MeV) are either absorbed in the graphite or radiate photons. There is a shoulder in the incoming electron spectrum at $p = 5$ MeV from the energy cut-off in GUINEAPIG.

The momentum spectra of photons and neutrons originating in the BeamCal and travelling back towards the IP are shown in Figure 5.12b. The spectra are shown for the two planes before and after the graphite. Neutrons are produced with a momentum of a few hundred MeV, with long tails and a maximum of 1 GeV. Photons are produced in a broad spectrum with a peak from the electron–positron annihilation at 511 keV. The photons are the largest part of the backscattering particles. For both particle types the effect of the graphite is visible; the average momentum is moved towards lower values.

The energy loss through ionisation is linear with the thickness of the material, so that a thicker graphite layer would reduce the energy of backscattering electrons further. The photon absorption only increases logarithmically with the thickness of the graphite. A thicker graphite layer would only offer a small improvement, but the available space in the forward region is already scarce.

5.5 Barrel Vertex Detector Radius

The hit rate in the vertex detector depends on the radius for two reasons. Because of the fairly small transverse momentum, the rate of the background particles for larger radii is reduced by the magnetic field. In addition there is a geometrical reduction of the hit density due to the increased surface of layers at larger radii. But, because of the additional background from backscattering particles, the p_{T} and angular spectrum alone do not allow a direct estimate of the dependence of the hit rate on the radius.

To estimate the hit density in the barrel layers for different radii, the radial position of the vertex layers were modified. The location of each VXD doublet was changed to scan the background rates for VXD radii from 31 mm to 80 mm in 1 mm steps with the MOKKA parameters `VXD_inner_radius`, `VXD_radius_r3`, and `VXD_radius_r5`. MOKKA automatically increases the number of modules and adjusts their position to cover the full azimuthal angle. The length of the modules was kept constant, therefore, the polar angle coverage is slightly reduced the further out the layers are located.

Figure 5.13 shows the resulting hit densities in the barrel layers averaged over the length of the modules. The total hit density (Figure 5.13a) falls from approximately $10 \cdot 10^{-3}$ Hits/mm^2/BX to $0.5 \cdot 10^{-3}$ Hits/mm^2/BX for radii between 31 mm and 80 mm. The azimuthal distribution (Figure 5.13b) shows an increased hit density on the right side ($X > 0$), originating from backscattered particles from the forward region and reflecting the asymmetric configuration of this region, as the LumiCal and BeamCal are centred on the outgoing beam axis. Direct hits (occurring within 15 ns, Figure 5.13c) and backscattered hits (occurring after 15 ns, Figure 5.13d) contribute approximately equally to the total hit rate for all radii.

The hit densities drop with increased radius, but there is no distinct point at which the background drops significantly enough to justify moving the vertex detectors farther away from the IP.

5.6 Magnetic Field

The solenoid field of the detector prevents the low-p_{T} part of the incoherent pairs from reaching the vertex detector. Figure 5.14 shows the rate in the layers of the VXD for a field of 3 T, 4 T and 5 T.

As expected, the stronger the magnetic field is the lower the background rate. However, the solenoid field only reduces the rate of direct hits (Figure 5.14b), whereas for hits from particles scattering back from the forward region the rates (Figure 5.14c) are almost independent of the magnetic field. Neutrons and photons are not affected by the magnetic field, but the low momentum electrons are focused more by a stronger field. With a stronger solenoid field, the inner most radius of the vertex detector could be decreased, but the expected gain is limited to the contribution from direct hits; the rate from backscattering particles is not affected.

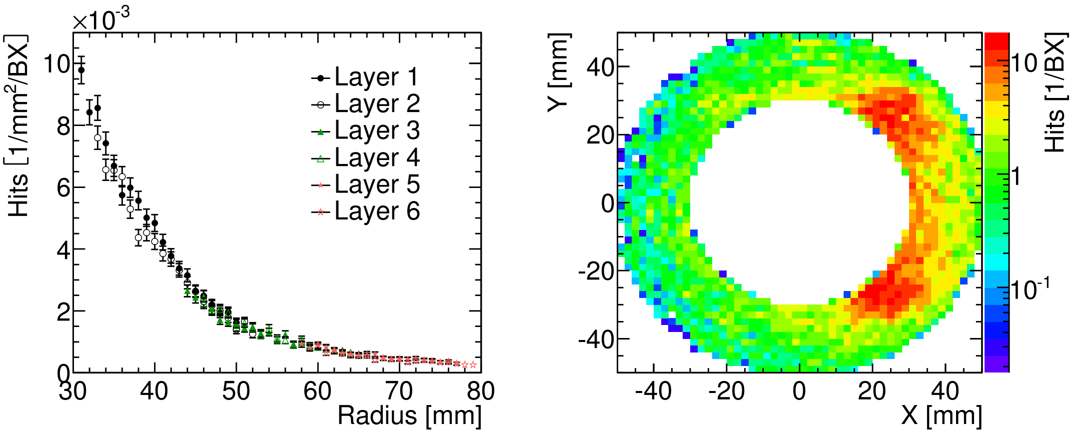

(a) Radial distribution

(b) XY distribution

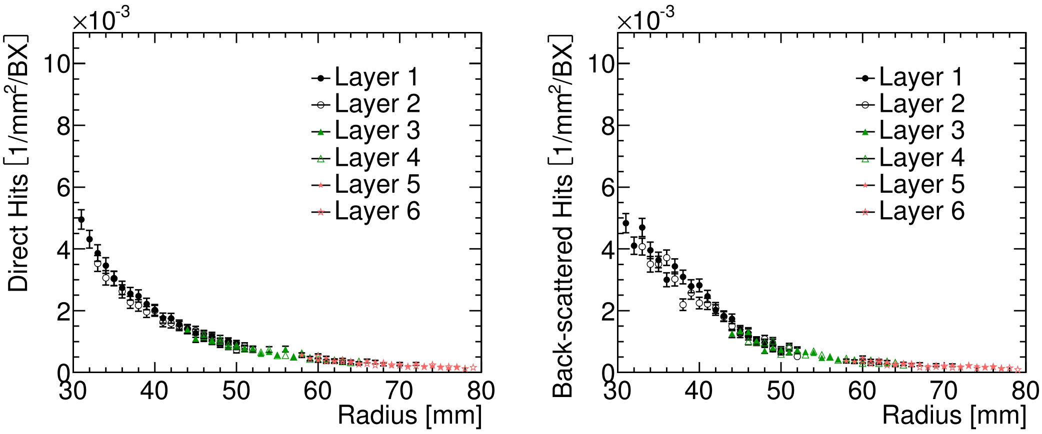

(c) Direct hits, $t < 15$ ns

(d) backscattered hits, $t > 15$ ns

Figure 5.13: Hit densities in the vertex detector barrel layers as function of the radius of the layer. Shown are (a) the radial and (b) the XY distribution of the total hit density, as well as separately the contributions from (c) direct and (d) backscattered hits.

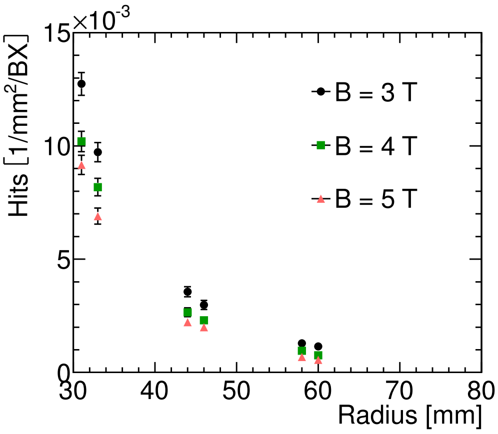

(a) All hits

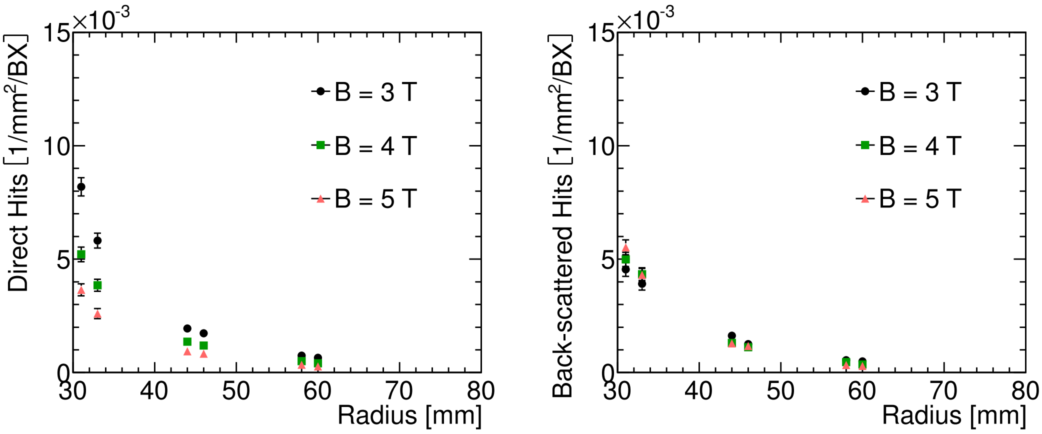

(b) Direct hits, $t < 15$ ns

(c) Backscattered hits, $t > 15$ ns

Figure 5.14: Hit densities from incoherent pairs in the six vertex-barrel layers as function of the radius of the respective layer for three different values of the magnetic field. Shown are (a) the total hit density, as well as separately the contributions from (b) direct and (c) backscattered hits

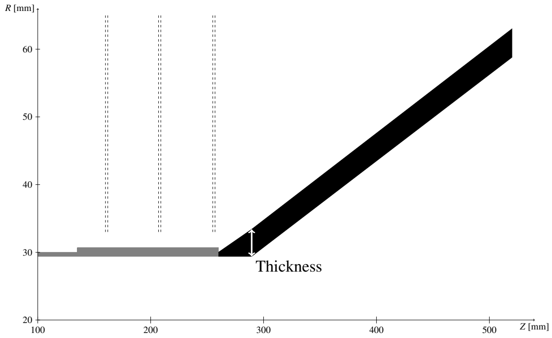

Figure 5.15: Sketch of the central part with the cylindrical and conical beam pipe used as a mask, including the definition of the thickness of the beam pipe. Gray marks beryllium and black marks iron. The dashed lines give the position of the FTD pixel disks.

5.7 Conical Beam Pipe as a Mask

Finally, the thickness and material of the beam pipe were varied to investigate the reduction in the number of hits in the vertex detector stemming from backscattering particles. Here, the thickness is the radial width of the beam pipe material as shown in Figure 5.15. The simulated materials were: aluminium, beryllium, iron, lead, titanium, and tungsten. The materials were chosen for the potential use for a vacuum pipe (aluminium, beryllium, iron, titanium), or because of their short radiation length (lead, tungsten). The resulting hit densities for different materials and thicknesses are summarised in Figure 5.16.

The hit density from backscatters in the vertex detector does not scale with the radiation length of the material of the conical beam pipe. For example, whereas the radiation length of 1.2 mm tungsten corresponds to an iron thickness of 6 mm, the hit density for iron with this thickness is lower. This can be explained, since the energy of the backscattering particles (cf. Figure 5.12) is around or below the critical energy (for iron, for example, 20 MeV), which is defined as the energy at which the ionisation loss per radiation length is equal to the electron energy [87]. The denser materials, tungsten and lead, offer slightly lower backgrounds at similar thicknesses than iron, but they are not suitable for a vacuum pipe.

With a beam pipe made out of iron and a thickness of 4 mm or more the hit density remains constant, implying that backscattered particles are efficiently absorbed. This beam pipe thickness was chosen for the CDR detector models. With this layout, the number of hits from backscattering particles was reduced by a factor of ten, from $5 \cdot 10^{-3}$ Hits/mm^2/BX (Figure 5.11) to $0.5 \cdot 10^{-3}$ Hits/mm^2/BX (Figure 5.17a). The hits from backscattering particles now cause only 10% of the hits in the vertex detector compared to hits from particles directly coming from the IP. Without a significant contribution from backscattering particles, there are no more hot spots from background hits on the vertex detector. The distribution of hits in all layers of the vertex detector is shown in Figure 5.17b; the significant contribution is from direct hits, and their distribution is independent of the azimuthal angle.

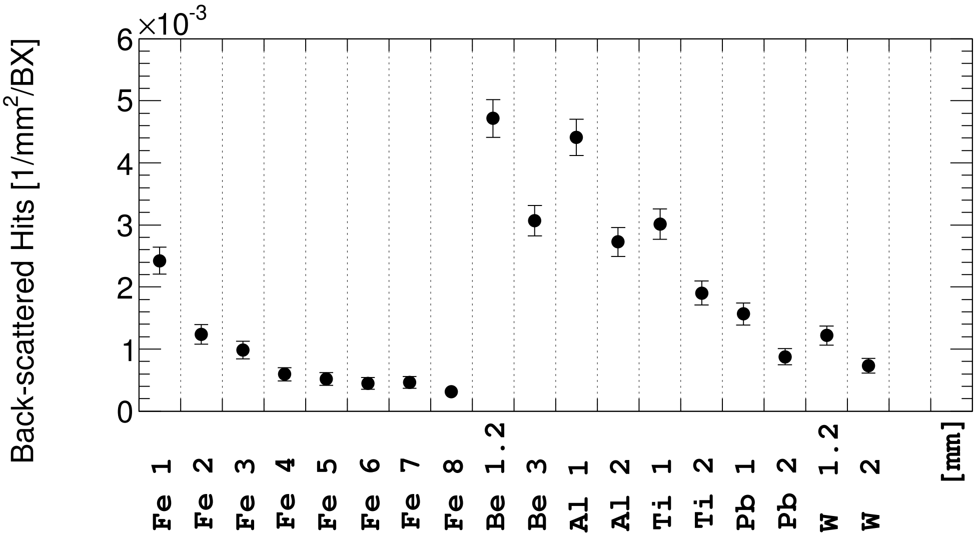

Figure 5.16: Hit densities in the innermost vertex layer from backscattered particles for different beam pipe materials and thicknesses.

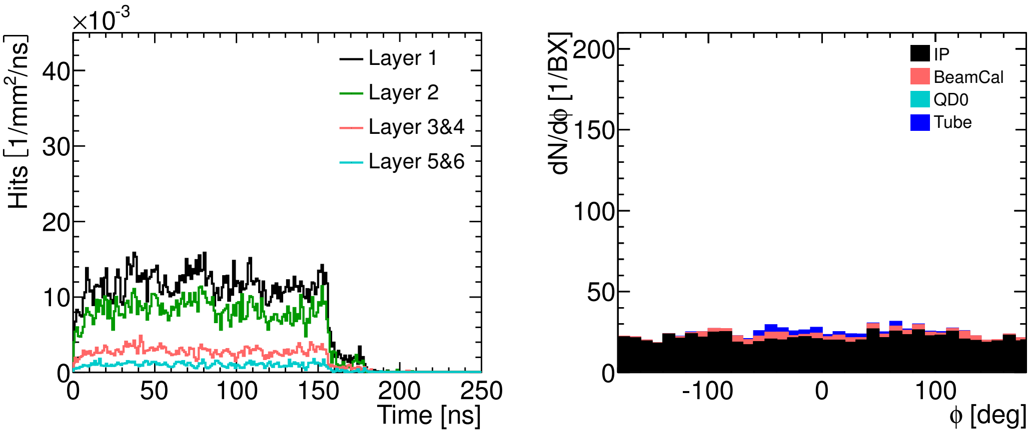

(a)

(b)

Figure 5.17: (a) Hit densities during one 156 ns long bunch train, for the 4 mm thick iron beam pipe. The entries for layer 3 and 4 and for layers 5 and 6 have been averaged. (b) Sum of hits in the vertex detector layers as a function of the azimuthal angle.

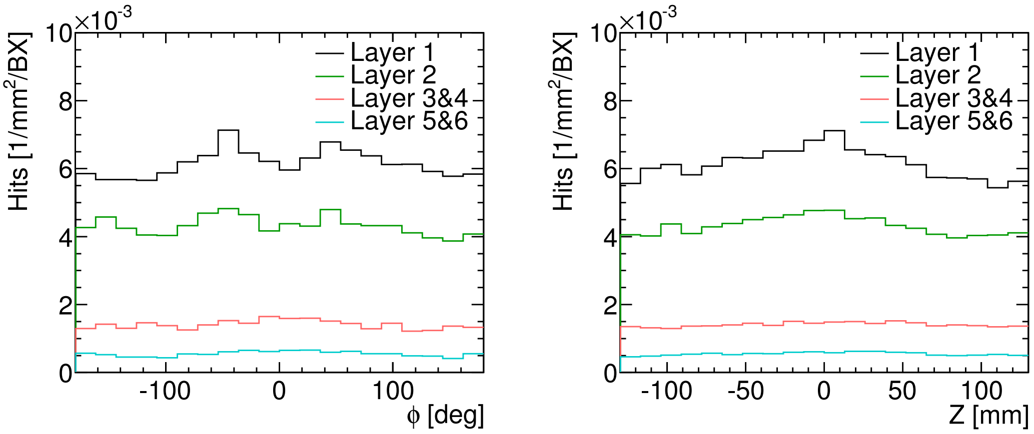

(a) Azimuthal distribution

(b) Longitudinal distribution

Figure 5.18: Distribution of hits from incoherent e^+e^- pairs along the (a) azimuthal angle ϕ and (b) length Z of the vertex detector. Layer 3 and 4, and layer 5 and 6 have been averaged.

5.8 Final Changes

The final step in the layout of the forward region was also taking the requirements from the detector and engineering point-of-view into account, leading to the detector model described in Chapter 4. Compared to Model 5 the position of the LumiCal, BeamCal, and QD0 were changed. All of them were moved further away from the IP. The LumiCal was moved behind the ECal endcap. Additional space for the vacuum valves and bellows is required, therefore, the BeamCal was moved further away from the IP. And the QD0 was moved to start aligned with the yoke endcap.

These changes have a negligible impact on the background in the central detector, as most of the backscattering particles no longer reach it. Figure 5.18 shows the distribution of hits in the different layers of the vertex detector. The distributions are flat over the azimuthal angle and length of the detector. The hit density in the innermost layer of the vertex detector from incoherent e^+e^- pairs is $6 \cdot 10^{-3}$ Hits/mm^2/BX.

5.9 Summary of Geometry Optimisation

Table 5.1 lists the total number of hits and the contributions from the different identified background provenances for the detector models discussed in this chapter.

The first models of the CLIC compatible forward region (Model 2 and 3) showed a large contribution of backscattering particles from incoherent e^+e^- pairs to the background in the vertex detector. These backscattering particles mostly originate near the BeamCal or in the beam pipe just downstream of it. Due to the projection of the backscattering particles on the vertex detector by the magnetic field areas with a hit density 5 times above the minimum exist.

Table 5.1: Sum of the number of hits per bunch crossing in the vertex detector identified by provenance for the different detector models.

	Total	IP	BeamCal	QD0	Beam Pipe
Model 1	9340	1030	730	100	7480
Model 2: 10 mrad outgoing beam pipe	2500	870	470	130	1030
Model 3: BeamCal closer to IP	2370	760	390	70	1150
Model 4: Improved BeamCal	1890	750	370	10	760
Model 5: Iron beam pipe	890	770	80	0	40

The amount of indirect background could be reduced by 30% with an improved design of the BeamCal absorber plates and graphite layer (Model 4), but hot spots with 3 times larger background rates in the vertex detector remain.

The contribution from backscattering particles to the background in the first layer of the vertex detector was further reduced—to a level of about 10% of the direct contribution—with a 4 mm thick iron beam pipe (Model 5). In this detector geometry the background distribution is also azimuthally flat, with a hit density of $6 \cdot 10^{-3}$ Hits/mm^2/BX in the first layer of the vertex detector.

6 Background in the Tracking Detectors

In this chapter the estimated hit densities, occupancies, and radiation levels for the tracking detectors are described: The barrel like tracking detectors (Vertex Detector (VXD), Silicon Inner Tracker (SIT), and Silicon External Tracker (SET)), and the disk-like tracking detectors (Forward Tracking Disks (FTDs) and Endcap Tracking Disks (ETDs)). The geometrical parameters of all subdetectors can be found in Section 4.3. Incoherent e^+e^- pairs from 312 BX and $\gamma\gamma \to$ hadron events from 67 bunch trains were simulated in MOKKA with the final CLIC_ILD_CDR detector model as it was described in Chapter 4.

6.1 Hit Densities and Occupancies in the Barrel Tracking Detectors

The final hit density in the vertex detector from incoherent e^+e^- pairs was discussed in Section 5.8: in the first layer the hit density is $6 \cdot 10^{-3}$ Hits/mm^2/BX. The hit density for the particles from the $\gamma\gamma \to$ hadron events in the layers of the vertex detector is shown in Figure 6.1. The average hit density in the first layer is $0.7 \cdot 10^{-3}$ Hits/mm^2/BX, in the centre of the layers the density is almost a factor 2 larger, but still much smaller than the hit density from the incoherent pairs.

The occupancy in the vertex detector is calculated with a pixel size of $20 \times 20\ \mu\text{m}^2$ (Table 4.2), an average cluster size of five per hit, and safety factors of five for the incoherent e^+e^- pairs and of two for the $\gamma\gamma \to$ hadron events (discussed in Section 4.10.1). In the first layer of the vertex detector the occupancy per train is 2% from the incoherent pairs and 0.2% from the $\gamma\gamma \to$ hadrons. Therefore, fast time-stamping will be necessary to keep the number of hits reasonable. Multiple hits in the same pixel are unlikely, so that no multi-hit capable readout electronics will be necessary [4, Chapter 10].

The hit densities of the SIT and SET along their length is shown in Figure 6.2. In the SITs the hit rate from incoherent pairs and $\gamma\gamma \to$ hadron events is almost equal. The hit densities in the first SIT layer is $5 \cdot 10^{-5}$ Hits/mm^2/BX from the incoherent pairs and $9 \cdot 10^{-5}$ Hits/mm^2/BX from $\gamma\gamma \to$ hadron events. The rate of hits is about a factor 100 below that of the first layer of the vertex detector at five times the radius. Using the originally foreseen sensor with a strip size of 9 cm × 50 µm—which gives an area per readout unit roughly ten-thousand times larger than in the VXD—the occupancy per train is about 100 times higher than in the VXD for the incoherent pairs alone. This results in multiple hits per strip during a bunch train, therefore shorter strips or multi-hit capable time-stamping will be required. The hit density in the SET layers from secondaries of incoherent pairs is dominated by the incoherent pairs and reaches up to $1 \cdot 10^{-6}$ Hits/mm^2/BX. The occupancy is around 17%, probably also requiring either shorter strips or time-stamping.

The average hit densities from both contributions for all the silicon barrel layers are shown in

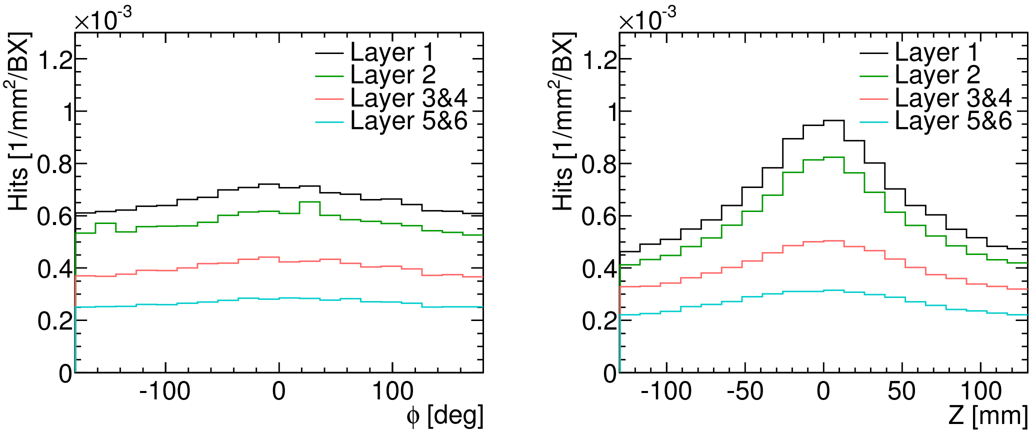

(a) Azimuthal distribution

(b) Longitudinal distribution

Figure 6.1: Distribution of hits from $\gamma\gamma \rightarrow$ hadron events along the (a) azimuthal angle ϕ and (b) length Z of the vertex detector. Layer 3 and 4, and layer 5 and 6 have been averaged.

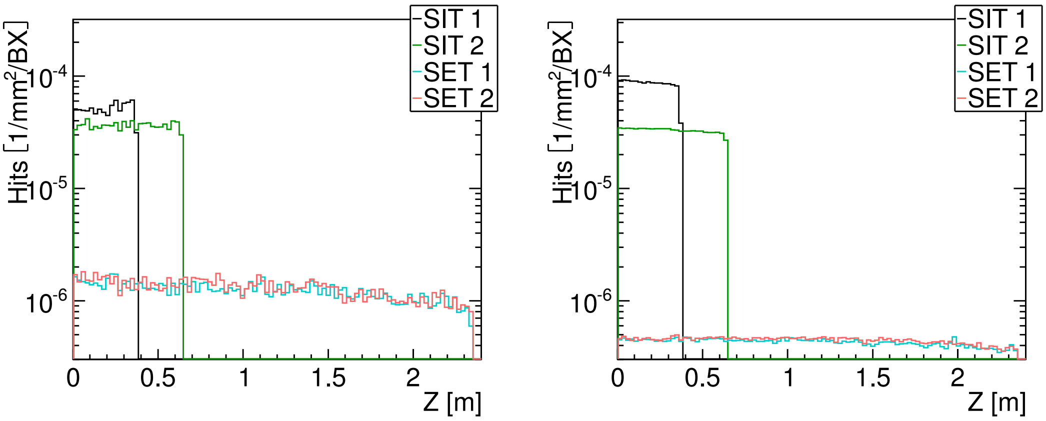

(a) Incoherent pairs

(b) $\gamma\gamma \rightarrow$ hadrons

Figure 6.2: Hit density in the SIT and SET for (a) incoherent pairs and (b) $\gamma\gamma \rightarrow$ hadrons along the detector length.

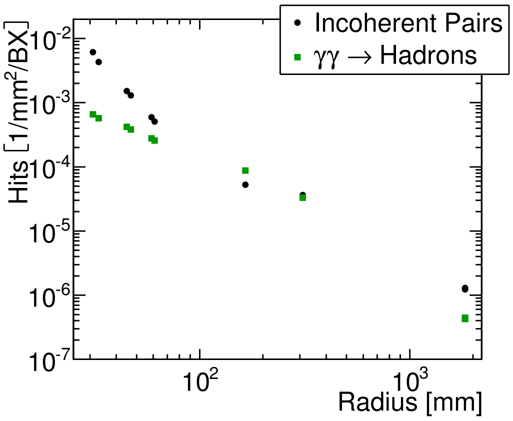

Figure 6.3: Hit densities in the silicon barrel layers.

Figure 6.3. It shows again, that at small radii the incoherent pairs are the dominant background in the vertex detector, at the SIT ($R \approx 300$ mm) the contributions are similar, at the SET ($R \approx 1.8$ m) the incoherent pairs are again dominant, as the contribution of indirect hits from conversion of neutral particles becomes more important. The average hit densities can also be found in Table 6.1.

6.2 Total Ionising Dose and Equivalent Neutron Flux in the Barrel Tracking Detectors

The equivalent neutron flux from incoherent pairs and $\gamma\gamma \to$ hadron events in the layers of the VXD is shown in Figure 6.4. As for the hit density the rate in the centre of the layers is slightly larger than at the ends. The $\gamma\gamma \to$ hadron events produce a larger equivalent flux than the incoherent e^+e^- pairs in the vertex detector, because the damage factor for hadrons is larger than for electrons [83].

The equivalent neutron flux in the SIT and SET is shown in Figure 6.5. For the $\gamma\gamma \to$ hadrons the equivalent neutron flux falls with increasing radius, but the equivalent flux from incoherent pairs in the second SIT layer (SIT2) is larger than in the first layer. In this region the equivalent neutron flux from the incoherent pairs is dominated by backscattered neutrons from the BeamCal. Because the SIT2 is longer and therefore closer to the BeamCal than SIT1, the flux is larger. It is also larger at similar Z-positions, because the angle of the SIT2 with respect to the neutrons coming from the BeamCal is less shallow and thus a larger flux is seen. The rate in the SET falls towards large Z, because of the distance to the IP, and because backscatters can only come from the BeamCal on the opposite side of the detector. The average of the equivalent neutron flux from incoherent pairs and $\gamma\gamma \to$ hadrons are shown in Figure 6.6a. The maximum 1 MeV-neutron-equivalent flux is $2 \cdot 10^{10}$ $\mathrm{n_{eq}/cm^2/yr}$ in the innermost layer of the vertex detector and generally falls with increasing radius to around $1 \cdot 10^{8}$ $\mathrm{n_{eq}/cm^2/yr}$ in the SET layers.

For the TID only the longitudinal and azimuthal average is shown (Figure 6.6b), its longitudi-

Table 6.1: Summary of the hit density, equivalent neutron flux and Total Ionising Dose (TID) for the barrel silicon detectors.

	Hit Density $[10^{-3}/\mathrm{mm}^2/\mathrm{BX}]$		Flux $[10^9 \mathrm{n_{eq}}/\mathrm{cm}^2/\mathrm{yr}]$		TID [Gy/yr]	
	Pairs	$\gamma\gamma$	Pairs	$\gamma\gamma$	Pairs	$\gamma\gamma$
VXD 1	6.14	0.66	3.87	11.51	39.43	4.57
VXD 2	4.32	0.57	2.88	8.57	27.83	4.01
VXD 3	1.52	0.42	1.12	5.25	9.09	2.80
VXD 4	1.30	0.38	0.96	4.48	7.88	2.52
VXD 5	0.59	0.28	0.49	3.18	3.57	1.81
VXD 6	0.51	0.26	0.44	2.81	3.10	1.68
SIT 1	0.05	0.09	0.15	0.50	0.23	0.43
SIT 2	0.04	0.03	0.21	0.25	0.15	0.17
SET 1	0.001	0.0004	0.07	0.08	0.004	0.002
SET 2	0.001	0.0004	0.07	0.08	0.004	0.002

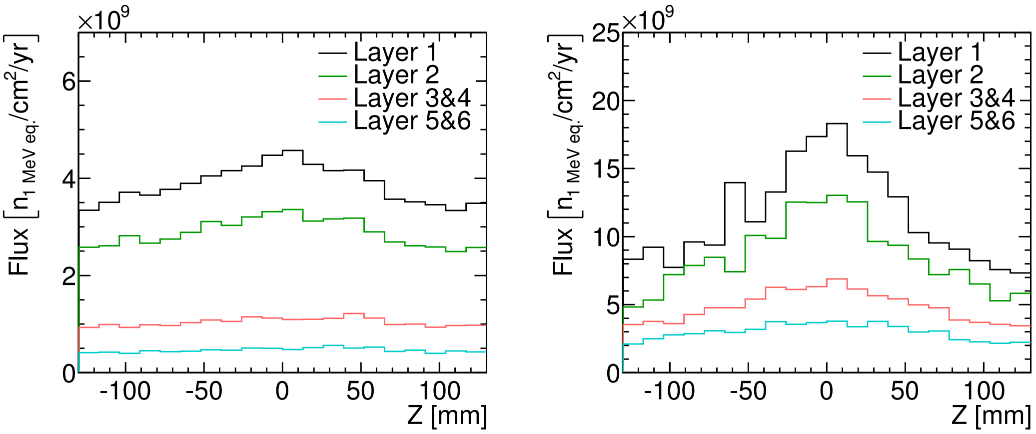

(a) Incoherent pairs

(b) $\gamma\gamma \rightarrow$ hadrons

Figure 6.4: Equivalent neutron flux along the length of the VXD (a) incoherent pairs and (b) $\gamma\gamma \rightarrow$ hadrons. Layer 3 and 4, and layer 5 and 6 have been averaged.

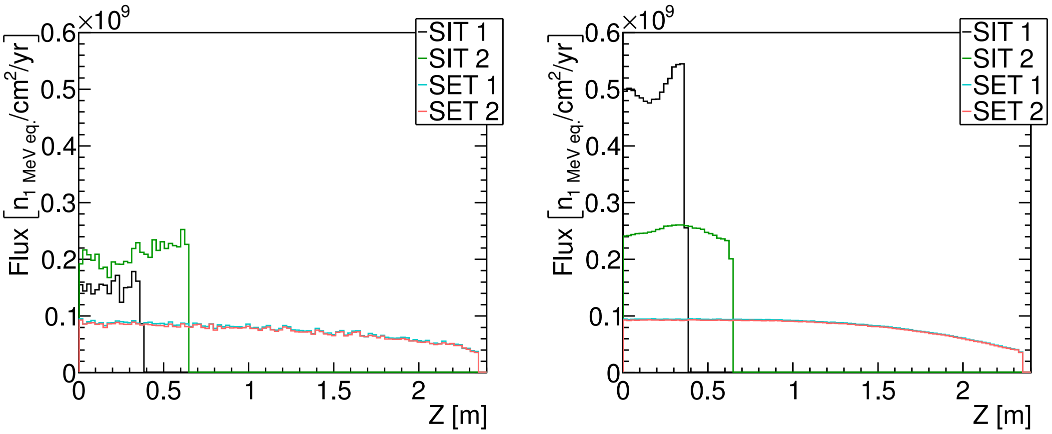

(a) Incoherent pairs

(b) $\gamma\gamma \rightarrow$ hadrons

Figure 6.5: Equivalent neutron flux along the length of the SIT and SET averaged between the forward and backward side of the detector for (a) incoherent pairs and (b) $\gamma\gamma \rightarrow$ hadrons.

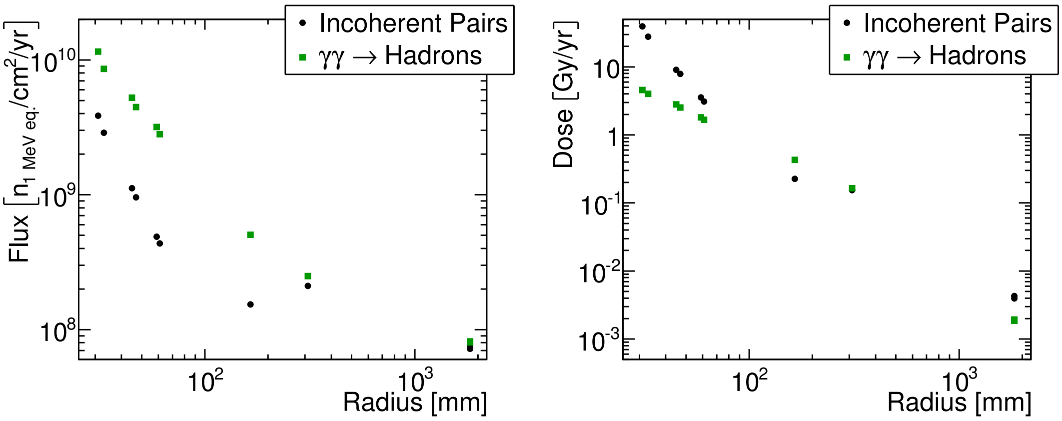

(a) Equivalent neutron flux

(b) Total ionising dose

Figure 6.6: (a) Equivalent neutron flux and (b) total ionising dose in the barrel silicon detectors induced by incoherent pairs and $\gamma\gamma \rightarrow$ hadrons.

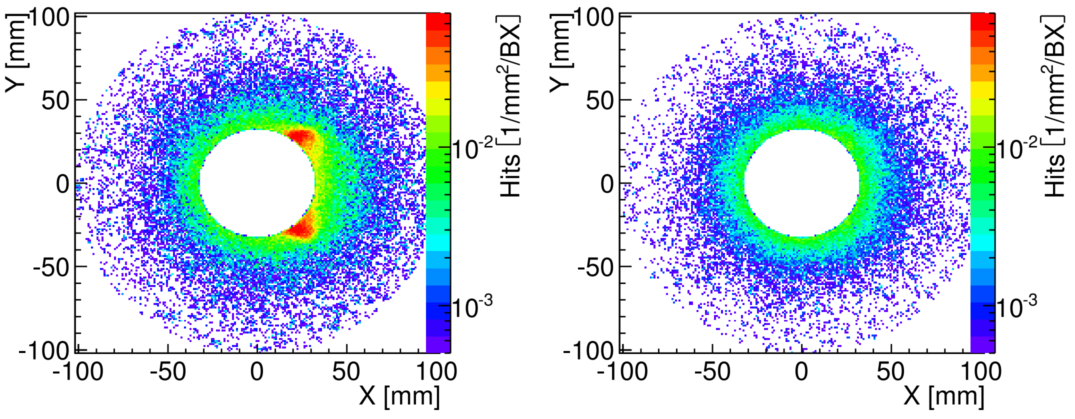

(a) Beryllium beam pipe

(b) Iron beam pipe

Figure 6.7: Hit densities from incoherent pairs in the innermost forward tracking disks for the beryllium and 4 mm iron beam pipe.

nal and azimuthal distribution is similar to the distribution of the hit density. The dose is falling with increasing radius. The maximum TID is around 50 Gy/yr (not including safety factors). The average values for the total ionising dose and equivalent neutron flux can also be found in Table 6.1.

6.3 Background in the Forward Tracking Disks

6.3.1 Effect of the Beam Pipe on the Background in the Forward Tracking Disks

Without the masking from the 4 mm iron beam pipe the inner FTDs also suffer from a large rate of backscattering particles, with a strong azimuthal dependence. Figure 6.7 shows the XY-distribution for the beryllium and iron beam pipe, respectively. With the beryllium beam pipe two high-density regions at low radius and at azimuthal angles of approximately 45° and 135° exist, similar to what was observed for the vertex detector barrels. In these regions the hit density is a factor ten higher than for other points at the same radius. These hot spots are removed with the iron beam pipe.

The disks further away from the beam axis benefit from the iron beam pipe as well. The number of backscattering particles giving energy deposits is reduced, as shown in Figure 6.8. For incoherent pairs the hit rate in the last disks is greatly reduced with the iron beam pipe.

There is, however, a small increase in the number of hits in disk 7 for $\gamma\gamma \to$ hadron events with the 4 mm iron beam pipe compared to the beryllium beam pipe (Figure 6.9). Close to the beam pipe the number of hits increases for the FTDs 7, 8 and 9, for disks 8 and 9 this is also visible for the beryllium beam pipe. This effect might be due to particles showering in the beam pipe and producing secondaries that hit the sensors. The vertex pixel disks are not negatively affected, because the secondaries are produced too far away.

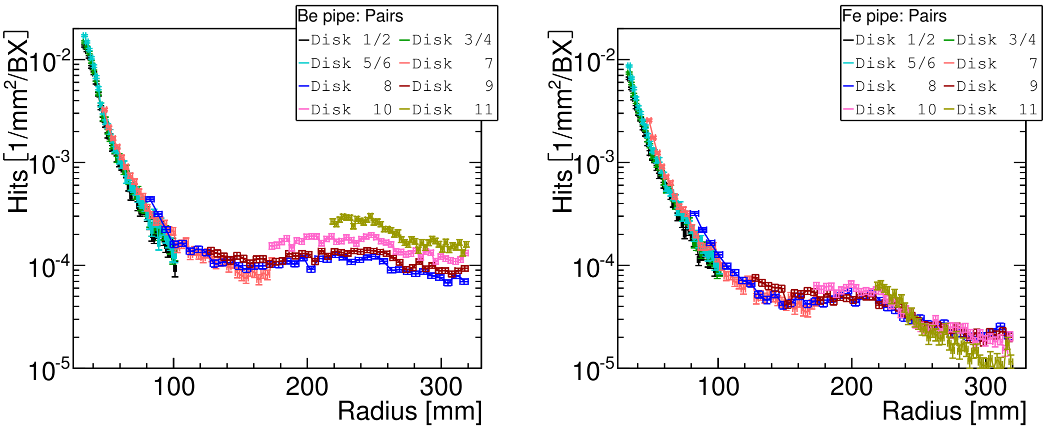

(a) Beryllium beam pipe

(b) Iron beam pipe

Figure 6.8: Radial distribution of the hit densities in the forward tracking disks for the beryllium and 4 mm iron beam pipe from incoherent pairs.

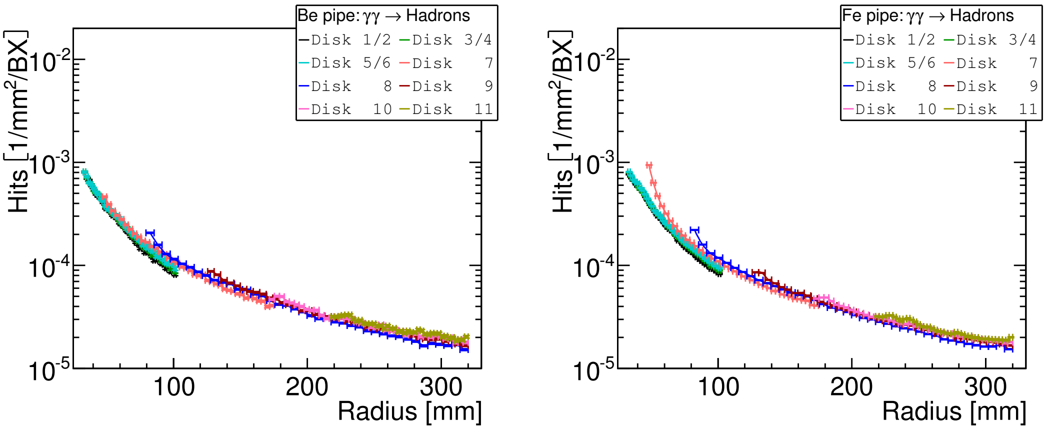

(a) Beryllium beam pipe

(b) Iron beam pipe

Figure 6.9: Radial distribution of the hit densities in the forward tracking disks for the beryllium and 4 mm iron beam pipe from $\gamma\gamma \to$ hadron events.

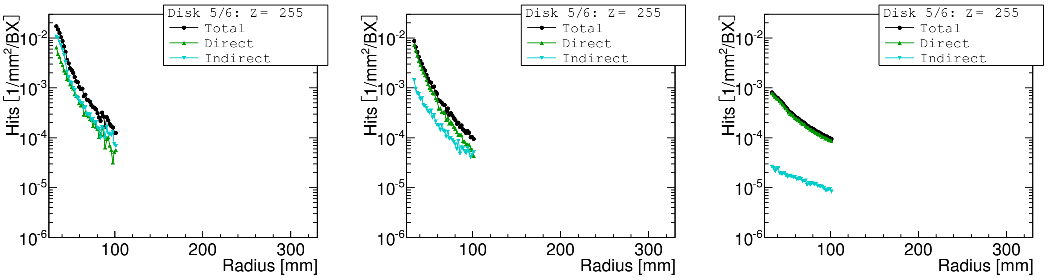

(a) Pairs: Beryllium beam pipe (b) Pairs: Iron beam pipe (c) $\gamma\gamma \rightarrow$ hadrons: Iron beam pipe

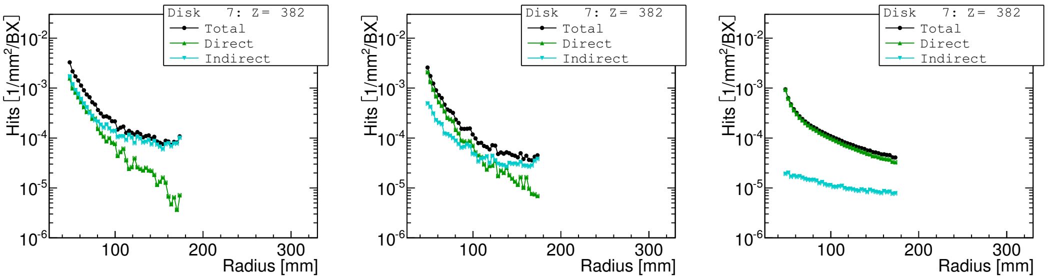

(d) Pairs: Beryllium beam pipe (e) Pairs: Iron beam pipe (f) $\gamma\gamma \rightarrow$ hadrons: Iron beam pipe

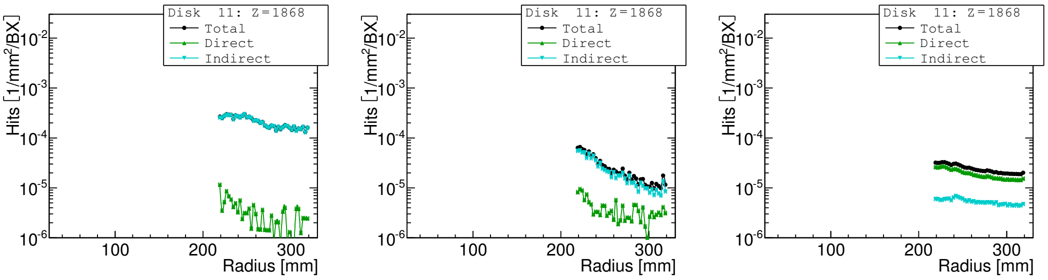

(g) Pairs: Beryllium beam pipe (h) Pairs: Iron beam pipe (i) $\gamma\gamma \rightarrow$ hadrons: Iron beam pipe

Figure 6.10: Hit rates in selected FTDs (rows), for different detector geometries and background types (columns). The hit rate is split between direct and indirect hits.

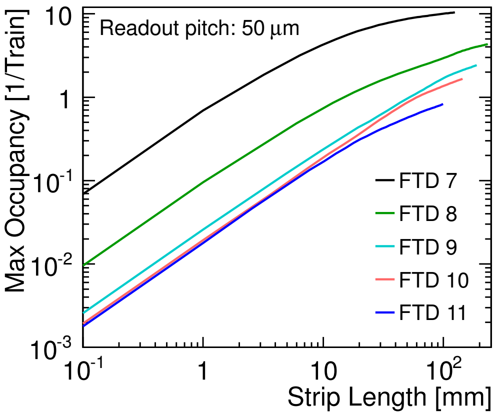

Figure 6.11: Maximum readout occupancy per train as a function of the strip length for the five outer FTDs. The hits from incoherent pairs and $\gamma\gamma \rightarrow$ hadrons are summed and integrated over the respective strip area, taking into account cluster formation and safety factors as discussed in Section 4.10.1.

Figure 6.10 shows the hit densities of selected FTDs: the last double pixel disks (FTD 5/6), the first strip-based disks (FTD 7), and the last strip-based disk (FTD 11). For incoherent pairs, the hit densities for the 1.2 mm beryllium and 4 mm iron beam pipe are shown, for the $\gamma\gamma \rightarrow$ hadrons only the 4 mm iron option is shown. Besides the total hit density, the rates of direct ($t_{\mathrm{Hit}} < 12$ ns) and indirect ($t_{\mathrm{Hit}} > 12$ ns) hits are also shown. It can be seen that for the $\gamma\gamma \rightarrow$ hadron events (Figure 6.10 c,f,i) the direct hits dominate. For the incoherent pairs this depends on the position of the disks and on the radius. For the inner disks the backscattering contribution is dominant with the beryllium beam pipe. With the iron beam pipe the direct component is dominant, except for the outer radii of disk 7. For the last disk (Figure 6.10 g,h), the indirect component is dominant, but is reduced with the 4 mm iron beam pipe.

6.3.2 Hit Densities in the Forward Tracking Disks

As can be seen in Figures 6.8b and 6.9b the hit rates, both from incoherent pairs and $\gamma\gamma \rightarrow$ hadron events, depend only on the radius, and are independent of the Z-position of the disk. The hit rates, equivalent neutron flux, and total ionising dose with the 4 mm beam pipe for all vertex and forward tracking disks can be found in Appendix B in Tables B.1 to B.8.

The maximum hit density is $1 \cdot 10^{-2}$ Hits/mm^2/BX at the inner radius of the third double layer. The number of hits increases here with increasing distance to the IP, because smaller polar angles are reached at the same radius. The first double layer, closer to the vertex barrel layers, has a hit density of $7 \cdot 10^{-3}$ Hits/mm^2/BX similar to the rate in the first vertex barrel layer. As the same pixel sizes are foreseen, the occupancy at the inner radius is the same as for the vertex barrels.

The readout occupancies per train, integrated over the respective readout unit and taking into account cluster formation and safety factors as discussed in Section 4.10.1, depend on the geom-

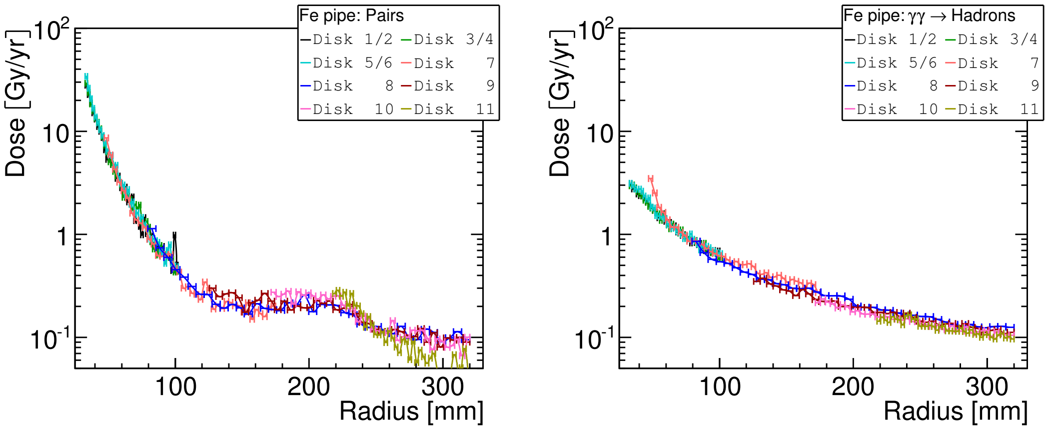

(a) Incoherent pairs

(b) $\gamma\gamma \to$ hadrons

Figure 6.12: Radial distribution of the total ionising dose in the forward tracking disks for incoherent pairs and $\gamma\gamma \to$ hadron events.

etry of the respective layers. The highest train occupancy in the pixel layers reaches 2.8% at the inner part of the third double disk. Figure 6.11 shows the maximum readout occupancy per train as a function of the strip length for the five outer FTDs. The innermost single disk layer (FTD 7), equipped with radial strips of approximately 10 cm × 50 µm in the CLIC_ILD_CDR detector model, would show a train occupancy of more than 1000%. The effective occupancy would be even higher, due to confusion from ghost hits. To avoid such very high occupancies, pixelated readout similar to FTD 1–6 will be needed also for FTD 7. A pixel size of 20×20 µm^2, as assumed for the inner pixel FTDs, would result in an occupancy of 0.6%.

The maximum occupancy in the outer strip disks decreases with increasing inner radius of the respective layer, from 290% in FTD 8 to 80% in the outermost disk FTD 11. Multiple readouts per train in combination with precise time-stamping of hits will help to reduce the effective occupancy of the strip disks to acceptable levels.

6.3.3 Total Ionising Dose and Equivalent Neutron Flux in Forward Tracking Disks

The total ionising dose in the FTDs is shown in Figure 6.12. The total ionising dose from incoherent pairs is higher than that of the $\gamma\gamma \to$ hadron events, and the maximum of the FTDs (found in the third double pixel disk) is 35 Gy/yr, not including safety factors. The ionising dose behaves similar to the hit density and is almost independent of the position of the disk, and only depends on the radius.

The equivalent neutron flux, on the other hand, shows a clear dependence on the position of the disk (Figure 6.13). Because the largest contribution to the equivalent neutron flux comes from neutrons produced by the electrons showering in the BeamCal, the flux in the outer FTDs is dominated by the contribution from incoherent pairs and falls with increasing distance to the BeamCal (Figure 6.13a). For radii between 80 mm and 320 mm it is approximately constant

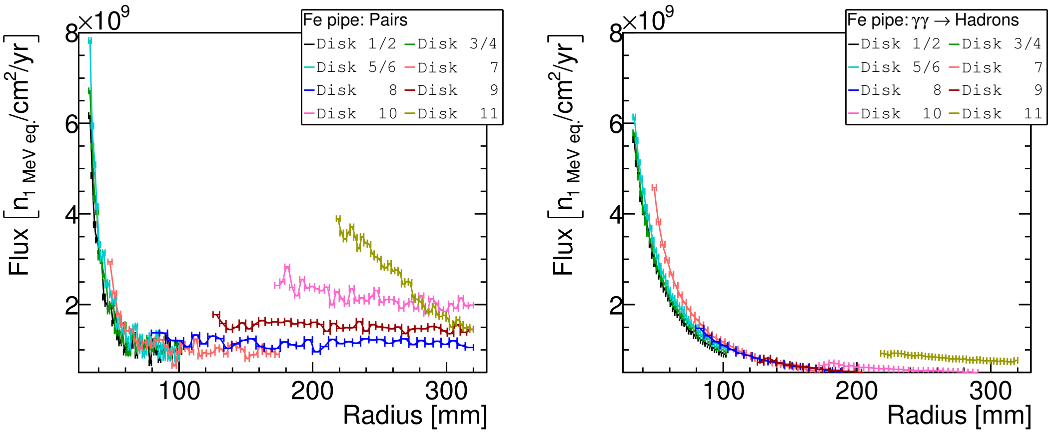

(a) Incoherent pairs

(b) $\gamma\gamma \rightarrow$ hadrons

Figure 6.13: Radial distribution of the equivalent neutron flux in the forward tracking disks for incoherent pairs and $\gamma\gamma \rightarrow$ hadron events.

over the radial extensions of the corresponding disks, except for FTD 11, where the flux at the outside of the disk is about a factor of two lower than at the inside. This variation for FTD 11 appears to be due to a shielding effect from the LumiCal. Closer to the IP the contribution of primary particles to the equivalent neutron flux is dominant and a clear dependence on the radius is visible, both for the incoherent pairs and the $\gamma\gamma \rightarrow$ hadron events. The maximum is again in the third double layer, the total is about $2 \cdot 10^{10}$ $\mathrm{n_{eq}/cm^2/yr}$. A complete list of the results can be found in Table B.1 to B.8 of Appendix B.

6.4 Background in the Endcap Tracking Disks

6.4.1 Hit Density in the Endcap Tracking Disks

Figure 6.14 and Table C.1 in Appendix C, show the hit density in the Endcap Tracking Disks (ETDs) as a function of the radius for the incoherent pairs and $\gamma\gamma \rightarrow$ hadron events. The maximum hit density for both backgrounds is around $1 \cdot 10^{-5}$ $\mathrm{Hits/mm^2/BX}$. At the inner part of the ETDs the contribution from $\gamma\gamma \rightarrow$ hadrons is larger than that of the incoherent pairs, up to $R \approx 0.75$ m. For larger radii the hits from incoherent pairs are dominant, due to the larger contribution from indirect hits.

Between $R = 0.6$ m and $R = 0.8$ m the hit density from the incoherent pairs is almost constant. This feature is only visible in the hits arriving 25 ns after the bunch crossing or later (Figure 6.15a). Figure 6.15b shows the distribution of hits as a function of the time of the hit. The second, larger peak at 30 ns stems from particles scattering back from the BeamCal. The distance travelled from the IP to the BeamCal, and back to the opposite ETD (as the nearer ETD is shielded by the calorimeters) is 8.8 m, not taking curling and transverse distance into account. A relativistic particle can travel this distance in about 29 ns.

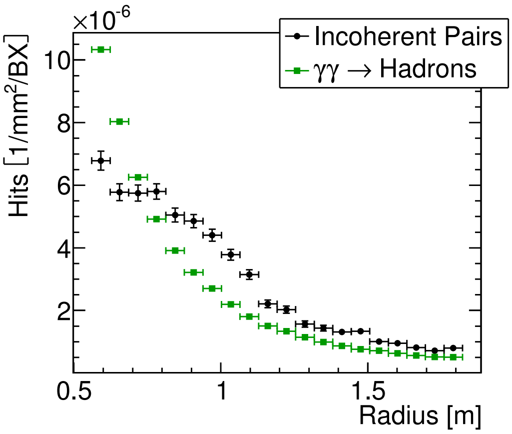

Figure 6.14: Radial hit distribution in the endcap tracking disks for incoherent pairs and $\gamma\gamma \rightarrow$ hadrons.

Figure 6.15a also shows the difference of the background hits from incoherent pairs between the beryllium and iron beam pipe. The direct hits for both beam pipe configurations are very similar, but the number of hits with $t > 25$ ns is reduced by a factor of two.

This difference between the two beam pipe configurations is also visible in the two-dimensional plot of the background densities from the incoherent pairs, shown in Figure 6.16. There is a slight asymmetry visible in the distribution of hits. Figure 6.17a shows hit densities as a function of the radius divided between $X > 0$ (right) and $X < 0$ (left). On the right side of the ETDs ($X > 0$) the higher hit density extends to larger radii. This asymmetry is caused by the LumiCal position, centred on the outgoing beam pipe. The LumiCal, and therefore the hole in its centre, is moved to the right side. Thus, in the detector reference frame, the hole has a larger radius at the right hand side and a smaller on the left. Therefore, the asymmetry is only visible in the backscattered particles (Figure 6.17b). Hits with $t < 25$ ns show no difference between left and right, but in the peak at $t = 30$ ns the right side receives almost twice as many hits, this translates to a smaller hit density on the left hand side of the ETDs.

The readout occupancy per train at the inner radius of the ETD reaches up to 77%, assuming sensors with a strip size of 30 cm × 50 µm and taking into account the safety factor and assumed cluster size discussed in Section 4.10.1. This will require a similar readout than for the strip forward tracking disks.

6.4.2 Total Ionising Dose and Equivalent Neutron Flux in Endcap Tracking Disks

Figure 6.18 and Table C.1 show the total ionising dose and equivalent neutron flux in the ETDs. The total ionising dose at the inner radius of the ETDs ($R = 0.5$ m) is 80 mGy/yr, not including safety factors, this connects well with the dose at the outer radius of the last forward tracking disk ($R = 0.3$ m) of 150 mGy/yr.

The equivalent neutron flux is about $7 \cdot 10^9$ $\mathrm{n_{eq}/cm^2/yr}$ at the inner edge of the ETDs, which is a factor of ten larger than at the outer radius of the last FTD (Table B.8). This effect is caused

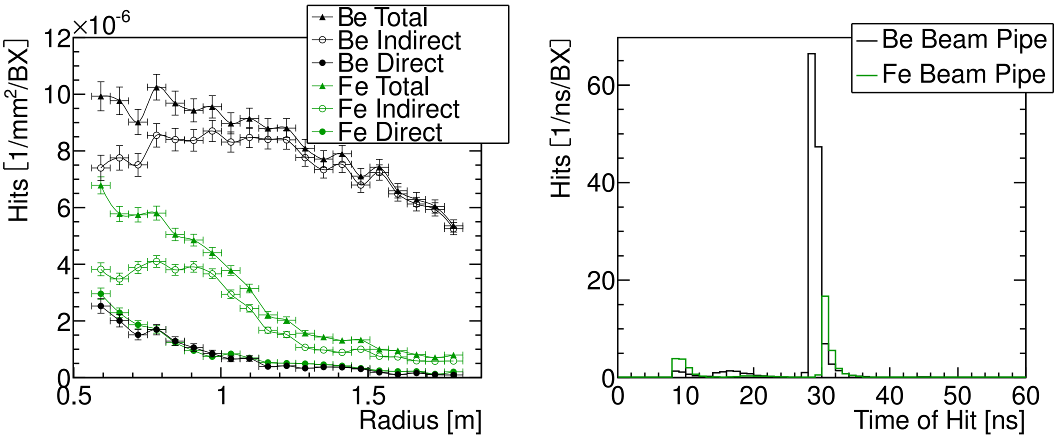

(a) Hits vs. radius

(b) Hits vs. time

Figure 6.15: Distribution of hits from the incoherent pairs in the ETDs for the 1.2 mm beryllium (Be) and 4 mm iron (Fe) beam pipe. (a) Hits versus radius for direct hits ($t < 25$ ns) and indirect hits ($t > 25$ ns) are shown, and (b) number of hits against time of the hit.

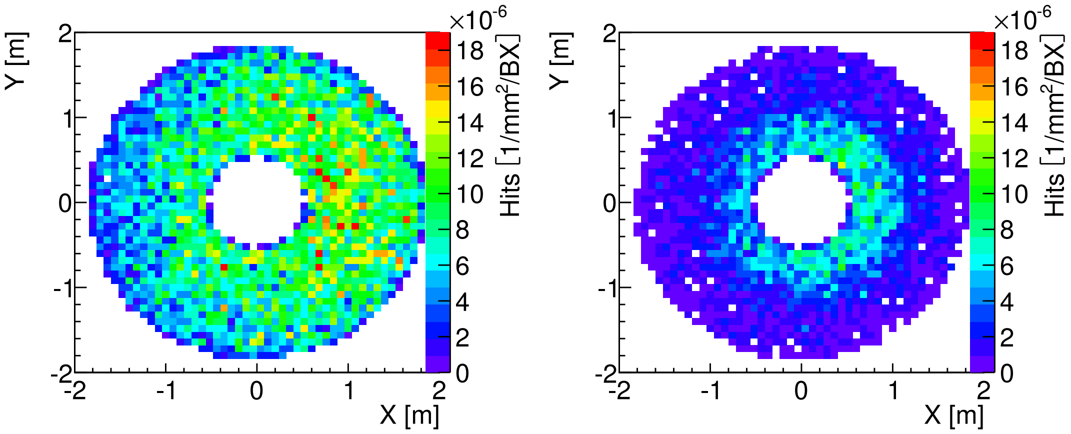

(a) Beryllium beam pipe

(b) Iron beam pipe

Figure 6.16: XY distribution of hits from incoherent pairs in the ETDs for the (a) 1.2 mm beryllium and (b) 4 mm iron beam pipe.

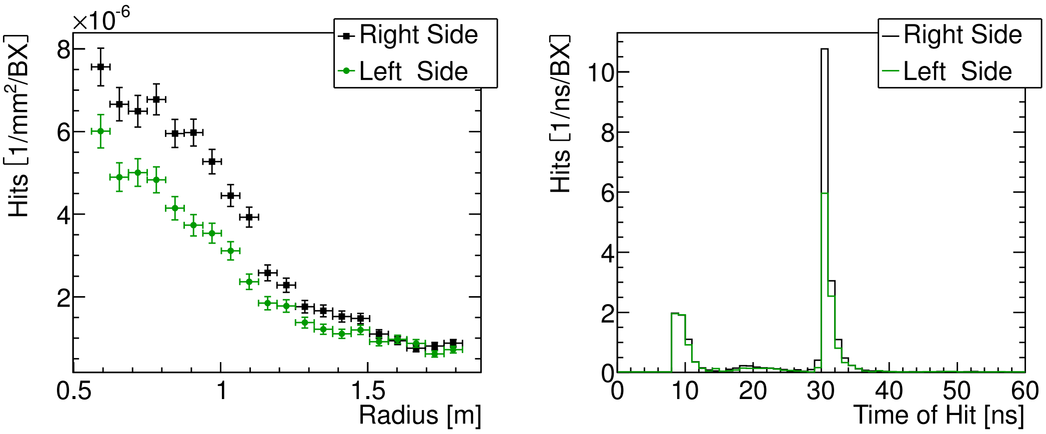

(a) Hits vs. radius

(b) Hits vs. time

Figure 6.17: Distribution of hits from incoherent pairs over the ETDs, separated between left (negative x and right (positive x) side. (a) All hits versus radius and (b) number of hits against time of the hit after the bunch crossing.

by the location of the ETDs, which are closer to the calorimeters than the last forward tracking disk, and therefore the flux of backscattered neutrons is larger.

6.5 Background Reduction in the Time Projection Chamber

To properly estimate the background in the TPC the charge deposit and drifting of charges has to be taken into account. A comprehensive study of the background in the TPC can be found elsewhere [88].

In order to illustrate the effect of the thicker beam pipe, the deposited energy (proportional to the induced charge) in the TPC is used. Figure 6.19 shows the deposited energy in the TPC as a function of the radius for the beryllium and iron beam pipe. An overall reduction of about 80% is observed with the iron beam pipe.

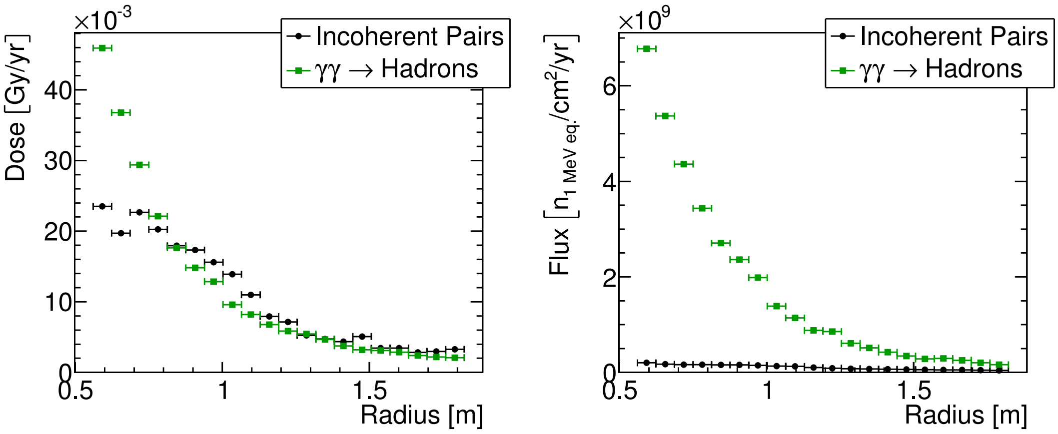

(a) Total ionising dose

(b) Equivalent neutron flux

Figure 6.18: (a) Total ionising dose and (b) equivalent neutron flux for incoherent pairs and $\gamma\gamma \rightarrow$ hadrons in the ETDs.

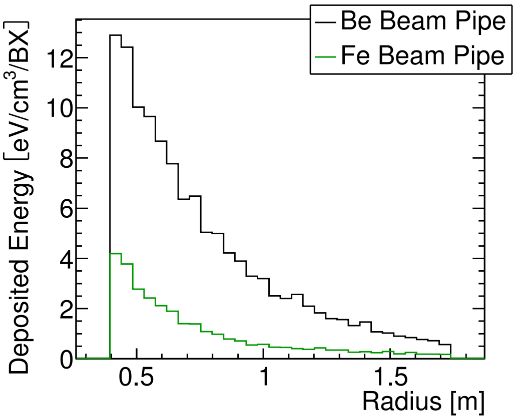

Figure 6.19: Deposited energy from incoherent pairs in the volume of the TPC as function of the radius.

7 Occupancies in the Calorimeter Endcaps

The barrel calorimeters are located at large radii and well shielded from backscatters from the forward detector regions. Therefore the expected maximal occupancies in the barrel calorimeters are much smaller than the corresponding occupancies for the endcap regions. The following detailed studies thus concentrate on the calorimeter endcap regions.

To estimate the occupancy from backgrounds in the calorimeters, some assumptions have to be made regarding the pad size and time resolution of the detectors. The pad sizes are fixed in the GEANT4 implementations of the detector models. The electromagnetic calorimeter (ECal) is a silicon–tungsten sandwich calorimeter with a 5.08×5.08 mm^2 pad size, and a silicon thickness of 0.5 mm. The hadronic calorimeter (HCal) endcap is a scintillator–steel sandwich calorimeter with 30×30 mm^2 pad size and 5 mm thick scintillators [56]. The yoke endcap consists of several centimetre thick layers of iron and RPCs in the gaps between them. The active material of the RPCs is a 2 mm thick layer of gas (80% Tetrafluoroethane, 10% nitrogen and 10% isobutane). The padsize is 30×30 mm^2.

Each CLIC bunch train is 156 ns long, but the hadronic shower development has long tails in time, therefore the maximum acceptance time of the readout was assumed to be 300 ns after the first bunch crossing. The total readout time of 300 ns is divided into 12 readout windows of 25 ns each, thus emulating a frontend system with moderate multi-hit readout capability (i.e., the possibility to record more than one time-stamp and signal size within a 300 ns window). The occupancy is quoted as the number of 25 ns readout windows with an energy deposit above threshold. For example, an occupancy of 2.0 means that for each pad two 25 ns windows received a significant energy deposit during the 300 ns related to a bunch train.

For the results given in this chapter, and to allow for sufficient statistical accuracy, the sample of simulated incoherent pairs was increased to 936 bunch crossings (3 bunch trains). The sample size of the $\gamma\gamma \rightarrow$ hadron events was kept at 67 bunch trains.

7.1 Deposited Energy in the Calorimeter Endcaps

Figure 7.1 shows the energy deposits from incoherent pairs and $\gamma\gamma \rightarrow$ hadrons in the ECal and HCal endcaps. A peak from MIPs can be seen in all distributions, except for the incoherent pairs in the HCal, where secondary neutrons from the showers in the BeamCal are the main contribution [89].

The total reconstructed energy* per train is 2 TeV in the ECal endcaps and 16 TeV in the HCal endcaps from secondaries of incoherent pairs and 11 TeV in the ECal endcaps and 6 TeV in the HCal endcaps from $\gamma\gamma \rightarrow$ hadron events.

---

*Deposited energy multiplied by the respective calibration constant.

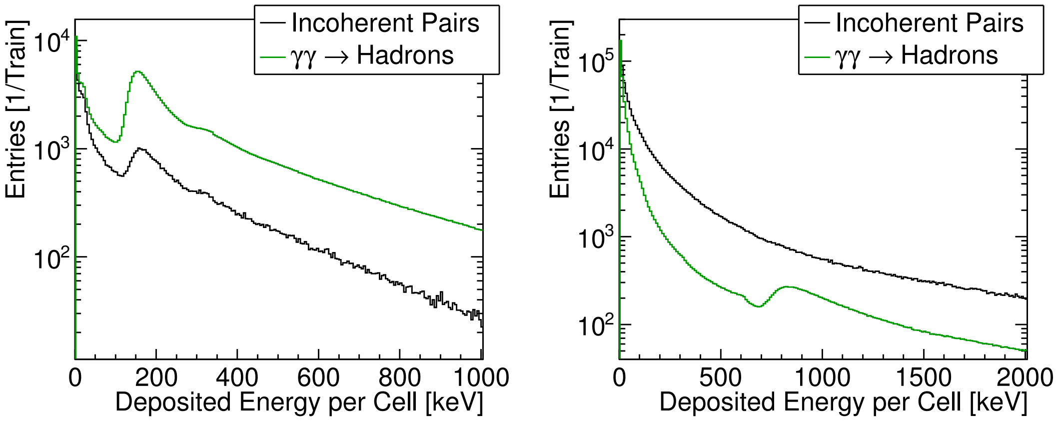

(a) ECal

(b) HCal

Figure 7.1: Distribution of the energy deposit in all calorimeter pads for the (a) ECal endcap and (b) HCal endcap from incoherent pairs and $\gamma\gamma \to$ hadrons.

The threshold for the analysis was set to 40 keV ($\approx$ 0.3 MIP) in the ECal and 300 keV ($\approx$ 0.3 MIP) in the HCal. The threshold in the ECal is chosen more conservatively than in the reconstruction for the detector studies of the CLIC conceptual design report, where thresholds of 0.5 MIP in the ECal and 0.3 MIP in the HCal are used [4]. The choice of the thresholds has an impact on the estimated occupancies: there is a large number of low energy hits in the calorimeters, and the thresholds are situated in the region of a steep slope (see Figure 7.1).

7.2 Time of Energy Deposits

The time of energy deposits, corrected for the time of flight[†], is shown in Figure 7.2. All distributions show a peak at $t = 0$ ns for particles directly hitting the calorimeters. After this peak follows a long tail from slower particles produced in showers, and from neutrons travelling through the detector. Besides the number of electrons from the incoherent pairs that directly reach the ECal, there are significant energy deposits from secondaries produced in the BeamCal. The time of hits in the ECal (Figure 7.2a) shows three peaks: the first for particles hitting the front face of the ECal endcap, the second for backscatters into the back side of the ECal endcap, and the third for backscatters into the front of the ECal endcap on the far side of the detector. The latter effect can also be seen in the timing of hits in the ETDs, as shown in Figure 6.15b.

In the HCal endcap (Figure 7.2b) the peak for direct hits is followed by a delayed plateau of secondary hits. These late hits are from neutrons [89] that are emitted isotropically from the BeamCal. Some are absorbed in the iron support tube, however, a significant fraction of the neutrons penetrate the iron support tube and reach the HCal endcap.

[†] The actual time of the energy deposit after the bunch crossing reduced by the distance from the IP to the pad divided by the speed of light.

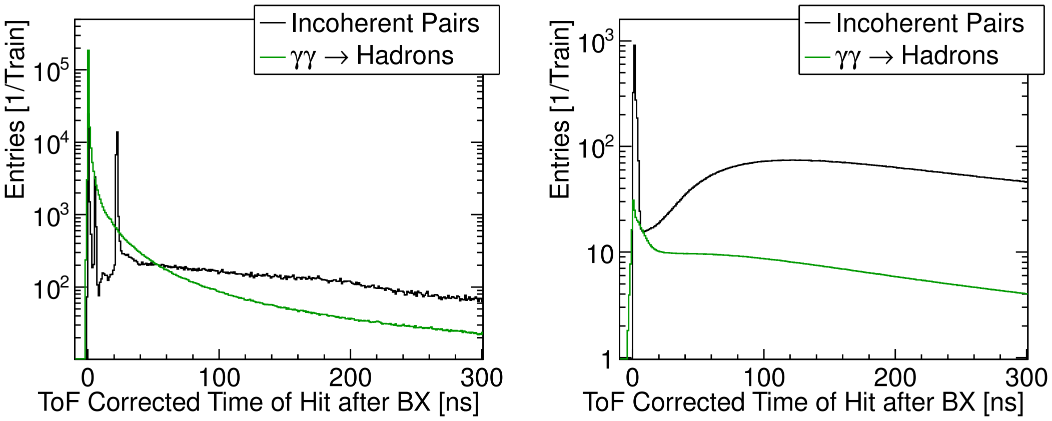

(a) ECal endcap

(b) HCal endcap

Figure 7.2: Distribution of the time-of-flight corrected time of the hits after a bunch crossing in (a) the ECal endcap and (b) the HCal endcap for incoherent pairs and $\gamma\gamma \to$ hadrons.

7.3 Occupancy in the Electromagnetic Calorimeter Endcap

The shower maximum for the particles from $\gamma\gamma \to$ hadrons is around the sixth ECal layer, whereas the lower energy particles from the incoherent pairs have their maximum already in the first layer (Figure 7.3a). The increase in the number of hits for incoherent pairs from layer 23 to 29 is caused by particles scattering into the backside of the ECal.

As expected from the number of hits per layer, the radial distribution averaged over the azimuthal angle shows that the background in the endcap of the ECal is dominated by particles from the $\gamma\gamma \to$ hadron interactions (Figure 7.3b). The highest occupancies are observed at small radii. The dip in the occupancy at $R \approx 0.25$ m is caused by the beam pipe, which shadows a part of the ECal endcap (see Figure 7.4b).

The two-dimensional distributions of the occupancy in the layers of the ECal with the highest occupancies are shown in Figure 7.4. The number of events in the sample is still limited, even though three bunch trains of incoherent pairs have been simulated. It is also visible, that the background is independent of the azimuthal angle, so that the averaged radial distributions provide a reliable estimate for the occupancy from incoherent pairs in the ECal endcap.

Figure 7.5 shows the radial distribution of the occupancy for all layers. Globally, the occupancy stays below 0.5 readout windows per pad and train for $\gamma\gamma \to$ hadron events and 0.2 readout windows per pad and train for incoherent pairs.

7.4 Occupancy in the Hadronic Calorimeter Endcap

For the $\gamma\gamma \to$ hadron events the majority of energy deposits is caused by direct hits into the HCal endcap, and the number of energy deposits decreases with increasing layer number (Figure 7.6a), except for a slight increase in the last few layers. This increase can be caused by particles

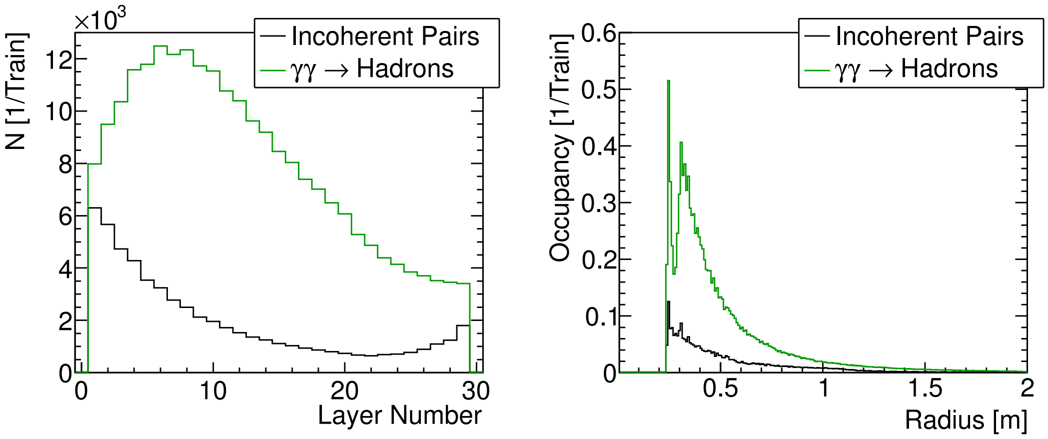

(a) Hits per layer

(b) Occupancy vs. radius

Figure 7.3: (a) Number of readout windows with energy deposits above threshold for the ECal endcap from incoherent pairs and $\gamma\gamma \to$ hadrons per layer. (b) The radial distribution of the train occupancy per pad, averaged over layers 5 to 10.

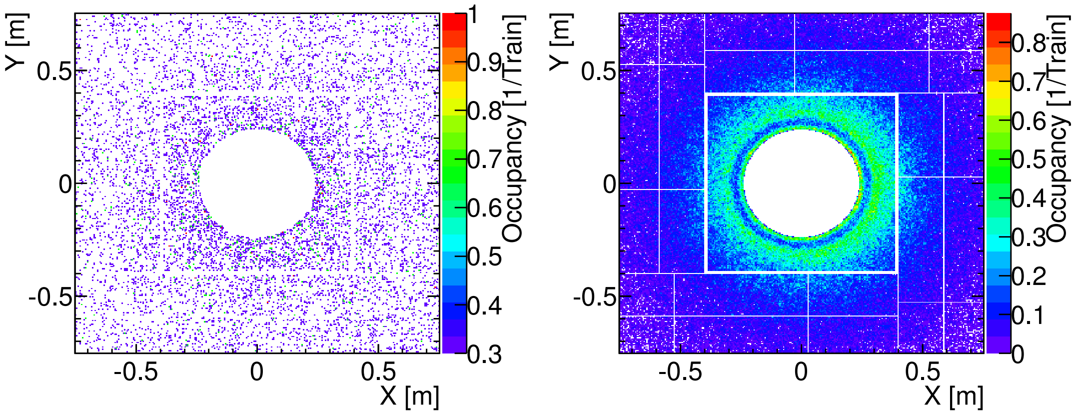

(a) Incoherent pairs: Layer 1

(b) $\gamma\gamma \to$ hadrons: Layer 6

Figure 7.4: Number of readout windows hit with energy deposits above thresholds in the ECal for (a) incoherent pairs and (b) $\gamma\gamma \to$ hadron events. The white rectangles are gaps between sensor modules.

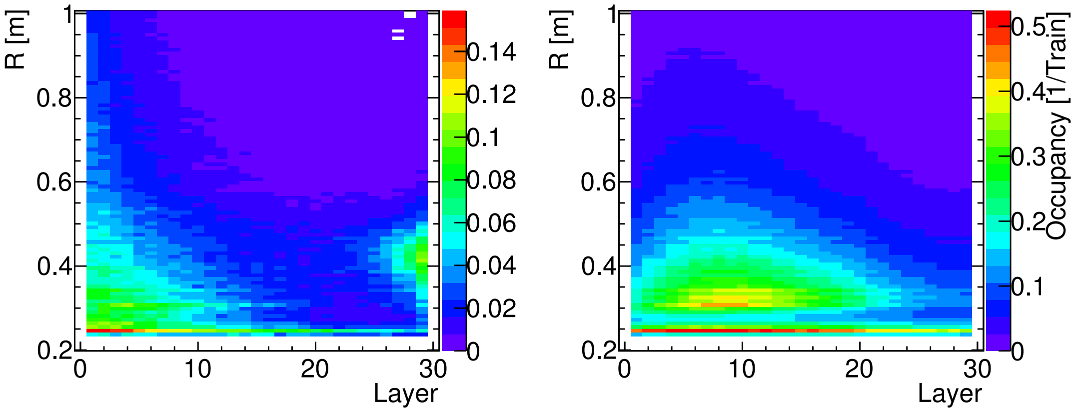

(a) Incoherent pairs

(b) $\gamma\gamma \rightarrow$ hadrons

Figure 7.5: Readout windows hit with energy deposits above threshold for all layers of the ECal endcap from (a) incoherent pairs and (b) $\gamma\gamma \rightarrow$ hadrons, averaged over the azimuthal angle.

scattering back from the front of the anti-solenoid or yoke plug. The inner polygon of the HCal endcap is a square, whereas the support tube is round. Therefore, particles can propagate in the gap between HCal endcap and the support tube and hit the anti-solenoid cylinder, from which they could scatter into HCal, causing showers extending from the back into the endcap. For products from the incoherent pairs, two broad peaks in the number of hits are visible in Figure 7.6a. This distribution is due to the provenance of the particles. A large number of secondary particles is produced by the showers of the incoherent pairs in the BeamCal, which is located inside the HCal endcap between layers 20 and 40. As there is an additional iron ‘BeamCal Support’ around the BeamCal (see Figure 4.2) and thus better shielding of the HCal, a dip is observed in the number of hits between layers 15 and 35.

Most of the energy deposits from secondaries produced in the BeamCal are at the innermost radius ($R = 0.4$ m) of the HCal endcap. In this region up to ten out of the twelve readout windows see an energy deposit. Beyond a radius of 0.6 m the occupancy falls to below one energy deposit above threshold per train (Figures 7.6b, 7.7 and 7.8). At $R = 1$ m the occupancy from $\gamma\gamma \rightarrow$ hadron events is equal to that of incoherent pair secondaries.

As can be seen in Figure 7.7, the energy deposits from the particles produced by the incoherent pairs are located at the inner edge of the HCal endcap only. The energy deposits from $\gamma\gamma \rightarrow$ hadron events have a radial distribution extending further outwards. The occupancy from the $\gamma\gamma \rightarrow$ hadron events also falls with an increasing layer number (Figure 7.8), whereas the occupancy from the incoherent pairs extends to the latter layers of the endcap.

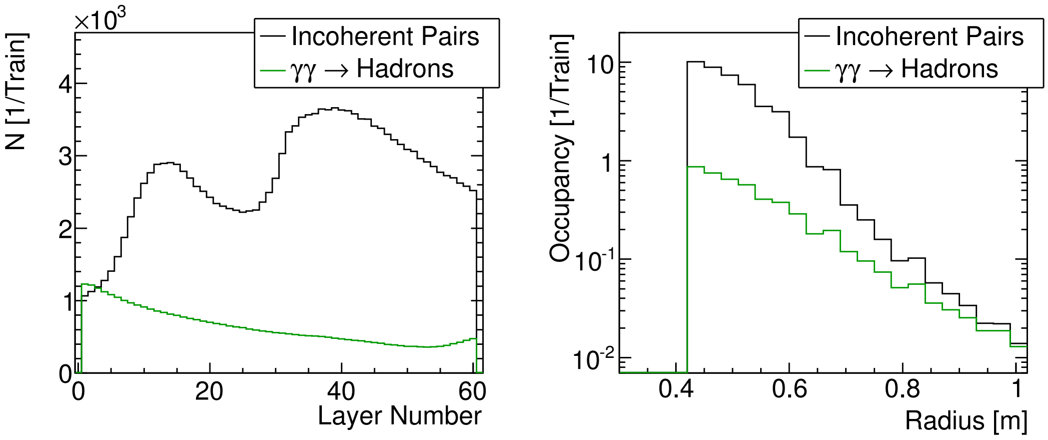

(a) Hits per Layer

(b) Occupancy vs. Radius

Figure 7.6: (a) Number of readout windows with energy deposits above threshold for the HCal endcap from incoherent pairs and $\gamma\gamma \to$ hadrons per layer. (b) The radial distribution of the train occupancy per pad, averaged over layers 35 to 45.

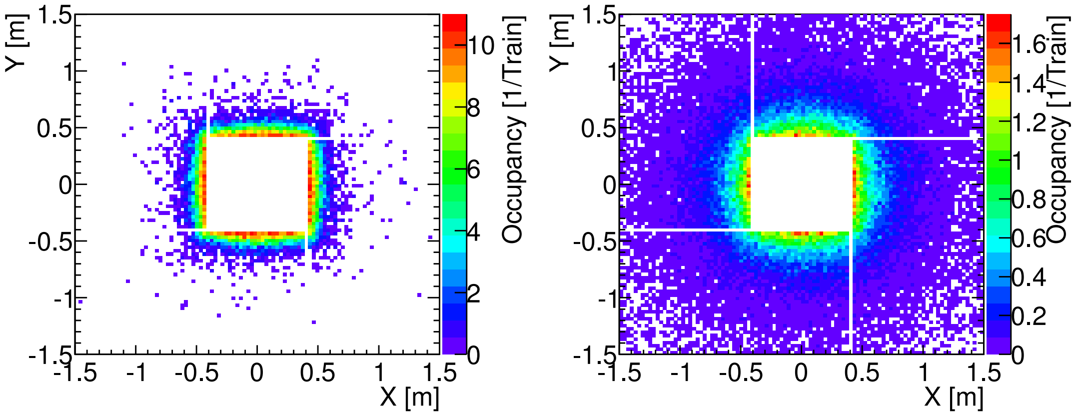

(a) Incoherent pairs: Layer 40

(b) $\gamma\gamma \to$ hadrons: Layer 1

Figure 7.7: Readout windows hit with energy deposits above threshold (a) in the fortieth layer of the HCal endcap for incoherent pairs and (b) in the first layer for $\gamma\gamma \to$ hadron events. The white lines are gaps between endcap modules.

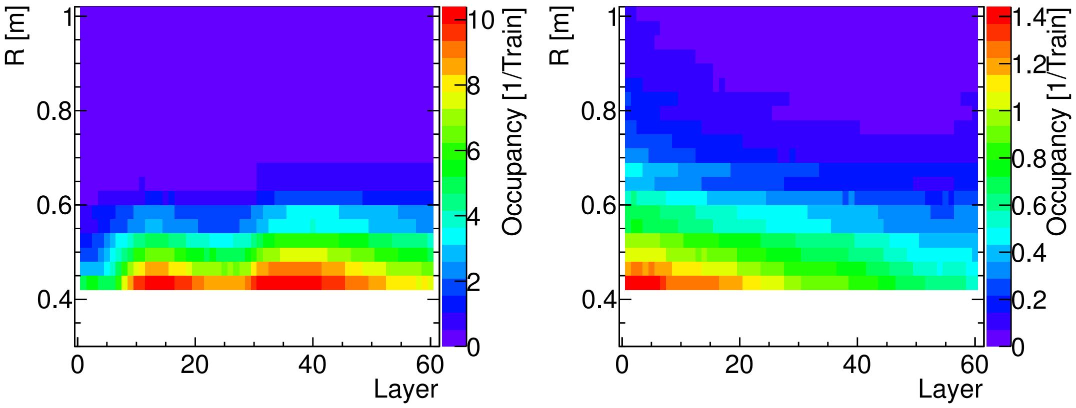

(a) Incoherent pairs

(b) $\gamma\gamma \to$ hadrons

Figure 7.8: Readout windows hit with energy deposits above threshold for all layers of the HCal endcap from (a) incoherent pairs and (b) $\gamma\gamma \to$ hadrons, averaged over the azimuthal angle.

7.4.1 Increased Granularity in the HCal Endcap

The very large occupancy at the inner radius of the HCal endcap of around 80% of the readout windows (without safety factors) is too large to separate energy deposits of distinct particles. To reduce the occupancy the size of the scintillator pads at small radii could be decreased—e.g., from 30 mm to 10 mm corresponding to a ninefold increase in granularity. Alternatively the length of the readout windows could be decreased, an approach that is technologically more challenging and reaches limitations with respect to the shower development and signal development in the scintillator.

Assuming a homogeneous distribution of hits over the volume of a single scintillator pad the effect will be equivalent for the two methods. For estimating the effect of increased granularity in the simulation it is easier to decrease the length of the readout windows during the analysis, instead of simulating different pad sizes. With shorter readout windows, the number of distinguishable hits rises, therefore the occupancy is given as the number of readout windows with deposits above threshold divided by the total number of readout windows, instead of the total number of time windows as was done before.

For incoherent pairs, Figure 7.9a shows the percentage of readout windows with an energy deposit above threshold as a function of the length of the readout time for the pad with the highest number of energy deposits above threshold. With a length of 25 ns, 80% of the readout windows see a significant energy deposit. For readout windows of 3 ns the occupancy is reduced to $\approx 20\%$. It should therefore be possible to reduce the occupancy to acceptable levels by decreasing the size of the scintillator pads. For $\gamma\gamma \to$ hadron events, the occupancy is much lower and increases linearly with the size of the time windows (Figure 7.9b), as it remains far below saturation.

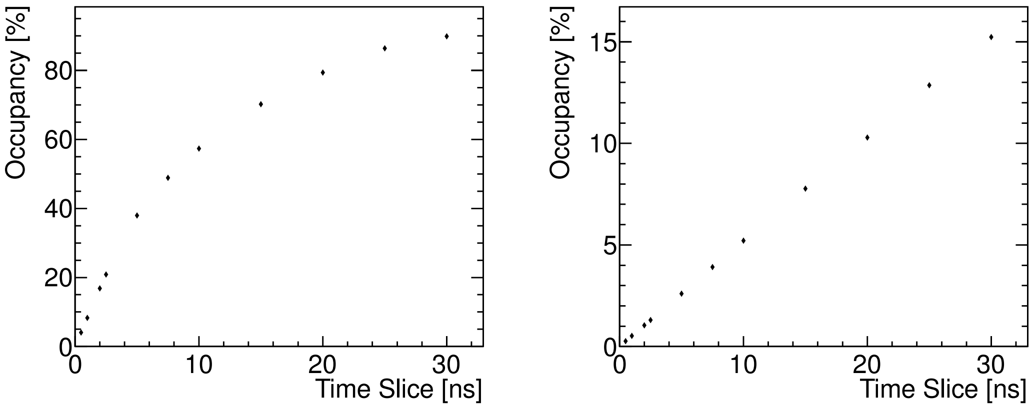

(a) Incoherent pairs

(b) $\gamma\gamma \to$ hadrons

Figure 7.9: Percentage of time windows with energy deposits above threshold for the HCal endcap (a) from incoherent pairs and (b) $\gamma\gamma \to$ hadrons as a function of the size of the time window.

7.5 Occupancy in the Yoke Endcap

The energy deposits from incoherent pairs and $\gamma\gamma \to$ hadron events in the muon system of the yoke endcap is shown in Figure 7.10a. As the active material is a thin layer of gas the energy deposits per pad are much smaller than in the ECal or HCal. The peak around an energy deposit of 1 keV corresponds to the peak from MIPs.

The MIP-peak was also estimated with 100 GeV muons. Their energy deposit per pad is shown in Figure 7.10b. The most probable value is also at 1 keV. For the estimate of the background occupancy a threshold of 0.3 keV is chosen.

The number of hits per layer is shown in Figure 7.11a. The increase of hits from incoherent pairs towards the end of the yoke endcap is an artifact, caused by the lack of cavern and accelerator tunnel walls in the simulations. Particles scattering in the beam pipe outside the detector hit the back side of the yoke endcap. This is possible in the simulation, because the beam pipes extend to $Z = \pm 12$ m, the support tube only to $Z = \pm 7.5$ m. Figure 7.11b shows the radial dependence of the occupancy per pad for averaged over the first five layers, which should not be affected too much by the backscattering particles, the occupancy is below $1.5 \cdot 10^{-2}$ per train. The pad occupancy for all layers is shown in Figure 7.12.

7.6 Occupancies in the Calorimeter Barrels

The maximal occupancies in the calorimeter barrels are estimated from the obtained results for the endcap sections closest to the barrels. For the ECal barrel ($R = 1.8$ m), the maximal occupancy is more than a factor of 50 below the one for the ECal endcaps. For the HCal barrel ($R = 2.1$ m), the corresponding difference is more than a factor of 1000.

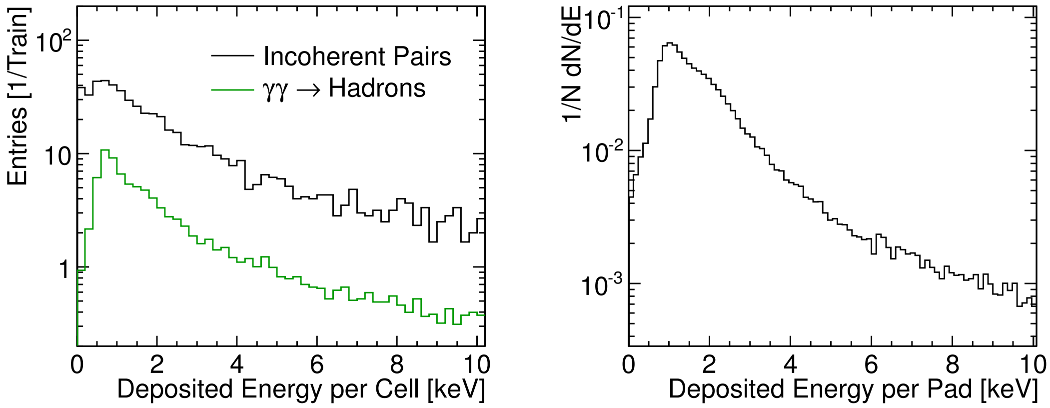

(a) (b)

Figure 7.10: (a) Energy deposits per pad caused by incoherent pairs and $\gamma\gamma \to$ hadron events, and (b) energy per pad from 100 GeV muons.

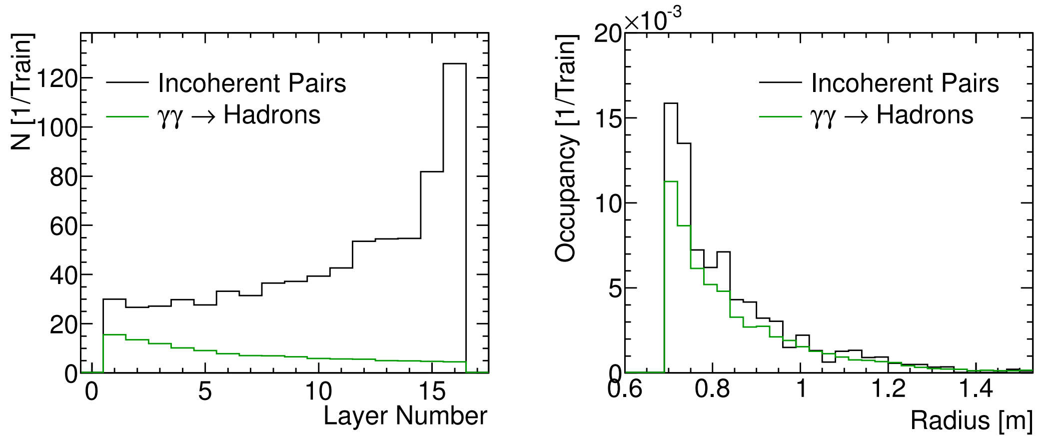

(a) (b)

Figure 7.11: (a) Number of hits in the layers of the yoke endcap. (b) Occupancy as a function of the radius for the average of the first five layers.

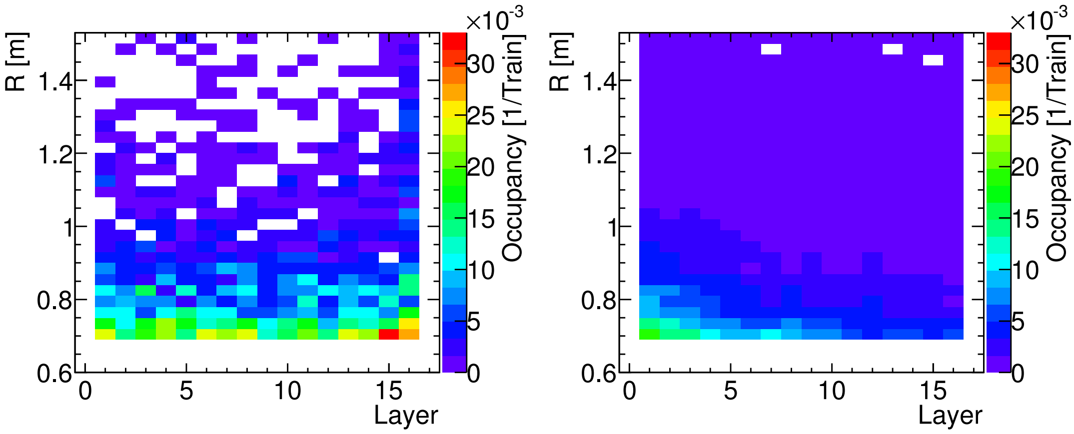

(a) (b)

Figure 7.12: Occupancy in all the layers of the yoke endcap from (a) incoherent pairs and (b) $\gamma\gamma \to$ hadron events.

7.7 Further Studies

The occupancy in the HCal endcap coming from neutrons produced in the showers from incoherent pairs is clearly too large. In addition to the increased granularity in the HCal it has also to be studied, whether it is possible to improve the shielding of the calorimeter from particles produced in the BeamCal. Currently the support tube inside the HCal endcap is represented by iron in the simulation. Iron, however, is not an optimal shield against neutrons. It could be possible to reduce the number of neutrons reaching the HCal endcap by adding a neutron absorbing material where possible.

Another possibility is removing the neutron source, by placing the BeamCal further downstream of the IP. This, however, clashes with the requirement of the intra-train-feedback system and QD0 to be positioned as close to the IP as possible.

It should also be studied, if the number of particles reaching the endcap yoke is decreased by adding the cavern and tunnel walls to the simulation, which could reduce the number of particles scattering into the yoke endcap from the outside of the detector.

8 Electron Tagging and Beam-Induced Background in the BeamCal

The beam calorimeter (BeamCal) is the most forward calorimeter in the detector. It covers a polar angle range of 10 mrad $< \theta <$ 42 mrad. The details of the BeamCal are described in Section 4.5.2. The large energy deposits from the incoherent e^+e^- pairs and resulting ionising and non-ionising radiation doses require the use of radiation hard sensors. Because of the large energy deposit in each bunch crossing the showers from physics events are not directly visible—i.e. the BeamCal cannot be used like the other calorimeters in the detector. However, by estimating the average energy deposit from the incoherent e^+e^- pairs some information about possible energy deposits from high energy electrons can be extracted.

8.1 Energy Deposit and Total Ionising Dose in the BeamCal

The BeamCal is the main absorber of incoherent e^+e^- pairs in the detector. There are several ten-thousand electrons and positrons with a total energy of 33 TeV per BX hitting each of the two BeamCal detectors. The total deposited energy in the sensors is 0.6 TeV/BX. This energy deposit is broadly spread across the volume of the BeamCal, so that almost all pads of the BeamCal will see an energy deposit in every bunch crossing. As for the other subdetectors, it will not be technically possible to read out the BeamCal after each bunch crossing. The deposited energy of several bunch crossings will have to be integrated, and the bunch train will be divided into 6 to 15 readout windows.

The total energy of particles from $\gamma\gamma \to$ hadron events inside the BeamCal is 150 GeV/BX and results in a deposited energy of only 1.5 GeV/BX, four-hundred times smaller than the energy deposited by the incoherent e^+e^- pairs. Therefore the energy deposit from $\gamma\gamma \to$ hadron events will be neglected for the following estimates of the background and for the electron tagging studies.

Figure 8.1 shows the energy deposit in the fourth and tenth layer of the two BeamCal detectors from ten bunch crossings of incoherent e^+e^- pairs. The different distributions in the forward and backward calorimeters are coming from the opposite charges of the repelled particles depending on the beam direction, and on the magnetic field and crossing angle.

Figure 8.2a shows the relative longitudinal distribution of the energy deposited by incoherent e^+e^- pairs. The energy deposit peaks in layer 4, and falls off quickly until layer 20. The last layer shows a peak in the deposited energy, because of particles scattering into the backside of the BeamCal.

The relative radial distribution in layer 4 with respect to the rings of the BeamCal is shown in Figure 8.2b. The energy deposits per ring fall quickly with increasing radius, as can be expected from the angular distribution of the incoherent e^+e^- pairs.

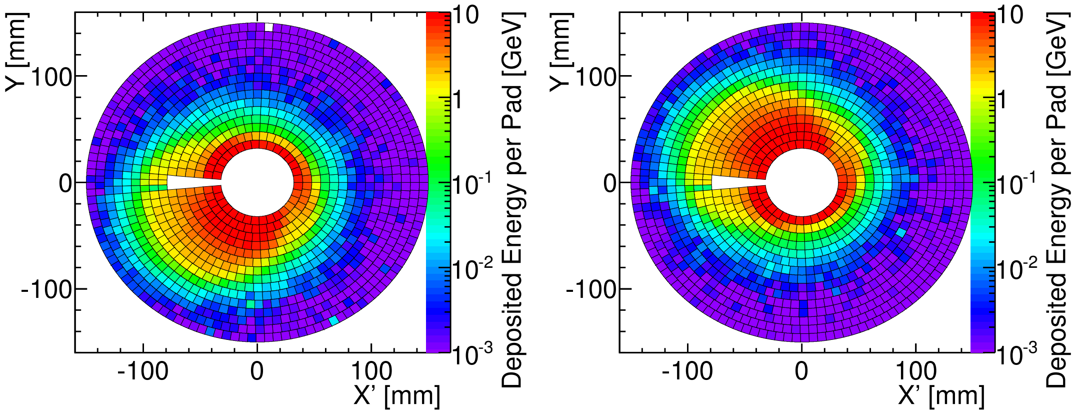

(a) Forward BeamCal: Layer 4

(b) Backward BeamCal: Layer 4

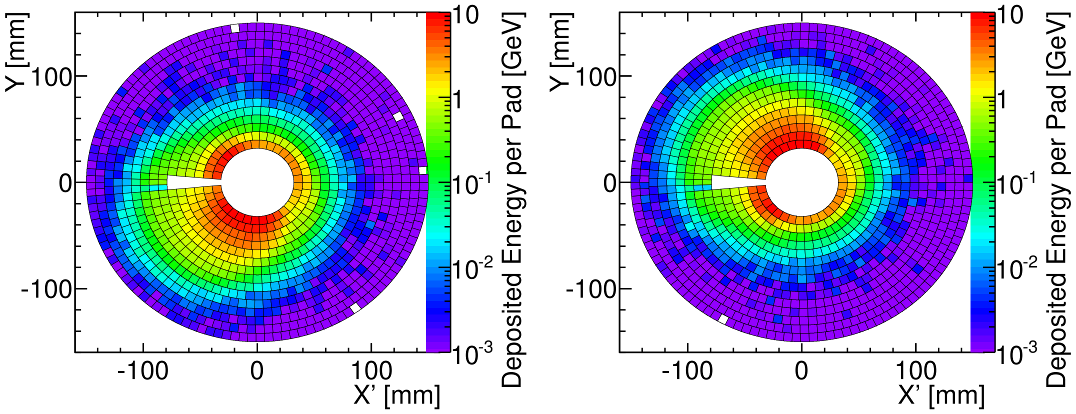

(c) Forward BeamCal: Layer 10

(d) Backward BeamCal: Layer 10

Figure 8.1: Energy deposit from 10 BX of incoherent e^+e^- pair background in the fourth and tenth layer of the forward and backward BeamCal.

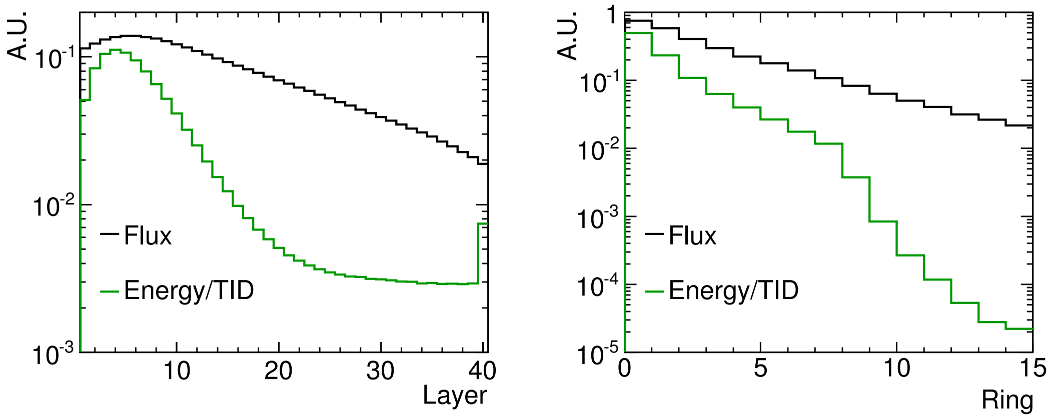

(a) Per layer

(b) Per ring

Figure 8.2: Fractional deposit of energy, total ionising dose and equivalent neutron flux (a) per layer of the BeamCal and (b) per ring in the fourth layer for the energy and TID and in the fifth layer for the equivalent neutron flux.

The energy deposit per pad from incoherent e^+e^- pairs of a single BX are shown in Figure 8.3a. The maximum energy deposit in a single pad is about 2 GeV/BX, a few percent of the pads receive more than 1 MeV/BX, but the majority of pads, especially at larger radii, record only small amounts of deposited energy.

The energy deposited in a single pad from a minimum ionising particle is about 150 keV. Figure 8.3b shows the energy deposits per pad from 150 GeV muons traversing the BeamCal; the MIP-peak at 150 keV is clearly visible.

8.1.1 Total Ionising Dose

The deposited energy in the sensors is also used to estimate the total ionising dose per year*. The dose is the deposited energy divided by the mass of the sensor volume in which the energy is deposited. The TID per year in the fourth layer of the BeamCal and the yearly dose for all pads are shown in Figure 8.4. The maximum expected dose, located at the inner edge of the BeamCal, is around 1 MGy/yr, further outside the dose falls to a few Gray per year.

8.1.2 Equivalent Neutron Flux

To estimate the neutron flux from incoherent e^+e^- pairs, the damage-factors for silicon from [83] are used to scale the neutrons to the 1 MeV equivalent. The NIEL damage cross-section from neutrons in diamond is smaller than in silicon. However, the relative scaling between the damage-factors at different energies is similar in diamond and silicon [90]. Therefore the silicon damage-factors can be used to approximate the 1 MeV neutron equivalent flux in diamond

---

*Assuming 100 days of operation with nominal beams.

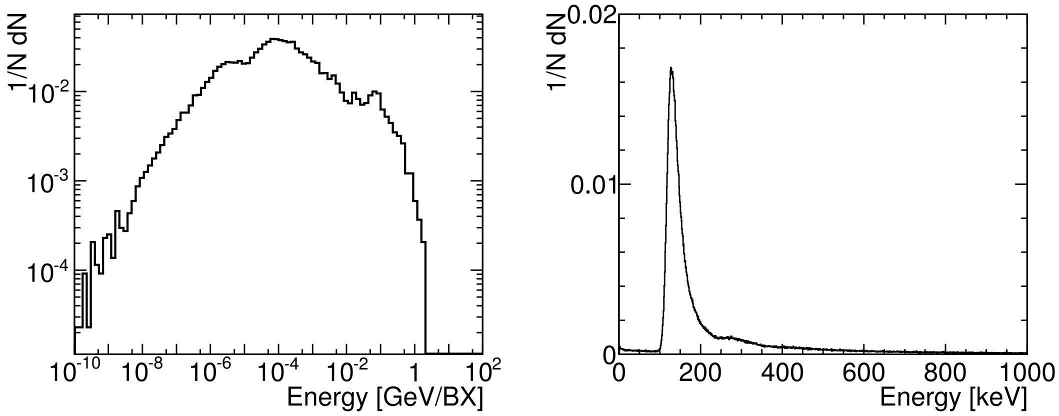

(a) Incoherent e^+e^- pairs

(b) Minimum ionising particles

Figure 8.3: (a) distribution of energy deposits in all pads of the BeamCal from incoherent e^+e^- pairs and (b) deposited energy per pad from 150 GeV muons.

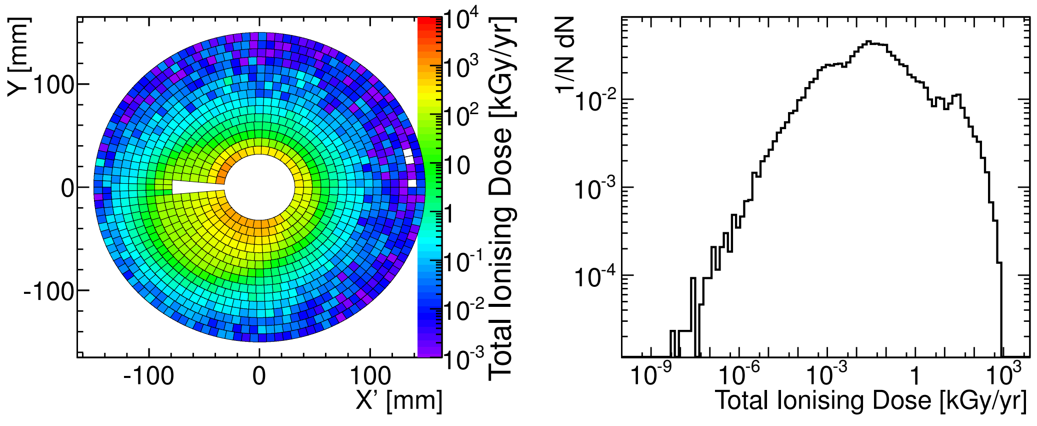

(a) TID in layer 4

(b) TID per pad

Figure 8.4: TID per year (a) in the fourth layer of BeamCal and (b) in all pads of the BeamCal.

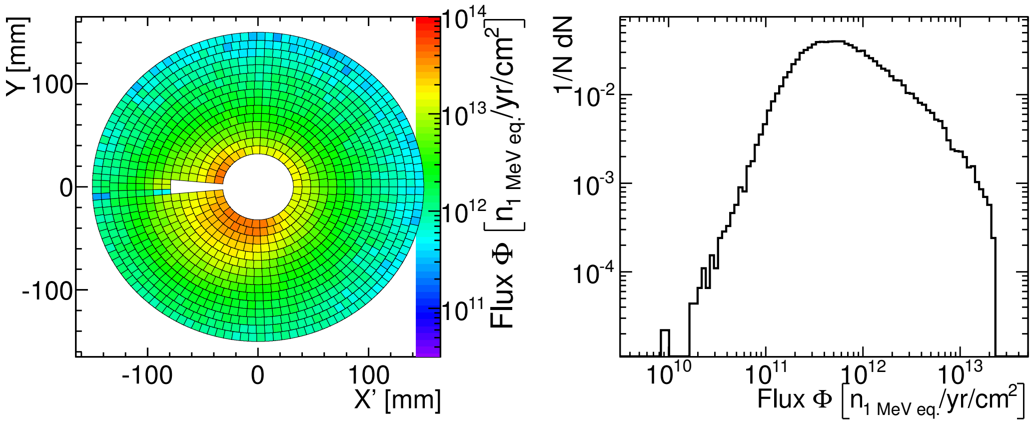

(a) Neutron flux in layer 5

(b) Neutron flux per pad

Figure 8.5: (a) Equivalent neutron flux per year in layer 5 of the BeamCal and (b) flux in all pads of the BeamCal.

as well. The spectrum of neutrons near the BeamCal is shown in Figure 5.12b. To record the passing of the neutrons through the sensor pads of the BeamCal the simulation in MOKKA was adapted. The *sensitive detector* in the simulation was changed to record the relative damage factor of neutrons instead of the deposited energy from of all particles.

Figure 8.2a shows the longitudinal distribution of the equivalent neutron flux in the BeamCal. It reaches its maximum in layer 5, one layer behind the maximum energy deposit, and falls off more slowly. Figure 8.2b shows the radial distribution of the equivalent neutron flux in the fifth layer, which falls more slowly than the radial distribution of the energy and total ionising dose.

Figure 8.5 shows the equivalent neutron flux pear year in the fifth layer and the flux pear year for the individual pads. In this layer, it falls more slowly with the radius than the energy deposit, being only one order of magnitude smaller at the outer radius than at the inner radius. In the BeamCal pads the equivalent neutron flux varies from $10^{10}\ \mathrm{n_{eq}/cm^2/yr}$ to $10^{13}\ \mathrm{n_{eq}/cm^2/yr}$.

8.1.3 Comparison with the ILC BeamCal

Table 8.1 summarises the maximum neutron flux and total ionising dose for the 3 TeV CLIC and the ILC at $\sqrt{s} = 500$ GeV. The different beam parameters for CLIC and ILC and BeamCal inner radii of 3.5 cm at CLIC and 2.0 cm at the ILC [66] result in similar energy deposits per bunch crossing in the BeamCal; which translates into similar radiation doses [91]. Therefore, radiation hard sensors are necessary, but the requirements at CLIC are not more severe than at the ILC.

8.2 Electron Tagging

Some measurements at linear colliders use the relatively simple topology of a lepton pair and missing energy. One example is the slepton pair production in supersymmetric models [92],

Table 8.1: Maximum expected equivalent neutron flux and total ionising dose in the BeamCal at the 3 TeV CLIC and at the 500 GeV ILC. ILC values taken from [91].

	CLIC	ILC
Equivalent neutron flux $[10^{13}/\mathrm{cm}^2/\mathrm{yr}]$	2.0	0.4[a]
Ionising dose [MGy/yr]	1.0	0.6

[a] Averaged neutron flux over the full face of the ILC BeamCal.

where the slepton $\tilde{\ell}$ decays to its Standard Model partner-lepton ℓ and the Lightest Supersymmetric Particle (LSP). In case of a neutralino $\tilde{\chi}^0$ LSP, it escapes the detector undetected, and thus causes missing energy [93, 94].

The main purpose of the electron tagging is the rejection of the spectator electrons from a multi-peripheral two-photon exchange $e^+e^- \to e^+e^-\ell\ell$ event, which is a major background in the search for supersymmetric slepton pairs. The spectator electrons generally retain a large part of the initial energy, and are only slightly deflected. Some of them will be contained in the BeamCal and can then be identified.

The luminosity spectrum at CLIC complicates the identification of these electrons, because a significant amount of energy can be radiated before the interaction, and therefore, also lower energy electrons will have to be identified in the BeamCal.

The large energy deposits from the incoherent e^+e^- pair background do not allow for a direct reconstruction of showers from high energy electrons. However, for electron tagging the identification of the electron's shower is more important than a precise reconstruction of its properties.

To identify the signal shower on top of the background of the incoherent pairs reliably, a significant excess of energy has to be identified. High energy electron-identification algorithms have been developed for the ILC BeamCal [70, 95]. The concept has been adapted for the CLIC case to reject more strongly the background energy deposits. The absolute fluctuation of the deposited energy per pad is larger at CLIC, since more than one bunch crossing of background will be integrated along with a high energy electron shower.

8.2.1 High-Energy Electron Shower Characteristics

To study the response of the BeamCal to high energy electrons, mono-energetic electrons from 0.5 TeV to 1.5 TeV in steps of 0.1 TeV have been simulated in the detector, uniformly distributed across the acceptance of the BeamCal.

Figure 8.6a shows the average total energy deposited in the sensors by electrons with energies of 0.5 TeV, 1.0 TeV, and 1.5 TeV with respect to their polar angle. At the inner edge of the BeamCal the showers are not completely contained. From 11 mrad onwards the showers are completely contained, and the average energy deposit is 26.2 GeV for 1.5 TeV electrons and 8.73 GeV for 0.5 TeV electrons.

At a polar angle of $\theta \approx 35$ mrad the BeamCal acceptance overlaps with the LumiCal. The energy deposit in the BeamCal drops rapidly and increases in the LumiCal. At first the showers are not completely contained by the LumiCal, so that a part of the energy is still deposited in the

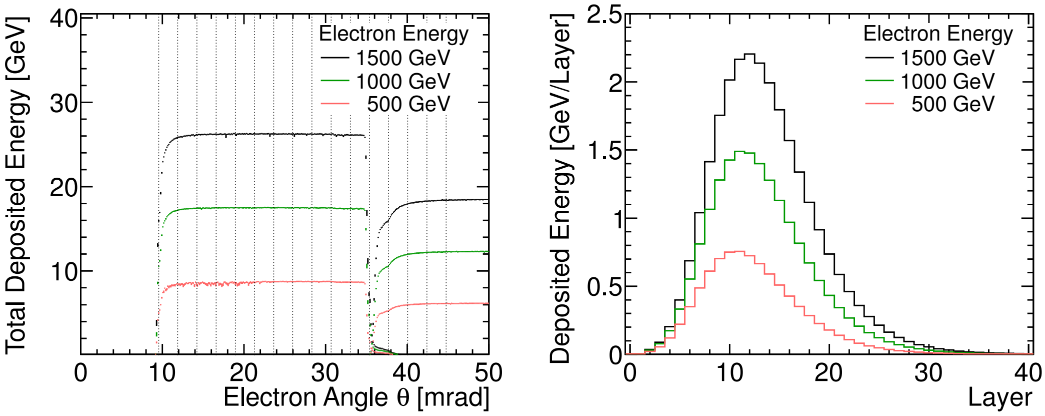

(a) Deposited energy w.r.t. polar angle

(b) Deposited energy per layer

Figure 8.6: Energy deposit for high energy electrons in the BeamCal: (a) Total deposited energy w.r.t. the electron polar angle θ. The increase from 35 mrad onwards shows the energy deposit in the LumiCal. (b) deposited energy per BeamCal layer for electrons between 14 mrad and 35 mrad.

BeamCal. There is also a vacuum tube inside the LumiCal extending to the BeamCal, which can start showers away from either detector, and absorb part of the energy. Because of the different sensor material and thickness the total energy deposit is smaller in the LumiCal.

Figure 8.6b shows the energy deposit per layer for different electron energies. The highest energy deposit is in layer ten to twelve. The maximal deposited energy per layer is 2.2 GeV for 1.5 TeV electrons, and 0.7 GeV for 0.5 TeV electrons. The higher energy of the electrons, compared to the incoherent pair particles hitting the BeamCal leads to a shower maximum several layers after the shower maximum of the background particles (layer 4, see Figure 8.2a). Therefore, the identification of the electrons will only use the layers 10 to 40, where the background level has dropped considerably and the high energy electron shower maximum has been reached.

Due to the small Molière radius in the BeamCal the electromagnetic showers are very narrow. If the shower is concentrated on one pad in each layer, then the highest energy density is achieved. If the shower occurs on the edge between two or more pads, the maximum energy deposit in a single pad is reduced, which will make it more challenging to identify the high energy electrons. Figure 8.7 shows the energy deposited in individual pads by high energy electron showers. In every shower a few pads receive more than 0.1 GeV with a maximum of 2 GeV in a single pad for 1.5 TeV electrons. For 0.5 TeV electrons this maximum energy deposit drops to 0.7 GeV.

8.2.2 BeamCal Readout Scheme

The large occupancy of close to 100% in at least some pads of the BeamCal requires a specialised readout scheme. One proposal is a gated integrator with correlated double sampling [96]. In

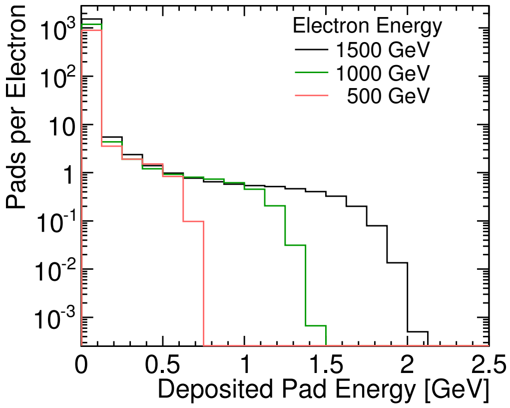

Figure 8.7: Frequency of deposited energy in individual pads from showers of 0.5 TeV, 1.0 TeV, and 1.5 TeV electrons. Empty pads are not counted.

this scheme the current pulses are continuously integrated and sampled in readout windows of 10 ns. The energy deposit in one readout window can then be reconstructed by subtracting two consecutive samples. In a 10 ns readout window 20 BX of background are integrated. As the studies for the BeamCal readout electronics have started recently, a worse case with a larger readout window of 20 ns (40 BX) is assumed here to estimate the electron identification.

8.2.3 Treatment of Simulated Background

As was shown in Section 3.10.2, the intra-train fluctuation of background production from vertical offsets has an effect on the azimuthal distribution of the incoherent e^+e^- pairs. This will also affect the average and variance of the energy deposits in the BeamCal.

To study the effect on the energy deposits in the BeamCal, the generated incoherent e^+e^- pairs from collisions with vertical offsets of 0.5 nm and 1.0 nm between the two bunches were simulated in MOKKA. For the head-on collisions 900 BX and for the two offsets 600 BX each were simulated.

Figure 8.8 shows the energy deposits from incoherent e^+e^- pairs in the pads of the first and second ring of the BeamCal from imperfect collisions relative to the nominal case of head-on collisions. For each case a readout window of 40 BX is assumed.

Imperfect collisions lead to smaller number of incoherent pairs, but as was shown in Section 3.10.2 the azimuthal distribution of the particles are not uniformly reduced. Therefore, also the energy reduction scales differently for different pads. In a few pads the energy deposit actually increases, and is therefore found to be higher than in the nominal case. The bunch to bunch fluctuation is increased, if non-nominal bunch crossings are considered. So, although the average energy deposit might be smaller, the absolute fluctuation from readout window to readout window increases.

The non-uniform reduction is caused by the deflection during the offset collisions, and not only by the reduced number of incoherent pairs. For comparison, the black lines in Figure 8.8

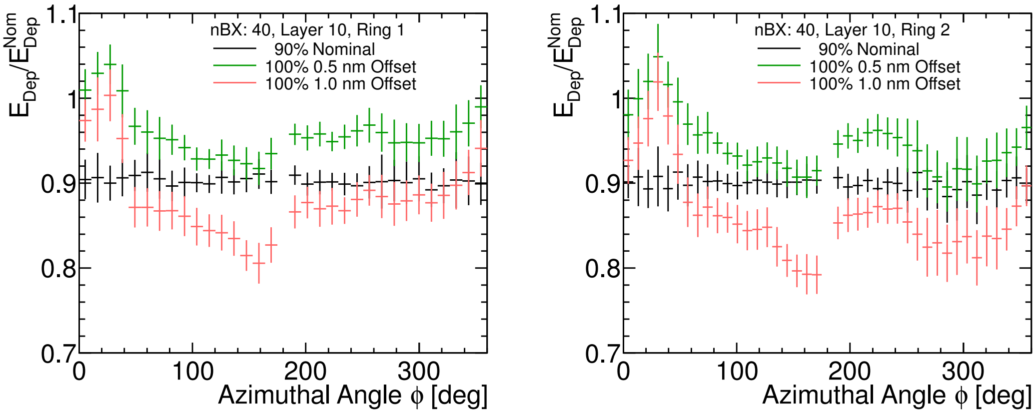

(a) Ring 1

(b) Ring 2

Figure 8.8: Relative energy deposit between (red) collisions with 1 nm vertical offset and nominal collisions, (green) collisions with 0.5 nm vertical offset and nominal collisions, and (black) for 90% of the particles from head-on collisions to 100% nominal collisions. Shown are (a) Ring 1 and (b) Ring 2 of the tenth layer.

mark a case in which only 90% of the particles—randomly chosen—from the nominal background were used. In this case the energy deposit is reduced uniformly by 10% for all pads.

For an approximation of the changing vertical offset between the two beams, the incoherent pairs from the head-on collisions and from the collisions with 1 nm offset are randomly mixed.

Figures 8.9a and 8.9b show the average energy deposits for a readout window of 40 BX in the first six rings in layer 10 of the BeamCal. In Figure 8.9a only nominal head-on collisions are used, and in Figure 8.9b a one-to-one mix of nominal and 1 nm offset collisions are used. Figures 8.9c and 8.9d show the standard deviation of the deposited energy per readout window for the same layer and rings. Figure 8.9c shows the standard deviation for the nominal only case, and Figure 8.9d the standard deviation for the mixed sample.

For the mixed case, the average energy deposit in the readout window is smaller compared to the nominal energy deposits, however, the standard deviation increases by 0.1 GeV in some pads, so the possibility for falsely identified showers could be slightly increased. In both cases the standard deviation in the inner rings, between 0.1 GeV and 0.5 GeV of deposited energy, is close to the maximal energy deposited by a 500 GeV electron in the tenth layer ≈ 0.7 GeV (see Figure 8.6b), especially if the energy deposit is spread across several pads. The influence of the imperfect collisions is limited, but the larger standard deviation will negatively affect the high energy electron identification efficiency. In the following, a background sample including beam offsets is systematically used.

8.2.4 Identification Algorithm

Figure 8.10 shows the energy deposit in the tenth layer from 5 BX and 40 BX of incoherent pair

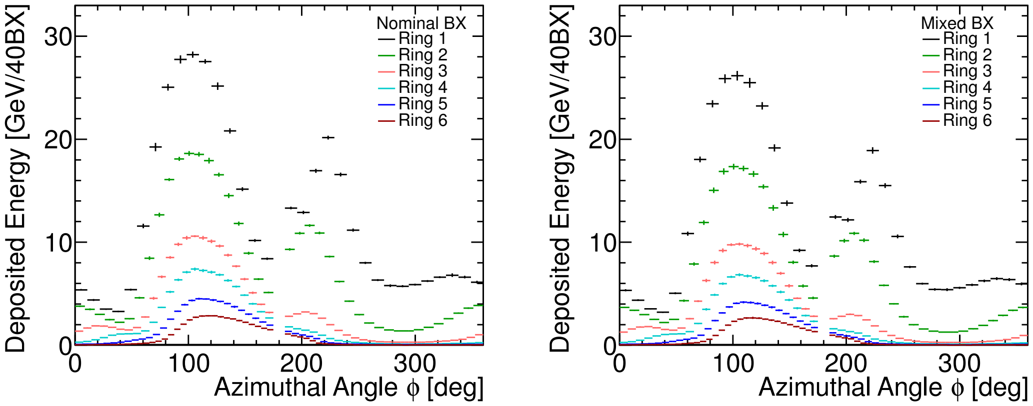

(a) Energy, nominal pairs

(b) Energy, mixed pairs

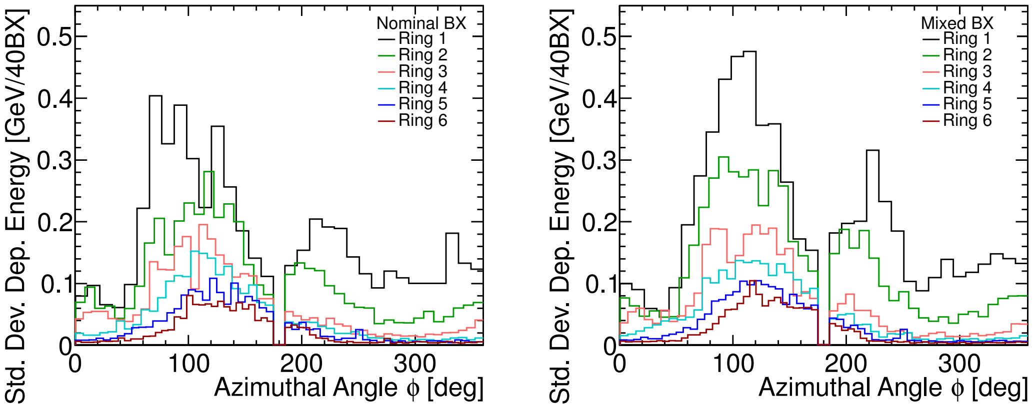

(c) Std. dev., nominal pairs

(d) Std. dev., mixed pairs

Figure 8.9: Deposited energy and standard deviation of the deposited energy in the first six rings of layer 10 of the backward BeamCal for 40BX of background. Left column: For incoherent pairs with head on collisions. Right column: For a one-to-one mixture of head-on and 1 nm offset collisions. In all figures every bin or marker corresponds to one pad.

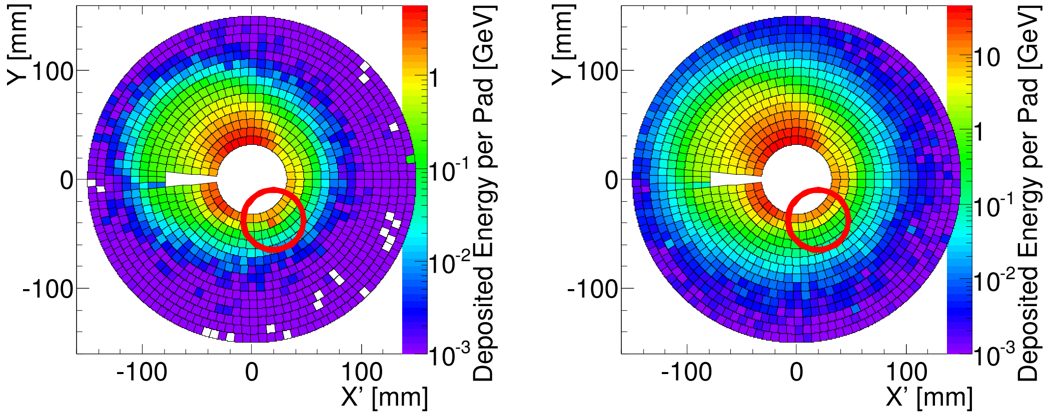

(a) 5 BX

(b) 40 BX

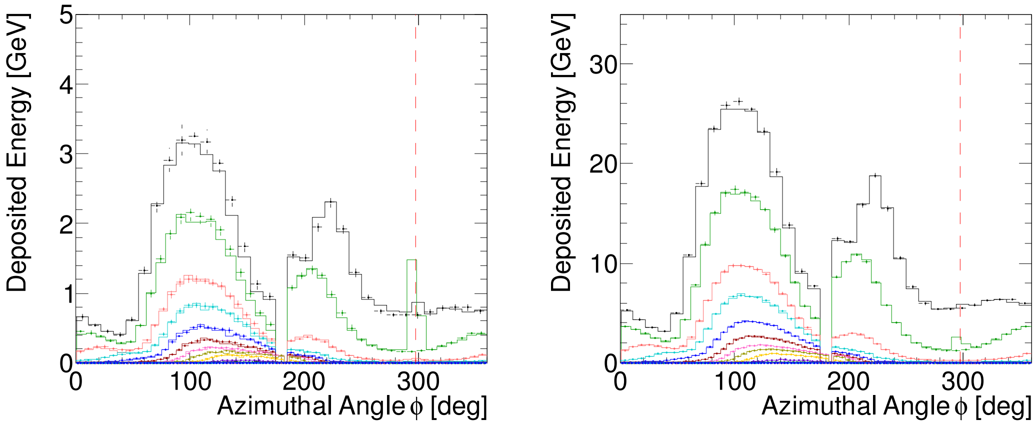

(c) 5 BX

(d) 40 BX

Figure 8.10: Energy deposit from an 1.5 TeV electron in the BeamCal on top of 5 BX and 40 BX integrated incoherent e^+e^- background, respectively. In the bottom row the crosses give the average and standard deviation of the energy deposit and the solid lines the energy deposit from the background and signal of the current readout window. The dashed vertical line marks the azimuthal angle of the electron.

background and from a 1.5 TeV electron. The excess energy above the average in the second ring is clearly visible for both 5 BX and 40 BX. In this event the shower is located on a relatively flat background region, if the shower were located in a region with rising background the cluster would be less visible.

The basic idea of the identification algorithm is: The energy distribution from the incoherent e^+e^- pairs is relatively stable. Therefore, the average and standard deviation of the background energy deposit in each pad can be reliably estimated. Any significant deviation from this average must therefore come from a high energy electron.

In the following, the identification algorithm for showers from high energy electrons is described. Figure 8.11 shows a flow chart of the first part of the algorithm, up to and including step 4. The rest of the algorithm is sketched in Figure 8.12.

From the sample of background energy deposits ten readout windows consisting of a fixed number N_{BX} of bunch crossings are chosen to calculate the average energy deposit $\vec{E}^{\mathrm{Average}}$ and the standard deviation of the energy deposit $\vec{\sigma}$ for each pad. The vector sign is symbolising that each pad of the BeamCal is considered separately.

The algorithm is then executed for each readout window (a.k.a. event), consisting of N_{BX} of incoherent pair background, and the energy deposits in the BeamCal from the signal event, which may or may not contain a high energy electron.

1. A sample of N_{BX} background bunch crossings is chosen randomly from the sample to calculate the energy from incoherent e^+e^- pairs in all pads $\vec{E}^{\mathrm{Event}}_{\mathrm{BKG}}$.
2. The energy deposit from the physics event $\vec{E}^{\mathrm{Event}}_{\mathrm{Signal}}$ is added to the background in the readout window, resulting in the total deposited energy for the readout window under consideration $\vec{E}^{\mathrm{Event}}_{\mathrm{Total}} = \vec{E}^{\mathrm{Event}}_{\mathrm{BKG}} + \vec{E}^{\mathrm{Event}}_{\mathrm{Signal}}$.
3. From the total deposited energy the average energy and standard deviation are subtracted $\vec{E}^{\mathrm{Event}}_{\mathrm{Remaining}} = \vec{E}^{\mathrm{Event}}_{\mathrm{Total}} - \vec{E}^{\mathrm{Average}} - \vec{\sigma}$. This can result in negative energies in some pads.
4. The remaining pad energies $\vec{E}^{\mathrm{Event}}_{\mathrm{Remaining}}$ are checked for unusually large fluctuations, either upward or downward. The tenth layer of the BeamCal is chosen as a reference point, as here the signal showers reach their maximum; and the first ring in this layer is used as here the background is largest. Only one of the correction is performed per readout window.
    a) If there are still more than four pads in the first ring of the tenth layer with more than 90% of one standard deviation of energy, i.e. $N(\vec{E}^{\mathrm{Event}}_{\mathrm{Remaining}} > 0.9\vec{\sigma}) > 4$, then 10% of the standard deviation is subtracted repeatedly from the remaining energy $\vec{E}^{\mathrm{Event}}_{\mathrm{Remaining}} = \vec{E}^{\mathrm{Event}}_{\mathrm{Remaining}} - 0.1\vec{\sigma}$, until the number of pads with ‘too much’ energy is smaller than four. This is done to avoid tagging upward fluctuations of the background as electrons.
    b) Similarly, if the energy in 25 pads in the first ring of the tenth layer is more than 90% of a standard deviation below 0, $N(\vec{E}^{\mathrm{Event}}_{\mathrm{Remaining}} < -0.9\vec{\sigma}) > 25$, then 10% of one standard deviation is added, until the number of pads is smaller than 25. This correction is applied to avoid losing electron clusters, if the background fluctuates downwards.

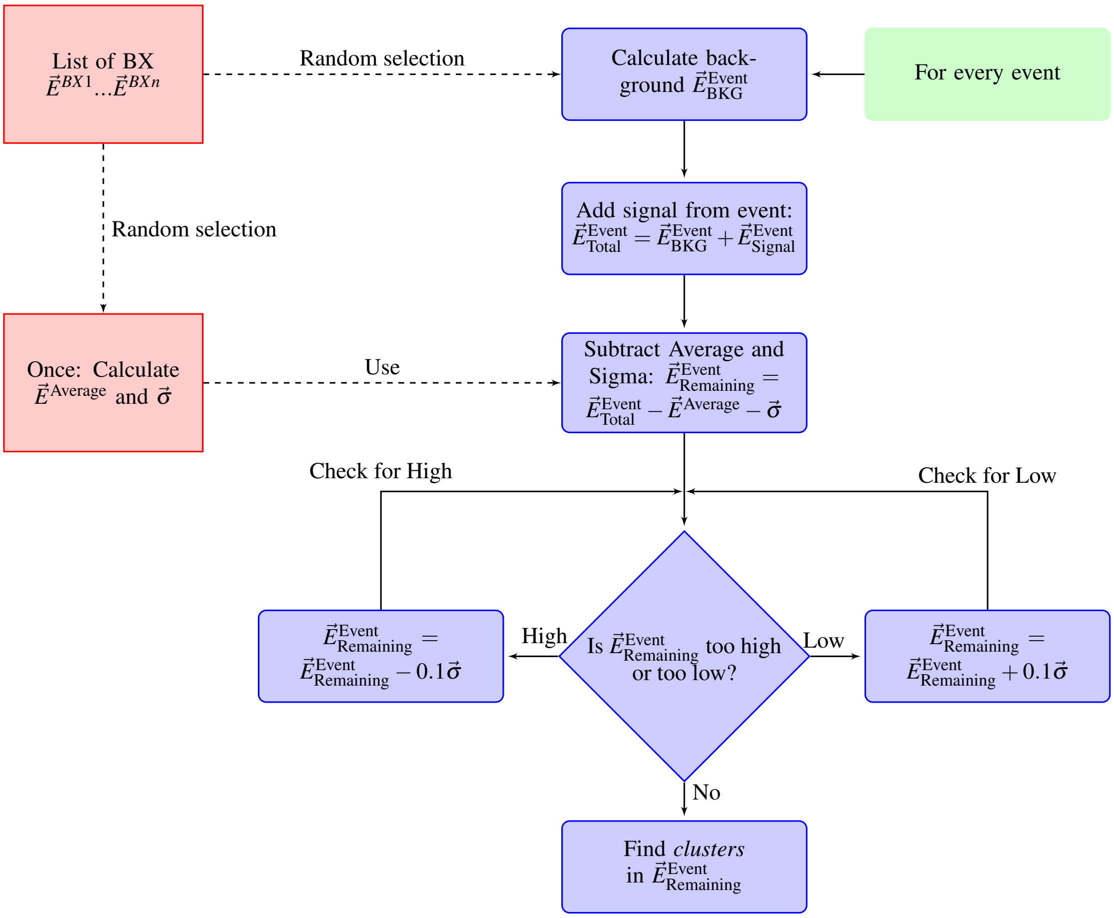

Figure 8.11: Flow chart showing the first part of the electron tagging algorithm. Continued in Figure 8.12.

These corrections on the energy distribution only have a small effect on the overall identification efficiency, but they do help to recover a few otherwise unidentified showers.

5. From the remaining energy in the pads $\vec{E}^{\text{Event}}_{\text{Remaining}}$, only those pads are selected with energy above the $E^{\text{Cut}}_{\text{Pad}}$ cut value. The cut may depend on the ring in which the pad is located. Only pads from layer 10 onward are used for the electron identification, because the energy deposit from the electrons reaches its peak in this layer, and because the energy deposit of the background is smaller than in earlier layers.

6. From the selected pads *towers* are created, which consist of pads at the same radial and azimuthal position, but in different layers. The tower with the most pads is chosen as the first tower for the cluster search. Towers neighbouring it are merged to form a cluster, if they have a minimum number of pads (more than three) associated with them.

7. Once a tower is part of a cluster it is removed from the list of towers, and if further towers remain, additional clusters are formed.

8. For each cluster the average ring number $\bar{R}$ is calculated from the ring numbers R_{Pad} of the pads, weighted with the energy of the pad E_{Pad} from all pads in the cluster

$$\bar{R} = \frac{1}{E_{\text{Cluster}}} \sum_{\text{Pads}} E_{\text{Pad}} R_{\text{Pad}}. \tag{8.1}$$

   The cluster energies $E_{\text{Cluster}} = \sum_{\text{Pads}} E_{\text{Pad}}$ are compared to the $E^{\text{Cut}}_{\text{Cluster}}$ cut value, which is chosen depending on the average ring of the cluster.

9. For the accepted clusters the polar angle θ_{Reco} is calculated from the average ring of the cluster, and the azimuthal angle ϕ_{Cluster} is calculated from the energy weighted azimuthal angle ϕ_{Pad} of the pads in the cluster

$$\phi_{\text{Cluster}} = \text{ATan2}\left(\frac{1}{E_{\text{Cluster}}} \sum_{\text{Pads}} E_{\text{Pad}} \sin\phi_{\text{Pad}}, \qquad \frac{1}{E_{\text{Cluster}}} \sum_{\text{Pads}} E_{\text{Pad}} \cos\phi_{\text{Pad}} \right) \tag{8.2}$$

   where the sums are the average position in Y and X, and ATan2 the two-argument arctangent function commonly found in computer math libraries [97].

8.2.5 Optimising the Cuts for a Minimal Fake Rate

Because the electron tagging will be used as a veto against two-photon events or similar topologies, the rate of background fluctuations tagged erroneously as electrons should be small.

The fake rate is the number of reconstructed clusters not belonging to an electron divided by the total number of readout windows looked at. The efficiency is the number of correctly reconstructed electrons divided by the number of all high energy electrons. Both are shown with respect to the polar angle. The efficiency is calculated for the true polar angle θ_{True} of the

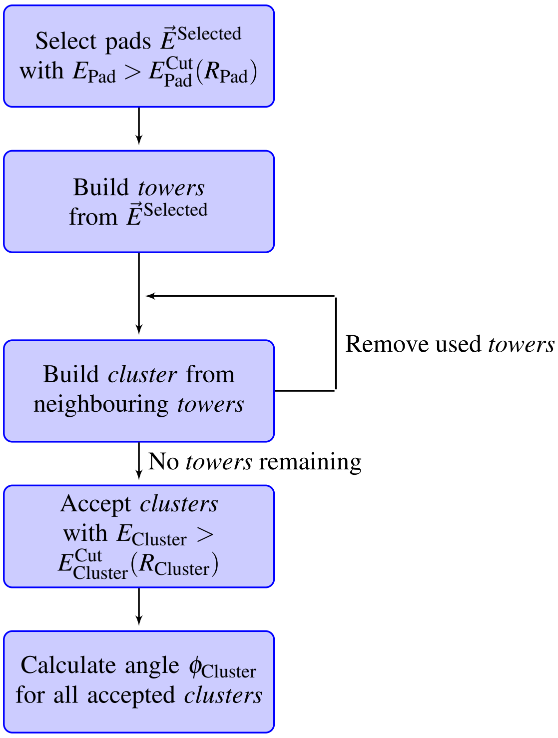

Figure 8.12: Flow chart showing the second part of the electron tagging algorithm

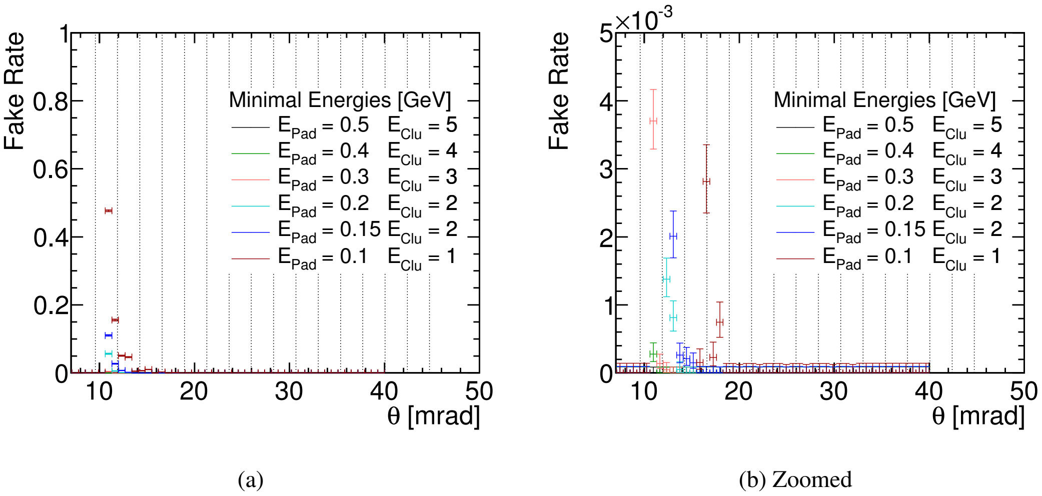

(a)

(b) Zoomed

Figure 8.13: Fake rates for different cuts on the remaining pad and cluster energy with 40 BX of background. The vertical lines mark the separation between the different rings of the BeamCal: (a) Overview and (b) zoom to smaller values.

electron taken from the Monte Carlo information, for the fake rate the reconstructed polar angle θ_{Reco} is used.

The minimal required energy $E_{\text{Pad}}^{\text{Cut}}$ that a pad has to have after the subtraction of the background to be considered in a *tower* is chosen to only depend on the ring of the pad, independent of the azimuthal angle or layer. The $E_{\text{Pad}}^{\text{Cut}}$ values can also be based on the standard deviations $\vec{\sigma}$ of the pads, and would then follow the energy deposits, as it is done in [70, 95]. Explicitly setting the $E_{\text{Pad}}^{\text{Cut}}$ values gives a direct handle on the selected pads, but it will result in a pessimistic estimate of the efficiency, as the deposited background energy clearly varies across azimuth and layer.

Figure 8.13 shows the fake rate as a function of the polar angle for different cuts used in for the electron identification. With $E_{\text{Pad}}^{\text{Cut}} = 0.1$ GeV and $E_{\text{Cluster}}^{\text{Cut}} = 1$ GeV a fake rate of almost 0.5 is reached at $\theta = 10$ mrad. This means that a fake high energy electron is found in every second readout window. With increasing polar angle the fake rate falls, until basically no fake electron is found.

With larger values for $E_{\text{Pad}}^{\text{Cut}}$ and $E_{\text{Cluster}}^{\text{Cut}}$ less and less electrons are found in the background. For energy cuts of $E_{\text{Pad}}^{\text{Cut}} = 0.5$ GeV and $E_{\text{Cluster}}^{\text{Cut}} = 5$ GeV basically no fake electrons (less than $2 \cdot 10^{-4}$ per readout window) are found. Table 8.2 lists the cuts, for which the number of fake electrons is consistent with zero. These cuts are used to determine the identification efficiency.

8.2.6 Electron Identification Efficiency

Using the cuts derived in the previous section and given in Table 8.2, showers from electrons of different energies are attempted to be identified. Close to the inner edge of the BeamCal and where the overlap with the LumiCal starts showers are not fully contained. This is also true

Table 8.2: Cuts used for the identification of electrons over 40 BX of background, resulting in a low fake rate. The (averaged) ring from which on the cuts are applied, the minimal required energy per pad $E_{\mathrm{Pad}}^{\mathrm{Cut}}$, and the minimal energy for a cluster $E_{\mathrm{Cluster}}^{\mathrm{Cut}}$.

Starting Ring	$E_{\mathrm{Pad}}^{\mathrm{Cut}}$ [GeV]	$E_{\mathrm{Cluster}}^{\mathrm{Cut}}$ [GeV]
0	0.5	5.0
1	0.4	4.0
1.5	0.3	3.0
2.5	0.2	2.0
3.5	0.15	2.0
4.5	0.1	1.0

for showers close to the insensitive area between the incoming and outgoing beam pipe. As the electron identification will suffer from the geometrical effects these regions are for now excluded from the study of the electron identification efficiency. Only electrons in the polar angle from 10 mrad to 33 mrad and with an azimuthal angle between $0^\circ < \phi < 170^\circ$ and $190^\circ < \phi < 360^\circ$ are used. Geometrical inefficiencies are described in Section 8.2.10.

Figure 8.14 shows the identification efficiency for electrons with an energy of 1.5 TeV, 1.0 TeV 0.5 TeV. Also drawn are vertical lines depicting the boundaries between the different rings of the BeamCal. The efficiencies for all energies between 1.5 TeV and 0.5 TeV can be found in Appendix D.

The identification efficiency reaches $\varepsilon = 1.0_{-0.003}$ from a certain polar angle onwards depending on the energy of the high energy electron. For the electrons with an energy above 1 TeV the high efficiency region starts at around 16 mrad. Close to the boundaries between two rings, the identification efficiency at small polar angles drops, because the deposited energy is distributed among several pads.

8.2.7 Energy Resolution

The rather severe cuts to reduce the influence of background fluctuations decrease the identified energy of the electron showers between 50% for 1.5 TeV electrons and 75% for 0.5 TeV electrons compared to the total deposited energy. Parts of the deposited energy are rejected, because only deposits from layer ten onwards are considered, and because the cut on the remaining energy above the background in each pad further reduces the considered deposited energy. Figure 8.15a shows the distribution of the energy found in each cluster for the different electron energies (cf. Figure 8.6a for the total deposited energy).

Figure 8.15b shows the mean reconstructed energy with respect to the electron energy. The error bars represent the standard deviation of the distribution of cluster energies $\sigma_{E_{\mathrm{Cluster}}}$. The distributions of the cluster energy found by the algorithm are fairly wide. A linear function

$$E_{\mathrm{Cluster}} = a \cdot E_{\mathrm{Electron}} + b \tag{8.3}$$

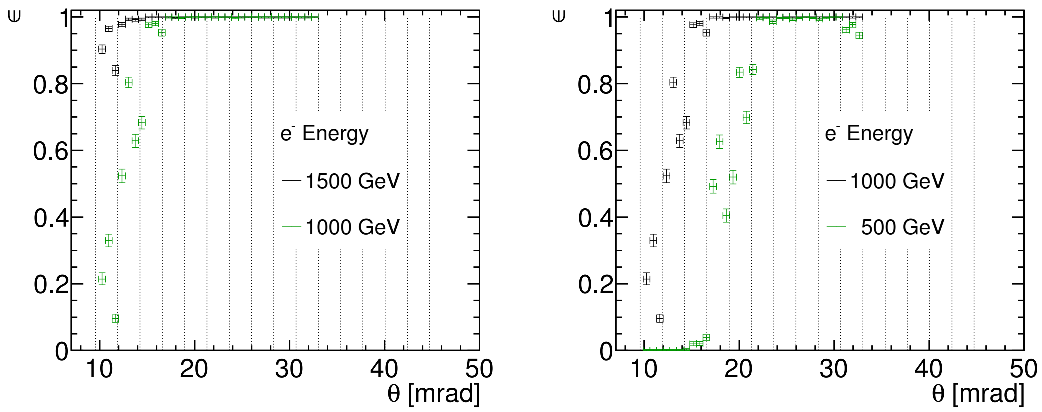

(a) 1.0 TeV and 1.5 TeV

(b) 0.5 TeV and 1.0 TeV

Figure 8.14: Efficiencies for electron tagging in the BeamCal for 40 BX of integrated background for electrons from 1.5 TeV, 1.0 TeV and 0.5 TeV.

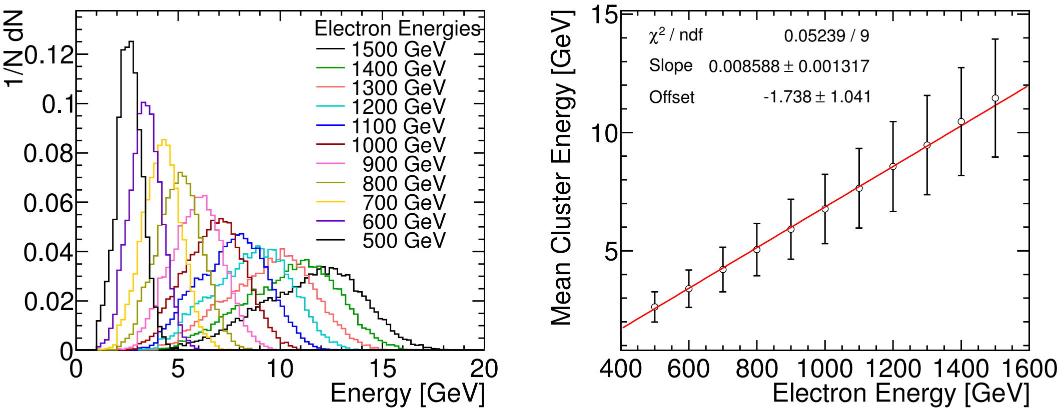

(a) Cluster Energy

(b) Mean Cluster Energy

Figure 8.15: (a) Distribution of reconstructed cluster energies for electrons with an energy between 0.5 TeV and 1.5 TeV in the selected region of the BeamCal with 40 BX of background and (b) dependence of the cluster energy on the electron energy.

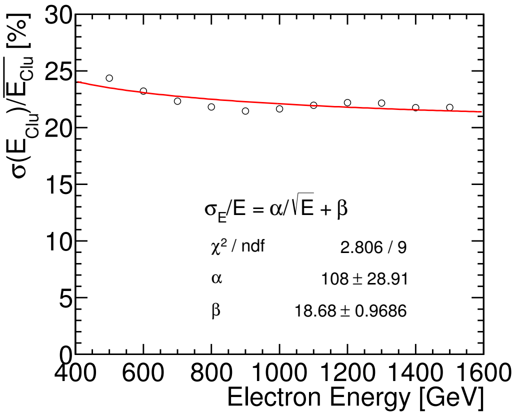

Figure 8.16: Energy resolution for electrons of 0.5 TeV to 1.5 TeV reconstructed in the BeamCal.

has been fitted to the points, where a is the slope and b the offset. In the energy range between 500 GeV and 1500 GeV, the relation between electron energy and reconstructed energy is linear. The BeamCal is therefore able to provide an estimate on the electron energy. Figure 8.16 shows the ratio $\sigma_{E_{\text{Cluster}}}/E_{\text{Cluster}}$ with respect to the electron energy fitted by the resolution function

$$\sigma_{E_{\text{Cluster}}}/E = \alpha/\sqrt{E_{\text{Cluster}}} + \beta, \tag{8.4}$$

resulting in an energy resolution of $100\%/\sqrt{(E[\text{GeV}])}$ with a large constant term of 19%. This is considerably worse than for the LumiCal, with which an energy resolution of $21\%/\sqrt{(E[\text{GeV}])}$ is reached in the fiducial volume [67], but in the LumiCal the background is much smaller.

8.2.8 Angular Resolution

Figure 8.17 shows the average resolution of the polar and azimuthal angle. The resolution is the standard deviation of the difference between the generated angle and the reconstructed angle. The effect of the magnetic field on the angle at which the electron hits the BeamCal was not corrected.

The polar angle resolution improves slightly with increasing electron energy. If the identified electron cluster consists of only one tower, the angular resolution can be expected to be the angular pad size divided by $\sqrt{12}$. Along the polar angle the pad size is constant, and the resolution can be expected to be $\sigma_\theta = 0.7$ mrad. For higher energy electrons more energy is deposited and it is more likely that more than one tower is part of a cluster, which gives a better resolution. The average polar angle resolution from identified electron showers is $\sigma_\theta^{\text{Reco}} = 0.43$ mrad.

For the azimuthal angle the pad size is constant in $r\phi$. In the innermost ring the resolution from a single pad is $\sigma_\phi = 3.2^\circ$. An average resolution of $\sigma_\phi^{\text{Reco}} = 2.6^\circ$ is found, which is smaller than what can be expected in the innermost layer, but larger than for the rings which finer azimuthal segmentation, due to the uncorrected angular bias.

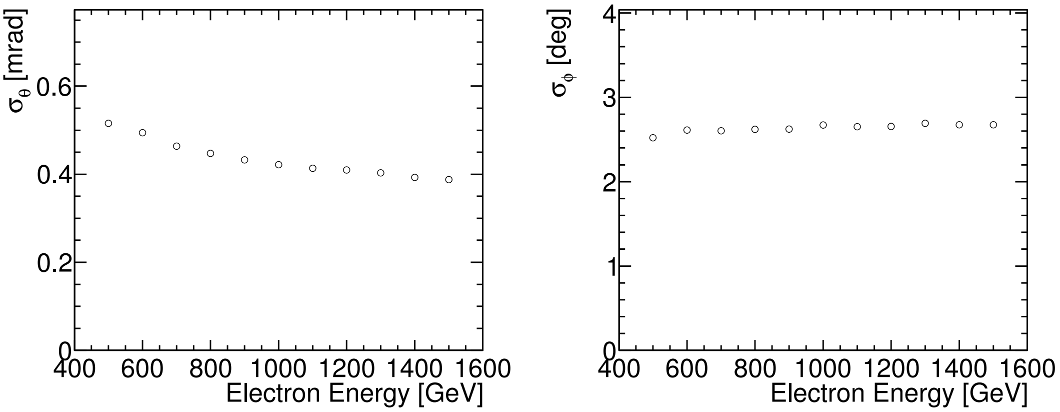

(a) Polar angle

(b) Azimuthal angle

Figure 8.17: Average resolution for the polar and azimuthal angle as a function of the electron energy.

8.2.9 Identification Efficiency with Respect to Readout Window Size

The identification efficiencies for different readout windows—ranging from 1 BX to 50 BX—were estimated, to compare the impact of faster or slower readout on the identification efficiency.

First, for each case, the cuts for a minimal fake rate were determined as previously for the 40 BX case. The cuts are summarised in Table 8.3. For these cuts Figure 8.18 shows the identification efficiency for 0.5 TeV and 1.0 TeV electrons as a function of the polar angle for the different readout windows.

The polar angle range, in which all 0.5 TeV electrons (Figure 8.18a) can be identified, grows for smaller readout windows, but only for a readout window of 1 BX does it extend all the way to the inner acceptance of the BeamCal.

The 1.0 TeV electrons are shown in Figure 8.18b. With a readout window integrating 10 BX of background or less the efficiency is above 95% across the full angular range. With 20 BX of integrated background the identification efficiency starts with almost 90% at the inner edge, drops to 75% between the first and second ring, before it rises to 95% and above.

For 40 BX and 50 BX the identification efficiency drops further. The required energy cuts are very similar, thus the efficiencies are also similar. Except in the centre of the first ring no significant differences are seen. From 15 mrad on, the efficiency is above 95%.

8.2.10 Geometrical Inefficiencies

Because of the crossing angle and the separation of the incoming and outgoing beam pipes, the BeamCal cannot offer full azimuthal coverage. This inherently reduces the identification efficiency.

Figure 8.19a shows the efficiency with respect to the polar and azimuthal angle for 1.0 TeV electrons. The complete loss of coverage at $\phi = 180°$, due to the insensitive area, is clearly

Table 8.3: Cuts used for different numbers of integrated background bunch crossings. Values for 40 BX are given in Table 8.2. All cut values given in GeV.

Starting Ring	1 BX		5 BX		10 BX		20 BX		50 BX	
	$E_{\mathrm{Pad}}^{\mathrm{Cut}}$	$E_{\mathrm{Cluster}}^{\mathrm{Cut}}$	$E_{\mathrm{Pad}}^{\mathrm{Cut}}$	$E_{\mathrm{Cluster}}^{\mathrm{Cut}}$	$E_{\mathrm{Pad}}^{\mathrm{Cut}}$	$E_{\mathrm{Cluster}}^{\mathrm{Cut}}$	$E_{\mathrm{Pad}}^{\mathrm{Cut}}$	$E_{\mathrm{Cluster}}^{\mathrm{Cut}}$	$E_{\mathrm{Pad}}^{\mathrm{Cut}}$	$E_{\mathrm{Cluster}}^{\mathrm{Cut}}$
0	0.1	1.0	0.15	2.0	0.2	2.0	0.3	3.0	0.5	5.0
1									0.4	4.0
1.5					0.15	2.0	0.2	2.0		
2			0.1	1.0					0.3	3.0
2.5					0.1	1.0	0.15	2.0	0.2	2.0
3.5							0.1		0.15	2.0
4.5									0.1	1.0

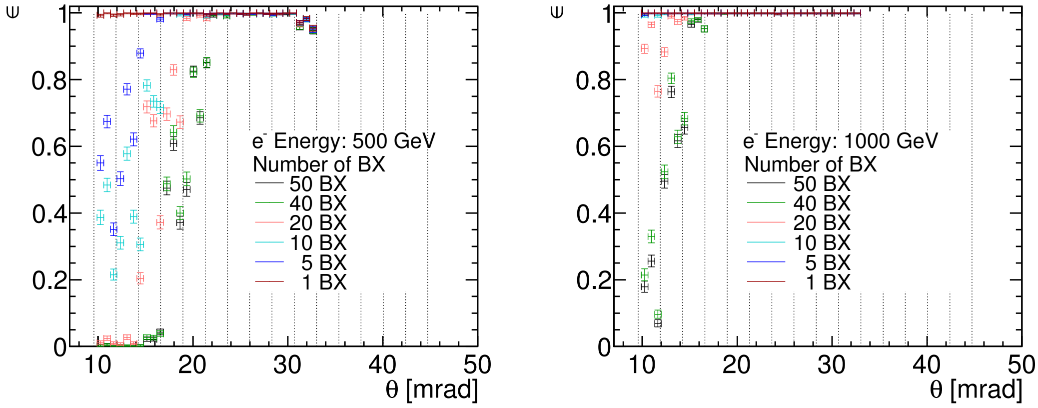

(a)

(b)

Figure 8.18: Identification efficiency for (a) 0.5 TeV and (b) 1 TeV electrons with readout windows of different sizes.

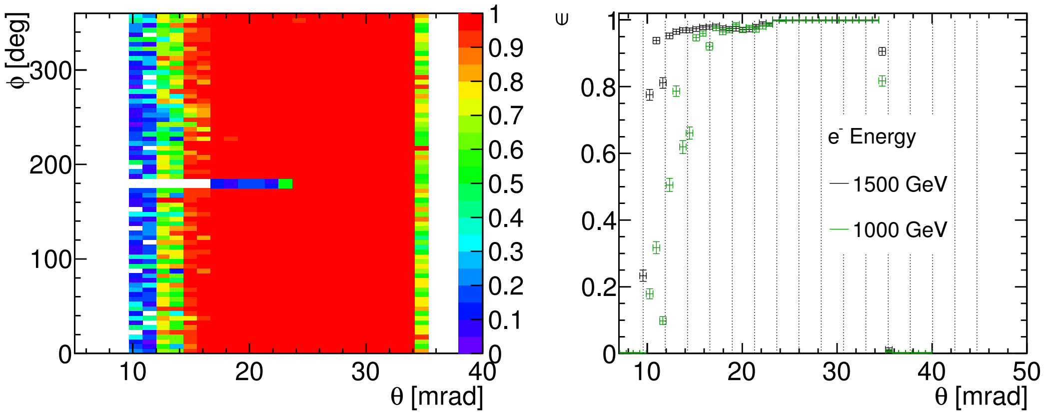

(a) Efficiency for 1.0 TeV electrons

(b) Efficiency for 1.0 TeV and 1.5 TeV electrons

Figure 8.19: Identification efficiency for the full BeamCal, including edges and the keyhole region. (a) Identification efficiency for 1.0 TeV electrons as a function of the polar and azimuthal angle and (b) efficiency for 1.0 TeV and 1.5 TeV electron energies as a function of the polar angle.

visible. The reduced efficiencies at small polar angles, from the impact of the background, and at the outer edge of the BeamCal can also be seen.

Figure 8.19b shows the efficiency with respect to the polar angle for electrons with an energy between 1.0 TeV and 1.5 TeV including all azimuthal angles. The reduced efficiency up to 24 mrad caused by the insensitive area can be seen compared to Figure 8.14. The efficiency at the outer edge of the BeamCal ($\theta \approx 35$ mrad) drops, the more the lower the electron energy.

8.2.11 Summary and Conclusions for the Electron Tagging

Despite the large energy deposits from the incoherent pairs and the short bunch spacing at CLIC, the BeamCal can still be used to identify high energy electrons. Between polar angles of 22 mrad and 35 mrad all electrons with an energy above 0.5 TeV can be identified with an efficiency close to 100%, even with a rather long readout window of 40 BX.

The identification efficiency clearly benefits from shorter readout windows, because of the smaller absolute variation of the energy deposits. For 1.0 TeV electrons a readout window of 20 BX would allow for an identification efficiency of around 80% in the first ring, compared to only 30% for 40 BX readout windows.

There are some inefficiencies in the identification due to the sharing of the energy deposit between several pads. This might be improved if the arrangement of the sensors is changed. In the simulation all sensor pads are aligned. Because of the cut-out due to the incoming beam pipe a simple rotation of alternating sensor layers, as it is might be done at the LumiCal, is not possible, but other design solutions might be found.

In this study the identification algorithm was tuned for a minimal fake rate. Depending on the requirements of the analysis a larger fake rate might be acceptable. It will be possible to optimise the algorithm for different use cases.

9 Stau Pair-Production and Two-Photon Events

The identification efficiencies for high energy electrons in the BeamCal, as given in Chapter 8, do not allow by themselves to quantify the actual gain of using BeamCal in a physics analysis. In order to asses this gain, the example of the stau pair-production

$$\mathrm{e}^{+}\mathrm{e}^{-} \rightarrow \tilde{\tau}^{+}\tilde{\tau}^{-} \rightarrow \tau^{+}\tilde{\chi}^{0}\tau^{-}\tilde{\chi}^{0}$$

is used. The major background is the two-photon process producing τ-leptons. The cross-section for two-photon events with two τ-leptons inside the detector acceptance is of the order of picobarn, while other processes producing a τ-pair have event rates corresponding to femtobarn, similar to the background processes for the smuon study in [94]. In the following, a generator-level study of stau pair-production at CLIC and the background rejection capability using the BeamCal is performed.

9.1 Stau Pair-Production and Stau Mass Measurement

The energy distribution of the τ-leptons from the decay of the staus has a rectangular box-shape, if no beam-beam or detector effects are considered [92]. The sharp endpoints of this distribution can be used to extract the mass of the stau and the neutralino in a combined fit [92]. Alternatively, if the neutralino mass is known from another measurement, the mass of the stau can be determined with just one of the endpoints. The endpoints $E_{\mathrm{max,min}}$ of the spectrum are fixed by the masses and the centre-of-mass energy through [98]

$$E_{\mathrm{max,min}} = \frac{\sqrt{s}}{4}\left(1 \pm \sqrt{1 - \frac{4m_{\tilde{\tau}}^{2}}{s}}\right)\left(1 - \frac{m_{\tilde{\chi}^{0}}^{2}}{m_{\tilde{\tau}}^{2}}\right), \tag{9.1}$$

where $m_{\tilde{\chi}^{0}}$ is the mass of the neutralino and $m_{\tilde{\tau}}$ the stau mass. The rectangular energy distribution is smeared out by the luminosity spectrum, and as there is at least one neutrino involved in the decay of τ-leptons, the visible energy in the detector will be lower, which further changes the shape of the energy distribution.

The stau and neutralino mass depends on the specific Supersymmetry (SuSy) model; for the example used here, the SuSy point K' [99] was chosen. In this model the stau is the lightest slepton with a mass of $m_{\tilde{\tau}} = 896$ GeV and decays into a τ-lepton and a neutralino with a mass of $m_{\tilde{\chi}^{0}} = 554$ GeV. The endpoints of the τ-lepton energy distribution are $E_{\mathrm{min}} = 92$ GeV and $E_{\mathrm{max}} = 835$ GeV. Smaller mass differences between the neutralino and the stau will lead to smaller minimal and maximal endpoints.

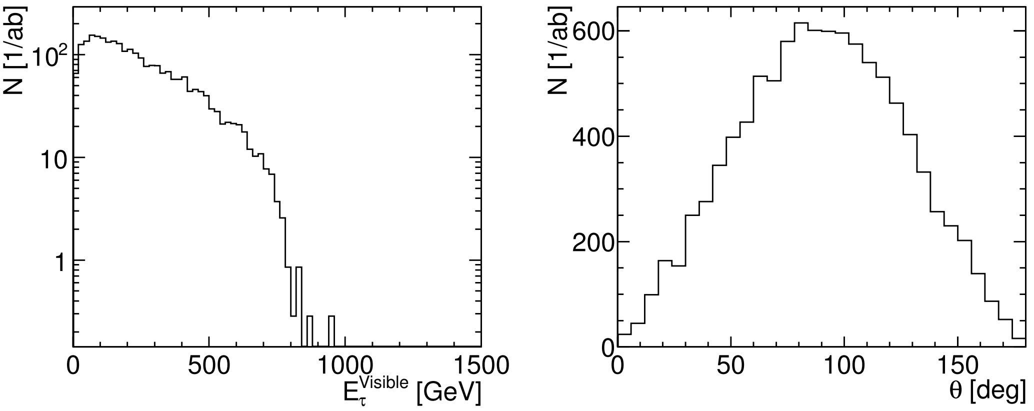

(a)

(b)

Figure 9.1: Spectrum of the τ-leptons from the stau-pair production: (a) visible energy, the edges in the energy distribution are smeared by the luminosity spectrum and the missing energy from the τ-decay. (b) Polar angle distribution.

The total cross-sections for the $\tilde{\tau}$-pair production in this model is 1.4 fb. The $e^+e^- \to \tilde{\tau}^+\tilde{\tau}^-$ events are generated with PYTHIA 6.215 [100] and ISASUGRA 7.69 [101]. The sample consists of 5000 events, which are weighted to correspond to an integrated luminosity of 1 ab^{-1} [102]. Figure 9.1a shows the visible energy from the decay products of the τ-leptons.

The angular distribution of the τ-leptons is shown in Figure 9.1b. The stau pairs, and the resulting τ-leptons, are produced centrally. For further analysis, events are accepted in which two τ-leptons with a visible energy $E_\tau > 10$ GeV and a polar angle $\theta_\tau > 20°$ exist. All decay channels of the τ-leptons are included and 100% efficiency in the tau reconstruction is assumed. The reconstruction inefficiencies will apply to all τ-leptons from either background or signal, and can be partially recovered with a larger integrated luminosity.

9.2 Two-Photon Events

The Landau–Lifschitz process, also called multi-peripheral two-photon exchange, produces a lepton pair from two virtual photons (Figure 3.4c)

$$e^+e^- \to e^+e^-\ell^+\ell^-. \tag{9.2}$$

The total cross-section for the two-photon process for a lepton of mass m_ℓ is [103]

$$\sigma_{e^+e^-\to e^+e^-\tau\tau} = \frac{28\alpha^4}{27\pi m_\ell^2}\left(\ln\frac{s}{m_e^2}\right)^2 \ln\frac{s}{m_\ell^2}. \tag{9.3}$$

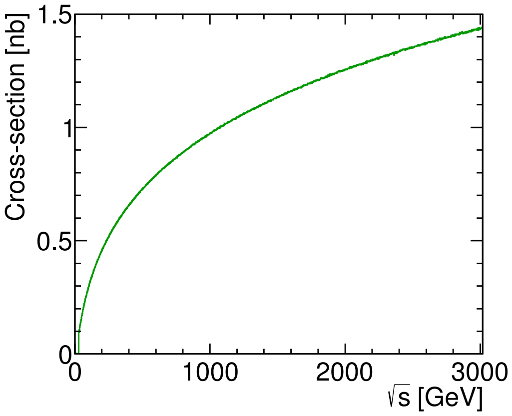

Figure 9.2: Total $e^+e^- \rightarrow e^+e^-\tau\tau$ cross-section calculated by RADCOR as a function of the centre-of-mass energy.

The two-photon cross-section rises logarithmically with the centre-of-mass energy. For the production of a τ-pair the total cross-section is of the order of a nanobarn at $\sqrt{s} = 3$ TeV.

The two-photon events producing a τ-pair were generated with the RADCOR* Monte Carlo generator [104]. RADCOR includes only the multi-peripheral two-photon exchange diagram and radiative corrections from initial state radiation. The minimal momentum transfer in the generator is $Q^2 > 4m_\ell^2$. Figure 9.2 shows the cross-sections of the $e^+e^- \rightarrow e^+e^-\tau\tau$ process calculated with RADCOR as a function of the centre-of-mass energy. The total cross-section weighted with the CLIC luminosity spectrum is 1.33 nb, six orders of magnitude larger than for the stau-pair production.

9.2.1 Generation of Two-Photon Events

The two-photon events were first generated at centre-of-mass energies between 100 GeV and 3017 GeV—the range covered by the CLIC luminosity spectrum (see Section 3.4)—and subsequently boosted to account for the asymmetric initial state energy.

During the generation of events, final state cuts on the τ-leptons were applied to reduce the event rate and avoid the generation of over a billion events. Only events with no τ-lepton below a polar angle of 10° and with no τ-lepton with an energy below 10 GeV were generated. As long as the τ-leptons are produced in opposite directions, a longitudinal boost will always reduce one of the τ-lepton's polar angle and energy so that no events are rejected that would pass the acceptance cuts after the longitudinal Lorentz-boost†.

From the boosted events only those are accepted with both τ-leptons at a polar angle above 20° and with an energy above 10 GeV, as it was done for the stau events. Additionally all events with at least one electron with an energy larger than 50 GeV and above a polar angle of 35 mrad were

---

[*] Also known as BDKRC after the last names of the authors.

[†] Events with two τ-leptons at polar angles below 10° on the same side of the detector could potentially be boosted into the acceptance region, but they would be excluded by the cut on the acollinearity.

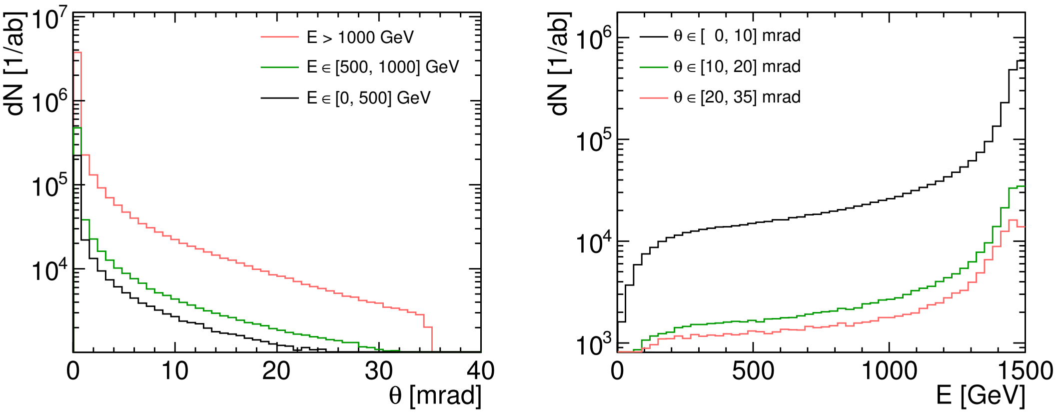

(a) Angular distribution

(b) Energy distribution

Figure 9.3: Angular and energy distribution for the spectator electrons and positrons from the $e^+e^- \to e^+e^-\tau\tau$ two-photon events with two τ-leptons in the detector.

rejected. This is justified, since the incoherent e^+e^- background is much lower outside of the BeamCal , and the electron identification efficiency is large enough to reject these events [105]. The effective cross-section after these cuts is 2.94 pb, still three orders of magnitude above the signal cross-section.

9.3 Impact of the Electron Tagging

Figure 9.3 shows the polar angle and energy spectrum of the spectator electrons and positrons from the accepted two-photon events. A large number of the particles has a polar angle below 10 mrad, and is therefore outside of the BeamCal acceptance. On the positive side, the majority of the particles has an energy above 1 TeV, which can be more efficiently identified with the BeamCal than the lower energy particles.

The electron identification efficiencies estimated in Chapter 8 were applied to the two-photon events. The efficiency depending on the energy and the azimuthal and polar angle was used to decide whether the electrons could be identified. If at least one electron could be identified the event was rejected.

Figure 9.4 shows the distribution of the visible τ-lepton-energies from the $e^+e^- \to e^+e^-\tau\tau$ and $e^+e^- \to \tilde{\tau}^+\tilde{\tau}^-$ processes. For the $e^+e^- \to e^+e^-\tau\tau$ events the number of entries are shown before and after the electron tagging. The electron tagging reduces the number of events from $2.9 \cdot 10^6$ to $2.6 \cdot 10^6$, the background distribution extends beyond the maximum energy edge of the signal, and at the lower energy endpoint the background is at least an order of magnitude above the signal.

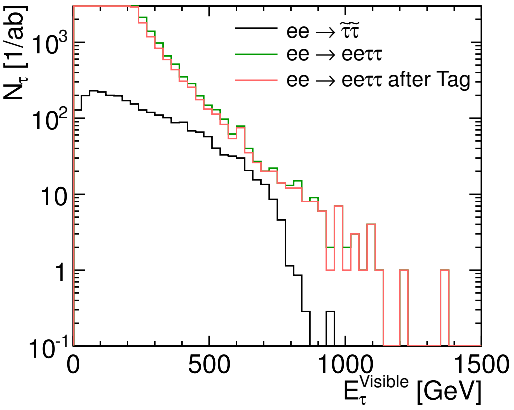

Figure 9.4: Energy distribution of the τ-leptons from the $e^+e^- \rightarrow e^+e^-\tau\tau$ and $e^+e^- \rightarrow \tilde{\tau}^+\tilde{\tau}^-$ events. For the two-photon events the number of τ-leptons before (green) and after (red) the electron tagging are shown.

9.4 Selection Cuts

The electron tagging with the BeamCal is clearly not sufficient to reduce the two-photon background to a reasonable level. Additional selection cuts are necessary.

As the endpoints of the tau energy spectrum are used to extract the stau mass, special care has to be taken to avoid biasing the tau energy distribution. The variables used for the selection cuts are: the acoplanarity, folded onto the range between 0° and 180°

$$\phi_{\text{Acopl}} = \phi_2 - \phi_1 - \pi. \tag{9.4}$$

The acollinearity

$$\theta_{\text{Acoll}} = (\theta_1 + \theta_2) - \pi, \tag{9.5}$$

which is limited to below 140° because of the acceptance cut on the τ-lepton angles. The polar angle of the missing momentum θ^{miss}, folded onto the range between 0° and 90°. And the scalar sum of the transverse momenta

$$p_{\text{T}}^{\text{Sum}} = p_{\text{T}}^1 + p_{\text{T}}^2. \tag{9.6}$$

$\phi_{1,2}$ are the respective azimuthal angles of the combined visible τ decay products from the two τ-leptons, $\theta_{1,2}$ the polar angles, and $p_{\text{T}}^{1,2}$ the transverse momenta.

Figure 9.5 shows the mean energy of the τ-leptons with respect to the individual selection variables. The mean energy only shows a weak dependence on ϕ_{Acopl}, θ_{Acoll}, and θ^{miss}, but it is strongly correlated with $p_{\text{T}}^{\text{Sum}}$. The cuts on ϕ_{Acopl}, θ_{Acoll}, and θ^{miss} have therefore the advantage that they do not bias the sample of stau-events. The cut on the sum of the transverse momentum primarily removes events with small tau energies.

Figure 9.6 shows the relative and cumulative distributions of the variables for the stau and two-photon events. The values for the cuts were chosen such that each of the angular cuts removes

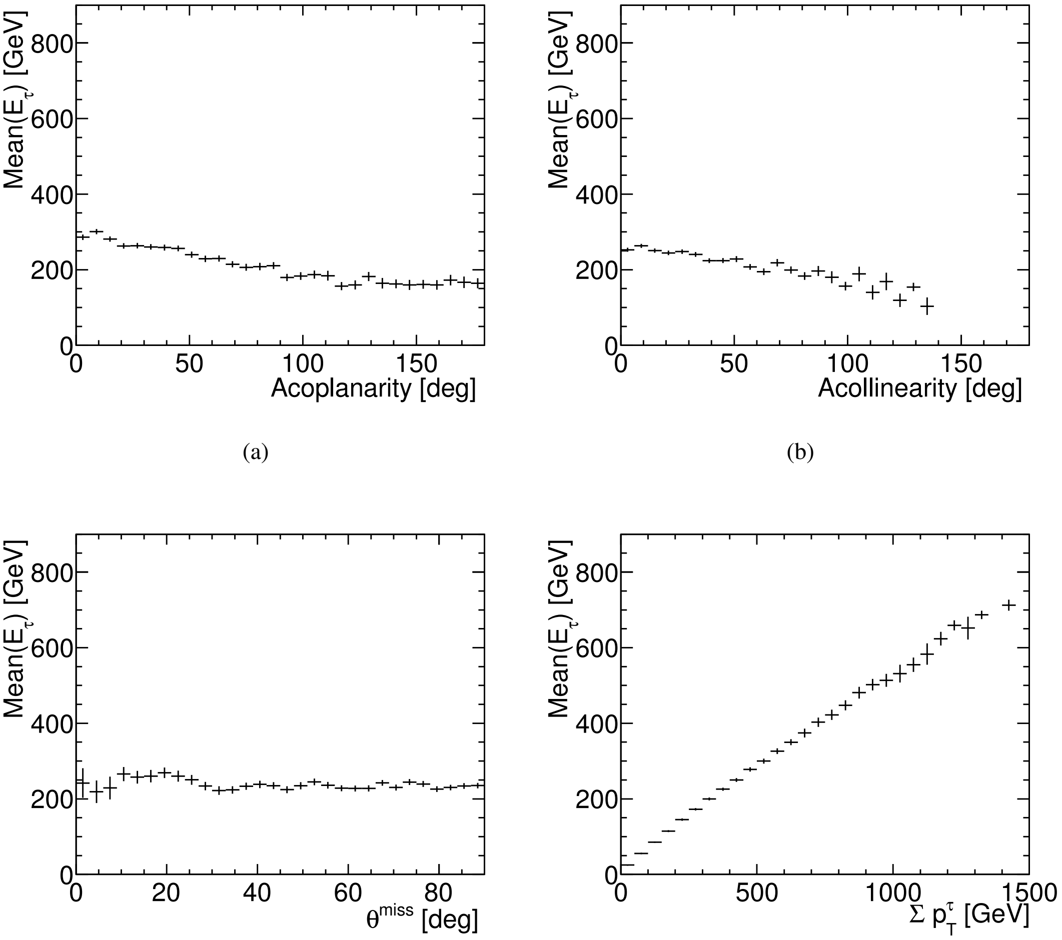

(a)

(b)

(c)

(d)

Figure 9.5: Correlations between the different selection cut variables and the energy distribution of the visible τ-lepton decay products.

10% of the stau events, the cut on $p_{\mathrm{T}}^{\mathrm{Sum}}$ is chosen to remove only 5% of the stau-events. The cuts are: $\phi_{\mathrm{Acopl}} > 9.3^\circ$, $\theta_{\mathrm{Acoll}} < 70.5^\circ$, $\theta_{\mathrm{Miss}} > 30.5^\circ$, and $p_{\mathrm{T}}^{\mathrm{Sum}} > 112.5$ GeV.

Table 9.1 lists the number of events before and after the individual cuts with and without the electron tagging for the $\mathrm{e}^+\mathrm{e}^- \rightarrow \tilde{\tau}^+\tilde{\tau}^-$ and $\mathrm{e}^+\mathrm{e}^- \rightarrow \mathrm{e}^+\mathrm{e}^-\tau\tau$ processes, and also the number of events if all the angular cuts are applied, and if all cuts are combined.

After the angular cuts, the selection efficiency of the stau events is 76%. Without the electron tag 8% of the two-photon events remain; the electron tag can reject an additional 50% of those events. Figure 9.7a shows the distribution of the visible τ-lepton-energies. At the lower edge of the energy spectrum the two-photon events are still an order of magnitude above the signal. The electron tag moves the edge, where the two-photon events intersect with the curve of the stau events, back by 60 GeV.

After also applying the transverse momentum cut 72% of the stau events remain and 0.03% of the two-photon events. In this case the electron tag can reject an additional 94% of the remaining events, from the initial 3 million events only about 50 remain with visible tau energies up to 250 GeV.

In summary, in combination with several selection cuts the BeamCal can be used to suppress greatly the two-photon background in the search for stau pairs. In the example given here the upper endpoint of the energy distribution is already background free without the application of the BeamCal electron tag. However, for SuSy scenarios with smaller mass differences between the neutralino and stau, the BeamCal will be more important to reject two-photon backgrounds, and it will be worth studying the benefit of the BeamCal in greater depth.

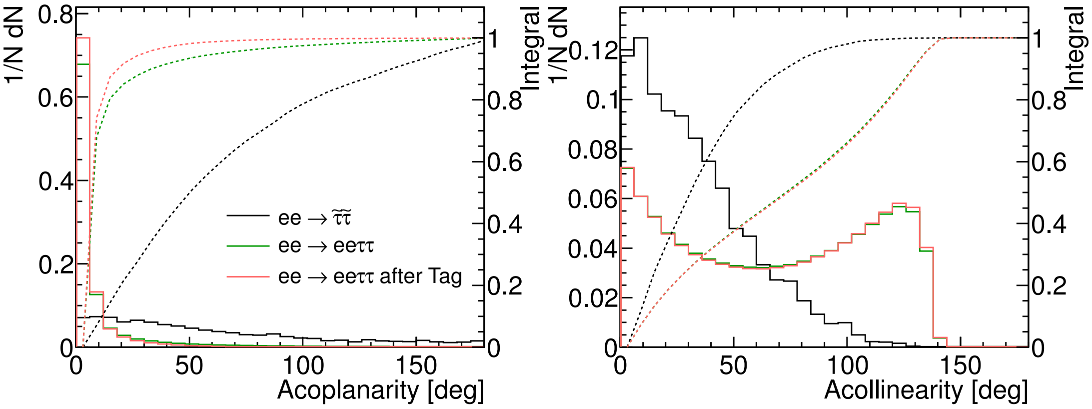

(a) Acoplanarity

(b) Acollinearity

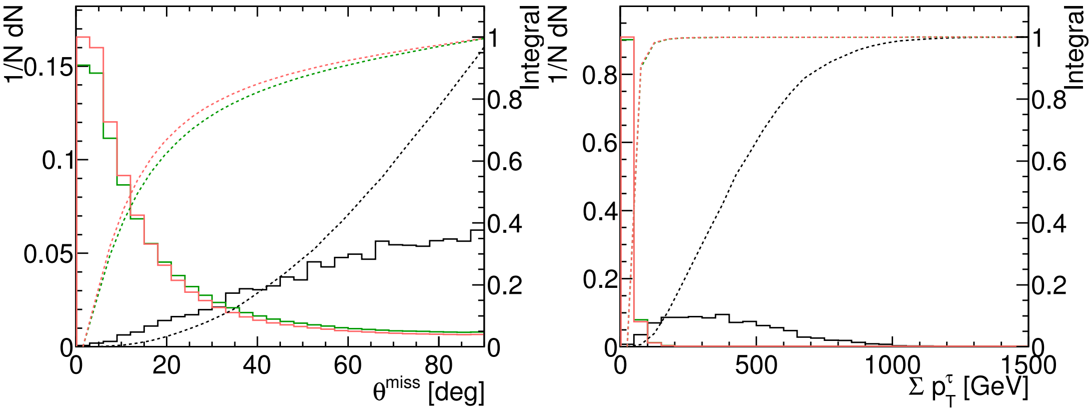

(c) Angle of missing momentum

(d) Sum of p_T

Figure 9.6: Distribution of the variables used for the selection cuts. Shown are the relative (solid lines) and cumulative (dashed lines) distributions of the $e^+e^- \to e^+e^-\tau\tau$ process before and after the electron tagging and the $e^+e^- \to \tilde{\tau}^+\tilde{\tau}^-$ process.

Table 9.1: Number of selected events for an integrated luminosity of 1 ab^{-1} from the $e^+e^- \to \tilde{\tau}^+\tilde{\tau}^-$ and $e^+e^- \to e^+e^-\tau\tau$ process with and without different selection cuts (see text). For the two-photon events the selected events before and after the electron tag are given.

		$e^+e^- \to e^+e^-\tau\tau$	
Cut	$e^+e^- \to \tilde{\tau}^+\tilde{\tau}^-$	Before electron tag	After electron tag
Without cuts	1261	2914251	2643332
Acollinearity	1139	1465347	1317124
Acoplanarity	1125	675960	432541
Angle of missing momentum	1133	683375	531055
Angular cuts combined	956	228218	117956
Sum of transverse momenta	1186	40345	34293
All cuts combined	902	864	47

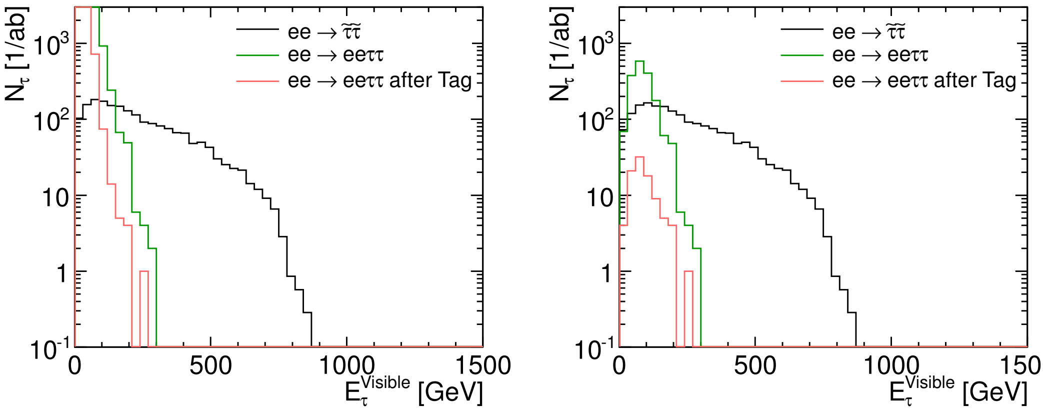

(a) Angular cuts combined

(b) All cuts combined

Figure 9.7: Distribution of the visible energy of the τ-leptons after the application of all the selection cuts described in the text. For the two-photon events the selected events before and after the electron tag are shown as well.

10 Summary, Conclusions, and Outlook

The small beam sizes and large energies at the CLIC interaction point create a huge number of background particles through different processes. The coherently produced particles are big in numbers, but they are safely transported out of the detector region. The incoherently produced electrons, positrons, and hadrons, however, will cause background in the detector: Some by directly transversing the tracking detectors and showering in the calorimeters, others through the production of secondary particles, which scatter into almost all subdetectors at varying rates.

An optimisation has been performed to reduce backscatters into the vertex detector. The design of the BeamCal absorbers was improved, which provided a reduction of the number of hits of about 25%. Based on this improvement the material and thickness of the beam pipe was optimised to reduce the amount of backscattering. For the final background studies in the various subdetectors a conical beam pipe made of 4 mm thick iron was chosen, leading to a reduction of the number of hits from backscattering particles by an order of magnitude compared to the initial layout. The overall hit density distributions are flat over the azimuthal angle and length of the detector.

The hit density incoherent e^+e^- pairs in the first layer of vertex detector from was found to be $6 \cdot 10^{-3}$ Hits/mm^2/BX. The particles from the $\gamma\gamma \to$ hadron events cause an average hit density of $0.7 \cdot 10^{-3}$ Hits/mm^2/BX in this layer. Assuming a pixel size of 20×20 µm^2, an average of three pixels per hit, and safety factors of five for incoherent pairs and two for the $\gamma\gamma \to$ hadron events a maximum occupancy of 2% in the vertex detector is found. This occupancy can be handled by a sensor and readout electronics with time-stamping of the order of 10 ns, but it does not require multi-hit capability [4].

For comparison, in the first layer of the ILD vertex detector (with $R = 15$ mm) at the 500 GeV ILC hit densities from $3 \cdot 10^{-2}$ Hits/mm^2/BX to $9 \cdot 10^{-2}$ Hits/mm^2/BX caused by incoherent e^+e^- pairs were found, depending on the beam parameters [7, 8]. The rate at the ILC is less critical, since the bunch spacing is much longer than at CLIC.

For subdetectors at larger radii the hit density becomes smaller, but not small enough to allow for the original design of silicon inner tracker ($R \approx 300$ mm) with 9 cm long strips. Shorter strips or multi-hit time-stamping capable sensors, or both, are necessary. The silicon external tracker at a radius $R \approx 1.8$ m with 44 cm long strips would have an occupancy of about 17%, requiring either shorter strips or time-stamping, as well.

The inner Forward Tracking Disks (FTDs) would suffer from similar hot spots than the vertex detector from backscattering particles induced by the showers from incoherent e^+e^- pairs. Also in this case the iron beam pipe reduces the hit density from backscattering particles.

The high occupancies in the FTDs will require that one more disk than originally planned be equipped with pixel readout. In the pixel FTDs the occupancies per bunch train are estimated to be between 0.6% and 2.8%. In the strip FTDs occupancies between 290% and 80% per train are found, therefore time-stamping and multi-hit capable readout is necessary. The maximum occupancy in the endcap tracking disks of 77% will require a similar readout.

The expected radiation exposure from non-ionising energy loss and total ionising dose has been estimated for the silicon pixel and strip detector regions. The non-ionising energy loss damage is dominated by particles from $\gamma\gamma \to$ hadron events and the equivalent neutron flux reaches up to $1.5 \cdot 10^{10}$ $\mathrm{n_{eq}/cm^2/yr}$ in the inner vertex layers. The total ionising dose is dominated by incoherent pairs and reaches up to 45 Gy/yr in the inner vertex layers. The radiation falls with increasing radius down to $7 \cdot 10^{8}$ $\mathrm{n_{eq}/cm^2/yr}$ and 0.6 Gy/yr in the SIT at $R \approx 300$ mm, and in the SET at $R \approx 1.8$ m about $2 \cdot 10^{8}$ $\mathrm{n_{eq}/cm^2/yr}$ and 6 mGy/yr. The numbers for the radiation are given without safety factors.

In comparison, for the 500 GeV ILC a total ionising dose of 170 Gy/yr and an equivalent neutron flux of $2 \cdot 10^{10}$ $\mathrm{n_{eq}/cm^2/yr}$ from incoherent e^+e^- pairs have been estimated in the innermost vertex layer ($R = 15$ mm) [106], about the same level of radiation as was found for the CLIC vertex detector, even combining incoherent e^+e^- pairs and $\gamma\gamma \to$ hadron events. Therefore, it should be possible to use sensors with radiation tolerances at CLIC, that are similar to the radiation tolerances required for the ILC. Radiation levels from $\gamma\gamma \to$ hadron events in the vertex detector have not been studied at the ILC so far [53]; however, the rate of $\gamma\gamma \to$ hadron events is known to be lower at the ILC than at CLIC.

For the ATLAS detector at the nominal 14 TeV LHC the radiation levels in the innermost pixel barrel ($R = 5$ cm) are expected to be $2.7 \cdot 10^{14}$ $\mathrm{n_{eq}/cm^2/yr}$ and 158 kGy/yr coming from minimum bias QCD interactions [107], these radiation levels are orders of magnitude above the expected radiation levels at a 3 TeV CLIC.

The largest occupancy in the electromagnetic calorimeter endcap is caused by the particles from $\gamma\gamma \to$ hadron events. The occupancy stays below 0.5 readout windows per pad and train for $\gamma\gamma \to$ hadron events and 0.2 readout windows per pad and train for incoherent pairs.

In the Hadronic Calorimeter (HCal) endcap the dominant contribution to the occupancy is coming from neutrons, which are produced by incoherent e^+e^- pairs in the BeamCal. At the innermost radius, ten out of twelve readout windows see an energy deposit per train. At $R = 0.6$ m the rate has fallen to one deposit per pad and train. The occupancy in the HCal endcap can be reduced with smaller pad sizes, but it also has to be studied, whether the endcap can be shielded better from the neutrons coming from the BeamCal.

The impact of the $\gamma\gamma \to$ hadron background on the particle flow reconstruction was studied with physics benchmarks for the conceptual design report. It was shown that precise measurements can be obtained, despite the challenging background [4]. Increasing the $\gamma\gamma \to$ hadron backgrounds by a factor of two, to allow for uncertainties in the simulation, only mildly affects the jet energy resolution with particle flow [62]. If, in a future detector layout, the impact from the incoherent e^+e^- pairs in the HCal can be reduced to a level similar to or below the $\gamma\gamma \to$ hadron events, they should not significantly reduce the precision of measurements at CLIC.

Each of the two BeamCal detectors is hit by several thousand incoherent e^+e^- pairs with a total energy of 33 TeV in every bunch crossing. The maximal Total Ionising Dose (TID), at the inner radius, is around 1 MGy/yr, and the maximal equivalent neutron flux is $2 \cdot 10^{13}$ $\mathrm{n_{eq}/cm^2/yr}$. The radiation levels in the BeamCal at CLIC and the ILC are very similar, so that the same radiation hard sensor technology can be used. However, the readout electronics will be different due to the much shorter bunch spacing at CLIC.

The identification of high energy electrons in the BeamCal was studied taking some imperfections for the beam collisions into account. It will be possible to identify high energy electrons on top of the incoherent e^+e^- pair background in the BeamCal at CLIC. Even with severe cuts on the deposited energies, to reduce the fake rate, and a rather long readout window of 40 BX, essentially all high energy electrons down to an energy of 500 GeV can be identified above 22 mrad with some geometrical inefficiencies due to the crossing angle and the incoming beam pipe. Between 10 mrad and 22 mrad the efficiency greatly depends on the energy of the electron. For 1.5 TeV electrons an efficiency higher than 80% up to 12 mrad, and 95% and better above 12 mrad was found. For 1.0 TeV electrons the efficiency is better than 95% above 14 mrad, and better than 99% from 17 mrad onwards. The electron tagging—together with several selection cuts using the full detector information—benefits the reduction of the two-photon backgrounds in the search for supersymmetric slepton pairs.

10.1 Outlook and Future Work

The occupancies and radiation levels in most of the subdetectors directly depend on the rate of the background processes, which in turn depend on the beam parameters. Changes in the beam parameters due to accelerator optimisation have to be closely monitored, and the backgrounds in the detector will have to be re-evaluated, if the rate of background particles, or their distributions changes significantly. As an example, at the ILC the background rate doubled with a changed set of beam parameters following a re-optimisation of the accelerator [8].

Since the detector model was designed for a maximal centre-of-mass energy of 3 TeV, it might be necessary to redesign the layout, especially of the vertex detector and very forward region, once the preferred centre-of-mass energy, based on the LHC results, is known.

A redesign of the very forward region, especially of the support tube and materials used for shielding is required to reduce the large impact on the HCal endcaps by the neutrons from incoherent e^+e^- pairs in the BeamCal. At the same time cavern and accelerator tunnel walls can be added in the simulation, to reduce the number of particles scattering into the back of the yoke endcaps, all the while making sure that the background conditions in the inner detector do not deteriorate.

For the estimate of the occupancies in the vertex and tracking detectors, only an average number of pixels per hit was used in this thesis. Detailed simulation of the digitisation of the charge deposit and sharing between pixels or strips should be done for a more realistic estimate of the occupancies. This can also take differences in sensor technologies and time-stamping windows into account. The estimated occupancies and radiation levels can be used as an input to the design and testing of possible sensors for a CLIC detector.

The BeamCal detector appears to be able to handle the CLIC background conditions, and can also bring benefit to physics analyses. Even if the envisioned readout windows of 20 BX (10 ns) in [96] cannot be reached, A background of 40 BX still allows for a reasonable high energy electron identification efficiency. The identification efficiency can probably be increased with more relaxed energy cuts, depending on the requirements of physics analysis. The pad structure could also be modified, to change the alignment of the pads from layer to layer, which could increase the efficiency to identify electron showers currently split between two rings.

A Background Generation using GUINEAPIG

Initial background samples were provided by Barbara Dalena (incoherent pairs, coherent pairs, radiative Bhabha events), Jakob Esberg (trident pairs, incoherent muons), and Daniel Schulte ($\gamma\gamma \rightarrow$ hadron events).

Additional samples for larger statistical samples and for non-nominal collisions (i.e., with vertical offsets) were self-produced with GUINEAPIG.

Normally the primary distribution of particles in the bunches will be done by GUINEAPIG based on the parameters given in the parameters. However the CLIC beams are not completely Gaussian (see Figure A.1a), and to take into account the distribution that can be expected for CLIC—including correlations between the positions and the energies of the particle (Figure A.1b)—particle distributions coming from the simulation of the main linac and the BDS [24] have to be used instead. These files can be found at `http://clic-beam-beam.web.cern.ch/clic-beam-beam/prod_3TeV_2010_Aug/beam_profiles/`. The files are loaded if the parameter `load_beams=3` is used. The parameters used for the production are:

```
$ACCELERATOR::default
{
energy=1500.0;particles=0.372;
beta_x=8.0;beta_y=0.15;
emitt_x=0.68;emitt_y=0.02;
sigma_z=45;espread=0.001;dist_z=0;waist_y=0;
f_rep=50.0;n_b=312;
offset_y=0.5*Offset;
}
$PARAMETERS::default
{
n_x=128;n_y=256;n_z=25;n_t=1;n_m=150000;load_beam=3;
cut_x=400.0;cut_y=15.0;cut_z=3.0*sigma_z.1;
grids=7;angle_y=0.5*0.0;force_symmetric=0;electron_ratio=1;
rndm_seed=SEED;
do_photons=1;store_photons=1;
do_coherent=1;store_beam=1;
do_pairs=1;track_pairs=1;store_pairs=1;
do_compt=0;photon_ratio=1;
ecm_min=2970.0;photon_ratio=1;hist_ee_bins=1010;
hist_ee_max=2.02*energy.1;charge_sign=-1.0;
}
```

For collisions with vertical offsets the variable `Offset` is set to the desired value in nanometre. GUINEAPIG will then move one side down by half this value and the other one by the same amount, thus resulting in the desired offset between the two beams. The vertical grid size (`cut_y`) also has to be increased to fully contain the bunches. The random seed `SEED` was to different values to run the program in parallel.

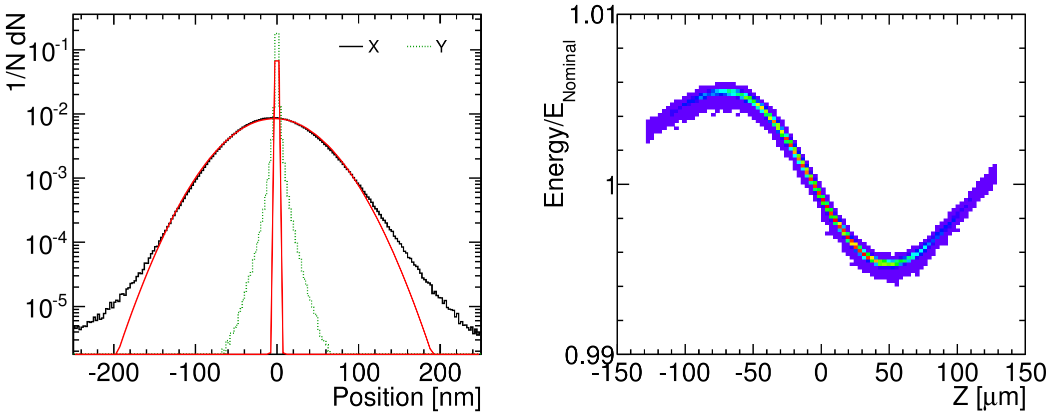

(a) Position in X and Y

(b) Position in Z vs. energy.

Figure A.1: (a) Horizontal and vertical distribution of the particles in the CLIC beams from the simulation of the main linac. Also plotted are Gaussian fits to the distribution.(b) Longitudinal position of the particles and energy relative to the nominal beam energy of 1.5 TeV.

B Tables: Hit Density, Equivalent Neutron Flux and Total Ionising Dose for the FTDs

The tables in this appendix contain the hit density, equivalent neutron flux, and total ionising dose in the forward tracking disks, without safety factors.

Table B.1: First disk doublet at $Z = 160$ mm.

Radius [m]	Hit Density $[10^{-3}/\mathrm{mm}^2/\mathrm{BX}]$		Flux $[10^9\ \mathrm{n_{eq}}/\mathrm{cm}^2/\mathrm{yr}]$		TID [Gy/yr]	
	Pairs	$\gamma\gamma$	Pairs	$\gamma\gamma$	Pairs	$\gamma\gamma$
33.56	6.57	0.77	6.17	5.64	27.99	3.10
35.29	5.25	0.70	4.85	5.11	22.74	2.76
37.03	4.19	0.66	3.76	4.86	18.76	2.77
38.76	3.45	0.61	3.42	4.34	15.15	2.46
40.49	2.99	0.57	3.13	4.05	13.19	2.37
42.23	2.62	0.54	2.97	3.84	11.14	2.36
43.96	2.16	0.51	2.17	3.64	10.01	2.23
45.69	1.88	0.46	2.03	3.33	8.72	2.08
47.42	1.53	0.43	1.96	3.08	6.64	1.91
49.16	1.24	0.39	1.97	2.90	5.34	1.83
50.89	1.11	0.36	1.59	2.75	5.45	1.71
52.62	1.05	0.33	1.78	2.63	4.77	1.63
54.35	0.89	0.31	1.29	2.45	4.59	1.45
56.09	0.74	0.29	1.15	2.34	3.51	1.50
57.82	0.74	0.28	1.37	2.24	3.68	1.59
59.55	0.60	0.26	0.95	2.14	2.83	1.34
61.28	0.58	0.24	1.18	2.02	2.64	1.25
63.02	0.57	0.23	0.94	1.91	2.87	1.30
64.75	0.47	0.22	1.09	1.83	2.06	1.23
66.48	0.40	0.21	1.32	1.78	2.30	1.21
68.21	0.38	0.19	0.89	1.72	2.30	1.06
69.95	0.30	0.18	1.07	1.61	1.36	1.04
71.68	0.30	0.17	1.17	1.58	1.38	0.98
73.41	0.26	0.16	1.04	1.47	1.19	0.99
75.14	0.20	0.15	1.08	1.41	0.99	0.93
76.88	0.28	0.15	1.13	1.40	1.45	0.92
78.61	0.22	0.14	0.71	1.31	1.02	0.82
80.34	0.19	0.14	1.19	1.32	1.17	0.86
82.08	0.17	0.13	0.95	1.26	0.96	0.83
83.81	0.17	0.12	0.96	1.21	0.81	0.79
85.54	0.11	0.12	0.78	1.18	0.83	0.82
87.27	0.13	0.11	0.99	1.14	0.75	0.74
89.01	0.13	0.11	0.87	1.11	0.65	0.70
90.74	0.14	0.10	1.28	1.08	0.76	0.69
92.47	0.11	0.10	1.12	1.05	0.64	0.67
94.20	0.11	0.09	0.84	1.01	0.61	0.68
95.94	0.11	0.09	0.98	1.02	0.61	0.70

Table B.2: Second disk doublet at $Z = 207$ mm.

Radius [m]	Hit Density [$10^{-3}/\text{mm}^2/\text{BX}$]		Flux [10^9 $\text{n}_{\text{eq}}/\text{cm}^2/\text{yr}$]		TID [Gy/yr]	
	Pairs	$\gamma\gamma$	Pairs	$\gamma\gamma$	Pairs	$\gamma\gamma$
33.56	7.38	0.80	6.72	5.79	29.25	2.96
35.29	5.84	0.72	5.49	5.27	23.85	3.01
37.03	4.54	0.67	4.34	4.81	18.42	2.82
38.76	3.87	0.64	4.04	4.45	15.90	2.60
40.49	3.14	0.57	3.05	4.08	13.36	2.47
42.23	2.69	0.55	2.97	3.82	12.27	2.36
43.96	2.42	0.51	2.63	3.57	10.61	2.14
45.69	2.12	0.47	2.48	3.41	8.90	2.04
47.42	1.66	0.44	1.86	3.22	7.33	1.87
49.16	1.45	0.40	2.00	2.98	6.29	1.80
50.89	1.15	0.37	2.03	2.81	5.07	1.72
52.62	1.07	0.34	1.42	2.71	4.79	1.62
54.35	0.95	0.32	1.37	2.56	4.08	1.59
56.09	0.90	0.30	1.40	2.46	3.71	1.37
57.82	0.79	0.29	1.19	2.35	3.41	1.56
59.55	0.65	0.27	1.54	2.22	3.02	1.43
61.28	0.54	0.25	0.93	2.11	2.29	1.24
63.02	0.54	0.24	0.93	2.01	2.51	1.13
64.75	0.56	0.23	1.29	1.96	2.38	1.26
66.48	0.46	0.21	1.31	1.87	2.17	1.16
68.21	0.38	0.20	0.97	1.75	1.73	1.12
69.95	0.38	0.19	1.23	1.74	1.96	1.03
71.68	0.33	0.18	1.26	1.68	1.79	1.11
73.41	0.30	0.17	1.03	1.60	1.93	0.97
75.14	0.29	0.16	1.16	1.54	1.33	0.91
76.88	0.27	0.15	1.26	1.50	1.27	0.95
78.61	0.27	0.15	1.05	1.42	1.33	0.93
80.34	0.22	0.14	0.97	1.36	1.17	0.85
82.08	0.17	0.14	1.19	1.32	0.85	0.87
83.81	0.16	0.13	1.06	1.30	0.72	0.81
85.54	0.15	0.13	1.09	1.25	0.84	0.77
87.27	0.13	0.12	0.92	1.26	0.63	0.80
89.01	0.15	0.12	0.89	1.16	0.78	0.82
90.74	0.15	0.11	1.03	1.13	0.73	0.73
92.47	0.13	0.11	0.96	1.13	0.64	0.70
94.20	0.11	0.10	0.92	1.08	0.60	0.66
95.94	0.12	0.10	0.95	1.05	0.60	0.67

Table B.3: Third disk doublet at $Z = 255$ mm.

Radius [m]	Hit Density $[10^{-3}/\mathrm{mm}^2/\mathrm{BX}]$		Flux $[10^9\ \mathrm{n_{eq}}/\mathrm{cm}^2/\mathrm{yr}]$		TID [Gy/yr]	
	Pairs	$\gamma\gamma$	Pairs	$\gamma\gamma$	Pairs	$\gamma\gamma$
33.56	8.66	0.81	7.83	6.14	34.12	3.13
35.29	6.59	0.74	5.94	5.63	26.21	2.96
37.03	5.22	0.68	5.08	5.14	20.71	2.76
38.76	4.21	0.64	4.16	4.79	16.73	2.73
40.49	3.44	0.62	3.33	4.50	13.79	2.76
42.23	3.02	0.56	3.02	4.14	12.09	2.62
43.96	2.49	0.53	3.14	3.95	10.36	2.36
45.69	2.23	0.49	2.43	3.68	9.12	2.19
47.42	1.83	0.45	2.47	3.42	7.66	2.26
49.16	1.53	0.41	2.21	3.20	6.44	1.84
50.89	1.32	0.38	2.06	3.05	5.84	1.80
52.62	1.27	0.34	2.18	2.84	5.81	1.52
54.35	1.04	0.32	1.52	2.72	4.50	1.50
56.09	1.06	0.31	1.70	2.62	4.69	1.49
57.82	0.84	0.29	1.40	2.47	3.44	1.48
59.55	0.76	0.27	1.37	2.32	3.13	1.42
61.28	0.56	0.25	1.23	2.17	3.01	1.24
63.02	0.54	0.25	1.06	2.14	2.39	1.24
64.75	0.51	0.23	1.41	2.05	2.72	1.15
66.48	0.47	0.22	1.50	1.98	1.96	1.15
68.21	0.45	0.21	1.53	1.90	2.07	1.07
69.95	0.33	0.20	0.99	1.89	1.56	1.04
71.68	0.39	0.19	1.28	1.76	1.63	1.00
73.41	0.29	0.18	0.88	1.67	1.41	0.91
75.14	0.31	0.17	0.94	1.61	1.46	0.96
76.88	0.28	0.16	1.16	1.56	1.24	0.90
78.61	0.25	0.16	1.31	1.51	1.14	1.01
80.34	0.23	0.15	1.12	1.49	0.90	0.90
82.08	0.19	0.14	1.16	1.41	0.91	0.87
83.81	0.20	0.14	1.37	1.32	0.91	0.80
85.54	0.17	0.13	0.88	1.33	0.87	0.71
87.27	0.18	0.13	1.09	1.29	0.84	0.76
89.01	0.15	0.12	0.83	1.24	0.69	0.76
90.74	0.14	0.12	1.05	1.20	0.67	0.77
92.47	0.12	0.11	0.82	1.14	0.52	0.74
94.20	0.14	0.11	0.98	1.15	0.70	0.70
95.94	0.13	0.11	1.01	1.13	0.79	0.69

Table B.4: Disk at $Z = 382$ mm.

Radius [m]	Hit Density $[10^{-3}/\mathrm{mm}^2/\mathrm{BX}]$		Flux $[10^9\ \mathrm{n_{eq}}/\mathrm{cm}^2/\mathrm{yr}]$		TID $[\mathrm{Gy}/\mathrm{yr}]$	
	Pairs	$\gamma\gamma$	Pairs	$\gamma\gamma$	Pairs	$\gamma\gamma$
48.49	2.57	0.94	2.94	4.58	8.63	3.49
51.69	1.75	0.63	2.25	3.83	5.90	2.52
54.89	1.24	0.47	1.79	3.32	4.28	1.83
58.10	0.91	0.38	1.56	2.98	3.20	1.64
61.30	0.72	0.32	1.42	2.67	2.65	1.38
64.50	0.63	0.27	1.46	2.42	2.25	1.18
67.70	0.47	0.24	1.20	2.21	1.60	1.18
70.91	0.37	0.21	1.04	2.05	1.38	1.05
74.11	0.35	0.19	1.17	1.90	1.29	0.98
77.31	0.32	0.18	1.09	1.77	1.17	0.86
80.52	0.23	0.17	1.14	1.67	0.90	0.87
83.72	0.20	0.15	1.22	1.55	0.81	0.86
86.92	0.15	0.14	1.22	1.44	0.62	0.80
90.12	0.15	0.13	1.09	1.34	0.61	0.73
93.33	0.15	0.12	0.96	1.28	0.64	0.68
96.53	0.16	0.12	0.65	1.23	0.64	0.65
99.73	0.12	0.11	0.97	1.18	0.47	0.62
102.94	0.10	0.10	1.12	1.13	0.43	0.61
106.14	0.08	0.10	1.03	1.07	0.30	0.57
109.34	0.08	0.09	0.95	1.01	0.31	0.53
112.54	0.07	0.09	1.24	0.97	0.27	0.54
115.75	0.07	0.08	0.87	0.93	0.26	0.51
118.95	0.06	0.08	0.94	0.88	0.23	0.51
122.15	0.07	0.08	0.91	0.85	0.34	0.52
125.36	0.07	0.07	0.94	0.81	0.29	0.49
128.56	0.05	0.07	1.05	0.78	0.19	0.42
131.76	0.05	0.07	1.01	0.75	0.21	0.41
134.96	0.05	0.06	0.91	0.73	0.19	0.42
138.17	0.05	0.06	1.10	0.71	0.22	0.38
141.37	0.05	0.06	1.11	0.69	0.22	0.39
144.57	0.05	0.06	1.05	0.67	0.20	0.40
147.78	0.04	0.05	1.01	0.63	0.20	0.38
150.98	0.04	0.05	0.81	0.64	0.18	0.34
154.18	0.05	0.05	0.89	0.61	0.22	0.36
157.38	0.04	0.05	0.89	0.60	0.15	0.35
160.59	0.04	0.05	1.06	0.59	0.19	0.34
163.79	0.04	0.05	0.96	0.55	0.17	0.32

Table B.5: Disk at $Z = 665$ mm.

Radius [m]	Hit Density [10^{-3}/mm^2/BX]		Flux [10^9 n$_{\mathrm{eq}}$/cm^2/yr]		TID [Gy/yr]	
	Pairs	$\gamma\gamma$	Pairs	$\gamma\gamma$	Pairs	$\gamma\gamma$
82.43	0.32	0.22	1.37	1.48	1.14	0.86
88.45	0.22	0.16	1.37	1.31	0.74	0.67
94.46	0.17	0.13	1.21	1.18	0.60	0.57
100.47	0.13	0.12	1.20	1.09	0.46	0.54
106.49	0.10	0.11	1.07	1.00	0.39	0.52
112.50	0.09	0.09	1.33	0.93	0.31	0.47
118.52	0.07	0.09	1.13	0.88	0.26	0.43
124.53	0.07	0.08	1.30	0.82	0.26	0.41
130.55	0.05	0.07	1.25	0.77	0.21	0.37
136.56	0.05	0.07	1.03	0.74	0.19	0.36
142.58	0.05	0.06	1.13	0.71	0.21	0.33
148.59	0.04	0.06	1.21	0.66	0.19	0.32
154.60	0.04	0.05	1.24	0.64	0.17	0.30
160.62	0.05	0.05	1.08	0.63	0.21	0.30
166.63	0.04	0.05	1.03	0.60	0.19	0.30
172.65	0.04	0.05	1.03	0.57	0.19	0.28
178.66	0.04	0.04	1.17	0.55	0.18	0.25
184.68	0.05	0.04	1.11	0.52	0.22	0.25
190.69	0.05	0.04	1.08	0.50	0.21	0.25
196.71	0.06	0.04	1.22	0.49	0.26	0.23
202.72	0.04	0.03	0.96	0.48	0.18	0.20
208.73	0.05	0.03	1.07	0.46	0.21	0.20
214.75	0.05	0.03	1.23	0.45	0.21	0.20
220.76	0.05	0.03	1.14	0.44	0.20	0.19
226.78	0.04	0.03	1.18	0.44	0.17	0.18
232.79	0.04	0.03	1.15	0.42	0.17	0.17
238.81	0.03	0.02	1.24	0.40	0.13	0.17
244.82	0.03	0.02	1.22	0.40	0.13	0.16
250.83	0.03	0.02	1.23	0.39	0.13	0.16
256.85	0.03	0.02	1.14	0.38	0.12	0.16
262.86	0.03	0.02	1.20	0.39	0.11	0.15
268.88	0.03	0.02	1.24	0.37	0.13	0.14
274.89	0.02	0.02	1.12	0.37	0.10	0.13
280.91	0.02	0.02	1.21	0.36	0.10	0.13
286.92	0.02	0.02	1.13	0.35	0.12	0.13
292.94	0.02	0.02	1.19	0.34	0.11	0.13
298.95	0.02	0.02	1.12	0.33	0.09	0.12

Table B.6: Disk at $Z = 1066$ mm.

Radius [m]	Hit Density $[10^{-3}/\text{mm}^2/\text{BX}]$		Flux $[10^9\ \text{n}_{\text{eq}}/\text{cm}^2/\text{yr}]$		TID [Gy/yr]	
	Pairs	$\gamma\gamma$	Pairs	$\gamma\gamma$	Pairs	$\gamma\gamma$
127.96	0.08	0.09	1.78	0.72	0.30	0.35
132.82	0.07	0.08	1.58	0.82	0.25	0.38
137.68	0.06	0.07	1.45	0.76	0.26	0.33
142.55	0.06	0.07	1.50	0.71	0.27	0.32
147.41	0.06	0.06	1.59	0.68	0.24	0.29
152.27	0.04	0.06	1.47	0.66	0.18	0.28
157.13	0.05	0.05	1.57	0.63	0.22	0.25
161.99	0.05	0.05	1.65	0.63	0.23	0.29
166.86	0.06	0.05	1.60	0.60	0.27	0.26
171.72	0.05	0.05	1.62	0.60	0.22	0.23
176.58	0.05	0.04	1.61	0.57	0.19	0.22
181.44	0.05	0.04	1.63	0.55	0.22	0.22
186.30	0.04	0.04	1.57	0.55	0.18	0.22
191.16	0.05	0.04	1.60	0.53	0.20	0.20
196.03	0.05	0.04	1.56	0.52	0.19	0.20
200.89	0.05	0.04	1.61	0.51	0.20	0.20
205.75	0.05	0.03	1.56	0.50	0.23	0.20
210.61	0.05	0.03	1.41	0.49	0.21	0.19
215.47	0.05	0.03	1.58	0.48	0.23	0.17
220.33	0.04	0.03	1.48	0.47	0.19	0.18
225.20	0.04	0.03	1.49	0.45	0.19	0.17
230.06	0.05	0.03	1.49	0.45	0.21	0.17
234.92	0.04	0.03	1.63	0.45	0.17	0.16
239.78	0.03	0.03	1.41	0.44	0.14	0.17
244.64	0.03	0.03	1.56	0.43	0.14	0.16
249.51	0.03	0.02	1.51	0.43	0.12	0.14
254.37	0.03	0.02	1.49	0.42	0.11	0.14
259.23	0.03	0.02	1.47	0.42	0.11	0.14
264.09	0.03	0.02	1.50	0.41	0.12	0.13
268.95	0.02	0.02	1.36	0.41	0.11	0.14
273.81	0.02	0.02	1.46	0.41	0.10	0.14
278.68	0.03	0.02	1.47	0.40	0.10	0.13
283.54	0.02	0.02	1.47	0.39	0.12	0.14
288.40	0.02	0.02	1.52	0.39	0.09	0.13
293.26	0.02	0.02	1.50	0.38	0.11	0.12
298.12	0.02	0.02	1.42	0.38	0.08	0.11
302.98	0.02	0.02	1.36	0.38	0.10	0.12

Table B.7: Disk at $Z = 1467$ mm.

Radius [m]	Hit Density $[10^{-3}/\mathrm{mm}^2/\mathrm{BX}]$		Flux $[10^9\ \mathrm{n_{eq}}/\mathrm{cm}^2/\mathrm{yr}]$		TID [Gy/yr]	
	Pairs	$\gamma\gamma$	Pairs	$\gamma\gamma$	Pairs	$\gamma\gamma$
173.52	0.06	0.05	2.42	0.65	0.27	0.22
177.23	0.06	0.05	2.50	0.68	0.25	0.24
180.93	0.06	0.05	2.83	0.71	0.26	0.22
184.64	0.06	0.05	2.38	0.70	0.28	0.21
188.35	0.05	0.04	2.20	0.67	0.21	0.19
192.06	0.06	0.04	2.55	0.64	0.28	0.21
195.77	0.06	0.04	2.36	0.65	0.26	0.20
199.48	0.07	0.04	2.40	0.62	0.27	0.18
203.18	0.06	0.04	2.35	0.61	0.25	0.18
206.89	0.06	0.03	2.31	0.61	0.24	0.17
210.60	0.06	0.03	2.38	0.60	0.26	0.17
214.31	0.05	0.03	1.99	0.59	0.24	0.17
218.02	0.06	0.03	2.28	0.58	0.25	0.16
221.73	0.06	0.03	2.13	0.59	0.25	0.16
225.44	0.05	0.03	2.02	0.58	0.21	0.16
229.14	0.04	0.03	2.36	0.57	0.19	0.15
232.85	0.05	0.03	2.09	0.57	0.19	0.15
236.56	0.03	0.03	2.15	0.56	0.14	0.15
240.27	0.04	0.03	2.08	0.56	0.16	0.15
243.98	0.03	0.03	2.18	0.55	0.15	0.14
247.69	0.03	0.03	2.31	0.54	0.12	0.14
251.39	0.03	0.03	2.05	0.55	0.12	0.14
255.10	0.02	0.02	2.11	0.54	0.11	0.13
258.81	0.02	0.02	2.11	0.54	0.11	0.13
262.52	0.03	0.02	2.07	0.54	0.15	0.13
266.23	0.02	0.02	1.92	0.53	0.09	0.12
269.94	0.02	0.02	2.01	0.53	0.10	0.12
273.64	0.03	0.02	2.07	0.52	0.10	0.13
277.35	0.03	0.02	1.91	0.52	0.12	0.12
281.06	0.02	0.02	2.19	0.51	0.12	0.12
284.77	0.02	0.02	1.81	0.51	0.12	0.13
288.48	0.02	0.02	2.13	0.50	0.10	0.11
292.19	0.02	0.02	2.03	0.50	0.08	0.11
295.90	0.02	0.02	1.89	0.50	0.10	0.12
299.60	0.02	0.02	1.85	0.49	0.09	0.12
303.31	0.02	0.02	2.02	0.49	0.08	0.10
307.02	0.02	0.02	1.92	0.49	0.08	0.11

Table B.8: Disk at $Z = 1868$ mm.

Radius [m]	Hit Density $[10^{-3}/\mathrm{mm}^2/\mathrm{BX}]$		Flux $[10^9\ \mathrm{n_{eq}}/\mathrm{cm}^2/\mathrm{yr}]$		TID [Gy/yr]	
	Pairs	$\gamma\gamma$	Pairs	$\gamma\gamma$	Pairs	$\gamma\gamma$
219.04	0.06	0.03	3.89	0.92	0.27	0.14
221.60	0.07	0.03	3.58	0.91	0.29	0.16
224.16	0.06	0.03	3.44	0.88	0.25	0.15
226.71	0.06	0.03	3.59	0.92	0.27	0.14
229.27	0.05	0.03	3.71	0.92	0.20	0.16
231.82	0.05	0.03	3.49	0.92	0.27	0.15
234.38	0.04	0.03	3.23	0.91	0.20	0.15
236.94	0.05	0.03	3.50	0.89	0.20	0.13
239.49	0.04	0.03	3.36	0.88	0.17	0.16
242.05	0.03	0.03	3.33	0.87	0.13	0.17
244.60	0.03	0.03	3.12	0.87	0.16	0.15
247.16	0.03	0.03	3.05	0.88	0.13	0.15
249.71	0.03	0.03	3.00	0.86	0.11	0.13
252.27	0.02	0.03	2.83	0.85	0.11	0.13
254.83	0.02	0.03	2.81	0.85	0.11	0.13
257.38	0.02	0.03	2.90	0.84	0.09	0.13
259.94	0.02	0.02	2.74	0.84	0.12	0.13
262.49	0.02	0.02	2.76	0.83	0.10	0.12
265.05	0.02	0.02	2.70	0.83	0.08	0.13
267.61	0.02	0.02	2.45	0.82	0.07	0.13
270.16	0.02	0.02	2.50	0.80	0.10	0.12
272.72	0.02	0.02	2.49	0.80	0.09	0.12
275.27	0.01	0.02	2.17	0.80	0.06	0.12
277.83	0.02	0.02	2.11	0.79	0.09	0.11
280.38	0.01	0.02	2.06	0.80	0.06	0.12
282.94	0.02	0.02	1.96	0.78	0.08	0.11
285.50	0.02	0.02	1.84	0.78	0.06	0.11
288.05	0.01	0.02	1.84	0.77	0.06	0.12
290.61	0.01	0.02	1.96	0.79	0.06	0.11
293.16	0.01	0.02	1.78	0.77	0.07	0.11
295.72	0.01	0.02	1.74	0.76	0.05	0.10
298.28	0.01	0.02	1.76	0.76	0.05	0.11
300.83	0.01	0.02	1.69	0.76	0.05	0.11
303.39	0.01	0.02	1.51	0.75	0.05	0.10
305.94	0.01	0.02	1.58	0.74	0.04	0.10
308.50	0.01	0.02	1.67	0.76	0.07	0.11
311.06	0.01	0.02	1.56	0.74	0.05	0.11

C Table: Hit Density, Equivalent Neutron Flux and Total Ionising Dose for the ETDs

The table in this appendix contains the hit density, equivalent neutron flux, and total ionising dose in the endcap tracking disks, without safety factors.

Table C.1: Hit density, equivalent neutron flux and total ionising dose in the ETDs for incoherent pairs and $\gamma\gamma \rightarrow$ hadrons.

Radius [m]	Hit Density [10^{-6}/mm^2/BX]		Flux [10^9 n$_{\mathrm{eq}}$/cm^2/yr]		TID [mGy/yr]	
	Pairs	$\gamma\gamma$	Pairs	$\gamma\gamma$	Pairs	$\gamma\gamma$
0.59	6.78	10.33	0.20	6.78	23.52	45.91
0.66	5.78	8.03	0.17	5.37	19.72	36.78
0.72	5.75	6.26	0.16	4.36	22.67	29.38
0.78	5.80	4.92	0.16	3.44	20.24	22.11
0.84	5.05	3.91	0.16	2.71	17.94	17.65
0.91	4.85	3.21	0.16	2.36	17.33	14.81
0.97	4.40	2.70	0.15	1.98	15.60	12.86
1.03	3.78	2.19	0.13	1.39	13.89	9.60
1.10	3.15	1.80	0.13	1.14	10.99	8.20
1.16	2.21	1.50	0.10	0.88	7.92	6.77
1.22	2.03	1.34	0.09	0.86	7.13	5.85
1.29	1.57	1.14	0.08	0.61	5.26	5.44
1.35	1.44	0.99	0.07	0.51	4.73	4.68
1.41	1.31	0.87	0.07	0.42	4.37	3.76
1.48	1.34	0.76	0.06	0.34	5.09	3.22
1.54	1.01	0.71	0.05	0.28	3.43	3.11
1.60	0.95	0.63	0.05	0.29	3.46	2.87
1.66	0.82	0.56	0.05	0.25	2.82	2.40
1.73	0.71	0.52	0.05	0.20	2.98	2.19
1.79	0.80	0.51	0.04	0.16	3.27	2.10

D Figures: Electron Identification Efficiencies in the BeamCal

The electron identification efficiency with 40 BX of the mixed incoherent e^+e^- pair background are shown in this appendix. Figures D.1 and D.2 show the efficiencies in the truncated region of the BeamCal excluding the sector with the incoming beam pipe and the inner and outer edge. Figures D.3 and D.4 show the efficiencies for the full BeamCal.

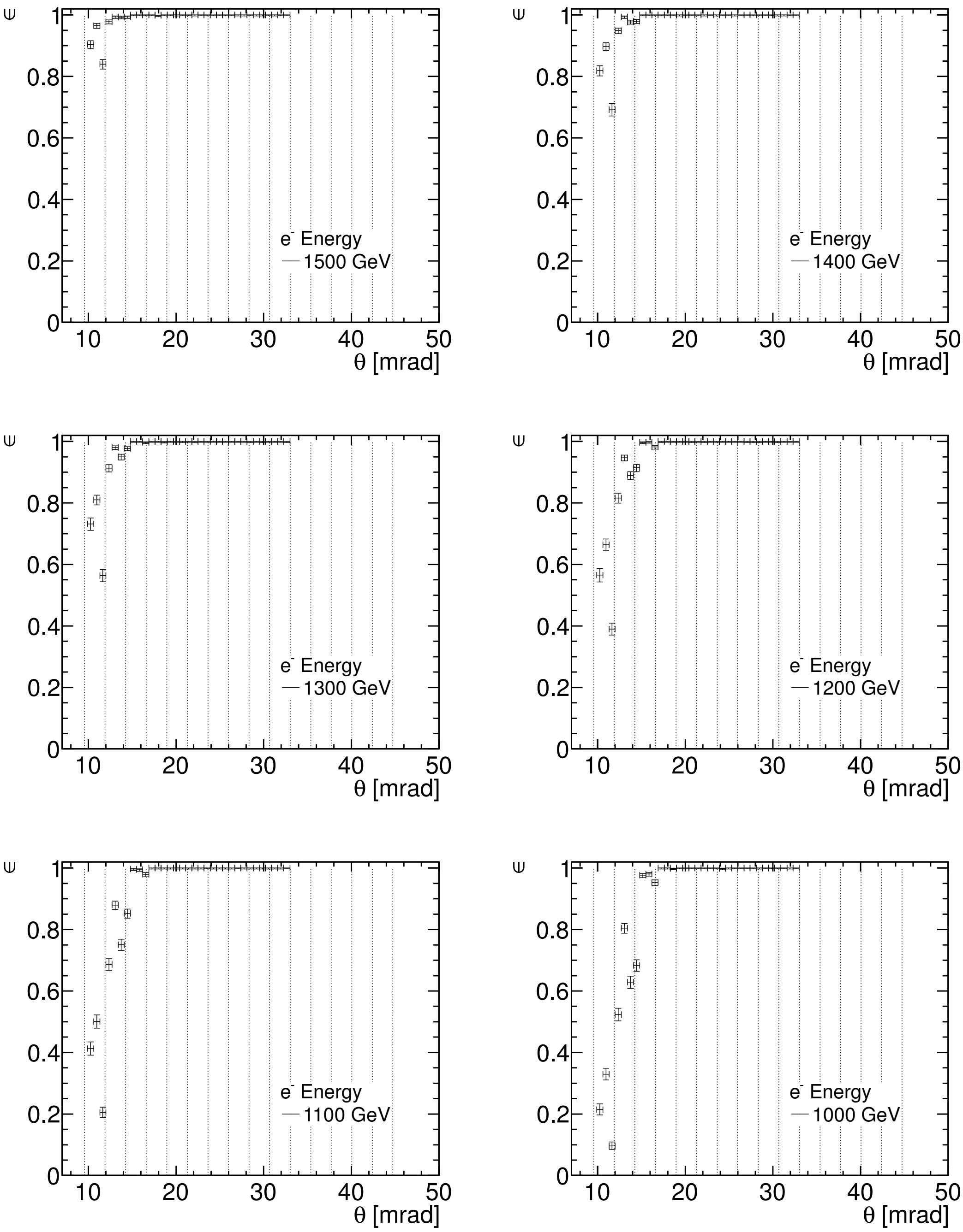

Figure D.1: Electron tagging efficiency in the truncated region of the BeamCal for electrons with an energy between 1500 GeV and 1000 GeV with 40 BX of incoherent e^+e^- pair background.

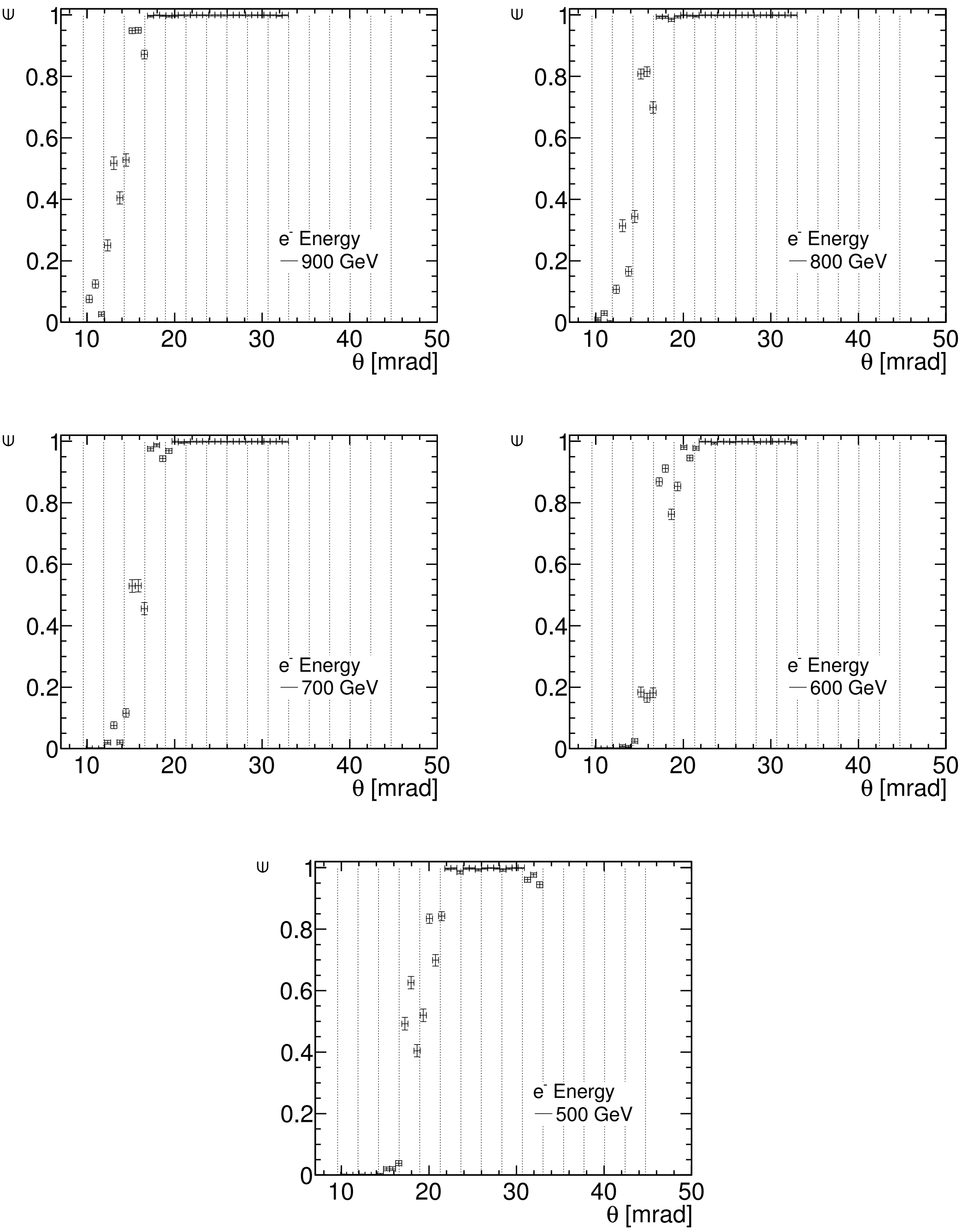

Figure D.2: Electron tagging efficiency in the truncated region of the BeamCal for electrons with an energy between 900 GeV and 500 GeV with 40 BX of incoherent e^+e^- pair background.

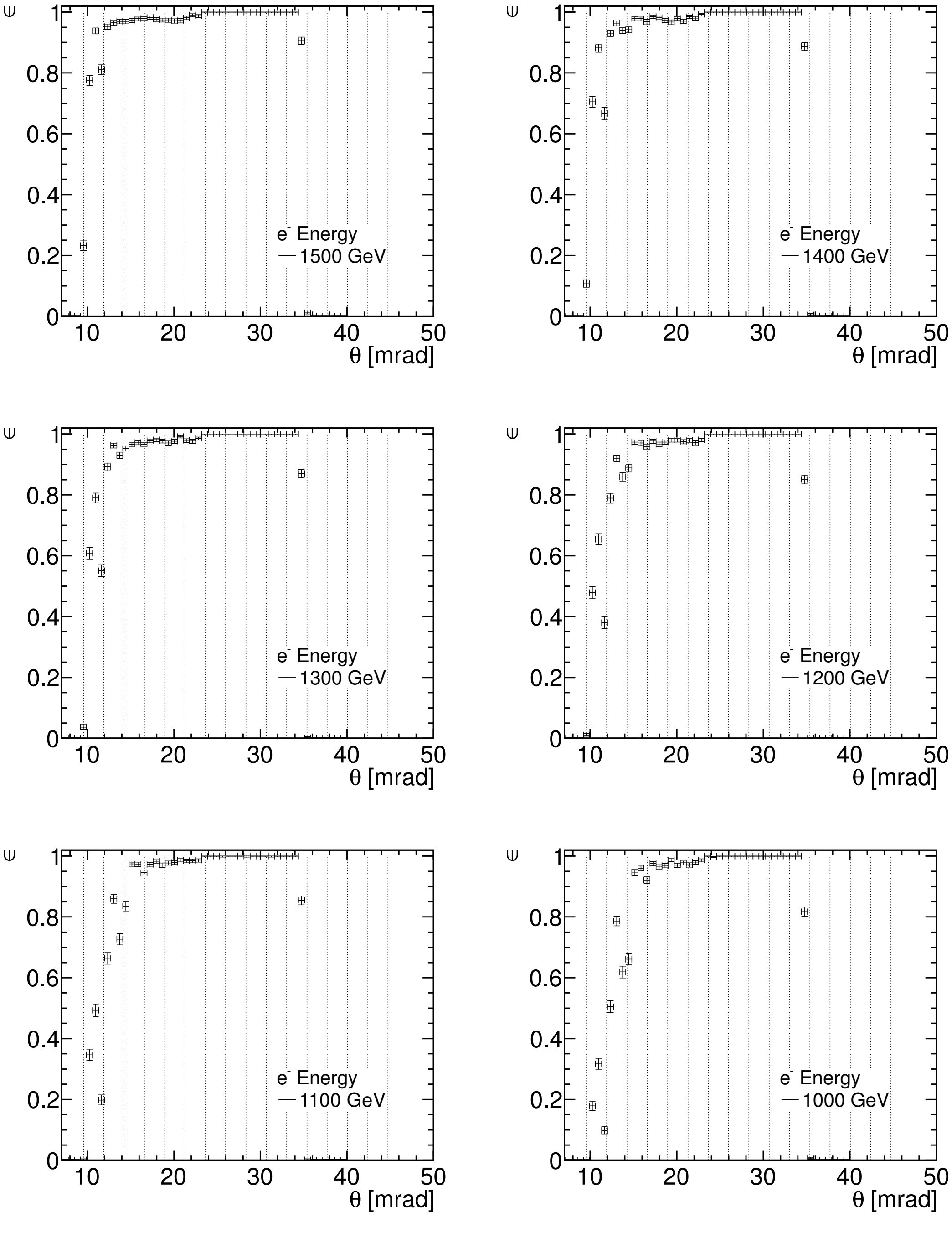

Figure D.3: Electron tagging efficiency in the full BeamCal for electrons with an energy between 1500 GeV and 1000 GeV with 40 BX of incoherent e^+e^- pair background.

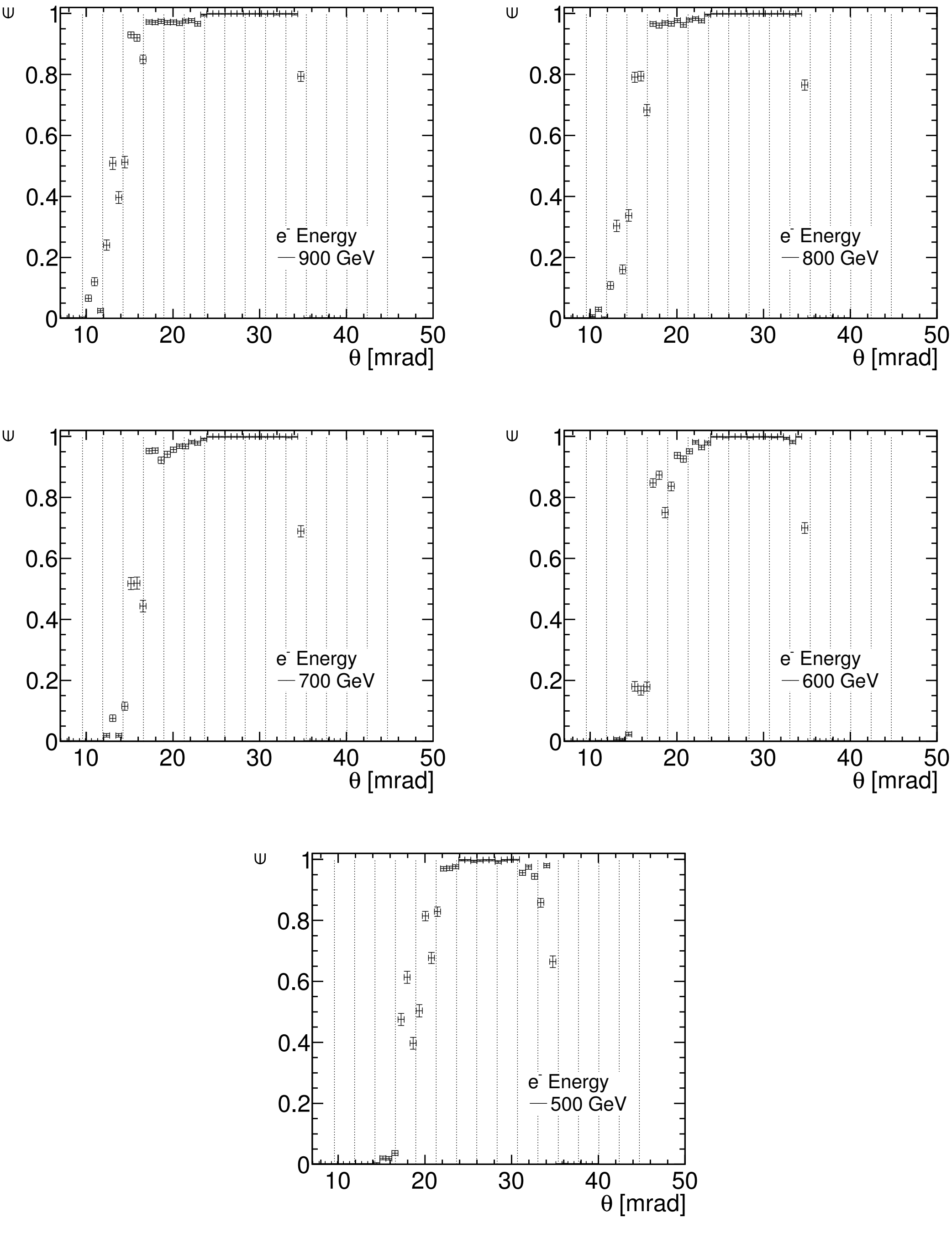

Figure D.4: Electron tagging efficiency in the full BeamCal for electrons with an energy between 900 GeV and 500 GeV with 40 BX of incoherent e^+e^- pair background.

List of Figures

List of Tables

References

[1] O. Brüning, P. Collier, P. Lebrun, S. Myers, R. Ostojic, J. Poole, and P. Proudlock, editors. *LHC Design Report: Volume 1, The LHC Main Ring*. CERN, Geneva, 2004. CERN-2004-003-V-1.

[2] ATLAS Collaboration, G. Aad, et al. Combined search for the Standard Model Higgs boson using up to 4.9 fb^{-1} of pp collision data at $\sqrt{s} = 7$ TeV with the ATLAS detector at the LHC. *Phys. Lett. B*, 710(1):49–66, 2012. arXiv:1202.1408. CERN-PH-EP-2012-019.

[3] CMS Collaboration, S. Chatrchyan, et al. Combined results of searches for the Standard Model Higgs boson in pp collisions at $\sqrt{s} = 7$ TeV. *Phys. Lett. B*, 710(1):26–48, 2012. CMS-HIG-11-032. arXiv:1202.1488v1.

[4] CLIC Detector Study, L. Linssen, A. Miyamoto, M. Stanitzki, and H. Weerts, editors. *Physics and Detectors at CLIC: CLIC Conceptual Design Report*. CERN, 2012. CERN-2012-003.

[5] H. Schmickler, P. Lebrun, N. Toge, N. Phinney, T. Garvey, P. Burrows, M. Draper, and M. Aicheler, editors. *A Multi-TeV Linear Collider based on CLIC technology: CLIC Conceptual Design Report*. CERN, 2012. To be published.

[6] J. Brau et al., editors. *ILC Reference Design Report Volume 1 – Executive Summary*. ILC, 2007. arXiv:0712.1950.

[7] A. Vogel. *Beam-Induced Backgrounds in Detectors at the ILC*. PhD thesis, Universität Hamburg, 2008. DESY-THESIS-2008-036.

[8] K. Wichmann. Beam backgrounds: Simulation & effects on reconstruction at ILD. In *International Workshop on Linear Colliders (LCWS 2010)*, Beijing, China, 2010.

[9] H. Padamsee. *RF Superconductivity: Science, Technology, and Applications*. Wiley-VCH Verlag GmbH & Co. KGaA, Weinheim, 2009.

[10] K. Nakamura et al. Review of particle physics, 2010-2011. review of particle properties. *J. Phys. G*, 37(7A):075021, 2010.

[11] H. Braun et al. CLIC 2008 parameters. Technical report, CERN, Oct 2008. CLIC-NOTE-764.

[12] A. Vorozhtsov, M. Modena, and D. Tommasini. Design and manufacture of a hybrid final focus quadrupole model for CLIC. Technical Report CERN-ATS-2012-020, CERN, Feb 2012.

[13] D. Schulte and F. Zimmermann. The crossing angle in CLIC. In *19th IEEE Particle Accelerator Conference*, Chicago, IL, July 2001. CLIC-Note-484. oai:cds.cern.ch:509990.

[14] P. Chen. Beamstrahlung and the QED, QCD backgrounds in linear colliders. In *9th International Workshop on Photon-photon Collisions*, La Jolla, CA, USA, Mar 1992. SLAC-PUB-5914.

[15] D. Schulte. Beam-beam simulations with GUINEA-PIG. In *5th International Computational Accelerator Physics Conference*, Monterey, CA, USA, Sept 1998. CLIC-NOTE 387.

[16] K. Yokoya and P. Chen. Beam-beam phenomena in linear colliders. In M. Dienes, M. Month, and S. Turner, editors, *Frontiers of Particle Beams*, volume 400 of *Lecture Notes in Physics, Berlin Springer Verlag*, 1992. KEK-91-2.

[17] P. Chen. An introduction to beamstrahlung and disruption. In M. Month and S. Turner, editors, *Frontiers of Particle Beams*, volume 296 of *Lecture Notes in Physics, Berlin Springer Verlag*, pages 495–532, 1988. SLAC-PUB-4379.

[18] P. Chen and K. Yokoya. Disruption effects from the interaction of round e^+e^- beams. *Phys. Rev. D*, 38:987–1000, Aug 1988. doi: 10.1103/PhysRevD.38.987. URL `http://link.aps.org/doi/10.1103/PhysRevD.38.987`.

[19] J. Schwinger. The quantum correction in the radiation by energetic accelerated electrons. *Proc. Natl. Acad. Sci.*, 40(2):132–136, 1954. URL `http://www.pnas.org/content/40/2/132.full.pdf+html`.

[20] R. J. Noble. Beamstrahlung from colliding electron-positron beams with negligible disruption. *Nucl. Instrum. Methods Phys. Res., Sect. A*, 256(3):427–433, 1987. ISSN 0168-9002. doi: 10.1016/0168-9002(87)90284-1. URL `http://www.sciencedirect.com/science/article/pii/0168900287902841`. SLAC-PUB-3871.

[21] K. Yokoya. *User's Manual of CAIN. Version 2.35.* KEK, 2003. `http://lcdev.kek.jp/~yokoya/CAIN/cain235/`.

[22] D. Schulte. *Study of Electromagnetic and Hadronic Background in the Interaction Region of the TESLA Collider.* PhD thesis, Universität Hamburg, Hamburg, 1997. Presented on Apr 1997. oai:cds.cern.ch:331845.

[23] P. Bambade et al. Results of the EUROTeV beam-beam simulation (BBSIM) task. Technical report, EUROTev, 2008. EUROTeV-Report-2008-065.

[24] D. Schulte et al. CLIC simulations from the start of the linac to the interaction point. In *8th European Particle Accelerator Conference*, Paris, France, July 2002. oai:cds.cern.ch:572820. CLIC-Note-529.

[25] P. Chen and V. Telnov. Coherent pair creation in linear colliders. *Phys. Rev. Lett.*, 63(17): 1796–1799, 1989.

[26] J. Esberg. Simulations of the interaction point for TeV-scale e^+e^- colliders. In *2nd International Particle Accelerator Conference (IPAC)*, San Sebastián, Spain, Sept 2011.

[27] B. Dalena, J. Esberg, and D. Schulte. Beam-induced backgrounds in the CLIC 3 TeV cm energy interaction region. In *International Workshop on Linear Colliders (LCWS)*, Granada, Spain, Oct 2011. arXiv:1202.0563.

[28] P. Chen, T. Tauchi, and D. V. Schroeder. Pair creation at large inherent angles. In *5th DPF Summer Study on High-energy Physics: Research Directions for the Decade (Snowmass 90)*, Snowmass, CO, USA, June 1990. SLAC-PUB-12486.

[29] M. Berggren. Private communication.

[30] M. Battaglia, A. de Roeck, J. R. Ellis, and D. Schulte, editors. *Physics at the CLIC Multi-TeV Linear Collider: Report of the CLIC Physics Working Group*. CERN, Geneva, 2004. CERN-2004-005.

[31] M. Drees and R. M. Godbole. Minijets and large hadronic backgrounds at e^+e^- supercolliders. *Phys. Rev. Lett.*, 67(10):1189–1192, Sept 1991. doi: 10.1103/PhysRevLett.67.1189.

[32] P. Chen, T. L. Barklow, and M. E. Peskin. Hadron production in $\gamma\gamma$ collisions as a background for e^+e^- linear colliders. *Phys. Rev. D*, 49(7):3209–3227, Apr 1994. doi: 10.1103/PhysRevD.49.3209. hep-ph/9305247. SLAC-PUB-5873.

[33] L3 Collaboration, M. Acciarri, et al. Total cross section in $\gamma\gamma$ collisions at LEP. *Phys. Lett. B*, 519(1–2):33–45, 2001. ISSN 0370-2693. doi: 10.1016/S0370-2693(01)01072-3. URL `http://www.sciencedirect.com/science/article/pii/S0370269301010723`.

[34] OPAL collaboration, G. Abbiendi, et al. Total hadronic cross-section of photon-photon interactions at LEP. *Eur. Phys. J. C*, 14:199, 2000. URL `doi:10.1007/s100520000352`.

[35] A. de Roeck. Total $\gamma-\gamma$ and $\gamma^*-\gamma^*$ cross sections measured at LEP. *Nucl. Phys. B, Proc. Suppl.*, 99(1–2):144–147, 2001. hep-ph/0101076.

[36] L. D. Landau, V. B. Berestetskii, E. M. Lifshitz, and L. P. Pitaevskii. *Relativistic quantum theory*. Course on Theoretical Physics. Pergamon, Oxford, 1971. Trans. from the Russian.

[37] G. A. Schuler and T. Sjöstrand. A scenario for high-energy $\gamma\gamma$ interactions. *Z. Phys. C*, 73: 677–688, May 1996. doi: 10.1007/s002880050359. hep-ph/9605240. CERN-TH-96-119. LUTP-96-13. oai:cds.cern.ch:302680.

[38] T. Barklow, D. Dannheim, O. Sahin, and D. Schulte. Simulation of $\gamma\gamma$ to hadrons background at CLIC. Technical report, CERN, 2011. LCD-Note-2011-020.

[39] T. Sjostrand. High-energy physics event generation with PYTHIA 5.7 and JETSET 7.4. *Comput. Phys. Commun.*, 82:74–90, 1994. doi: 10.1016/0010-4655(94)90132-5.

[40] The $\gamma\gamma \to$ hadron event samples were provided by D. Schulte.

[41] P. Schmüser. *Feynman-Graphen und Eichtheorien für Experimentalphysiker*. Springer-Verlag, Berlin, 2^{nd} edition, 1995.

[42] D. A. Karlen. *A Study of low Q^2 Radiative Bhabha Scattering*. PhD thesis, Stanford University, 1988. SLAC-325.

[43] S. Jadach, W. Placzek, and B. F. L. Ward. BHWIDE 1.00: $\mathscr{O}(\alpha)$ YFS exponentiated Monte Carlo for Bhabha scattering at wide angles for LEP1/SLC and LEP2. Technical report, CERN, Geneva, Aug 1996. hep-ph/9608412. UTHEP-95-1001. oai:cds.cern.ch:309289.

[44] W. Kilian, T. Ohl, and J. Reuter. WHIZARD: Simulating multi-particle processes at LHC and ILC. *Eur. Phys. J. C*, 71(9), 2011. hep-ph/0708.4233.

[45] M. Moretti, T. Ohl, and J. Reuter. O'Mega: An optimizing matrix element generator. Technical report, Desy, 2001. hep-ph/0102195. LC-TOOL-2001-040-rev.

[46] W. Placzek et al. Precision calculation of Bhabha scattering at LEP. In *4th International Symposium on Radiative Corrections : Application of Quantum Field Theory to Phenomenology*, Barcelone, Spain, Sept 1998. hep-ph/9903381. CERN-TH-99-007. UTHEP-98-1101.

[47] C. Rimbault, P. Bambade, K. Mönig, and D. Schulte. Impact of beam-beam effects on precision luminosity measurements at the ILC. *J. Instrum.*, 2:P09001, 2007. doi: 10.1088/1748-0221/2/09/P09001.

[48] The WHIZARD sample of Bhabha events was provided by S. Poss.

[49] B. Dalena and D. Schulte. Beam-beam background in CLIC in presence of imperfections. Technical report, CERN, 2010. CERN-ATS-2010-080. CLIC-Note-835.

[50] R. Tomás et al. Summary of the bds and mdi clic08 working group. Technical report, CERN, Geneva, Oct 2008. CERN-OPEN-2009-018. CLIC-Note-776. oai:cds.cern.ch:1216866.

[51] M. Modena and A. Vorozhtsov. Status of CLIC magnets studies. In *2nd International Particle Accelerator Conference (IPAC)*, San Sebastián, Spain, Sept 2011. CERN-ATS-2011-256. oai:cds.cern.ch:1407909.

[52] R. B. Appleby, M. Salt, L. C. Deacon, and E. Gschwendtner. Background and energy deposition studies for the clic post-collision line. In *2nd International Particle Accelerator Conference (IPAC)*, San Sebastián, Spain, Sept 2011. EuCARD-CON-2011-016. oai:cds.cern.ch:1403134.

[53] ILD Concept Group. The international large detector letter of intent, 2009. URL `http://ilcild.org`. DESY-09-087. arXiv:1006.3396v1.

[54] H. Aihara, P. Burrows, and M. Oreglia, editors. *SiD Letter of Intent*. ILC, Oct 2009. arXiv:0911.0006.

[55] M. A. Thomson. Particle flow calorimetry and the PandoraPFA algorithm. *Nucl. Instrum. Methods Phys. Res., Sect. A*, 611(1):25–40, 2009. ISSN 0168-9002. doi: 10.1016/j.nima.2009.09.009. URL `http://www.sciencedirect.com/science/article/pii/S0168900209017264`. arXiv:0907.3577. CU-HEP-09-11.

[56] A. Münnich and A. Sailer. The CLIC_ILD_CDR geometry for the CDR Monte Carlo mass production. Technical report, CERN, 2011. LCD-Note-2011-002.

[57] D. Dannheim and M. Vos. Layout simulation studies for the vertex and tracking region of the CLIC detectors. Technical report, CERN, 2011. LCD-Note-2011-031.

[58] M. Killenberg and J. Nardulli. Tracking performance and momentum resolution of the CLIC_ILD detector for single muons. Technical report, CERN, 2011. LCD-Note-2011-013.

[59] M. Killenberg and J. Nardulli. Tracking performace in high multiplicity environment for the CLIC_ILD detector. Technical report, CERN, 2011. LCD-Note-2011-014.

[60] A. Lucaci-Timoce and R. Diener. Description of the HCal detector in Mokka. Technical report, DESY, 2008.

[61] E. van der Kraaij and B. Schmidt. Muon system design studies for detectors at CLIC. Technical report, CERN, 2011. LCD-Note-2011-008.

[62] J. Marshall, A. Münnich, and M. A. Thomson. PFA: Particle flow performance at CLIC. Technical report, CERN, 2011. LCD-Note-2011-028.

[63] E. van der Kraaij and J. Marshall. Development of the PANDORA PFA New muon reconstruction algorithm. Technical report, CERN, 2011. LCD-Note-2011-004.

[64] J. Resta-López and P. N. Burrows. The beam-based intra-train feedback system of CLIC. In *1st International Particle Accelerator Conference (IPAC)*, Kyoto, Japan, May 2010.

[65] B. Dalena, D. Schulte, and R. Tomas. Impact of the experiment solenoid on the CLIC luminosity. In *1st International Particle Accelerator Conference (IPAC)*, Kyoto, Japan, May 2010. CERN-ATS-2010-081. CLIC-Note-831. oai:cds.cern.ch:1271354.

[66] FCal Collaboration, H. Abramowicz, et al. Forward instrumentation for ILC detectors. *J. Instrum.*, 5:12002, 2010. arXiv:1009.2433v2.

[67] I. Sadeh et al. A luminosity calorimeter for CLIC. Technical report, CERN, 2009. LCD-Note-2009-002.

[68] H. Gerwig. Private communication, 2011.

[69] H. Abramowicz et al. Influence of the shape of the beampipe on the luminosity measurement at the ILC. Technical report, Tel Aviv University, 2008. LC-PHSM-2008-007.

[70] FCal Collaboration, H. Abramowicz, et al. Instrumentation of the very forward region of a linear collider detector. *IEEE Transactions on Nuclear Science*, 51(6):2983–2989, Dec 2004.

[71] P. Mora de Freitas and H. Videau. Detector simulation with MOKKA / GEANT4: Present and future. In *International Workshop on Linear Colliders (LCWS)*, Jeju Island, Korea, Aug 2002. URL `http://www-flc.desy.de/lcnotes/notes/LC-TOOL-2003-010.ps.gz`. LC-TOOL-2003-010.

[72] S. Agostinelli et al. GEANT4 – a simulation toolkit. *Nucl. Instrum. Methods Phys. Res., Sect. A*, 506(3):250–303, July 2003. URL `http://www.sciencedirect.com/science/article/B6TJM-48TJFY8-5/2/23ea98096ce11c1be446850c04cfa498`.

[73] J. Allison et al. Geant4 developments and applications. *IEEE T. Nucl. Sci.*, 53(1):270–278, Feb 2006. doi: 10.1109/TNS.2006.869826.

[74] F. Gaede et al. LCIO: A persistency framework for linear collider simulation studies. Technical report, SLAC, 2003. physics/0306114. SLAC-PUB-9992.

[75] F. Hartmann. *Evolution of silicon sensor technology in particle physics*. Springer tracts in modern physics. Springer, Berlin, 2009.

[76] M. Moll. *Radiation damage in silicon particle detectors: microscopic defects and macroscopic properties*. PhD thesis, Universität Hamburg, Hamburg, 1999. oai:cds.cern.ch:425274.

[77] Hall G. Semiconductor particle tracking detectors. *Rep. Prog. Phys.*, 57(5):481–531, 1994.

[78] M. Moll. Radiation tolerant semiconductor sensors for tracking detectors. *Nucl. Instrum. Methods Phys. Res., Sect. A*, 565(1):202–211, 2006.

[79] R. Wunstorf et al. Damage-induced surface effects in silicon detectors. *Nucl. Instrum. Methods Phys. Res., Sect. A*, 377(2–3):290–297, 1996. ISSN 0168-9002. doi: 10.1016/0168-9002(96)00218-5. URL `http://www.sciencedirect.com/science/article/pii/0168900296002185`. Proceedings of the Seventh European Symposium on Semiconductor.

[80] J. Wüstenfeld. *Characterisation of Ionisation-Induced Surface Effects for the Optimisation of Silicon-Detectors for Particle Physics Applications*. PhD thesis, Universität Dortmund, 2001.

[81] F. Gaede. Marlin and LCCD: Software tools for the ILC. *Nucl. Instrum. Methods Phys. Res., Sect. A*, 559:177–180, 2006.

[82] R. Brun and F. Rademakers. ROOT – an object oriented data analysis framework. *Nucl. Instrum. Methods Phys. Res., Sect. A*, 389(1–2):81–86, Apr 1997. Proceedings AIHENP'96 Workshop, Lausanne, Sep. 1996.

[83] A. Vasilescu (INPE Bucharest) and G. Lindstroem (University of Hamburg). Displacement damage in silicon, on-line compilation, 2000. URL `http://sesam.desy.de/members/gunnar/Si-dfuncs.html`.

[84] A. Seryi, T. Maruyama, and B. Parker. IR optimization, DID and anti-DID. Technical Report SLAC-PUB-11662, SLAC, Stanford, CA, Feb 2006.

[85] M. Anduze, H. Videau, and M. Joré. Note on the beam tube for ILD. Technical report, ILD, 2009.

[86] A. A. Alves et al. The LHCb detector at the LHC. *J. Instrum.*, 3:S08005, 2008. Also published by CERN Geneva in 2010.

[87] W.-M. Yao et al. Review of particle physics. *J. Phys. G: Nucl. Part. Phys.*, 33(1):1+, 2006. doi: 10.1088/0954-3899/33/1/001. URL `http://pdg.lbl.gov`.

[88] M. Killenberg. Occupancy in the CLIC_ILD time projection chamber. Technical report, CERN, 2011. LCD-Note-2011-029.

[89] A. Cattai, L. Linssen, and A. Sapronov. CLIC forward region studies status report. In *Proceedings of the Workshop of the Collaboration on Forward Calorimetry at ILC*, Belgrade, Serbia, Sept 2008.

[90] W. de Boer et al. Radiation hardness of diamond and silicon sensors compared. *Phys. Status Solidi*, 204(9):3004–3010, Sept 2007. arXiv:0705.0171.

[91] C. Coca et al. Expected electromagnetic and neutron doses for the BeamCal at ILD. *Rom. Journ. Phys.*, 55(7–8):687–706, 2010.

[92] S. P. Martin. A supersymmetry primer, 2011. hep-ph/9709356v6.

[93] P. Bechtle et al. Prospects for the study of the $\tilde{\tau}$ system in sps1a' at the ILC. *Phys. Rev. D*, 82(5), 2010. hep-ex/0908.0876v2.

[94] M. Battaglia et al. Physics performances for scalar electrons, scalar muons and scalar neutrinos searches at CLIC. Technical report, CERN, 2011. LCD-Note-2011-018.

[95] O. Novgorodova. Studies on the electron reconstruction efficiency for the beam calorimeter of an ILC detector. In *International Workshop on Linear Colliders (LCWS)*, Beijing, China, June 2010. arXiv:1006.3402.

[96] S. Kulis and M. Idzik. Study of readout architectures for triggerless high event rate detectors at CLIC. Technical report, CERN, 2011. LCD-Note-2011-015.

[97] E. W. Weisstein. Inverse tangent, 2012. URL `http://mathworld.wolfram.com/InverseTangent.html`. From MathWorld–A Wolfram Web Resource.

[98] J. L. Feng and D. E. Finnell. Squark mass determination at the next generation of linear e^+e^- colliders. *Phys. Rev. D*, 49:2369–2381, Mar 1994. doi: 10.1103/PhysRevD.49.2369. URL `http://link.aps.org/doi/10.1103/PhysRevD.49.2369`.

[99] M. Battaglia et al. Updated post-WMAP benchmarks for supersymmetry. *Eur. Phys. J. C*, 33(2):273–296, Mar 2004.

[100] T. Sjöstrand, L. Lönnblad, and S. Mrenna. Pythia 6.2 physics and manual. Technical Report hep-ph/0108264, Lunds Univ. Dept. Theor. Phys., Lund, Aug 2001.

[101] H. W. Baer, F. E. Paige, S. D. Protopopescu, and X. Tata. ISAJET 7.48: A Monte Carlo event generator for pp, $\bar{\mathrm{p}}\mathrm{p}$ and $\mathrm{e}^+\mathrm{e}^-$ interactions. Technical Report hep-ph/0001086, Jan 2000.

[102] The $\mathrm{e}^+\mathrm{e}^- \to \tilde{\tau}^+\tilde{\tau}^-$ event sample was provided by M. Battaglia.

[103] V. M. Budnev, I. F. Ginzburg, G.V. Meledin, and V.G. Serbo. The two-photon particle production mechanism. physical problems. applications. equivalent photon approximation. *Physics Reports*, 15(4):181–282, 1975. ISSN 0370-1573. doi: 10.1016/0370-1573(75)90009-5. URL `http://www.sciencedirect.com/science/article/pii/0370157375900095`.

[104] F. A. Berends, P. H. Daverveldt, and R. Kleiss. Monte Carlo simulation of two-photon processes: I: Radiative corrections to multiperipheral $\mathrm{e}^+\mathrm{e}^-\mu^+\mu^-$ production. *Comput. Phys. Commun.*, 40(2–3):271–284, 1986. ISSN 0010-4655. doi: 10.1016/0010-4655(86)90114-1. URL `http://www.sciencedirect.com/science/article/pii/0010465586901141`.

[105] J. Nardulli. Particle identification algorithm for the CLIC_ILD and CLIC_SiD detectors. Technical report, CERN LCD, 2011. CERN LCD-Note-2011-005.

[106] A Besson et al. A vertex detector for the international linear collider based on CMOS sensors. *Nucl. Instrum. Methods Phys. Res., Sect. A*, 568(1):233–239, 2006. doi: 10.1016/j.nima.2006.05.279.

[107] ATLAS Collaboration, G. Aad, et al. The ATLAS experiment at the CERN large hadron collider. *J. Instrum.*, 3:S08003. 437 p, 2008. Also published by CERN Geneva in 2010.

List of Publications

[1] A. Sailer. Studies of the measurement of differential luminosity using Bhabha events at the international linear collider. Diplomarbeit, Humboldt-Universiät zu Berlin, 2009.

[2] FCal Collaboration, J. Aguilar and A. Sailer, editors. Report for the ILC detector R&D Panel instrumentation of the very forward region, 2009.

[3] FCal Collaboration, H. Abramowicz, et al. Forward instrumentation for ILC detectors. *J. Instrum.*, 5:12002, 2010. arXiv:1009.2433v2.

[4] E. Teodorescu and A. Sailer. Radiation dose to the QD0 quadrupole in the CLIC interaction region. Technical report, CERN, 2010.

[5] A. Sailer. Simulations of beam-beam background at CLIC. In *Proceedings of the Linear Collider Workshop (LCWS)*, Beijing, China, 2010.

[6] E. Gschwendtner et al. The CLIC post-collision line. In *International Particle Accelerator Conference (IPAC)*, 2010.

[7] M. Battaglia et al. Physics performances for scalar electrons, scalar muons and scalar neutrinos searches at CLIC. Technical report, CERN, 2011. LCD-Note-2011-018.

[8] A. Münnich and A. Sailer. The CLIC_ILD_CDR geometry for the CDR Monte Carlo mass production. Technical report, CERN-LCD, 2011.

[9] A. Sailer. Update on forward region layout and backgrounds at CLIC. In *Proceedings of the 18th FCal Collaboration Meeting*, Predeal, Romania, 2011.

[10] A. Sailer. Background in the calorimeter endcaps. In *Proceedings of the 19th FCal Collaboration Meeting*, Belgrade, Serbia, 2011.

[11] D. Dannheim and A. Sailer. Beam-induced backgrounds in the CLIC detectors. Technical report, CERN-LCD, 2011.

[12] D. Dannheim et al. CLIC background studies and optimization of the innermost tracker elements. In *Proceedings of the International Workshop on Linear Colliders (LCWS)*, Granada, Spain, October 2011.

[13] CLIC Detector Study, L. Linssen, A. Miyamoto, M. Stanitzki, and H. Weerts, editors. *Physics and Detectors at CLIC: CLIC Conceptual Design Report*. CERN, 2012. CERN-2012-003.

Abbreviations and Acronyms

ATLAS	A Toroidal LHC Apparatus
BDS	Beam Delivery System
BPM	Beam Position Monitor
BX	Bunch Crossing
CDR	Conceptual Design Report
CLIC	Compact Linear Collider
CMS	Compact Muon Solenoid
ECal	Electromagnetic Calorimeter
ETD	Endcap Tracking Disk
FTD	Forward Tracking Disk
HCal	Hadronic Calorimeter
HP	High Precision
ILC	International Linear Collider
ILD	International Large Detector
IP	Interaction Point
IR	Interaction Region
LCIO	Linear Collider I/O—the persistent data format used in the linear collider detector studies.
LEP	Large Electron–Positron Collider
LHC	Large Hadron Collider
LSP	Lightest Supersymmetric Particle
MIP	Minimum Ionising Particle
NIEL	Non-Ionising Energy Loss

QD0	final focus quadrupole
RF	Radio Frequency
RPC	Resistive Plate Chamber
SET	Silicon External Tracker
SIT	Silicon Inner Tracker
SiD	Silicon Detector
SM	Standard Model
SuSy	Supersymmetry
TID	Total Ionising Dose
TPC	Time Projection Chamber
VXD	Vertex Detector

Acknowledgement

This work was supported by the Bundesministerium für Bildung und Forschung by creating the Wolfgang-Gentner programme, giving me the opportunity to work in the inspiring environment of CERN.

I would like to thank the linear collider community in general, especially Frank Gaede, Steve Aplin, Paulo Mora de Freitas, and Gabriel Musat for the help with the simulation and analysis software.

Thanks to Barbara Dalena, Jakob Esberg, and Daniel Schulte for many discussions about GUINEAPIG and the help with the various background samples, to Hubert Gerwig and Andrea Gaddi for the crash course in detector engineering, and Ray Veness for the discussions about the vacuum tubes. Thanks to Iftach Sadeh and Adrian Vogel for getting me started.

I also want to thank all the current and former members of the Linear Collider Detector group at CERN for a great environment, both at and away from work. I am most thankful to Konrad Elsener and Lucie Linssen for the guidance and supervision, and for giving me the opportunities and responsibilities to grow, both as a person and as a physicist.

Last but not least my thanks go to my parents for always being there.

Selbständigkeitserklärung

Ich erkläre, dass ich die vorliegende Arbeit selbständig und nur unter Verwendung der angegebenen Literatur und Hilfsmittel angefertigt habe.

Berlin, den 9.05.2012 André Sailer